Nitrogen cycling in the South Atlantic and South Indian Oceans investigated using nitrate isotopes: implications for nutrient supply, ocean fertility, carbon export, and climate

Tanya Anne Marshall

A thesis presented for the degree of
Doctor of Philosophy

Department of Oceanography
Faculty of Science
University of Cape Town
Supervisor: Associate Professor Sarah E. Fawcett

June 2023

Plagiarism declaration

I know the meaning of plagiarism and declare that all of the work in this thesis, except for that which is properly acknowledged, is my own. The contents of this thesis have not been submitted in whole or in part for consideration for any other degree or qualification in this, or any other university. This thesis does not include any work as a result of collaboration unless specified in the text.

I confirm that I have been granted permission by the University of Cape Town's Doctoral Degrees Board to include the following publications in my PhD thesis, and where co-authorships are involved, my co-authors have agreed that I may include the publications:

1. Marshall, T. A., Granger, J., Casciotti, K. L., Dahnke, K., Emeis, K. C., Marconi, D., McIlvin, M.E., Noble, A.E., Saito, M.A., Sigman, D.M. and Fawcett, S.E., (2022). The Angola Gyre is a hotspot of dinitrogen fixation in the South Atlantic Ocean. Nature Communications Earth & Environment, 3(151), 151. https://doi.org/10.1038/s43247-022-00474-x
2. Marshall, T. A., Sigman, D. M., Beal, L. M., Foreman, A., Martínez-García, A., Blain, S., Campbell, E., Fripiat, F., Granger, R., Harris, E., Haug, G.H., Marconi, D., Oleynik, S., Rafter, P.A., Roman, R., Sinyanya, K., Smart, S.M., and Fawcett, S.E. (2023). The Agulhas Current transports signals of local and remote Indian Ocean nitrogen cycling. Journal of Geophysical Research: Oceans, 128, e2022JC019413. https://doi.org/10.1029/2022JC019413

Signature: Signed by candidate Date: 30 June 2023

Student Name: Tanya Marshall Student Number: MRSTAN001

Acknowledgements

I would like to acknowledge the Department of Oceanography at UCT, which has been my home since embarking on my B.Sc. Hons in 2016. Prof Isabelle Ansorge, I vividly remember attending my first Oceanography lecture in 2014 where you spoke about heat and salt transport via Agulhas leakage. I would not have been in that lecture without Casey Lyttle asking me to accompany her. Isabelle, I am so appreciative of all your efforts to listen to postgraduate students and morph the department into what it is today. Cashifa, the heart and soul of the department, thank you for remedying any problem with your magic, and for always having an open door. Raymond, thank you for listening to my (CTD/ADCP) struggles and for going the extra mile to help me understand the route of my data troubles.

To the Fawketieri Group, our early isotope journal club meetings filled with mass confusion and plenty note making will always make me smile (I still have these notes!). Thank you for all the laughs, challenges, and feedback, and for keeping friendly peer review alive during the COVID pandemic. Raq, thanks for always offering a helping hand and for being a sounding board for all things N isotopes. Jess, I could not have done this without your shoulder to cry on and definitely not without our strictly work-oriented Zoom calls.

To all the brilliant scientists and collaborators that have nurtured, encouraged, and inspired me along the way, thank you. I am especially grateful to Katye Altieri, Lisa Beal, Julie Granger (my fairy godmother), and Danny Sigman. Thank you for listening to all my ideas, fielding my questions, and guiding me toward being a more well-rounded scientist.

To my inherited and chosen family, thank you for your support and kindness on this journey. The saying, "*it takes a village*" couldn't be truer, most family members have labelled, taped, cut, emptied, stacked, and packed sample bottles (and always with a smile). Mom and Dad, thank you for cheering me on when I decided to choose this career path, for listening to practise presentations, for proof reading my writing, for listening to my struggles over coffee, wine, and trails, and for your relentless, unwavering, persistent, never-ending belief in me – it means the most! To my husband, Fred, thank you for being a team player when it counted most, for allowing me one-sided work discussions that only became verbal mid-way through, and for kindly pretending to follow along as I drew out all my ideas for figures on paper. Your support has been, and continues to be, instrumental.

Lastly, to the boss, Sarah. There are not enough words to describe my gratitude for you. Compiling this thesis has allowed me to reflect on the past six and a half years, which have been filled to the brim with the brain expanding science. Thank you for investing in me, giving me the freedom to explore 1 billion rabbit holes, for trusting me to think independently, for never diminishing my curiosity, and of particular importance, for allowing me to give a voice to the South Atlantic (and South Indian) Ocean. I look forward to conducting very nerdy science together in future.

Funding sources for this work are gratefully acknowledged: The South African National Research Foundation (114673, 130826), the University of Cape Town (960000000356), and the VC doctoral research scholarship and postgraduate funding.

Thesis abstract

Bioavailable nitrogen (N) limits phytoplankton growth across much of the (sub)tropical ocean, thereby modulating ocean fertility and climate. Dinitrogen (N_2) fixation is the dominant source of new N to the ocean and is thought to occur mainly in well-lit, warm, oligotrophic waters. The under-sampled South Atlantic and South Indian Ocean basins are predicted by models to host widespread N_2 fixation; for the South Atlantic, this predication contradicts the limited available observations and for the South Indian, is yet to be confirmed by measurements. In this thesis, four new nitrate isotope datasets from the South Atlantic and South Indian Oceans are presented alongside coincident nutrient and hydrographic data, and other published nitrate isotope datasets. Combined, these data provide a means of quantifying the rate and distribution of N_2 fixation, along with characterizing additional co-occurring N cycle processes, mechanisms of subsurface nutrient supply, and water mass circulation.

Measurements of nitrate N isotope ratios ($\delta^{15}N$) and nutrient stoichiometry (i.e., nitrate to phosphate ratios; N:P) from a zonal transect of the tropical South Atlantic (at ~12°S) and a meridional transect along the Angola margin (at ~12°E) reveal an N_2 fixation hotspot in the eastern tropical Angola Gyre. Here, thermocline nitrate $\delta^{15}N$ is low and N:P is high relative to the underlying source water and the western tropical basin thermocline. The N_2 fixation rate estimated from the Angola Gyre nitrate $\delta^{15}N$ data of 1.4-5.4 Tg N.a^{-1} accounts for 28-108% of the rate predicted for the South Atlantic basin. These findings contradict recent model diagnoses of N_2 fixation, which predict high rates in the western tropical basin and none to the east. The overlapping biogeography of a basin-wide P excess relative to N and bioavailable iron supplied locally from the Angola margin likely control N_2 fixation in the Angola Gyre. Analogous conditions elsewhere in the ocean, such as in other eastern boundary shadow zones and retentive near-coast subtropical systems, should also favour N_2 fixation.

The western boundary current of the South Indian Ocean, the Agulhas Current, is the strongest boundary current on Earth, yet nutrient cycling in this subtropical system remains largely uncharacterized. Measurements of the dual isotope ratios (N and oxygen) of nitrate from within and upstream of the greater Agulhas region provide insights into regional circulation and N cycle dynamics. The nitrate isotopes reveal both local and remote signals of Indian Ocean N cycling such as denitrification in the Arabian Sea and partial nitrate assimilation in Southern Ocean surface waters, as well as evidence of local N_2 fixation and coupled partial nitrate assimilation and nitrification. Using a one-box model to simulate the newly-fixed nitrate flux, the local N_2 fixation rate for the greater Agulhas region is estimated to be 7-25 Tg N.a^{-1}; this value is the first observation-based N_2 fixation rate estimate for the South

Indian Ocean. Local N cycling imprints an isotopic signal on Indian Ocean nitrate that can be tracked beyond the Indian Ocean because it persists in Agulhas eddies that “leak” into the South Atlantic at the Agulhas Retroflection. If this signal is retained in plankton that sink to the seafloor, it could be used to reconstruct past Agulhas leakage, yielding quantitative insights into the strength of the Atlantic Meridional Overturning Circulation in the past.

The Agulhas Current system, like other western boundary current systems, is characterised by high energy and turbulence. A novel application of the dual isotopes of nitrate reveals the occurrence of three (sub)mesoscale mechanisms of upward nitrate supply; entrainment at the edges of a mesoscale anticyclonic eddy, inshore upwelling likely driven by a frontal eddy, and overturning at the offshore edge of the current core likely driven by coupled mesoscale-submesoscale instabilities. The intensity and (sub)surface expression of these nutrient supply events are not always apparent in the hydrographic data, highlighting the utility of the nitrate isotopes for exploring physical ocean processes. The conditions driving the nitrate supply mechanisms in the Agulhas region are common to western boundary currents, implying that the (sub)mesoscale vertical nitrate supply is quantitatively significant at the global scale. Additionally, these events of upward nitrate supply likely increase regional fertility in all western boundary current systems, with implications for the sustenance of higher trophic levels. Finally, increasing turbulence observed along mid-latitude western boundaries may enhance the upward nutrient supply to subtropical surface waters, and possibly compensate for the diminished productivity predicted as a result of increasing subtropical gyre stratification.

Collectively, the work detailed in this thesis reveals the strong regionality of N cycling in the historically under-studied South Atlantic and South Indian Oceans, as well as the importance of interpreting biogeochemical data in the context of ocean dynamics across various scales. Improved predictions of N fluxes at the basin- and global scale, which are critical for estimating the ocean’s CO_2 sink and fertility, will require careful consideration of these southern basins so as not to mischaracterise their functioning, as has occurred in the past.

Table of contents

List of figures and tables

Chapter 1:

Chapter 2:

Appendix A:

Chapter 3:

Appendix B:

Chapter 4

1. Introduction and literature review

1.1. Nitrogen in the ocean

Nitrogen (N) is essential for all life on Earth, including for phytoplankton in the sunlit, surface ocean. The availability of N therefore strongly controls both the rate and distribution of primary productivity, with implications for the extent to which marine organisms remove atmospheric carbon dioxide (CO_2) and thus modulate climate (Falkowski, 1997; Moore, et al., 2013). For millennia, the ocean has played a role in changing Earth's climate through its influence on atmospheric CO_2 concentrations (Barnola, et al., 1987; Petit, et al., 1999; Lüthi, et al., 2008). Estimates of the sources and sinks of marine N are used to approximate budgets, which can be used to infer ocean productivity. Uncertainties around global N fluxes, as well as changes in these fluxes over time, cloud our understanding of ocean fertility and carbon export (Codispoti, 1995; Gruber & Sarmiento, 1997; Brandes & Devol, 2002; Deutsch, et al., 2007; Codispoti, 2007; Weber & Deutsch, 2014; Somes & Oschlies, 2015; Wang, et al., 2019). Improving our knowledge of N fluxes, their natural variability, and how anthropogenic activities might perturb the N cycle, is important for predicting future changes to climate.

The global marine N budget, that is, the sum of all sources and sinks (Figure 1.1), is largely microbially-mediated. N_2 fixation is the ultimate source of bioavailable ("fixed") N to the ocean. This process typically occurs in warm, sunlit regions of the ocean, such as the surface waters of the subtropics and tropics (Landolfi, et al., 2018; Zehr & Capone, 2021). Observation- and model-based estimates of N_2 fixation for the global ocean range ~2.5 fold, from 89-213 Tg $N.a^{-1}$ (Gruber & Sarmiento, 1997; Deutsch, et al., 2007; Luo, et al., 2012; Landolfi, et al., 2018; Wang, et al., 2019). Denitrification, including anaerobic ammonium oxidation (i.e., anammox), is the dominant sink of fixed N and occurs under the (near-)anoxic conditions that occur in the water column of the ocean's oxygen deficient zones (ODZs) and sediments. Estimates of oceanic denitrification rates based on observations and models range ~2 fold, from 170-300 Tg $N.a^{-1}$ (Gruber & Sarmiento, 1997; Brandes & Devol, 2002; Codispoti, 2007; DeVries, et al., 2013; Wang, et al., 2019), and on average, exceed rates of N_2 fixation. Other processes also supply fixed N to the ocean, such as atmospheric deposition (~32 Tg $N.a^{-1}$) and river runoff (~40 Tg $N.a^{-1}$) (Duce, et al., 1991; Jickells, et al., 2017; Wang, et al., 2019), both of which are quantitatively less significant than N_2 fixation. The apparent imbalance of global N sources and sinks has been interpreted as indicating that the ocean is losing N (Codispoti, 1995; Codispoti, 2007), although this idea is disputed by many researchers (Brandes & Devol, 2002; Deutsch, et al., 2007; Weber & Deutsch, 2014; Wang, et al., 2019). A more likely explanation, that in part stems from the large uncertainties in estimates of global ocean N fluxes, is that our current understanding of the controls on the rates and distributions of N sources and sinks is inadequate, which limits our ability to accurately quantify and characterise them.

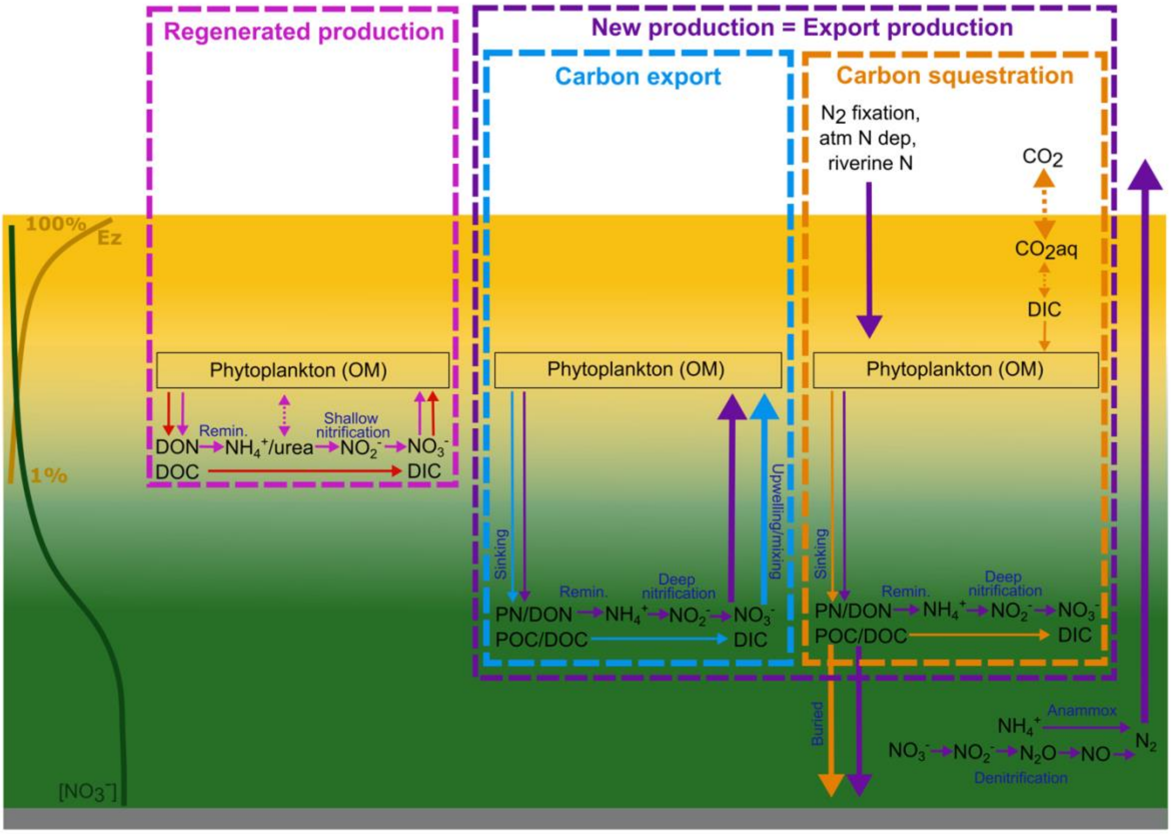

Figure 1.1. Overview of the marine nitrogen cycle, the new production paradigm, and its implications for carbon export and sequestration. Sunlight rapidly attenuates in the surface ocean (mustard shading and profile), with the depth of 1% of surface photosynthetically-available radiation indicating the base of the euphotic zone (Ez). Nutrients such as nitrate (NO_3^-) exist in high concentrations below the Ez (green shading and profile). Phytoplankton consume NO_3^- and other N forms and nutrients to grow their organic matter (OM); some amount of this OM is released from phytoplankton cells as dissolved organic N and carbon (DON and DOC), while most remain as particulate N (PN). The remineralisation of DON and PN by heterotrophic bacteria and consumption of PN by zooplankton releases ammonium (NH_4^+) and/or simple organic compounds such as urea into the water column. Heterotrophic bacteria coincidentally respire DOC to produce CO_2, which rapidly equilibrates with other forms of dissolved inorganic carbon (DIC, including carbonate and bicarbonate). In the Ez, the recycled NH_4^+ is rapidly re-consumed by phytoplankton, while in aphotic waters, it is oxidised to nitrite (NO_2^-) and then NO_3^- by nitrifying microorganisms. N is ultimately supplied to the ocean via N_2 fixation and to a lesser extent via atmospheric deposition and rivers. N is removed from the ocean via canonical denitrification (the stepwise reduction of NO_3^- to NO_2^- to nitrous oxide (N_2O) to nitric oxide (NO) and finally, to N_2 gas) and anammox (the anaerobic oxidation of ammonium by NO_2^- to N_2 gas), both of which produce inert N_2 gas that is ultimately lost to the atmosphere. In a mass balance sense, productivity fuelled by regenerated N (e.g., NH_4^+**,** urea, and NO_2^- and NO_3^- produced via nitrification in the Ez) equates to no OM export (pink box) (Dugdale & Goering, 1967; Bronk, et al., 1994; Yool, et al., 2007). By contrast, productivity fuelled by N that is new to the Ez (e.g., NO_3^- produced via subsurface nitrification that is mixed up into the Ez, N_2 fixation, atmospheric N deposition, and riverine N) must be balanced by OM export out of the surface layer over appropriate timescale, typically annually

(purple box) (Dugdale & Goering, 1967; Eppley & Peterson, 1979; Bronk, et al., 1994; Yool, et al., 2007). In the case of new production fuelled by subsurface NO_3^- mixed up into the euphotic zone, the resultant carbon export offsets the DIC upwelled alongside the NO_3^- (blue box). By contrast, the new production fuelled by N from N_2 fixation, atmospheric N deposition, and riverine N, while also exporting carbon, results in atmospheric CO_2 sequestration in the ocean interior (orange box).

Once supplied, fixed N is rapidly recycled within the ocean (Figure 1.1). A simple view of the marine N cycle is as follows; N_2 gas dissolved in the surface ocean from the atmosphere is "fixed" into a bioavailable form by specialised plankton (termed diazotrophs), with the subsequent remineralisation of the particulate organic N (PN) biomass of diazotrophs yielding newly-fixed N, which other phytoplankton can incorporate into their biomass. Most PN breaks down to form dissolved organic N (DON), while a small amount sinks to the deep ocean. The remineralisation by heterotrophic organisms of PN and some DON yields ammonium (NH_4^+), which is rapidly re-consumed by phytoplankton in the sunlit upper layer or nitrified at depth. During nitrification, ammonium is oxidised to nitrite (NO_2^-), and then nitrate (NO_3^-). Nitrate is then ultimately denitrified back to N_2 gas in the ODZs and sediments, and the N_2 gas is lost to the atmosphere. Both nitrification and denitrification can result in the production of N_2O, a potent greenhouse gas, with denitrification also removing N_2O through the formation of N_2 gas (Pan et al., 2023). A minute amount of fixed N trapped in sinking organic matter reaches the seafloor and is buried in the sediment, also representing N loss.

In the oligotrophic (sub)tropical ocean, the supply of bioavailable N to the sunlit upper layer typically exerts the dominant control on primary productivity (Smith, 1984; Codispoti, 1989). Here, nutrients including nitrate are supplied from the thermocline to (sub)tropical surface waters during deep winter and/or spring convective mixing (Michaels, et al., 1994; Williams & Follows, 2003; Lomas, et al., 2013). The injection of these nutrients fuels a brief period of elevated productivity, often classified as the spring bloom. Throughout summer, increased solar radiation warms and stratifies the upper water column, creating a density boundary that separates nutrient-rich thermocline waters from nutrient-poor surface waters. This strong stratification in summer through autumn inhibits the upward supply of nutrients. As such, primary productivity over the warm season is typically fuelled near-exclusively by N that is recycled within the shallow surface mixed layer (Menzel & Ryther, 1960; Lipschultz, et al., 2002). N_2 fixation can also supply N to surface waters to fuel productivity provided that the macro- and micro-nutrients required for this process are available. N_2 fixation rates are generally higher in summer when stratification impedes upward N supply, allowing diazotrophs to outcompete other phytoplankton, versus in winter when N is supplied from below and temporarily alleviates N limitation, although this seasonality appears to vary regionally (Orcutt, et al., 2001; Church, et al., 2009; Knapp, 2012; White, et al., 2018; Zehr & Capone, 2021).

Geochemical estimates of subtropical ocean primary productivity exceed those that can be supported by the nutrients supplied by both seasonal convective mixing and N_2 fixation (Shulenberger & Reid, 1981; Jenkins & Goldman, 1985; Michaels, et al., 1994; Orcutt, et al., 2001; McGillicuddy, et al., 1998; Emerson, et al., 2001; Stanley, et al., 2015). The implication of this imbalance is that other nutrient supply mechanisms must be important for fuelling primary productivity. For example, the mean N flux required to sustain primary productivity in the northwest Sargasso Sea is estimated to be 0.5 ± 0.14 mol $N.m^{-2}.a^{-1}$, while the sum of winter mixing, diapycnal diffusion, and advection amounts to 0.34 ± 0.07 mol $N.m^{-2}.a^{-1}$ (McGillicuddy, et al., 1998). The shortfall has been attributed to N_2 fixation, eddy-induced upwelling of nitrate, and other meso- and submesoscale ocean processes that drive an upward nitrate flux (Jenkins, 1988; Falkowski, et al., 1991; McGillicuddy, et al., 1998; Lipschultz, et al., 2002; Johnson, et al., 2010). Indeed, regions characterised by strong (sub)mesoscale instabilities (combined scales of 1-100 km, days to month), such as the mid-latitude western boundaries, are thought to host strong vertical nutrient fluxes; however, observations of these fluxes, and evidence for their impact on local productivity, are lacking (Lévy, et al., 2012; Lévy, et al., 2018). One reason for limited observations of (sub)mesoscale N fluxes is that the small spatio-temporal scales over which these fluxes operate are difficult to sample using traditional ship-based, discrete-depth sampling techniques. As such, the relative importance of the various N fluxes for fuelling subtropical ocean primary productivity remains uncertain.

The new production paradigm provides a framework within which to quantitatively assess ocean fertility; that is, the capacity of a marine system to sustain higher trophic levels (Dugdale & Goering, 1967). Phytoplankton growth fuelled by N that is newly available to the euphotic zone is termed “new production”, while phytoplankton growth supported by recycled forms of N is termed “regenerated production” (Dugdale & Goering, 1967). New production is fuelled by N_2 fixation and nitrate supplied to the euphotic zone from below the mixed layer, while regenerated production is supported by ammonium, simple dissolved organic compounds such as urea, and nitrate and nitrite produced in the euphotic zone (Figure 1.1; (Dugdale & Goering, 1967; Bronk, et al., 1994; Yool, et al., 2007)). Since both light and nutrients limit phytoplankton growth, the depth of the euphotic zone relative to the nutricline (taken here to be the depth at which the nitrate concentration reaches 1 μM, which in the (sub)tropics is largely coincident with the depth of the mixed layer) is important for characterizing new versus regenerated production. For example, in the (sub)tropics, the depth of the euphotic zone is typically between 100 and 170 m year-round, while the mixed layer depth (MLD) varies from as shallow as 20 m in summer to >300 m in winter (Stramska & Cieszyńska, 2015). As such, phytoplankton growth in summer is more strongly influenced by nutrient availability while in winter, light availability plays a dominant role. New and regenerated production have different implications for ocean fertility. New production increases primary productivity, thereby enhancing ocean fertility, while regenerated production maintains primary productivity with no net effect on fertility (Dugdale & Goering, 1967). In a mass balance sense, the flux of new N assimilated by plankton in the surface layer must equal the flux of N sinking out of the seasonal mixed layer as organic matter (Dugdale & Goering, 1967). The relationship between ocean fertility and carbon export and sequestration will be addressed in section 1.2.

1.2. The link between nitrogen, other ocean elements, and climate

Nitrogen is stoichiometrically linked to oxygen (O_2), carbon (C), and phosphorus (P) in that the average molar ratio in which these elements are altered in the global ocean is approximately -150 O_2:106 C:16 N:1 P (Redfield, 1934; Redfield, et al., 1963; Anderson & Sarmiento, 1994). This "Redfield ratio" reflects the average ratio in which typical marine plankton consume (during photosynthesis) and return (via organic matter remineralisation) these elements to the ocean (Redfield, 1934; Redfield, et al., 1963; Weber & Deutsch, 2010; Deutsch & Weber, 2012; Falkowski, 2012), although noting that significant regional variability exists in both seawater nutrients and plankton biomass (Anderson & Sarmiento, 1994; Martiny, et al., 2013; DeVries & Deutsch, 2014). Nevertheless, over appropriate scales of time and space, deviations from expected nutrient ratios yield insights into the biogeochemical processes occurring in the ocean. More specifically, deviations observed in global ocean nutrient ratios reflect changes to ocean processes occurring over centennial timescales (e.g., (Gruber & Sarmiento, 1997; Deutsch, et al., 2007; Weber & Deutsch, 2012)), while deviations in regional thermocline nutrient ratios reflect more local ocean processes occurring over annual to decadal timescales (e.g., (Marconi, et al., 2017; Peters, et al., 2018; Harms, et al., 2019)).

The ocean is estimated to be a net sink for 2-3 Pg C.a^{-1}, which amounts to 25-30% of the atmospheric CO_2 emitted by anthropogenic activities (Hauck, et al., 2020; Watson, et al., 2020). This carbon sink is both biologically- and physically-mediated via the biological and solubility pumps, respectively. Phytoplankton fix dissolved inorganic carbon (DIC; including CO_2) during photosynthesis to grow their biomass, thereby lowering surface ocean DIC concentrations and generating an air-sea CO_2 gradient that can drive a net flux of CO_2 into surface waters (Figure 1.1). The eventual sinking of surface-produced organic matter below the winter/spring mixed layer (i.e., below the depth of annual ventilation) results in the export of carbon, and other elements, from the surface ocean. The remineralisation of this organic matter returns carbon and nutrients to their inorganic forms. This biologically-driven removal of CO_2 from the atmosphere is referred to as the “biological carbon pump” (Volk & Hoffert, 1985). Additionally, upper ocean temperature strongly controls the solubility of CO_2 in the ocean, with cooler waters holding more gas than warmer waters. The circulation of cool, CO_2-rich surface waters to depth, typically via deep water formation, transports DIC to the deep ocean (Volk & Hoffert, 1985; Baker, et al., 2022). The physically-driven removal of carbon from the atmosphere is referred to as the “solubility pump”. While the solubility pump largely sets the magnitude of the oceanic carbon sink, the biological carbon pump generates a CO_2 (DIC) concentration gradient between the surface ocean and atmosphere that drives the solubility pump, thereby maintaining atmospheric CO_2 concentrations.

In the (sub)tropical ocean, the biological carbon pump is relatively weak in that the quantity of nutrients supplied to the surface waters is lower than in regions such as the Southern Ocean and eastern boundaries, resulting in less organic matter production and lower net carbon export (Sarmiento & Toggweiler, 1984; Falkowski, et al., 1998). However, the efficiency of the biological carbon pump in the (sub)tropical ocean is high in that on an annual basis, the nutrients supplied to the surface waters are completely consumed. In contrast, in regions such as the Southern Ocean where surface productivity is limited by micro- rather than macronutrients, the biological carbon pump is inefficient, making the Southern Ocean a “leak” in the global ocean’s carbon sink (Sarmiento & Toggweiler, 1984; Siegenthaler & Wenk, 1984; Knox & McElroy, 1984; Sigman & Hain, 2012). In theory, there are three mechanisms by which the biological carbon pump could increase the air-sea CO_2 flux, i) if surface ocean nutrients were more completely consumed in regions where they currently are not, ii) if the carbon-to-nutrient ratio of sinking organic matter increased, and iii) if the global ocean nutrient inventory increased (i.e., N addition in excess of N loss) (Sigman, et al., 2010). In the (sub)tropical ocean, the complete consumption of surface nutrients implies that only high carbon-to-nutrient organic matter, and increased N_2 fixation and/or decreased denitrification, are means by which the biological carbon pump could be strengthened.

The near-constant stoichiometry of carbon and N in the global ocean can be leveraged to quantify the biological carbon pump using the new production paradigm. Over appropriate timescales (i.e., annually), the magnitude of productivity fuelled by allochthonous nutrients (i.e., new production) must be balanced by the flux of organic matter out of the surface ocean (Figure 1.1) (Eppley & Peterson, 1979). The flux of sinking organic matter to the deep ocean, termed “export production”, is thus equivalent to new production (Eppley & Peterson, 1979). In other words, the consumption of N supplied to the surface ocean via N_2 fixation, atmospheric deposition, rivers, and various upward mixing mechanisms can be used to approximate the flux of carbon to the deep ocean (Dugdale & Goering, 1967; Bronk, et al., 1994; Yool, et al., 2007).

According to the new production paradigm, an increase in new production will equate to an increase in export production, and thus an enhanced flux of carbon into the deep ocean (Dugdale & Goering, 1967; Eppley & Peterson, 1979). However, increased carbon export does not necessarily drive higher atmospheric CO_2 removal (i.e., carbon sequestration; Figure 1.1). This is because the upward mixing of deep nitrate, which derives from organic matter remineralised at depth, also supplies a stoichiometric quantity of DIC to the surface, which will outgas to the atmosphere as CO_2. Phytoplankton consumption of upwelled nitrate and the subsequent fixation of DIC thus only compensates for the CO_2 lost during ventilation of deep waters. By contrast, N_2 fixation, atmospheric deposition, and rivers introduce new N to surface waters without supplying DIC, such that carbon production supported by this new N will drive the net removal of atmospheric CO_2.

Over the past millennia, climate (i.e., planetary temperature and ice volume) and atmospheric CO_2 concentrations appear to have varied in concert (Barnola, et al., 1987; Petit, et al., 1999; Lüthi, et al., 2008). The exchange of carbon between the ocean and atmosphere over glacial-interglacial cycles (at least the last two million years) has played an important role in climate regulation (Lüthi, et al., 2008; Sigman, et al., 2010). For example, during glacial periods, an increase in dust deposition to the iron-limited surface waters of the Subantarctic Southern Ocean is thought to have increased the efficiency of the Southern Ocean's biological carbon pump (i.e., the degree of nutrient utilisation), in net increasing carbon drawdown (Martin, 1990; Sigman, et al., 2010; Martínez-García, et al., 2014). Additionally, during ice ages, rates of (subtropical) N_2 fixation appear to have declined in response to reduced N loss (Altabet, et al., 1995; Ganeshram, et al., 1995; Ren, et al., 2009). The subsequent deglacial increase in both denitrification and N_2 fixation, and a decrease in atmospheric CO_2 concentrations, highlight the strong link between N and carbon over millennial timescales (Meckler, et al., 2007; Ren, et al., 2009). The impact of rising anthropogenic N sources to the ocean is predicted to increase the global ocean N inventory (Yang & Gruber, 2016), which could increase carbon export and decrease atmospheric CO_2 concentrations; however the net impact of a rise in allochthonous N supply on N_2 fixation and climate is still highly uncertain (Yang & Gruber, 2016; Wrightson & Tagliabue, 2020). Nonetheless, it is clear that N is a critical element in global ocean biogeochemistry, and that the supply of nutrients to the surface ocean has major implications for ocean fertility, carbon export, and climate.

1.3. Tools to study nitrogen cycling in the ocean

To understand ocean biogeochemistry, researchers observe, measure, reconstruct, and model the Earth system through time. Given the complexity of such a multiscale system, both integrative and instantaneous approaches are required to study the ocean. Combining knowledge provided by biogeochemical tools with information on physical ocean processes (e.g., circulation and residence time) offer a way to identify and quantify often overlapping biogeochemical processes that drive nutrient supply and cycling in the ocean.

1.3.1. Nitrogen isotope ratios

Nitrogen has two stable isotopes, atomically lighter ^{14}N and heavier ^{15}N. The lighter ^{14}N comprises 99.63% of all N on Earth. Due to its lower atomic mass, ^{14}N has a faster translational velocity than ^{15}N, such that many chemical and biological processes that transfer N from the substrate to the product pool preferentially transfer ^{14}N (Mariotti, et al., 1981; Sigman & Fripiat, 2019). The extent of the discrimination against ^{15}N, termed isotope fractionation, is governed by kinetics or thermodynamic equilibrium. In the case of the marine N cycle, most isotope fractionating processes are kinetic in that they are irreversible and unidirectional (Mariotti, et al., 1981; Sharp, 2017). The degree to which isotopes are fractionated by a process is quantified by the isotope effect (ε);

$$\varepsilon = (1 - {}^{15}k \div {}^{14}k) \times 10^3 \qquad \text{eq. 1.1}$$

where ^{15}k and ^{14}k are the rate coefficients of a reaction for ^{15}N and ^{14}N, respectively. When the isotope effect is relatively small (i.e., ε <<1000‰), it is approximated by the difference in the isotopic composition of the substrate and instantaneously-generated product. Two models, the Rayleigh and steady-state models, demonstrate the relationship between the degree of substrate utilisation and the N isotopic composition of the substrate and product pools (Mariotti, et al., 1981; Casciotti, 2016; Sigman & Fripiat, 2019). In the Rayleigh model, the supply of substrate is finite (i.e., a closed system), while in the steady state model, the supply of the substrate is continually replenished (i.e., an open system). The N isotopic composition of the instantaneously-generated product in the case of the Rayleigh model and the product in the steady state case is equal to the isotopic composition of the substrate at a given degree of consumption minus the isotope effect (i.e., during consumption, the N isotopic composition of the substrate and instantaneous product are offset by a constant value, ε). For the Rayleigh model, the N isotopic composition of the accumulated product pool, following complete consumption of the substrate, is equal to that of the substrate at the start of the reaction since all the N isotopes have now been transferred to the product pool.

The isotopic composition of N is reported as the ratio of ^{15}N to ^{14}N, in delta (δ) notation, with units of per mil (‰). Typically, measurements of N isotope ratios are made relative to an internal laboratory standard and reported relative to N_2 in air, such that the $\delta^{15}N$ of N_2 is equal to 0‰;

$$\delta^{15}N\ [‰] = [(^{15}N/^{14}N)_{sample} \div (^{15}N/^{14}N)_{N2air} - 1] \times 10^3 \qquad \text{eq. 1.2}$$

The $\delta^{15}N$ of various fixed N pools in the ocean has been shown to yield a time and space-integrated record of the overlapping physical and biogeochemical processes acting on the N inventory (e.g., (Mariotti, et al., 1981; Altabet & Francois, 1994; Sigman, et al., 1999a; Sigman, et al., 2005; Knapp, et al., 2008; Fawcett, et al., 2011; Fawcett, et al., 2015; Altieri, et al., 2021)). Nitrate is the pool of fixed N most frequently measured for its $\delta^{15}N$ (Fripiat, et al., 2021). Measurements of the isotopic composition of other forms of oceanic fixed N are increasingly available; for example, nitrite, ammonium, DON and PN pools — including flow cytometrically sorted particles —, zooplankton, fish, and other higher trophic level species (e.g., (Knapp, et al., 2005; Casciotti & McIlvin, 2007; Knapp, et al., 2011; Fawcett, et al., 2011; Buchwald & Casciotti, 2013; Mcmahon, et al., 2013; Busquets-Vass, et al., 2017; Lueders-Dumont, et al., 2018)). Moreover, for the organic N pools, measurements of bulk organic matter have been combined with isotopic measurements of specific amino acids, chlorophyll derivatives, and other compounds (Sachs, et al., 1999; McCarthy, et al., 2007; Popp, et al., 2007; Harada, et al., 2022). In addition, measurements of the N isotope ratios of tiny quantities of organic matter retained in fossil matrices, which appears to be near-immune to the fractionating impact of degradation, are increasingly being used as paleo-proxies. These include the shells of some planktic foraminifera (single-celled zooplankton) (Ren, et al., 2009; Smart, et al., 2018; Smart, et al., 2020), diatoms (Sigman, et al., 1999a; Robinson, et al., 2004; Studer, et al., 2013), corals (Wang, et al., 2015; Ren, et al., 2017), fish otoliths (Rowell, et al., 2010; Lueders-Dumont, et al., 2018; Lueders-Dumont, et al., 2022), fish lenses (Harada, et al., 2022), and tooth enamel (Martínez-García, et al., 2022).

The source, sink, and recycling processes mediating the N cycle produce unique isotopic signatures in the ocean (Figure 1.2a; (Sigman & Fripiat, 2019)). The $\delta^{15}N$ of newly-fixed organic matter is relatively low, ranging from -2-0‰ (Hoering & Ford, 1960; Minagawa & Wada, 1986; Carpenter, et al., 1997). The remineralisation of this organic matter produces nitrate with a similarly low δ^{15}N (Liu, et al., 1996; Knapp, et al., 2005; Knapp, et al., 2008). While typically a lesser source, atmospheric N deposition (of both natural and anthropogenic origin) supplies N with a relatively wide range of δ^{15}N values to the ocean, from -14-20‰ (Hastings, et al., 2003; Morin, et al., 2009; Knapp, et al., 2010; Altieri, et al., 2021), with a mean of ~-4‰. The δ^{15}N of river runoff is perhaps the most unconstrained N source to the ocean, with measurements ranging from -5-20‰ and averaging ~7‰ (Matiatos, et al., 2021). The relatively similar δ^{15}N endmembers for N_2 fixation and atmospheric N deposition can make separating their contributions difficult. For example, in the Mediterranean Sea, low-δ^{15}N thermocline nitrate (of ~3‰) was originally attributed to N_2 fixation (Pantoja, et al., 2002), but was later explained by atmospheric N deposition (Mara, et al., 2009) since there is almost no direct evidence for N_2 fixation in the Mediterranean Sea (Agawin, et al., 2011)and the latter explanation is more consistent with the seasonal timing of deposition (Mara, et al., 2009; Altieri, et al., 2021). While the similar δ^{15}N endmembers for N_2 fixation and N deposition may not allow the source of low-δ^{15}N thermocline nitrate to be determined, coupling the δ^{15}N with information on the period and area over which the thermocline signal accumulates (i.e., estimating the hypothetical flux of N_2 fixation and N deposition), and comparing these rates to other independently measured and/or modelled rates, can provide enough information to deduce the ultimate N source (Knapp, et al., 2008; Mara, et al., 2009).

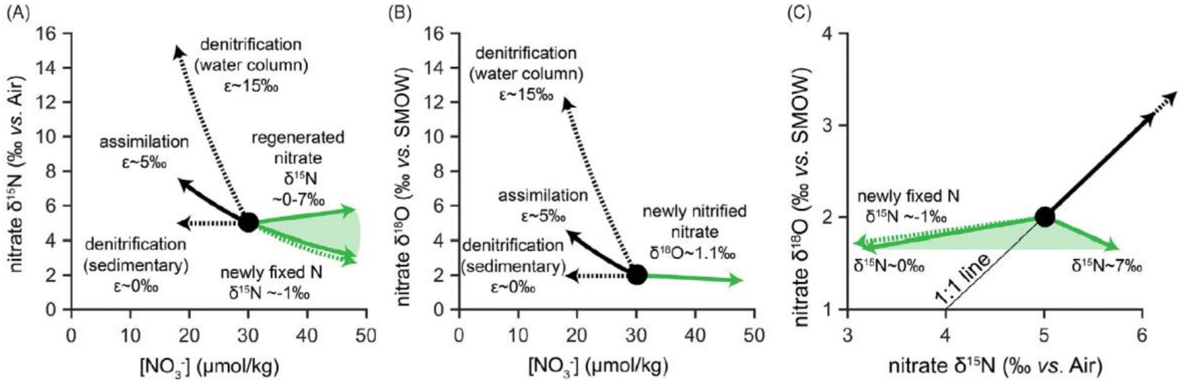

Figure 1.2. The effect of marine N cycling on the N and O isotope ratios of nitrate. a) nitrate δ^{15}N [‰] versus nitrate concentration [µmol.kg^{-1}], **b**) nitrate δ^{18}O [‰] versus nitrate concentration [µmol.kg^{-1}], and **c**) nitrate δ^{18}O [‰] versus nitrate δ^{15}N [‰]. The effect of different marine N cycle processes acting on the nitrate pool is illustrated assuming a starting nitrate concentration, δ^{15}N, and δ^{18}O of 30 µmol.kg^{-1}, 5‰, and 2‰, respectively. The trajectories are for typical estimates of the isotope effects, and they depend on the starting nitrate δ^{15}N and δ^{18}O, as well as on the relative amplitude of the changes in nitrate concentration (30% for each process). A dashed arrow denotes a process that adds or removes fixed N from the ocean, while a solid arrow denotes a component of the internal cycle of oceanic fixed N. The δ^{15}N of nitrate regenerated in the ocean interior is denoted by the solid green arrows in panel **a** and **c**, while δ^{15}N of the organic N sinking into the

ocean interior is denoted by the dashed green arrows. This figure is courtesy of Dario Marconi and taken from Sigman & Fripiat (2019).

Under low oxygen conditions (<10 μM ambient O_2), specialised bacteria ("denitrifiers") reduce nitrate to N_2 gas with a large isotope effect (of ~15‰, noting that larger values have been used in earlier studies; (Kritee, et al., 2012; Casciotti, et al., 2013; Marconi, et al., 2017)), producing heavily ^{15}N-enriched nitrate (the reducing substrate) (Mariotti, et al., 1981; Cline & Kaplan, 1975; Liu & Kaplan, 1989; Brandes, et al., 1998). Water column denitrification occurs mainly in the three major ODZs found in the eastern tropical north and south Pacific and the Arabian Sea in the northwest Indian Ocean. Here, nitrate δ^{15}N can be >15‰ (Cline & Kaplan, 1975; Brandes, et al., 1998; Casciotti, et al., 2013; Martin & Casciotti, 2017). Sedimentary denitrification, by contrast, seldom imprints a denitrification signal on the water column N pool since nitrate in the sediment pore waters is rapidly and completely consumed (Brandes & Devol, 1997; Lehmann, et al., 2007). That said, coupled nitrification-denitrification at the sediment-water interface can force the expression of the denitrification isotope effect on the water column N pool (Granger, et al., 2011; Flynn, et al., 2020).

The rapid cycling of N between its various organic and inorganic forms is dominated by phytoplankton nitrate assimilation in the surface ocean and remineralisation of organic matter back to nitrate via ammonification and nitrification, which occurs in both the surface and subsurface. The isotope effect associated with the assimilatory nitrate reductase enzyme, which is located intracellularly, is large ~26.6‰ (Ledgard, et al., 1985; Schmidt & Medina, 1991; Needoba, et al., 2004; Karsh, et al., 2012); however, its expression in the environment is determined by the degree of nitrate efflux out of the cell (along with a small contribution of transport isotope effects), such that it is never fully expressed (Granger, et al., 2004; Needoba, et al., 2004; Granger, et al., 2010; Karsh, et al., 2014). The expressed nitrate assimilation isotope effect has been estimated from culture experiments to range broadly, from 0-20‰ (Wada & Hattori, 1978; Montoya & McCarthy, 1995; Waser, et al., 1998; Granger, et al., 2004; Granger, et al., 2010), while in the ocean it has been observed to range from 2-11‰ (Sigman, et al., 1999b; Altabet, 2001; DiFiore, et al., 2006; Smart, et al., 2015; Fripiat, et al., 2019), converging on 5-7‰. As such, the δ^{15}N of partially consumed nitrate in the surface ocean is elevated relative to the underlying nitrate source (i.e., >>5‰) (Sigman, et al., 1999b). The isotope effect associated with the assimilation of ammonium can be high ~20‰; however, at the low concentrations typical of the open ocean (i.e., <5 μM), the isotope effect appears to be near 0‰ (Hoch, et al., 1992; Pennock, et al., 1996; Waser, et al., 1998; Liu, et al., 2013). The assimilation isotope effect associated with other forms of N in the surface ocean, such as nitrite and urea, appears to be low near 1‰ (Waser, et al., 1998), and its expression is limited by the almost always complete consumption of these N pools, unlike for nitrate (Sigman & Fripiat, 2019).

The remineralisation of PN back to nitrate involves numerous processes, the isotope effects of which are difficult to isolate and quantify. Culture studies suggest that the processes producing ammonium preferentially remove ^{14}N, and that the net isotope effect of organic matter remineralisation is ~3‰ (Checkley & Miller, 1989; Möbius, 2013; Sigman & Fripiat, 2019), although this value may be higher for DON remineralisation (see below; (Knapp, et al., 2018a; Zhang, et al., 2020). The subsequent oxidation of ammonium to nitrite has an isotope effect ranging from 14-19‰ (Mariotti, et al., 1981; Casciotti, et al., 2003) while the oxidation of nitrite to nitrate occurs with an inverse isotope effect of ~-13‰ (Casciotti, 2009). While nitrite does not accumulate to a significant degree (i.e., >1 μM) in the open ocean, its $\delta^{15}N$ can be as low as -100‰ (Casciotti, 2009; Casciotti, et al., 2013; Gaye, et al., 2013; Smart, et al., 2015; Kemeny, et al., 2016; Fripiat, et al., 2019), in part due to the isotope effects associated with nitrification. In net, however, the $\delta^{15}N$ of newly nitrified nitrate is approximately equal to the $\delta^{15}N$ of the organic matter being remineralised since nitrification typically competes with no other process in the interior ocean and the reaction (i.e., conversion of PN substrate to nitrate product) is almost always complete. In cases where nitrification competes with ammonium and nitrite assimilation, the $\delta^{15}N$ of newly nitrified nitrate can be higher than the organic matter source (Casciotti, et al., 2011). The fluxes and isotope effects of other internal N cycle processes are a field of active investigation (Santoro, et al., 2011; Buchwald & Casciotti, 2013; Kemeny, et al., 2016; Knapp, et al., 2018a; Zhang, et al., 2020). For example, preferential remineralisation of ^{14}N during DON degradation to nitrate with an isotope effect of ~5‰ has recently been suggested for some subtropical systems, which would contribute low-$\delta^{15}N$ N to the nitrate pool (Knapp, et al., 2018a; Zhang, et al., 2020).

Measurements of N isotope ratios have numerous applications for investigating biogeochemical cycling, ocean circulation, and ecosystem change in the modern ocean, as well as over recent decades, centuries, and millennia (e.g., (Sigman, et al., 2000; Knapp, et al., 2008; Martínez-García, et al., 2014; Fripiat, et al., 2021)). Coupling measurements of N isotopes with nutrient concentrations and information on ocean circulation can be used to identify, characterise, and at times, quantify, various processes across a range of temporal and spatial scales. For example, basin-scale and global rates of N_2 fixation and N loss have been estimating by combining nitrate $\delta^{15}N$ data with information on water mass residence time (e.g., (Knapp, et al., 2008; Somes, et al., 2010; DeVries, et al., 2013; Marconi, et al., 2017)). Additionally, coincident measurements of the $\delta^{15}N$ of more than one marine N pool have been used to characterise internal N cycling (e.g., (Fawcett, et al., 2011; Knapp, et al., 2018a; Smart, et al., 2020)), while the relative importance of lateral versus vertical nutrient fluxes have been demonstrated using N isotope observations incorporated into a box model (Fripiat, et al., 2021; Fripiat, et al., 2023). With regards to recent change, coral-bound $\delta^{15}N$ has been used to demonstrate that rising anthropogenic N emissions are impacting some marine ecosystems (Ren, et al., 2017) but not others (Wang, et al., 2018). Nitrogen isotopes are thus a powerful tool for studying a range of biogeochemical processes in the ocean.

1.3.2. The dual isotope ratios of nitrate

Nitrate comprises both N and O atoms, and with the advent of the denitrifier method in the early 2000s, both the N and O isotope ratios of nitrate in seawater can be measured (Sigman, et al., 2001; Casciotti, et al., 2002). The denitrifier method (also referred to as the “bacterial” method) involves the reduction of nitrate to nitrite, then to nitric oxide (NO), and finally to nitrous oxide (N_2O) by the denitrifying bacteria, *Pseudomonas chlororaphis* or *Pseudomonas aureofaciens*. These denitrifiers lacks the enzyme required to reduce N_2O to N_2 gas (N_2O reductase), the final step in the denitrification reaction. Provided that sample nitrate is completely reduced to N_2O, the latter will have an N isotope ratio that matches and an O isotope ratio that is strongly correlated with those of the initial nitrate. Using gas chromatography and isotope ratio mass spectrometry, the N and O isotope ratios of the produced N_2O can be measured (Sigman, et al., 2001; Casciotti, et al., 2002; McIlvin & Casciotti, 2011; Weigand, et al., 2016).

Oxygen has three stable isotopes, ^{16}O, ^{17}O, and ^{18}O. The occurrence of ^{17}O is extremely rare, since it comprises only 0.04% of O atoms on Earth. Most nitrate O isotope measurements are thus of the ratio of heavier ^{18}O to lighter ^{16}O, quantified as $\delta^{18}O$. Measurements of $\delta^{18}O$ in N_2O are made relative to an internal laboratory standard and reported relative to Vienna Standard Mean Ocean Water (VSMOW), such that the $\delta^{18}O$ of seawater is equal to 0‰;

$$\delta^{18}O\ [‰] = [(^{18}O/^{16}O)_{sample} \div (^{18}O/^{16}O)_{VSMOW} - 1] \times 10^3 \qquad \text{eq. 1.3}$$

The cycle of O atoms in nitrate is different from that of the N atoms in that nitrification is the ultimate source of O atoms and nitrate assimilation is the ultimate sink (Figure 1.2a versus b; (Sigman, et al., 2005)). During the first step of nitrification, ammonia oxidation to nitrite, one O atom each is sourced from seawater ($\delta^{18}O$ = ~0‰) and dissolved oxygen ($\delta^{18}O$ = ~24‰; (Benson & Krause, 1980)). During the second step of nitrification, nitrite oxidation to nitrate, a further O atom from seawater is incorporated (Andersson & Hooper, 1983; Kumar, et al., 1983). However, measurements from culture experiments and the environment have repeatedly shown that the $\delta^{18}O$ of newly nitrified nitrate is offset from that of seawater $\delta^{18}O$ by only ~1‰ (Casciotti, et al., 2002; Sigman, et al., 2009a; Buchwald, et al., 2012; Boshers, et al., 2019; Marconi, et al., 2019), which is far lower than expected if just two thirds of O atoms derive from seawater and one third from dissolved oxygen (i.e., newly nitrified nitrate should have a $\delta^{18}O$ on the order of 8-10‰; (Amberger & Schmidt, 1987)). The significantly lower $\delta^{18}O$ occurs because various steps in the nitrification pathway are associated with (sometimes inverse) kinetic isotopic effects, as well as biotic and abiotic O atom exchange between nitrite and seawater (that occurs with a temperature-dependent equilibrium isotope effect (Casciotti, et al., 2007; Casciotti, et al., 2010; Buchwald & Casciotti, 2013)). This exchange incorporates additional O atoms from seawater into the nitrite (and thus the nitrate) pool (Buchwald, et al., 2012; Boshers, et al., 2019). As such, the $\delta^{18}O$ of newly nitrified nitrate is set by the $\delta^{18}O$ of seawater (equal to ~0‰; (Schmidt, et al., 1999); Global Seawater Oxygen-18 Database, available at https://data.giss.nasa.gov/o18data/) plus an isotopic offset of ~1.1‰ (Figure 1.2b) (Sigman, et al., 2009a; Buchwald, et al., 2012; Boshers, et al., 2019; Marconi, et al., 2019).

The (de)coupling of the N and O isotope systematics yields an additional framework within which to study N cycling (Figure 1.3). Coupled measurements of nitrate N and O isotope ratios allow for the disentanglement of processes that coincide in the water column. For example, N_2 fixation and denitrification (Sigman, et al., 2005; Wankel, et al., 2007; Rafter, et al., 2013) or nitrate assimilation and nitrification (Knapp, et al., 2008; Smart, et al., 2015; Fawcett, et al., 2015). During nitrate assimilation and denitrification, the N and O isotopes are fractionated to the same extent, which means that the $\delta^{15}N$ and $\delta^{18}O$ of the residual nitrate pool rise in a ratio of ~1:1 (Granger, et al., 2004; Granger, et al., 2008; Granger, et al., 2010; Karsh, et al., 2012; Rohde, et al., 2015). By contrast, nitrification resets the $\delta^{18}O$ of nitrate to ~1.1‰, while its $\delta^{15}N$ is set by that of the organic matter and ammonium being remineralised (Sigman, et al., 2009a; Buchwald, et al., 2012; Boshers, et al., 2019; Marconi, et al., 2019). As an example of the utility of the dual nitrate isotopes, examining the relationship between nitrate $\delta^{18}O$ and $\delta^{15}N$ in the upper ocean (<500 m) can reveal the co-occurrence of partial nitrate assimilation and nitrification at the base of the euphotic zone (Figure 1.3) (Wankel, et al., 2007; Sigman, et al., 2009a; Rafter, et al., 2013; Fawcett, et al., 2015). The partial assimilation of nitrate raises its $\delta^{15}N$ and $\delta^{18}O$ in tandem, while the remineralisation and nitrification of the biomass produced therefrom results in a $\delta^{18}O$ for the combined nitrate pool (i.e., partially assimilated plus newly nitrified) that is higher than that initially removed by phytoplankton, and a $\delta^{15}N$ that is unchanged (since N is not lost from the system). Similarly, the remineralisation of newly-fixed organic matter decouples nitrate δ^{15}N and δ^{18}O since N_2 fixation introduces low-δ^{15}N organic matter (of ~-1‰; (Hoering & Ford, 1960)) relative to subsurface nitrate (typically 3-7‰; (Sigman, et al., 1999b; Knapp, et al., 2008; Rafter, et al., 2013; Fripiat, et al., 2021)). N_2 fixation is thus associated with nitrate that has a δ^{15}N nitrate that has been lowered more than its δ^{18}O (Sigman, et al., 2005; Knapp, et al., 2008; Rafter, et al., 2013).

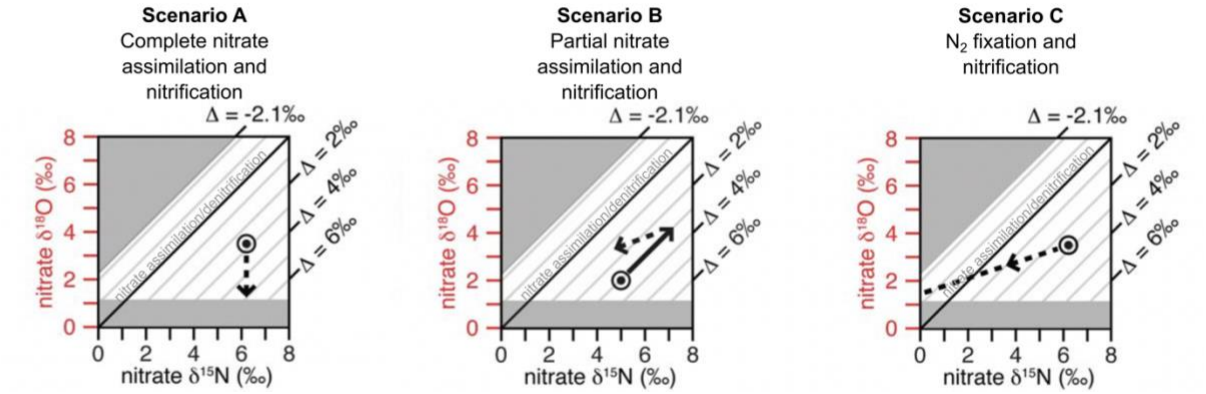

Figure 1.3. Dynamics of the coupled nitrogen and oxygen isotope ratios of remineralised nitrate. Nitrate δ^{18}O [‰] versus nitrate δ^{15}N [‰]. In scenario **A**, surface nitrate is completely assimilated and the produced PN is then remineralised back to nitrate (dashed line). In scenario **B**, partial nitrate assimilation elevates the residual nitrate δ^{15}N and δ^{18}O (solid arrow), while remineralisation of the produced PN introduces newly nitrified nitrate (δ^{15}N = 2‰; δ^{18}O = 1.1‰) that in net, raises the δ^{18}O of the combined nitrate pool more than its δ^{15}N (i.e., above the 1:1 line). In scenario **C**, N_2 fixation produces organic matter with a low δ^{15}N, the remineralisation of which will lower the δ^{15}N of nitrate more than its δ^{18}O. For all scenarios, Δ(15-18) (= δ^{15}N – δ^{18}O) is also shown (see text for details). Gray indicates isotopic values that are outside the bounds of known deep water nitrate isotope systematics. Figure adapted from Rafter et al. (2013).

The difference between the δ^{15}N and δ^{18}O of nitrate, termed nitrate Δ(15-18) (= δ^{15}N – δ^{18}O), quantifies the degree of N and O isotope decoupling (Sigman, et al., 2005; Rafter, et al., 2013). Phytoplankton assimilation of nitrate in the surface ocean, as well as denitrification, raises its δ^{15}N and δ^{18}O in unison (Granger, et al., 2004; Granger, et al., 2008; Granger, et al., 2010), which causes no change in nitrate Δ(15-18) even as δ^{15}N and δ^{18}O can exceed 20‰ (Figure 1.3) (Sigman, et al., 2005; Rafter, et al., 2013; Fawcett, et al., 2015). By contrast, there are other processes (and at times combinations of processes) that decouple the N and O isotope ratios of nitrate, thus altering Δ(15-18). To follow are three scenarios (A-C) that illustrate the utility of nitrate Δ(15-18) for deducing these processes, taking as a starting point mean global ocean nitrate with a δ^{15}N of 5.0‰, δ^{18}O of 2.0‰, and Δ(15-18) of 3.0‰ (Figure 1.3).

A. In scenario A, consider that all nitrate is completely assimilated by phytoplankton, with the produced PN then regenerated and nitrified (scenario A in Figure 1.3). In net, nitrification of PN resulting from the complete assimilation of nitrate will act to raise Δ(15-18) by returning N to the nitrate pool with a δ^{15}N equal to that of the PN (itself equal to the nitrate source of 5‰) and a δ^{18}O of ~1.1‰. The resulting nitrate Δ(15-18) in scenario A is 3.9‰ (= 5‰ − 1.1‰), which is higher than the starting nitrate Δ(15-18) of 3.0‰ (Rafter, et al., 2013).

B. In scenario B, consider that only a fraction of nitrate supplied to phytoplankton is assimilated, with the produced (low-δ^{15}N) PN then regenerated and nitrified (scenario B in Figure 1.3). The δ^{15}N and δ^{18}O of the unconsumed nitrate will rise in concert, for example, by 2‰, to 7‰ and 4‰, respectively, while nitrate Δ(15-18) remains 3‰ (= 7‰ − 4‰). The nitrification of PN resulting from the incomplete consumption of nitrate will act to lower nitrate Δ(15-18) by returning low-δ^{15}N N to the nitrate pool (approximated here by the δ^{15}N of the substrate minus the isotope effect, = 7‰ − 5‰), and a δ^{18}O of ~1.1‰. The resulting nitrate Δ(15-18) in scenario B is 0.9‰ (= 2‰ – 1.1‰), lower than the starting nitrate Δ(15-18) of 3.0‰ (Rafter, et al., 2013). The Δ(15-18) of the combined nitrate pool (i.e., partially assimilated plus newly nitrified) will thus be lower than that of the starting nitrate.

C. In scenario C, consider that diazotrophs produce organic matter from N_2 with a δ^{15}N of -1‰ (Hoering & Ford, 1960) (scenario C in Figure 1.3). The regeneration and nitrification of the newly-fixed PN yields nitrate with a similarly low δ^{15}N of -1‰ (Knapp, et al., 2005; Knapp, et al., 2008) and a δ^{18}O of ~1.1‰. The resulting Δ(15-18) associated with N_2 fixation in scenario C is -2.1‰ (= -1‰ − 1.1‰), lower than the mean ocean nitrate Δ(15-18) of 3.0‰ (Sigman, et al., 2005; Rafter, et al., 2013).

Nitrate Δ(15-18) can also be used to identify processes other than biologically-mediated N cycling. During physical mixing of two water parcels with different (or the same) nitrate concentrations, δ^{15}N, and δ^{18}O, the nitrate Δ(15-18) of the combined water parcel is equal to the concentration-weighted mean of the nitrate Δ(15-18) from both source waters (Rafter, et al., 2013). As such, nitrate Δ(15-18) can act as a conservative tracer of mixing in the ocean. The dual isotope ratios of nitrate have been used to trace water mass circulation and mixing over large spatial scales (i.e., basin-scales) (Rafter, et al., 2013; Marconi, et al., 2015; Lehmann, et al., 2018). However, the potential for tracing fine-scale mixing using nitrate Δ(15-18), particularly in the vertical, has yet to be explored. Consider mixing thermocline water with a nitrate concentration of 5 μM and a Δ(15-18) of 3‰ with overlying nitrate-free surface water. The nitrate Δ(15-18) of the combined thermocline and surface water mixture is equal to 3‰, the concentration-weighted mean of the thermocline and surface waters, while the nitrate concentration of the mixture has decreased (to an extent dependent on the mixing fraction). Now consider that phytoplankton in surface waters assimilate the nitrate mixture, which will further lower its concentration while raising both its $\delta^{15}N$ and $\delta^{18}O$ (Sigman, et al., 1999b; Granger, et al., 2004; Granger, et al., 2010). However, the Δ(15-18) of the partially assimilated nitrate mixture remains unchanged at 3‰. As such, the upward supply of deep nutrients and their subsequent consumption in surface waters can be recorded in the N and O isotope ratios of nitrate.

The integrative nature of the nitrate N and O isotopes, over both time and space, has limitations, however. Regional differences in circulation (e.g., retention versus rapid lateral advection) and the multiple timescales over which the various pools of fixed N can vary make it particularly difficult to quantify internal N cycle fluxes using nitrate N and O isotopes alone. For example, N isotope budgets are currently limited by our ability to quantify some N fluxes (particularly DON) across the upper ocean. Additionally, estimates of regional N_2 fixation rates based on measurements of N isotope ratios oftentimes require assumptions about lateral and vertical N fluxes (Knapp, et al., 2008; Marconi, et al., 2017). Coherent interpretation of the rapidly expanding N (and O) isotope records will thus require additional quantitative tools such as general circulation models that can simulate multiple N fluxes in time and space.

1.3.3. Nutrient ratios

Nutrient ratios offer another set of geochemical tools from which to study ocean biogeochemistry and the N cycle. The molar stoichiometry of nutrients found in seawater and plankton biomass can reveal key N source and sink processes, such as N_2 fixation and denitrification (Broecker & Peng, 1982; Naqvi & Sen Gupta, 1985; Gruber & Sarmiento, 1997; Deutsch, et al., 2007). Diazotrophs fix N in a ratio to P that is typically much greater than the Redfield ratio (i.e., >>16:1), although with significant plasticity observed in field data and culture experiments, ranging from 14-182:1 (White, et al., 2006). The excess N relative to P that is introduced to surface waters by diazotrophs is eventually remineralised to inorganic nutrients in the thermocline, yielding elevated nutrient N:P ratios along mid-depth isopycnals (typically potential density anomalies, σ_θ, of ~25.0-26.0 kg.m^{-3}) (Gruber & Sarmiento, 1997). Conversely, denitrification results in the disproportionate loss of N relative to P, in a ratio of ~-104:1 (Gruber & Sarmiento, 1997), generating an N deficit (i.e., <<16:1) in waters influenced by ODZs and denitrifying sediments. As such, deviations in nutrient ratios are often used to estimate regional and global rates of N_2 fixation and denitrification, and to approximate or constrain N budgets (e.g., (Gruber & Sarmiento, 1997; Deutsch, et al., 2007; Peters, et al., 2018; Harms, et al., 2019)).

The first applications of nutrient ratios aimed to identify and quantify N addition and loss by computing regional and/or global deficits and excesses of N relative to P (Broecker & Peng, 1982; Naqvi & Sen Gupta, 1985; Gruber & Sarmiento, 1997). The first global application defined the parameter N* as;

$$N^* \, [\mu M] = ([NO_3^-] - 16 \times [PO_4^{3-}] + 2.9) \times 0.87 \qquad \text{eq. 1.4}$$

where 16 represents the expected mean molar N:P ratio associated with nutrient uptake by phytoplankton and remineralisation of organic matter (Redfield, et al., 1963), 2.9 represents the mean global ocean P excess, such that its addition sets N* values to zero, and 0.87 represents the P excess (y-intercept) when N* is equal to zero (Gruber & Sarmiento, 1997). However, more recent applications disregard the normalisation of N* as well as the global P excess, and simplify N* as follows;

$$N^* \, [\mu M] = ([NO_3^-] - 16 \times [PO_4^{3-}]) \qquad \text{eq. 1.5}$$

Notably, because the relationship between N and P is not linear (i.e., due to the global P excess), it is non-conservative, such that interpretations of N:P alone — particularly at low nutrient concentrations — can be erroneous (Gruber & Sarmiento, 1997). One advantage to the N* approach for diagnosing N_2 fixation is its sole reliance on nitrate and phosphate concentrations, which are relatively widely available at high spatio-temporal resolution, unlike rate estimates from incubation-based experiments. The first large-scale application of N* provided insight into the global distribution of N_2 fixation and denitrification, revealing the apparent dominance of N_2 fixation in the (sub)tropical North Atlantic and Mediterranean Sea and a dominance of denitrification in the Arabian Sea, eastern tropical North and South Pacific, and along continental margins (Gruber & Sarmiento, 1997). These conclusions are broadly consistent with subsequent findings from observations and models (Luo, et al., 2012; DeVries, et al., 2013; Wang, et al., 2019), except for the Mediterranean Sea where atmospheric deposition is likely responsible for the elevated N* signal (Altieri, et al., 2021). Incorporating information on water mass age and circulation from a model allowed Gruber & Sarmiento (1997) to estimate a N_2 fixation rate of 28 Tg $N.a^{-1}$ for the North Atlantic using thermocline N* anomalies, which is in agreement with other estimates from models using nutrient stoichiometry and scaled N_2 fixation rate incubation experiments that range from 20-40 Tg

N.a^{-1} (Deutsch, et al., 2007; Coles & Hood, 2007; Moore, et al., 2009; Luo, et al., 2012; Fonseca-Batista, et al., 2017; Marconi, et al., 2017; Wang, et al., 2019).

A similar geochemical tracer, termed P*, can also be used with other information to quantify N_2 fixation rates (Deutsch, et al., 2007). P* is commonly defined as;

$$P^* \, [\mu M] = [PO_4^{3-}] - [NO_3^-] \div 16 \qquad \text{eq. 5}$$

where 16 represents the N:P uptake and remineralisation ratio for global ocean biomass. However, Deutsch et al. (2007), who first defined P*, set this constant to 15 since non-diazotrophic organic matter must be <16:1 if diazotrophs, which have high N:P biomass, are incorporated into the bulk biomass to yield a combined ratio of 16:1. Surface distributions of P* (i.e., without considering a P flux from surface to deep waters), while not quantitative, are useful for identifying regions of P excess and deficit as they indicate potential regions of P* divergence (i.e., generation) and convergence (i.e., loss). The removal of P from surface waters by diazotrophs, without the stoichiometric removal of fixed N, is termed P* convergence. Estimates of P* convergence thus require information on water volume and nutrient fluxes, which can be sourced from inverse models (Deutsch, et al., 2007) or box models (Palter, et al., 2011). In other words, surface P* and P* convergence are not synonymous and provide different insights into N_2 fixation. The global N_2 fixation rates of 130-158 Tg N.a^{-1} predicted using P* convergence (Deutsch, et al., 2007) are similar to the rates of N_2 fixation estimated by other approaches (e.g., N* and other nutrient stoichiometry). They also equate to estimates of the global ocean denitrification rate, suggesting an approximately balanced marine N budget (Deutsch, et al., 2007; Gruber & Sarmiento, 1997; DeVries, et al., 2013; Wang, et al., 2019).

One dilemma surrounding the utility of both N* and P* is the occurrence of variable N:P ratios, observed for both diazotrophic (White, et al., 2006) and non-diazotrophic organic matter (Weber & Deutsch, 2010; Weber & Deutsch, 2012; Martiny, et al., 2013). Indeed, model simulations that incorporate flexible organic matter stoichiometry and/or preferential remineralisation of P over N apparently better estimate N_2 fixation rates than simulations that assume Redfield stoichiometry (Mills & Arrigo, 2010; Somes & Oschlies, 2015; Letscher & Moore, 2015b). As such, the inclusion of variable, but still prescribed, organic matter N:P ratios in explicit (i.e., prognostic) and implicit (i.e., inverse) model simulations of N_2 fixation is increasing (Coles & Hood, 2007; Wang, et al., 2019). Other limitations of the nutrient stoichiometry framework include challenges with simulating the dissolved organic nutrient pools with accuracy, the difficulty associated with measuring, and thus constraining, the rate of recycling between dissolved and inorganic nutrient pools, and precisely estimating the residence (i.e., turnover) time of various and often overlapping nutrient pools.

Perhaps the greatest contribution made by the global application of the nutrient stoichiometry-based (largely P*) framework is the ideas put forward on the regulation of N_2 fixation, including the spatial and quantitative coupling of N_2 fixation to N loss, whether valid or flawed. Indeed, the primary biogeochemical control on N_2 fixation has been debated for decades, oscillating among excess P availability (Sañudo-Wilhelmy, et al., 2001; Deutsch, et al., 2007; Moutin, et al., 2008), iron limitation (Moore, et al., 2009; Knapp, et al., 2016; Bonnet, et al., 2017), and both (Mills, et al., 2004; Snow, et al., 2015; Browning, et al., 2017; Held, et al., 2020; Cerdan-Garcia, et al., 2022). Iron is an important micro-nutrient for diazotrophs because the nitrogenase enzyme dominantly used to fix N_2 in the ocean, has a large iron requirement (Berman-Frank, et al., 2001). Initial findings based on P* suggested that N_2 fixation is spatially coupled to denitrification, since N_2 fixation is predicted to occur in waters characterized by an N deficit relative to P. The upwelling and lateral export of recently denitrified waters from ODZs carry a substantial P excess, which should favour N_2 fixation (Deutsch, et al., 2007). Because of the apparent spatial coupling of N_2 fixation predicted by P* convergence and N loss in the ODZs, Deutsch et al. (2007) hypothesised that P excess exerts the dominant control on N_2 fixation, and that iron may have a less important role. These ideas contrast those of Moore et al. (2009), whose data from a meridional transect across the Atlantic Ocean showed that incubation based N_2 fixation rates are positivity correlated with dissolved iron availability and not with P*, suggesting that iron exerts the dominant control on N_2 fixation distributions (Moore, et al., 2009). Because of these apparently opposing findings, research that tests these hypotheses has exploded (e.g., (Dekaezemacker, et al., 2013; Shiozaki, et al., 2014; Shiozaki, et al., 2015; Snow, et al., 2015; Knapp, et al., 2016; Bonnet, et al., 2017; Singh, et al., 2017; Tang, et al., 2019; Chen, et al., 2019; Wen, et al., 2022) (Horii, et al., 2023)).

Most of the global surface ocean hosts a P excess relative to N (Deutsch, et al., 2007; Garcia, et al., 2018), which is ultimately generated in the ODZs and other poorly ventilated shelf domains, and is transported across ocean basins via a combination of global overturning circulation and mixing in the Southern Ocean. As such, completely disregarding the role of excess P in controlling N_2 fixation is impractical. Additionally, iron supplied via dust deposition was traditionally thought to be the only quantitatively important source of this micro-nutrient to the surface ocean (Moore, et al., 2002; Mahowald, et al., 2005). More recently however, our ability to measure, identify, and approximate numerous other oceanic iron sources and their fluxes has improved (Tagliabue, et al., 2010; Conway & John, 2014; Rijkenberg, et al., 2014; Tagliabue, et al., 2019; Bonnet, et al., 2023). For instance, iron supplied from both oxygenated and anoxic ocean sediments and hydrothermal vents has been shown to be significant (Conway & John, 2014; Fitzsimmons, et al., 2014; Scholz, et al., 2014; Homoky, et al., 2021). The low oxygen environments that host N loss via denitrification appear to also be characterized by iron release from reducing margin sediments (within a narrow redox window; (Scholz, et al., 2014)). Indeed, the coincidence of increased iron availability and denitrification over glacial timescales has been inferred for the Peruvian Upwelling System (Scholz, et al., 2014). These findings intimate a spatial and temporal coupling of N loss and iron availability. The differing spatial and temporal scales over which both P and iron integrate have been suggested to exert variable control over N_2 fixation, with model results indicating that iron availability governs N_2 fixation regionally and that N loss (i.e., P* generation) governs N_2 fixation globally (Weber & Deutsch, 2014).

Combined, nutrient stoichiometry and N isotope ratios can yield complementary spatio-temporal information on the sources, sinks, and key processes governing N_2 fixation rates and distributions, as well as those of other important biogeochemical pathways.

1.4. The South Atlantic and South Indian Oceans

The mid-to-low latitude southern hemisphere oceans (i.e., 0-40°S) are perhaps the least studied with respect to general oceanography. The biogeochemical functioning of the South Atlantic and South Indian Oceans, particularly the latter, has received little research attention, which is perhaps (at least partly) a consequence of the assumption that these ocean basins function similarly to their northern hemisphere counterparts. Indeed, both the South Atlantic and South Indian Oceans are characterised by oligotrophic subtropical gyres and highly dynamic western boundary currents (WBC); however, the remaining circulation features and the oceans' physical properties are relatively unique (Figure 1.4). For example, the South Atlantic meridional heat transport is from the poles to the equator (Garzoli, et al., 2013); the air-sea CO_2 flux in the subtropical South Atlantic is negative (net CO_2 flux from the ocean) (Takahashi, et al., 2009; Friedlingstein, et al., 2022); the eastern boundary of the South Indian Ocean is not an upwelling system (Talley, et al., 2011); the Agulhas Current, the WBC of the South Indian Ocean, undergoes a 180º retroflection that directs the majority of its waters back into the subtropical Indian Ocean (Bang, 1970) while also leaking Indian Ocean water into the South Atlantic (Gordon, 1985). The South Atlantic and South Indian subtropical gyres are thus connected to form the southern hemisphere supergyre (Ridgway & Dunn, 2007; Speich, et al., 2007); some of the highest eddy kinetic energy in the world occurs at the termination of the Agulhas Current (i.e., the retroflection) and the Brazil Current (the WBC of the South Atlantic Ocean), as well as in the Cape Basin (southeast subtropical South Atlantic) (Ducet, et al., 2000; Ferrari & Wunsch, 2009). These unique characteristics have important implications for the ocean's role in regulating climate (e.g., (Beal, et al., 2011; Rahmstorf, et al., 2015)) and presumably also for ocean productivity, yet this latter topic has been poorly studied in the South Atlantic and South Indian Oceans.

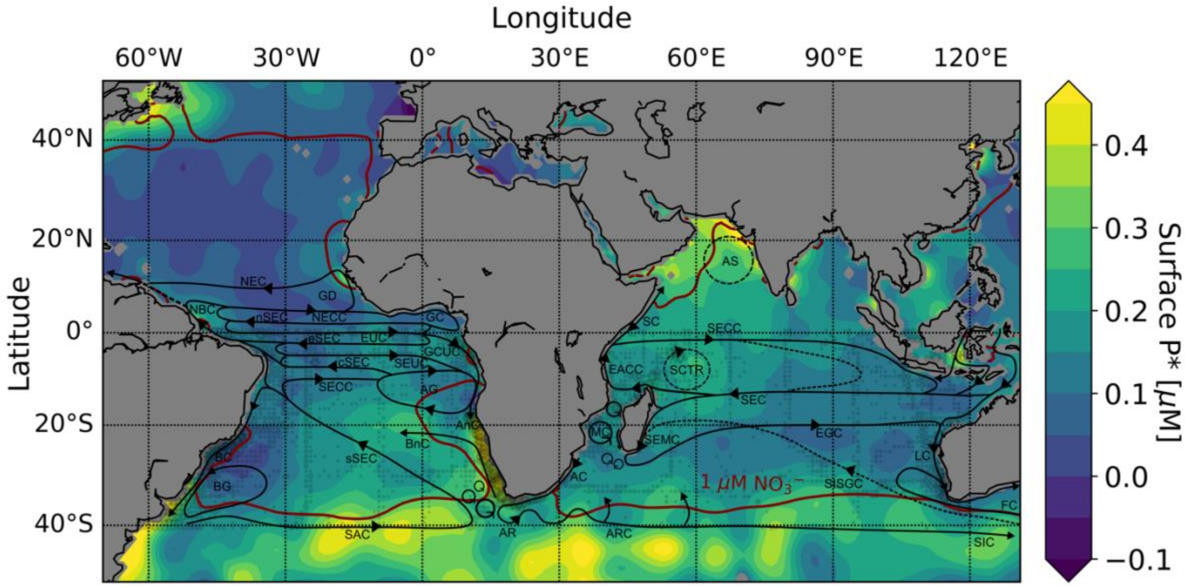

Figure 1.4. Circulation of the N-limited South Atlantic and South Indian Oceans. Map showing surface P* distributions (in μM; = [PO_4^{3-}] – [NO_3^-] ÷ 16) for the Atlantic and Indian Oceans, with circulation of the South Atlantic and South Indian Oceans overlain in black, and the 1 μM surface nitrate concentration contoured in maroon. The size of the grey points indicates the number of surface nitrate concentration observations per 1°×1° grid cell, with a maximum of 413 (in the Benguela Upwelling System), a mean of 2, and a median of 0. Surface P* and nitrate concentration data are from the World Ocean Atlas 2018 (Garcia, et al., 2018). Only circulation directly impacting the South Atlantic and South Indian Oceans is shown. Table 1.1 provides a list of the acronyms annotated on the map.

1.4.1. South Atlantic Ocean circulation and biogeochemical setting

The subtropical South Atlantic (i.e., 20-40°S) is characterised by anticyclonic gyre circulation over the upper 1000 m (Stramma & England, 1999; Talley, et al., 2011). This three-limbed subtropical gyre is bounded by the eastward South Atlantic Current (~40°S), the north-westward south South Equatorial Current that originates from the northward Benguela Current along the west coast of southern Africa (~34°S) and terminates at the east coast of southern America (~10°S), and the southward Brazil Current (Figure 1.4, Table 1.1). The gyre is also bounded by two regions of high eddy kinetic energy, one at the confluence of the Brazil Current with the Malvinas Current and the other in the Cape Basin where warm Indian Ocean waters are injected into the cooler South Atlantic (Ducet, et al., 2000). North of the subtropical gyre is a cyclonic tropical gyre (5-20°S) bounded by the north-westward south South Equatorial Current, the eastward South Equatorial Undercurrent (~4°S), and the southward Angola Current (Stramma & England, 1999; Talley, et al., 2011). Embedded within this tropical gyre is the Angola Gyre, a permanent cyclonic cell reaching to 400 m depth in the eastern basin (Moroshkin, et al., 1970; Gordon & Bosley, 1990). The southward Angola Current meets the eastern boundary Benguela Upwelling System at the Angola-Benguela Frontal Zone at ~17°S.

Table 1.1. Names of currents and circulation features shown in Figure 1.4.

Abbrev.	Full name	Abbrev.	Full name
AC	Agulhas Current	LC	Leeuwin Current
AG	Angola Gyre	MC	Mozambique Channel
AnC	Angola Current	NBC	North Brazil Current
AR	Agulhas Retroflection	NEC	North Equatorial Current
ARC	Agulhas Return Current	NECC	North Equatorial Countercurrent
AS	Arabian Sea	nSEC	north South Equatorial Current
BC	Brazil Current	SAC	South Atlantic Current
BG	Brazil Gyre	SC	Somali Current
BnC	Benguela Current	SCTR	Seychelles-Chagos Thermocline Ridge
cSEC	central South Equatorial Current	SEC	South Equatorial Current
EACC	East African Coastal Current	SECC	South Equatorial Current
EGC	East Gyral Current	SECC	South Equatorial Countercurrent
eSEC	equatorial South Equatorial Current	SEMC	Southeast Madagascar Current
EUC	Equatorial Under Current	SEUC	South Equatorial Under Current
FC	Flinders Current	SIC	South Indian Current
GC	Guinea Current	SISTC	South Indian Subtropical Gyre Current
GCUC	Gabon-Conga Under Current	sSEC	south South Equatorial Current
GD	Guinea Dome		

Moderate winter- and springtime convective mixing (to depths of 100-150 m; (Zhang, et al., 2018)), coupled with the anticyclonic (i.e., downwelling) circulation of the upper subtropical South Atlantic, yields a well-oxygenated ocean interior (Garcia, et al., 2018) and moderate subtropical gyre productivity (Kulk, et al., 2020). Along the eastern boundary, however, upwelling favourable winds supply nutrients to surface waters that fuel some of the highest rates of ocean productivity and biomass accumulation, which lower oxygen availability in the subsurface following intense organic matter remineralisation (Carr, 2001; Monteiro, et al., 2006; Mohrholz, et al., 2008; Flynn, et al., 2020). The Benguela Upwelling System is divided into two subsystems, the northern and southern Benguela Upwelling Systems, which are distinguished by the (sub)seasonality of the wind forcing that drives the upwelling (Hutchings, et al., 2009). In the tropics where seasonal convective mixing is less important, the perennial upwelling of nutrients to Angola Gyre surface waters in the eastern basin fuels high rates of productivity (Berger, 1989). The subsequent remineralisation of this surface-produced organic matter generates an intense oxygen minimum zone (40-60 μM) between 200 and 800 m (Gordon & Bosley, 1990; Mercier, et al., 2003). In the western tropical basin, upwelling does not occur and productivity is low, akin to that of typical stratified tropical waters (Kulk, et al., 2020).

Since South Atlantic surface waters host a basin-wide P excess (Deutsch, et al., 2007; Garcia, et al., 2018) (Figure 1.4), the minimal iron supplied by limited dust deposition (Sarthou, et al., 2003; Jickells, et al., 2005) has been proposed to constrain N_2 fixation in the South Atlantic (Moore, et al., 2009; Snow, et al., 2015). More regionally, along the subtropical eastern boundary, upwelling and offshore advection of waters with a P excess deriving from N loss on the low-oxygen northern Benguela shelf (Kuypers, et al., 2005) should favour N_2 fixation (Deutsch, et al., 2007), yet incubation experiments and nutrient and N isotope ratios provide little evidence of quantitatively significant N_2 fixation in the subtropical waters offshore of the northern Benguela Upwelling System (Nagel, et al., 2013; Flohr, et al., 2014; Wasmund, et al., 2015; Fonseca-Batista, et al., 2017). Other observational data from the South Atlantic, although exceptionally sparse, suggest a relatively low basin-wide rate of 1.8-5.0 Tg N.a^{-1} (Luo, et al., 2012; Marconi, et al., 2017; Fonseca-Batista, et al., 2017). Contrastingly, results from models indicate that the South Atlantic hosts significant N_2 fixation, at rates ranging from 7.5-8.4 Tg N.a^{-1} (Deutsch, et al., 2007; Coles & Hood, 2007; Somes & Oschlies, 2015; Wang, et al., 2019). More concerning than the discrepancy in the absolute N_2 fixation rates between observations and models, however, is the discrepancy in the spatial distribution of N_2 fixation predicted by various models (the limited observations do not provide robust insights into the distribution). For example, some models predict hotspots of N_2 fixation in the western tropical and central subtropical South Atlantic, while others show elevated N_2 fixation more broadly across the basin (Deutsch, et al., 2007; Coles & Hood, 2007; Somes & Oschlies, 2015; Wang, et al., 2019). The implication of the mismatch in the rate and spatial distribution of N_2 fixation predicted by various models and the observations is that our understanding of the controls on N_2 fixation is inadequate.

1.4.2. South Indian Ocean circulation and biogeochemical setting

The Indian Ocean as a whole is characterised by unique circulation, largely due to the Eurasian landmass obstructing flow beyond ~30°N, which causes strong monsoonal wind forcing over the North Indian Ocean (Schott & Fieux, 1985). Additionally, the throughflow of fresh Pacific waters into the Indian Ocean between 7°S and 15°S (Gordon, 1986) and the lack of equatorial and eastern boundary upwelling (Smith, et al., 1991; Talley, et al., 2011) make this ocean basin distinct. Between 0°S and 10°S exists a basin-wide tropical cyclonic gyre, with an upwelling cell (the Seychelles-Chagos Thermocline Ridge) embedded in the western tropical basin (Figure 1.4) (Hermes & Reason, 2008; Resplandy, et al., 2009). The South Indian Ocean is largely defined as the waters south of the tropical gyre (i.e., south of 10°S) where the westward South Equatorial Current forms the northern limb of the South Indian Ocean subtropical gyre and the seasonality is relatively unimpacted by monsoons (Stramma & Lutjeharms, 1997). The eastern limb of the subtropical gyre is mainly formed by the north-westward Flinders Current and characterized by generally north-westward flow in the subsurface (~200 m) since the eastern boundary Leeuwin Current flows southward (Smith, et al., 1991; Talley, et al., 2011). The western limb of the subtropical gyre includes the southward Southeast Madagascar Current, mesoscale eddies propagating southward through the Mozambique Channel, and the south-westward Agulhas Current (Stramma & Lutjeharms, 1997). At the Agulhas Retroflection, the eastward flowing waters form the Agulhas Return Current, which feeds into the also-eastward South Indian Current that constitutes the southern limb of the subtropical gyre at ~40°S (Stramma & Lutjeharms, 1997; Talley, et al., 2011).

The circulation of the southwest Indian ocean is different from that of other western boundary regions (Gründlingh, et al., 1991; Stramma & Lutjeharms, 1997). Here, western intensification typical of all subtropical gyres forms a particularly intense anticyclonic recirculation cell, the southwest Indian subgyre (Stramma & Lutjeharms, 1997; Ridgway & Dunn, 2007). The circulation of the subgyre entrains waters from its southern boundary, such that 70% of the waters from Agulhas Return Current recirculate back into the southwest Indian Ocean by 70°E (Stramma & Lutjeharms, 1997; Lutjeharms & Ansorge, 2001). The Agulhas Current is the strongest boundary current for its latitude (Bryden, et al., 2005) and transports 77 ± 5 Sv (1 Sv = 1×10^6 $m^3.s^{-1}$) south-westward along the African continental boundary (Beal, et al., 2015). Three sources supply the Agulhas Current with its waters, including eddies from the Mozambique Channel (Ridderinkhof, et al., 2010), eddies from the Southeast Madagascar Current (Ponsoni, et al., 2016), and subtropical water recirculation (Stramma & Lutjeharms, 1997; Beal, et al., 2015). The convergence of waters along the western boundary results in elevated eddy kinetic energy across the southwest Indian Ocean, particularly along the western and southern boundary (Imawaki, et al., 2013; Martínez-Moreno, et al., 2021).

Relatively deep winter- and springtime mixed layers, reaching 250 m over the subtropical South India Ocean (Zhang, et al., 2018), bring nutrients into the euphotic zone to fuel elevated winter and spring productivity (Gaube, et al., 2013). Satellite-derived chlorophyll-a concentrations are elevated year-round over large areas of both the eastern and western boundaries and have been attributed to omnipresent mesoscale eddies (Tew-Kai & Marsac, 2009; Gaube, et al., 2013; Dufois, et al., 2014; Dufois, et al., 2016). Curiously, in the subtropical eastern basin, westward propagating anticyclonic eddies formed in winter are characterised by higher chlorophyll-a concentrations than cyclonic eddies (Gaube, et al., 2013; Dufois, et al., 2014). A combination of lateral entrainment of previously-productive west Australian shelf waters (Moore, et al., 2007) and eddy-induced Ekman upwelling from deeper winter mixed layers (Gaube, et al., 2013) are thought to enhance nutrient supply and productivity in anticyclones beyond that of cyclones (Dufois, et al., 2014; He, et al., 2017). In the western South Indian Ocean, Mozambique Channel eddies, which are ~300 km in diameter and bottom-reaching (~1200 m) (Ridderinkhof, et al., 2001; de Ruijter, et al., 2002; Swart, et al., 2010), similarly entrain previously productive coastal waters (and possibly nutrients) and fuel local productivity (Tew-Kai & Marsac, 2009; Kolasinski, et al., 2012; Lamont, et al., 2018).

In addition to the typical spring bloom, a second, more significant late-summer bloom occasionally occurs southeast of Madagascar and is referred to as the “southwest Madagascar bloom”, with chlorophyll-a concentrations >1 $mg.m^{-3}$ and reaching 2-3 $mg.m^{-3}$, which are significantly higher than mean spring bloom concentrations of 0.11 $mg.m^{-3}$ (Longhurst, 2001; Dilmahamod, et al., 2019). The conditions that initiate and sustain the southwest Madagascar bloom have been debated for more than two decades, with hypotheses including variable mixed layer depths perturbed by eddies, coastal upwelling, and rain from tropical cyclones (Longhurst, 2001; Uz, 2007; Raj, et al., 2010), terrestrial runoff from Madagascar (Uz, 2007; Srokosz, et al., 2015), various modes of Indian Ocean variability (Dilmahamod, et al., 2019), and potential lateral nutrient advection (Dilmahamod, et al., 2020). However, the proposed controls on the anomalous bloom have yet to be proven via direct observations. Nevertheless, during the 2005 bloom, diazotrophs were shown to dominate the phytoplankton community (Poulton, et al., 2009) and during the 2020 bloom, relatively high surface N_2 fixation rates were measured from incubation experiments (Metzl, et al., 2022). Both these studies suggest an important role for N_2 fixation in the region and possibly also in the sustenance of the bloom.

Geochemical proxies suggest that N_2 fixation in the southwest Indian Ocean could be significant (Gruber & Sarmiento, 1997; Deutsch, et al., 2007; Grand, et al., 2015c; Harms, et al., 2019). Observations of diazotrophs (Poulton, et al., 2009), particularly at the southern entrance to the Mozambique Channel (Horstmann, et al., 2021; Karlusich, et al., 2021), as well as elevated rates of N_2 fixation from incubation experiments (all from 50-75°E) (Shiozaki, et al., 2014; Horstmann, et al., 2021; Metzl, et al., 2022) indicate that N_2 fixation is regionally important. Indeed, North Indian waters carrying a P excess generated by denitrification in the Arabian Sea ODZ (predicted to result in the loss of ~40 Tg $N.a^{-1}$; (Bianchi, et al., 2012; DeVries, et al., 2013; Wang, et al., 2019)) circulate into the southwest Indian Ocean (Deutsch, et al., 2007) via the Mozambique Channel and Southeast Madagascar Current (Figure 1.4) (Beal, et al., 2000; Beal, et al., 2006; Roman & Lutjeharms, 2009). Here, the shallow shelf margin adjacent to the Agulhas Current supplies iron to the overlying waters (Grand, et al., 2015c). Combined, the excess P and iron supplied to the oligotrophic southwest Indian Ocean surface should favour diazotroph growth and thus, N_2 fixation. However, a regional characterisation of the biogeochemical functioning of the southwest Indian Ocean, including the potential for significant N_2 fixation, is currently lacking.

Productivity in the southwest Indian Ocean, and more specifically the Agulhas Current, may be fuelled by other mechanisms of nutrient supply that augment convective mixing (and possibly, N_2 fixation). The high degree of mixing and turbulence characteristic of the Agulhas Current, and other WBC systems, likely favour the upward supply of nutrients. Persistent fronts (e.g., WBCs) are characterised by strong horizontal and vertical gradients in velocity, density, and potential vorticity (Imawaki, et al., 2013; Palter, et al., 2013; Lévy, et al., 2018). The potential energy stored in these fronts fuels instabilities, which then dissipate energy via turbulence (Gill, et al., 1974; Buckingham, et al., 2019). Both mesoscale (scales of 10-100 km, weeks to months) and submesoscale (scales of 1-10 km, hours to days) instabilities are common to WBC systems (D'Asaro, et al., 2011; Lévy, et al., 2012; Gula, et al., 2016). As such, turbulent features like eddies, meanders, fronts, and filaments created by (sub)mesoscale instabilities are also common to WBC systems. These instabilities can also drive substantial secondary vertical circulations, which are predicted by models to occur at 50-100 $m.d^{-1}$ (Mahadevan & Tandon, 2006; Klein & Lapeyre, 2009). Along the length of WBCs, nutrient-rich thermocline waters shoal toward the surface, forming fast flowing subsurface nutrient streams (directly observed in the Gulf Stream and Kuroshio Current; (Pelegrí & Csanady, 1991; Palter, et al., 2005; Guo, et al., 2012)). While cross-frontal exchange of upper stream waters is largely inhibited by the strong lateral gradient in potential vorticity (Bower, et al., 1985; Beal, et al., 2006), the horizontal exchange of nutrients across the edges of WBCs has been shown to be significant (Williams & Follows, 1998; Palter, et al., 2005; Palter, et al., 2011; Letscher, et al., 2016; Yamamoto, et al., 2018). By contrast, vertical mixing of nutrients in WBC systems has only recently been investigated for the Kuroshio and Brazil boundary currents, with the results of these studies indicating substantial upward nitrate fluxes induced by the currents (Nagai, et al., 2019; Lazaneo, et al., 2020; Liao, et al., 2022). Whether similar dynamics drive upward nutrient fluxes in the Agulhas Current system remains to be seen.

In sum, the biogeochemical settings of the South Atlantic and South Indian Oceans appear to be regionally variable. Despite the paucity of biogeochemical data available for these basins, their unique characteristic features likely play a central role in shaping the regional biogeochemistry, including nutrient supply, ocean productivity, and carbon export.

1.5. Thesis scope

The goal of this thesis is to characterise N cycling in the South Atlantic and South Indian Oceans, two historically under sampled basins, with the broad aim of better understanding their biogeochemical functioning. Using the dual isotopes of nitrate as a primary tool, in addition to nutrient ratios and other physical ocean data, the research detailed in this thesis investigates nutrient supply, ocean fertility, and carbon export potential in the oceans surrounding southern Africa, along with the implications for climate. The broad scope of each thesis chapter (1-5) is outlined below.

Chapter 1: Introduction and literature review

In chapter 1, a description of the marine N cycle is provided, highlighting key processes that govern the sources, sinks, and recycling of various species of N. The magnitudes of and controls on N fluxes and their connection to ocean fertility (i.e., new and regenerated production) are then introduced, followed by a review of the implications of N fluxes for the cycling of other ocean elements, particularly carbon and phosphorus. Also included is a review of two biogeochemical tools that underpin the majority of the research described in the thesis; nitrate isotope ratios (i.e., δ^{15}N, δ^{18}O, and Δ(15-18)) and nutrient ratios (i.e., N* and P*). Both tools can be used to identify, characterise, and when coupled with appropriate spatio-temporal information, quantify, the various N cycle processes. Chapter 1 ends by reviewing the literature available on the South Atlantic and South Indian Oceans, highlighting their unique circulation and biogeochemical settings.

Chapter 2: The Angola Gyre is a hotspot of dinitrogen fixation in the South Atlantic Ocean

Chapter 2 characterises the N cycle across the tropical South Atlantic, with a particular focus on the sources of N to the euphotic zone. A zonal comparison of the hydrographic and biogeochemical properties measured for a cross-basin transect, as well as a meridional transect along the tropical eastern boundary, reveals that the thermocline of the cyclonic Angola Gyre to the east of the basin hosts low-oxygen concentrations and low-δ^{15}N nitrate, both of which are absent in the tropical western basin. The low-δ^{15}N of Angola Gyre thermocline nitrate is concluded to derive from local N_2 fixation, which is estimated to occur at a rate of 1.4-5.4 Tg N.a^{-1}. N_2 fixation in the Angola Gyre, and the South Atlantic more broadly, appears to be controlled by the overlapping biogeography of a basin-wide P excess relative to N and iron supplied locally from the low-oxygen Angolan margin. The characterisation of N cycling across the tropical South Atlantic basin yields new information on the strong regionality of ocean fertility and has implications for better understanding the controls on N_2 fixation elsewhere in the global ocean.

Chapter 3: The Agulhas Current transports signals of local and remote Indian Ocean nitrogen cycling

Chapter 3 investigates N cycling across the southwest Indian in the context of the dominant water masses present in the system. Nitrate isotope data from three cruises in and upstream of the Agulhas Current, augmented by nutrient and physical data, yield new information on the origins and modifications of the water masses circulating within and through the southwest Indian Ocean. Local N_2 fixation in the oligotrophic surface waters of the southwestern basin, estimated for the first time to occur at a rate of 7-25 Tg N.a^{-1}, explains the low δ^{15}N, and thus low Δ(15-18), of nitrate present in the thermocline. Between the top of the thermocline and the surface, a further lowering of nitrate Δ(15-18) reveals that partial nitrate assimilation co-occurs with nitrification at the base of the mixed layer, but that phytoplankton nitrate assimilation is still the dominant process acting on the mixed-layer nitrate pool. The low-Δ(15-18) nitrate generated by local N cycling in the southwest Indian Ocean appears to be retained in the waters that are laterally advected into the Cape Basin (i.e., the eastern subtropical South Atlantic) via Agulhas leakage at the Retroflection. This Indian Ocean nitrate is distinct from the high-Δ(15-18) Atlantic Ocean nitrate, such that it could provide a new means of tracing and/or quantifying Indo-Atlantic exchange of waters. This finding also has implications for inferring the intensity of Agulhas leakage over glacial-interglacial timescales.

Chapter 4: Agulhas Current dynamics enhance upward nitrate supply in the southwest subtropical Indian Ocean

Chapter 4 builds on the work detailed in Chapter 3, identifying the role that the highly-turbulent Agulhas Current plays in facilitating (sub)mesoscale upward nitrate supply to the overlying sunlit waters. Nitrate Δ(15-18) is leveraged as a tracer of both physical mixing and the source of biologically assimilated nitrate, providing novel spatio-temporal information about the flux of deep nitrate to shallow waters at (sub)mesoscales. Observations of relatively high-Δ(15-18) nitrate in shallow, low-nutrient waters, in combination with other physical and biogeochemical data, reveal three mechanisms of upward nitrate supply that fuel local productivity – these mechanisms include nitrate entrainment via an anticyclonic eddy, inshore upwelling driven by a frontal eddy, and overturning driven by coupled mesoscale-submesoscale dynamics at the high-shear edge of the Agulhas Current. This third mechanism has yet to be observed in the Agulhas Current. The characterisation of upward nitrate supply facilitated by the Agulhas Current has implications for our understanding of nutrient cycling in other WBCs, as well as for the present and future productivity of these systems.

Chapter 5: Concluding remarks and future work

Chapters 2 to 4 each conclude with a comprehensive discussion of the implications of the findings detailed therein for our broader understanding of nutrient supply and cycling, ocean productivity, and carbon export potential. As such, chapter 5 does not repeat these insights, but instead provides concluding remarks that reflect upon the entirety of the research articulated in this thesis. Also provided is a summary of the knowledge gaps and potential directions for future work suggested by the findings described in all three chapters.

Chapter 2: The Angola Gyre is a hotspot of dinitrogen fixation in the South Atlantic Ocean

This chapter has been published as:

Marshall, T. A., Granger, J., Casciotti, K. L., Dähnke, K., Emeis, K. C., Marconi, D., McIlvin, M.E., Noble, A.E., Saito, M.A., Sigman, D.M. and Fawcett, S.E., (2022). The Angola Gyre is a hotspot of dinitrogen fixation in the South Atlantic Ocean. Nature Communications Earth & Environment, 3(151), 151. https://doi.org/10.1038/s43247-022-00474-x

Abstract

Biological dinitrogen fixation is the major source of new nitrogen to marine systems and thus essential to the ocean's biological pump. Constraining the distribution and global rate of dinitrogen fixation has proven challenging owing largely to uncertainty surrounding the controls thereon. Existing South Atlantic dinitrogen fixation rate estimates vary five-fold, with models attributing most dinitrogen fixation to the western basin. From hydrographic properties and nitrate isotope ratios, we show that the Angola Gyre in the eastern tropical South Atlantic supports the fixation of 1.4-5.4 Tg N.a^{-1}, 28-108% of the existing (highly uncertain) estimates for the basin. Our observations contradict model diagnoses, revealing a substantial input of newly-fixed N to the tropical eastern basin and no dinitrogen fixation west of 7.5˚W. We propose that dinitrogen fixation in the South Atlantic occurs in "hotspots" controlled by the overlapping biogeography of excess phosphorus relative to N and bioavailable iron from margin sediments. Similar conditions may promote dinitrogen fixation in analogous ocean regions. Our analysis suggests that local iron availability causes the phosphorus-driven coupling of oceanic dinitrogen fixation to N loss to vary on a regional basis.

2.1. Introduction

The cycling of nitrogen (N) controls the fertility of the global ocean (Smith, 1984; Codispoti, 1989)and influences the ocean's role in climate (Broecker & Henderson, 1998). The ultimate source of marine N to the ocean is N_2 fixation, whereby specialized plankton, diazotrophs, transform inert N_2 gas into bioavailable ammonium. This process occurs dominantly in the warm, sunlit surface of the (sub)tropical ocean. The ultimate sink for marine N is denitrification, the bacterial reduction of oxidized N species to N_2 gas in oxygen-deficient waters and sediments. Considerable uncertainty exists regarding the magnitude of the global N source and sink terms, including whether these are balanced on timescales of ocean mixing (Codispoti, 1995; Deutsch, et al., 2002; Deutsch, et al., 2007; Brandes & Devol, 2002). An incomplete understanding of the controls on N_2 fixation, particularly at the regional scale, likely contributes to the apparent discrepancies in estimates of oceanic N loss and gain.

A stoichiometric phosphorus (P) excess relative to N, termed 'excess P', is a condition proposed to favour N_2 fixation (Deutsch, et al., 2007). Much of the global surface ocean hosts excess P (Boyer, et al., 2018), which ultimately derives from denitrification in oxygen deficient zones and sediments (Deutsch, et al., 2007; Moore, et al., 2009). The South Atlantic receives excess P both remotely and regionally, in the latter case following seasonal N loss in the northern Benguela upwelling system (NBUS) (Deutsch, et al., 2007; Flohr, et al., 2014; Nagel, et al., 2013), yet this basin appears to support little N_2 fixation. Direct and geochemical estimates of South Atlantic N_2 fixation rates, although notably sparse, range from 1.8 to 8.4 Tg $N.a^{-1}$, with disagreement as to the regional distribution (Table 2.1) (Coles & Hood, 2007; Deutsch, et al., 2007; Wang, et al., 2019; Marconi, et al., 2017; Fonseca-Batista, et al., 2017; Luo, et al., 2012; Snow, et al., 2015). These low rates have been attributed to iron limitation of diazotrophs (Moore, et al., 2009; Sohm, et al., 2011a; Marconi, et al., 2017; Snow, et al., 2015; Browning, et al., 2017) as the South Atlantic receives at least a hundred-times less aeolian iron than the North Atlantic (3 ± 2 versus 896 ± 14 $nmol.m^{-2}.d^{-1}$) (Sarthou, et al., 2003) where N_2 fixation is considerably higher, with estimates ranging from 24 to 47 Tg $N.a^{-1}$ (Table A1) (Coles & Hood, 2007; Hansell, et al., 2007; Deutsch, et al., 2007; Moore, et al., 2009; Fonseca-Batista, et al., 2017; Wang, et al., 2019; Luo, et al., 2012; Marconi, et al., 2017). The excess P that goes largely unused in the South Atlantic traverses the basin in its equatorward-flowing surface layer, ultimately fuelling N_2 fixation in the (sub)tropical North Atlantic following its entrainment into iron-replete, P-limited surface waters (Moore, et al., 2009; Marconi, et al., 2017). Nevertheless, some N_2 fixation likely occurs in the South Atlantic, yet its magnitude and distribution, and the controls thereon, remain poorly characterized.

The estimation of N_2 fixation has often relied on ocean models, most of which exploit regional variations in the nitrate-to-phosphate (NO_3^-:PO_4^{3-}) ratio (Deutsch, et al., 2007; Wang, et al., 2019; Coles & Hood, 2007) to derive rates from inverse circulation fields. Variations in N:P are typically quantified by the parameters N* and P* (Gruber & Sarmiento, 1997; Deutsch, et al., 2007; Hansell, et al., 2004), defined here as $[NO_3^-]–15.5\times[PO_4^{3-}]$ (Gruber & Sarmiento, 1997) and $[PO_4^{3-}]–[NO_3^-]\div15.5$ (Deutsch, et al., 2007), respectively, where 15.5:1 is the mean N:P ratio of nutrients supplied to the tropical South Atlantic thermocline (A.2). The conceptual basis for the estimation is that diazotrophy pairs the production of newly-fixed N with the assimilation of P. N_2 fixation thus removes P but not N from surface waters and leads to a sinking organic matter (OM) flux with an N:P ratio that is higher than that of the net supply of nitrate and phosphate to the surface (Deutsch, et al., 2007; Weber & Deutsch, 2012; Gruber & Sarmiento, 1997). However, the N:P ratio of plankton biomass, and thus of sinking OM, varies regionally (Martiny, et al., 2013), complicating the calculation of N_2 fixation rates based on nutrient stoichiometry (Mills & Arrigo, 2010). Recent modelling efforts have attempted to address this shortcoming by including variable, yet still prescribed, OM N:P ratios (Wang, et al., 2019).

Table 2.1. Existing areal N_2 fixation rate estimates (Tg $N.a^{-1}$) for the South Atlantic. The arithmetic mean (±1 SD) for 5°S to 35°S is 5.0 ± 3.3 Tg $N.a^{-1}$. This average excludes our N_2 fixation estimate, which is relevant to the tropical South Atlantic domain only. For a detailed list of the available areal N_2 fixation rate estimates, see Table A1.

Domain	Method	Rate [Tg $N.a^{-1}$]	Reference
0°S - 25°S	N* plus forward circulation model	8.4	(Coles & Hood, 2007)
11°S - 35°S	N:P plus inverse circulation model	8.3	(Wang, et al., 2019)
0°S - 40°S	P* plus inverse circulation model	7.5 [a]	(Deutsch, et al., 2007)
11°S - 30°S	Nitrate isotopes plus volume flux	3 ± 0.5	(Marconi, et al., 2017)
10°S - 45°S	Direct rate measurements	5 ± 2 [b]	(Fonseca-Batista, et al., 2017)
0°S - 40°S	Direct rate measurements	1.8 ± 0.6 [b]	(Luo, et al., 2012)
6°S - 15°S	Nitrate isotopes plus residence time	2.0 - 4.1	This study

[a] Estimated from a homogenised rate for the South Atlantic (area = 27×10^{12} m^2 for 0-40°S (Luo, et al., 2012))

[b] compilation of direct measurements made by others

Nitrate isotope ratio measurements provide an important alternative source of information for diagnosing N_2 fixation (Knapp, et al., 2008; Marconi, et al., 2017; Rafter, et al., 2013). N_2 fixation introduces nitrate to the thermocline with a $\delta^{15}N$ of -2 to 0‰ (Minagawa & Wada, 1986; Carpenter, et al., 1997; Knapp, et al., 2005; Knapp, et al., 2008), distinct from that of deep-ocean nitrate (≥5‰ (Sigman, et al., 2000); $\delta^{15}N = [(^{15}N/^{14}N)_{sample}/(^{15}N/^{14}N)_{ref} - 1]\times10^3$, in ‰ vs. N_2 in air). Negative excursions in source-to-thermocline nitrate $\delta^{15}N$ can thus be used to diagnose and quantify N_2 fixation (Knapp, et al., 2008). The N isotope ratios have some major advantages over N:P ratios in this regard. In particular, the $\delta^{15}N$ of newly-fixed N is relatively well-constrained (Minagawa & Wada, 1986; Carpenter, et al., 1997), whereas the N:P ratios of both diazotrophs and non-N_2-fixing plankton are uncertain and potentially dynamic (Weber & Deutsch, 2012; Martiny, et al., 2013; Mills & Arrigo, 2010).

Here we analyse nitrate isotope ratios and nutrient stoichiometries for the tropical South Atlantic Ocean based on new and existing measurements (Noble, et al., 2012; Marconi, et al.,

2017) (see Methods 2.3). These data reveal substantial N_2 fixation in the Angola Gyre to the east of the basin and none in the west, in contrast to current notions that N_2 fixation occurs predominantly in the western tropical South Atlantic (Figure 2.1) (Deutsch, et al., 2007; Wang, et al., 2019). We hypothesise that the confluence of remote and regional sources of excess P and iron supplied proximately from the ocean margin determines the incidence of N_2 fixation in the Angola Gyre. Our findings have implications for explaining regional variations in N_2 fixation and its coupling to N loss throughout the global ocean (Weber & Deutsch, 2014; Knapp, et al., 2016).

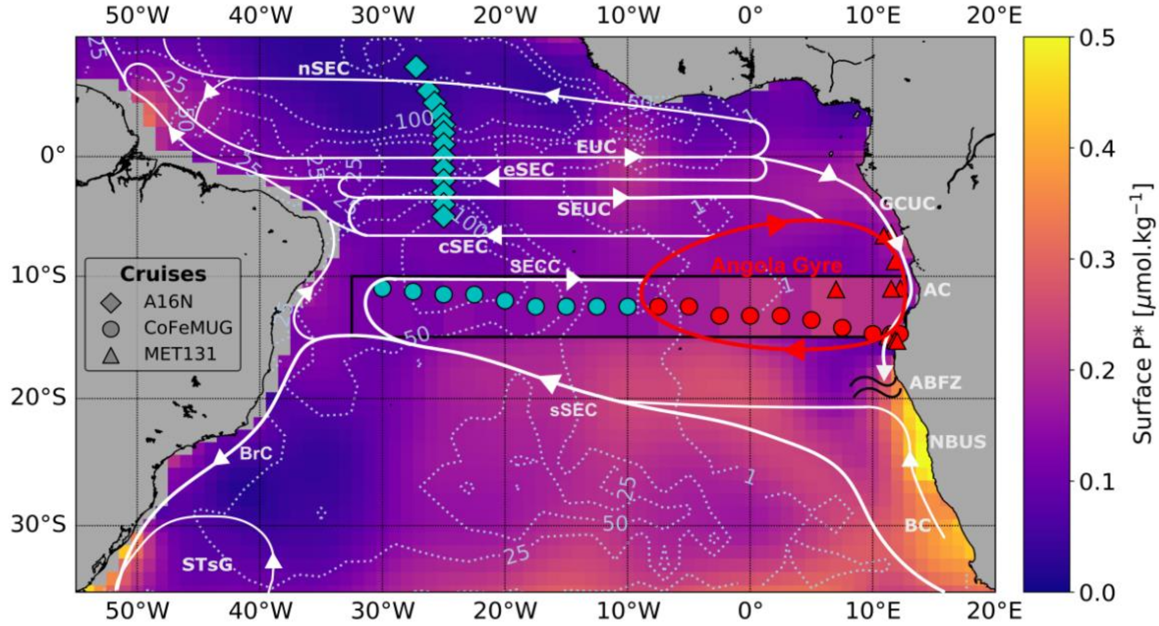

Figure 2.1. Surface P* across the South Atlantic Ocean. Station locations (coloured symbols) overlaid on an annual climatology of the South Atlantic surface P* concentration (=$[PO_4^{3-}]–[NO_3^-]÷15.5$; A.2). As indicated in the legend, circles represent stations sampled during the CoFeMUG cruise in November/December 2007 (Marconi, et al., 2017; Noble, et al., 2012), triangles show stations sampled during the MET131 cruise in October 2016, and diamonds indicate stations sampled during the CLIVAR/GO-SHIP A16N cruise in September/October 2013 (Marconi, et al., 2017; Marconi, et al., 2019). Red symbols show Angola Gyre stations and blue symbols represent western basin stations. The red cell indicates the approximate position of the Angola Gyre, and the white arrows show the circulation of thermocline waters in the tropical South Atlantic Ocean. The black box encloses P* values calculated from the CoFeMUG dataset, while the other P* data are from WOA18 (Boyer, et al., 2018) (A.2). The dotted light-grey contours show the distribution of a recent modelled 1, 25, 50 and 100 mmol $N.m^{-2}.a^{-1}$ water column-integrated N_2 fixation rates for the South Atlantic (Wang, et al., 2019). The South Atlantic Tropical Gyre is defined by the sSEC, SEUC and AC, where sSEC is south South Equatorial Current, SEUC is South Equatorial Undercurrent, and AC is Angola Current. Additionally, nSEC is north South Equatorial Current, EUC is Equatorial Undercurrent, eSEC is equatorial South Equatorial Current, cSEC is central South Equatorial Current, SECC is South Equatorial Countercurrent, GCUC is Gabon-Congo Undercurrent, ABFZ is Angola-Benguela Frontal Zone (indicated by the parallel wavy lines), NBUS is northern Benguela upwelling system, BC is Benguela Current, BrC is Brazil Current, and STsG is Subtropical subgyre.

2.2. Results and Discussion

2.2.1. Properties of the Angola Gyre

The Angola Gyre, a permanent upwelling feature embedded within the larger-scale cyclonic South Atlantic Tropical Gyre (Moroshkin, et al., 1970; Gordon & Bosley, 1990; Peterson & Stramma, 1991), was encountered east of 7.5°W along a zonal transect of the Atlantic at 6-15°S (Figure 2.1; CoFeMUG (Noble, et al., 2012; Marconi, et al., 2017) and MET131 cruises; see Methods 2.3). The gyre is characterised by a shoaling of the thermocline, defined as the waters between potential density anomalies (σ_θ; in kg.m^{-3}) 26.2 and 27.0, overlying an oxygen minimum zone (OMZ) where apparent oxygen utilization (AOU, = $O_{2saturated} - O_{2observed}$) is >240 μM (Figure 2.2a,b) (Gordon & Bosley, 1990; Mercier, et al., 2003; Peterson & Stramma, 1991). High rates of primary productivity fuelled by persistent nutrient upwelling drive elevated OM export from the Angola Gyre mixed layer, which is remineralised in the aphotic zone below the surface (Berger, 1989; Mohrholz, et al., 2008). A subsurface iron plume emanating from the nearby low-oxygen marginal sediments penetrates the Angola Gyre (dFe ~0.8-2 nM; Figure 2.2c). Intense remineralisation and repeated cycles of supply and export retain this bioavailable iron within Angola Gyre waters (Noble, et al., 2012). Local remineralisation also yields a nitrate concentration maximum (>40 μM) beneath the thermocline (σ_θ>27.0), contrasting with the lower concentration of sub-thermocline nitrate (<35 μM) and AOU (<180 μM) in the tropical western basin (west of 7.5°W; Figure 2.2b, 2.3a).

Nitrate δ^{15}N across the transect is consistently high in Tropical Surface Water (TSW; σ_θ<26.2) due to isotopic fractionation during nitrate assimilation by phytoplankton, which raises nitrate δ^{15}N (and δ^{18}O (Granger, et al., 2004; Granger, et al., 2010); which, in ‰ vs. VSMOW, $=[(^{18}O/^{16}O)_{sample}/(^{18}O/^{16}O)_{ref} - 1]\times10^3$; A.3) to >12‰. By contrast, mean thermocline nitrate δ^{15}N in the Angola Gyre is 5.7 ± 0.7‰, reaching as low as 4.6‰, a salient decrease from the western tropical basin where the average δ^{15}N of thermocline nitrate is 6.3 ± 0.1‰ (Figure 2.2d, 2.3b). Subantarctic Mode Water (SAMW; σ_θ=27.0–27.25), recently formed in the Southern Ocean, underlies the thermocline of the tropical South Atlantic and is the ultimate source of nutrients to its surface waters (Sarmiento, et al., 2004). In the western tropical basin, SAMW nitrate δ^{15}N is 6.2 ± 0.1‰, indistinguishable from the δ^{15}N of SAMW nitrate beneath the Angola Gyre (6.4 ± 0.1‰; $t(150)= -12.05$, $p=0.01$) (Figure 2.2d, 2.3b).

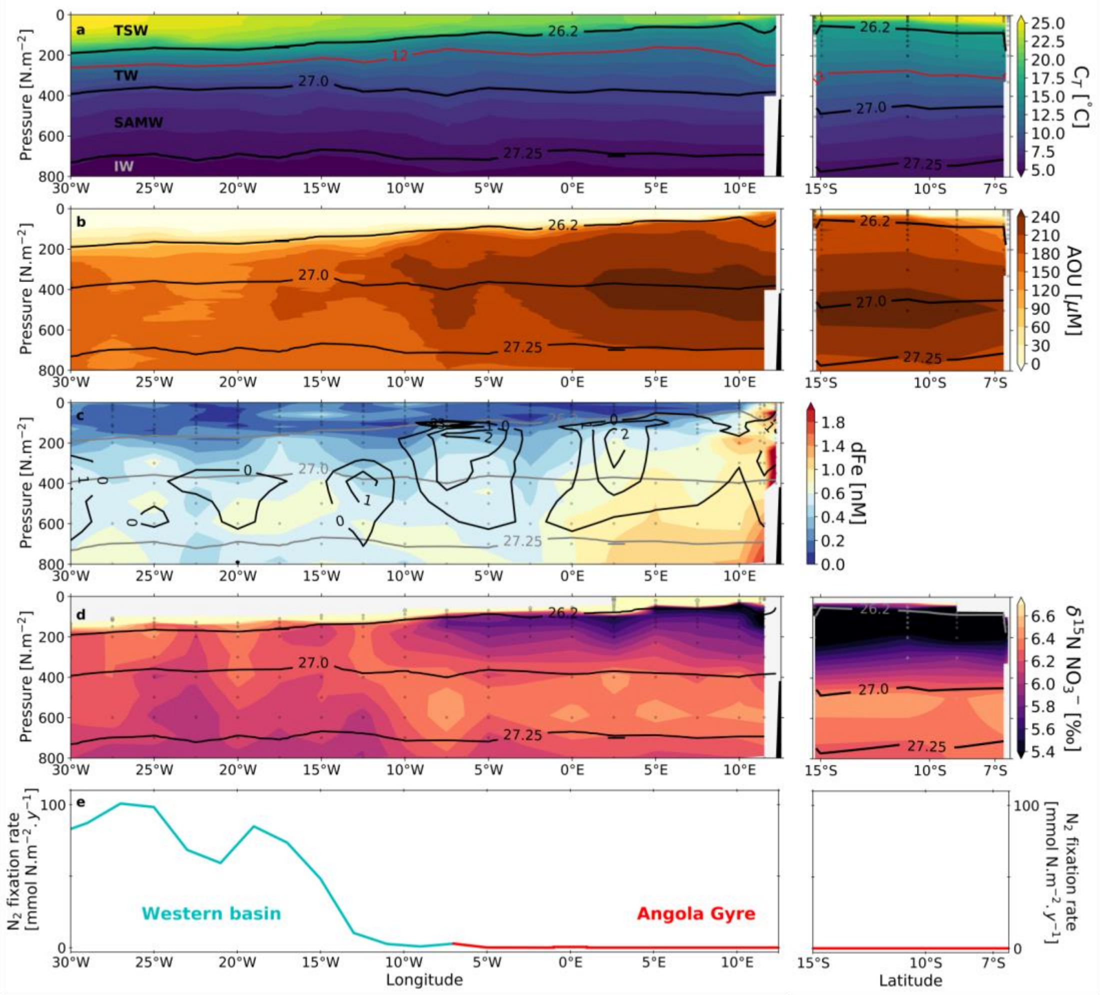

Figure 2.2. Zonal trends in physical and biogeochemical properties across the tropical South Atlantic. Gridded section plots across the CoFeMUG (30°W to 12°E; left panels) and MET131 (6°S to 15.1°S; right panels) transects of (**a**) conservative temperature in °C, where the red contour denotes the 12°C isotherm, the shoaling of which between 7.5°W and 12.2°E marks the approximate zonal extent of the Angola Gyre (Gordon & Bosley, 1990); (**b**) apparent oxygen utilisation (AOU) in μM; (**c**) dissolved iron concentrations in nM (Noble, et al., 2012) overlaid by N* contours (black) in μM; and (**d**) nitrate d^{15}N in ‰ vs. N_2 in air (CoFeMUG data from (Marconi, et al., 2017)). Panel (**e**) shows a recent modelled water column-integrated N_2 fixation rate along 11°S (left) and 11°E (right) in mmol N.m^{-2}.a^{-1} (Wang, et al., 2019), with the western basin values in blue and the Angola Gyre values in red. Black (grey) contours on **a, b, and d** (**e**) are potential density surfaces indicating tropical water masses, where TSW is Tropical Surface Water, TW is Thermocline Water, SAMW is Subantarctic Mode Water and IW is Intermediate Water (A.1). Small grey circles in **c** and **d** indicate the sampling resolution.

Mean SAMW N* is 0.0 ± 0.1 μM across the basin, increasing in the Angola Gyre thermocline to 0.7 ± 0.9 μM, coincident with the source-to-thermocline decline in nitrate δ^{15}N. N* decreases into the western tropical basin thermocline, to -0.4 ± 0.5 μM (Figure 2.3c and A.2, A.4).

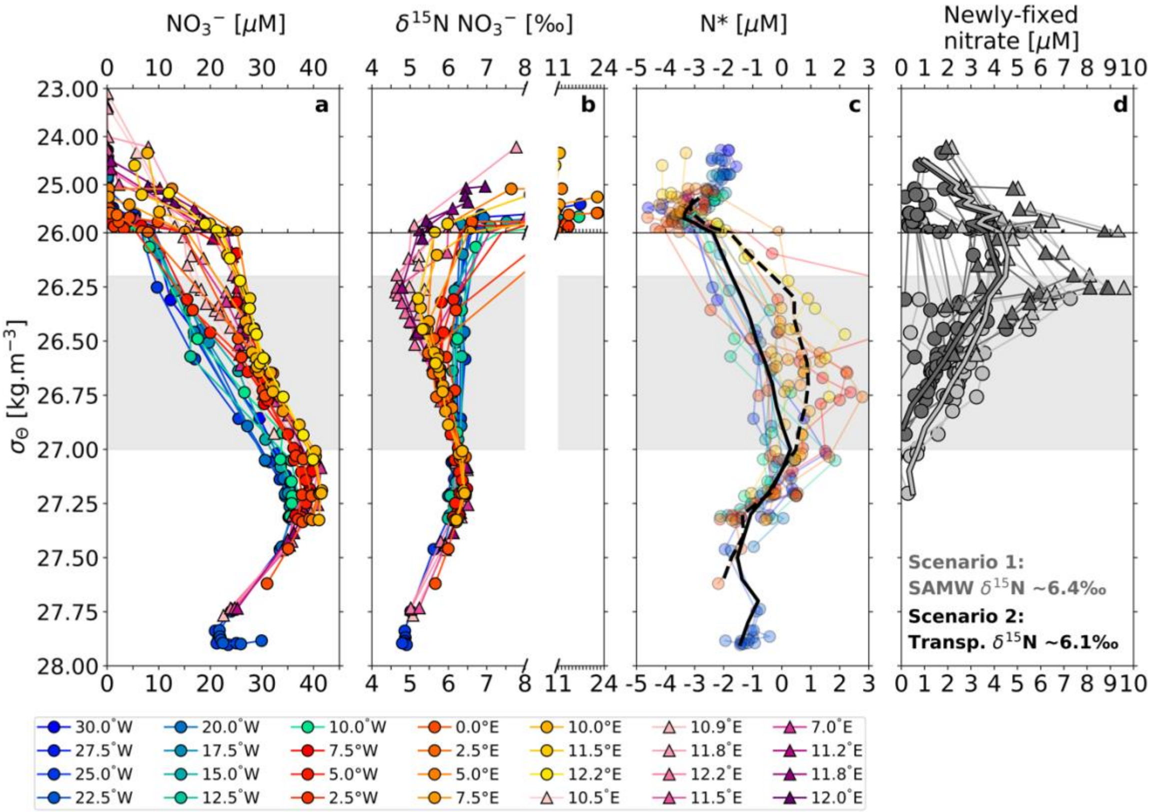

Figure 2.3. Characteristics of tropical South Atlantic nitrate. Density profiles of (**a**) nitrate concentrations in μM; (**b**) nitrate $\delta^{15}N$ in ‰ vs. N_2 in air; (**c**) N* (=$[NO_3^-]–15.5\times[PO_4^{3-}]$; A.2) in μM; and (**d**) the depth-specific concentration of newly-fixed nitrate in μM**.** In **a**-**c**, warm (cool) coloured profiles represent stations from the Angola Gyre (tropical western basin). Round-markers show data from the CoFeMUG transect while triangle-markers represent data from the MET131 transect. The legend provides station longitude. The grey shading on **a-d** indicates the density range of TW. In panel **c**, the dashed (solid) black line indicates the mean gridded N* for the Angola Gyre (western basin) stations; only CoFeMUG data are shown here because of the higher depth-resolution of this sample set. Panel **d** shows the concentration of newly-fixed nitrate, computed by multiplying the depth-specific fraction of newly-fixed nitrate ($f_{depth\_specific}$; equation A3b) by the corresponding nitrate concentration at each depth. To calculate $f_{depth\_specific}$, a nitrate $\delta^{18}O$-based correction is applied to the $\delta^{15}N$ data to remove the phytoplankton nitrate assimilation signal from TSW (A.7). Light grey data show results from scenario 1 while dark grey data represent scenario 2 (see text for details). The mean of each scenario is indicated by the bold line of corresponding colour.

2.2.2. Zonal trends in the tropical South Atlantic: evidence for an exogenous source of N to the Angola Gyre

Thermocline nitrate $\delta^{15}N$ in the western tropical South Atlantic basin is similar to that of the underlying source (6.3 ± 0.1‰ versus 6.2 ± 0.1‰) while the $\delta^{15}N$ of nitrate in the Angola Gyre thermocline is distinctly lower, by 0.7–1.8‰ (Figure 2.2d, 2.3b). Since nitrate in TSW is generally completely consumed, and given that nitrification in the ocean interior typically competes with no other process – thus negating the impact of isotopic fractionation during remineralisation in the subsurface –, remineralised OM produced from TSW will return nitrate to the thermocline with a δ^{15}N that is indistinguishable from the underlying SAMW source (Sigman, et al., 2009; Rafter, et al., 2013; Marconi, et al., 2019). The fact that the δ^{15}N of thermocline nitrate in the Angola Gyre is lower than SAMW nitrate δ^{15}N signals an exogenous source of N to surface waters, the consumption and subsequent remineralisation of which yields low-δ^{15}N nitrate in the Angola Gyre thermocline (Knapp, et al., 2005; Knapp, et al., 2008).

Zonal and vertical changes in nutrient stoichiometry corroborate the notion of an exogenous source of N to the Angola Gyre. The SAMW-to-thermocline N* increase in the gyre is consistent with the addition of N in stoichiometric excess of P (i.e., relative to the N:P ratio of the regional nutrient supply, 15.5:1) while the decrease in SAMW-to-thermocline N* in the western tropical basin suggests that sinking OM may be lower in N:P than the regional nutrient supply (A.4).

Despite the existing data pointing to complete nitrate consumption in the Angola Gyre surface, instances of incomplete nitrate assimilation could occur in this perennially-upwelling feature, and these could cause the loss of high-δ^{15}N nitrate (by advection), with low-δ^{15}N OM retained and remineralised in the gyre thermocline (Rafter, et al., 2013; Lehmann, et al., 2018). However, the regeneration of OM deriving from partial nitrate assimilation, which would have an N:P of ~15.5:1, could not yield the high N* observed in the thermocline. Additionally, mixed-layer nitrate was measurable at only three of 19 stations at the time of our sampling, reinforcing the view that nitrate is seldom unconsumed in Angola Gyre surface waters in spring, and likewise in autumn (Mohrholz, et al., 2008). The δ^{15}N of thermocline nitrate could arguably be lowered by the lateral export of high-δ^{15}N dissolved organic N (DON) from the gyre surface. However, high-δ^{15}N DON export also cannot account for the regional increase in thermocline N*. We thus rule out partial nitrate assimilation and DON export as explanations for the low δ^{15}N of Angola Gyre thermocline nitrate.

Atmospheric deposition can introduce exogenous N to the surface ocean with a δ^{15}N <0‰ (Altieri, et al., 2021) and an N:P ratio >1000:1 (Baker, et al., 2010), potentially explaining both the low-δ^{15}N nitrate and high N* of the Angola Gyre thermocline. However, estimates of the N deposition flux to the South Atlantic are orders of magnitude too low to account for our observations (Baker, et al., 2010) (A.5). We thus conclude that the exogenous N in the Angola Gyre thermocline must derive from N_2 fixation.

2.2.3. Origin of the N_2 fixation signal in the Angola Gyre thermocline

The low $\delta^{15}N$ of Angola Gyre thermocline nitrate could originate, at least partly, in the tropical North Atlantic basin where N_2 fixation rates are elevated (Marconi, et al., 2017; Marconi, et al., 2019; Knapp, et al., 2008; Snow, et al., 2015), and be transported into the gyre by equatorial feeder currents (Figure 2.1). We address this possibility by estimating the concentration-weighted influx of nitrate $\delta^{15}N$ by the three Angola Gyre feeder currents; the Equatorial Undercurrent (EUC), the South Equatorial Undercurrent (SEUC), and the South Equatorial Countercurrent (SECC) (Gordon & Bosley, 1990). We estimate the $\delta^{15}N$ of the EUC, SEUC, and SECC end-members to be 5.7‰, 6.0‰, and 6.3‰, respectively (Methods 2.3; A.6). The relative contribution of each current to Angola Gyre thermocline nitrate based on transport volumes (Mercier, et al., 2003) yields a mean flux-weighted nitrate-$\delta^{15}N$ of 6.1 ± 0.1‰. While lower than the $\delta^{15}N$ of underlying SAMW (6.4‰), this end-member is not low enough to decrease Angola Gyre thermocline nitrate $\delta^{15}N$ to 5.7‰ (nor to the observed minimum of 4.6‰). Thus, some amount of the low-$\delta^{15}N$ signal must derive from local N_2 fixation.

Our conclusion that N_2 fixation occurs in the Angola Gyre is further supported by the lower $\delta^{15}N$ of nitrate at the depth of the AOU maximum compared to that of core SAMW (6.2‰ versus 6.4‰; Figure 2.2b and d). The OM remineralised at the AOU maximum is lower in $\delta^{15}N$ than SAMW nitrate, confirming that it must originate in Angola Gyre surface waters following *in situ* N_2 fixation given that the provenance of the high AOU signal is *in situ* primary production (Gordon & Bosley, 1990). Additional support comes from direct rate measurements made during the CoFeMUG cruise (Sohm, et al., 2011b) and other rate data from near the Angola Gyre (Fonseca-Batista, et al., 2017; Subramaniam, et al., 2013; Staal, et al., 2003), which indicate N_2 fixation rates ranging from undetectable to ~170 μmol $N.m^{-2}.d^{-1}$. Regional observations of diazotrophs (*Trichodesmium* spp. being the most abundant) and diatoms hosting N_2-fixing symbionts (*Rhizosolenia* and *Chaetoceros* spp.) further substantiate the occurrence of N_2 fixation in the Angola Gyre (An, 1971; Foster, et al., 2009; Subramaniam, et al., 2013; Sohm, et al., 2011b).

2.2.4. Quantifying the N_2 fixation rate in the Angola Gyre

Using our nitrate $\delta^{15}N$ data, we estimate the annual rate of N_2 fixation in the Angola Gyre, considering two scenarios: 1) the low-$\delta^{15}N$ of thermocline nitrate is generated solely from *in situ* N_2 fixation and superimposed on SAMW nitrate, and 2) local N_2 fixation contributes the fraction of low-$d^{15}N$ thermocline nitrate that is not supplied by the equatorial feeder currents. For both scenarios, we estimate the fraction (*f*) of newly-fixed nitrate in the Angola Gyre as:

$$f = \frac{\delta^{15}\mathrm{N}_{\mathrm{AGmean}} - \delta^{15}\mathrm{N}_{\mathrm{scenario\_mean}}}{\delta^{15}\mathrm{N}_{\mathrm{N_2fix}} - \delta^{15}\mathrm{N}_{\mathrm{scenario\_mean}}} \tag{2.1}$$

$\delta^{15}N_{AGmean}$ is the mean concentration-weighted $\delta^{15}N$ of Angola Gyre nitrate for the upper water column ($\sigma_\theta \leq 27.0$), estimated to be 5.7 ± 0.4‰ (5.5-5.9‰; 5th-95th percentiles; Methods 2.3), $\delta^{15}N_{N2fix}$ is the $\delta^{15}N$ of nitrate regenerated from diazotrophic OM, -1‰ (Minagawa & Wada, 1986; Carpenter, et al., 1997), and $\delta^{15}N_{scenario\_mean}$ is the scenario-specific mean concentration-weighted $\delta^{15}N$ of nitrate supplied to the Angola Gyre thermocline (6.4 ± 0.1‰ and 6.1 ± 0.1‰ for scenarios 1 and 2, respectively).

For scenario 1, *f* = 9% (6-12%; 5th-95th percentiles) and for scenario 2, *f* = 6% (2-9%; 5th-95th percentiles). On average, therefore, 6% to 9% (associated with scenario 2 and 1, respectively) of the nitrate above SAMW originates from local N_2 fixation. This mass-balance approach neglects particulate organic N, although this pool contributes negligibly to total N, accounting for <1% of the fixed N reservoir above $\sigma_\theta=27.0$. Our approach is further validated by the concentration-weighted $\delta^{15}N$ that it yields for nitrate above $\sigma_\theta=27.0$ in the western tropical basin of 6.3 ± 0.1‰ (6.2-6.4‰; 5th-95th percentiles), indistinguishable from that of SAMW (6.2 ± 0.1‰). This correspondence further confirms that N_2 fixation is negligible in the tropical waters west of the Angola Gyre.

To visualize the depth distribution of newly-fixed nitrate in the Angola Gyre, we calculate $f_{depth\_specific}$ (i.e., the fraction of the nitrate pool at each depth that is newly-fixed) for each sample above $\sigma_\theta=27.0$, after removing the signal of phytoplankton assimilation from nitrate $\delta^{15}N$ using the coincident $\delta^{18}O$ data (Methods 2.3; A.7). This exercise reveals that a substantial fraction of TSW nitrate is newly-fixed, which is not apparent from the nitrate $\delta^{15}N$ profiles because fractionation during nitrate assimilation overprints the isotopic signal of newly-nitrified N (Figure 2.3b and d). It is not appropriate, however, to integrate these depth-specific estimates to yield a measure of the newly-fixed N inventory due to the likelihood of 'double-counting' – that is, low-$\delta^{15}N$ nitrate assimilated in the surface is returned to the thermocline when the resulting OM is exported and remineralised, such that at the scale of the water-column, correction of shallow nitrate-$\delta^{15}N$ for nitrate assimilation is unnecessary (Knapp, et al., 2008). Instead, the mass-balance approach represented by equation 2.1 is most appropriate for estimating the water column burden of newly-fixed N.

Multiplying *f* (equation 2.1) by the mean Angola Gyre nitrate concentration for $\sigma_\theta \leq 27.0$ indicates that local N_2 fixation supplies 313-641 mmol N.m^{-2} to the thermocline nitrate reservoir. The residence time of thermocline waters in the Angola Gyre is 4.4 to 8.5 years

(Gordon & Bosley, 1990) and its areal extent is 2.6×10^{12} m^2. These constraints yield an N_2 fixation rate of 2.8–5.4 Tg $N.a^{-1}$ (mean of 4.1 ± 2.8 Tg $N.a^{-1}$) for scenario 1 and 1.4–2.6 Tg $N.a^{-1}$ (mean of 2.0 ± 3.0 Tg $N.a^{-1}$) for scenario 2, considering both extrema for residence time (Methods 2.3; A.8). Our estimates are equivalent to rates of 102–390 mmol $N.m^{-2}.d^{-1}$, comparable to direct N_2 fixation rates measured near the Angola Gyre (Sohm, et al., 2011b; Fonseca-Batista, et al., 2017; Subramaniam, et al., 2013; Staal, et al., 2003) (A.9).

2.2.5. The Angola Gyre is a hotspot for N_2 fixation in the South Atlantic

Our N_2 fixation rate estimates imply that the Angola Gyre accounts for 28-108% of the highly uncertain mean South Atlantic N_2 fixation rate of 5.0 ± 3.3 Tg $N.a^{-1}$ (Table 2.1). Since the latter derives from few observations that are sparsely distributed across the basin, it would be unwise to conclude that the Angola Gyre makes a disproportionate contribution to South Atlantic N_2 fixation. Nonetheless, since the Angola Gyre occupies only ~10% of the South Atlantic by area, our data indicate that it is a “hotspot” for N_2 fixation. Conditions particular to the Angola Gyre must thus render this feature favourable for N_2 fixation.

The phosphate-bearing, nitrate-deplete surface waters of the South Atlantic receive a limited supply of aeolian iron (Sarthou, et al., 2003), a condition proposed to limit N_2 fixation across the basin (Moore, et al., 2009; Marconi, et al., 2017; Wang, et al., 2019; Knapp, et al., 2016; Snow, et al., 2015). The non-aeolian iron supply to the Angola Gyre must thus be substantial. The Congo-shelf-zone near the Angola Gyre has been reported to supply a substantive quantity of iron to the marginal ocean, equivalent to 40 ± 15% of the entire South Atlantic aeolian iron flux (Vieira, et al., 2020), and the elevated iron concentrations observed in the vicinity of the Angola Gyre (Figure 2.2c) are evidence of this marginal iron supply. We hypothesize that the subsurface iron plume, which is trapped by the retentive regional circulation of the Angola Gyre through repeated cycles of upward supply, export, and remineralisation (Noble, et al., 2012), relieves diazotrophs in the overlying surface waters of iron limitation.

We thus conclude that N_2 fixation occurs in the Angola Gyre because of the overlapping biogeography of excess P and bioavailable iron. While the iron supply to the Angola Gyre is local, originating from the nearby low-oxygen margin sediments, the excess P derives from regional and remote N loss. The apparent importance of margin-derived iron echoes a growing body of work showing that sedimentary iron sources are important to the global ocean iron budget (Scholz, et al., 2014; Conway & John, 2014; Tagliabue, et al., 2016; Homoky, et al., 2021). The notion that both iron and excess P together limit N_2 fixation at the regional scale in the South Atlantic is compatible with previous work showing negligible rates of N_2 fixation in the western tropical basin where measurements were made in P-bearing but iron-limited waters (Moore, et al., 2009; Snow, et al., 2015; Schlosser, et al., 2014).

2.2.6. The possibility of additional N_2 fixation hotspots

We hypothesize that N_2 fixation hotspots are likely inherent to ocean regions characterized by biogeochemical conditions analogous to those encountered in the Angola Gyre, possibly enhanced by retentive circulation features (A.10). In the subtropical South Atlantic where the Brazil Current recirculation forms a subgyre adjacent to the continental shelf (Peterson & Stramma, 1991) (Figure 2.1), an N_2 fixation hotspot should result as waters bearing a remote (i.e., Southern Ocean-derived) and regional (i.e., NBUS-derived) supply of excess P (Deutsch, et al., 2007) (Figure 2.1) encounter a local supply of sediment-derived iron (Homoky, et al., 2021). Observations of diazotroph blooms (Lima, et al., 2019) and low-$\delta^{15}N$ thermocline nitrate (Tuerena, et al., 2015) in the Brazil subgyre validate this prediction. In addition, the cyclonic Guinea Dome in the eastern tropical North Atlantic receives excess P from local upwelling of P-rich subsurface waters (Boyer, et al., 2018) and iron from dust deposition, possibly augmented by an iron flux from the nearby low-oxygen margin sediments (Conway & John, 2014). Direct N_2 fixation rate measurements (Fonseca-Batista, et al., 2017; Luo, et al., 2012), the identification of diazotrophs (Luo, et al., 2012; Benavides & Voss, 2015), and low-$\delta^{15}N$ thermocline nitrate (Marconi, et al., 2015) in the vicinity of the Guinea Dome are consistent with this region also being an N_2 fixation hotspot.

The surface waters above or just offshore of the ocean's major suboxic zones would, in general, appear well-suited to host hotspots of N_2 fixation. Denitrification in both the shallow subsurface water column and the adjacent sediments generates an N deficit (i.e., a P excess) (Deutsch, et al., 2007). At the same time, the adjacency of these zones to low-oxygen margin sediments, coupled with water column suboxia overlying some of the sediments, supplies iron to the water column (Scholz, et al., 2014; Pinedo-González, et al., 2015; Moffett & German, 2020). These regions are also characterized by upwelling, which would transport both the excess P and the iron into the surface mixed layer. In these surface waters or just offshore, phytoplankton assimilation leaves nitrate-free but P- and iron-bearing surface waters (Deutsch, et al., 2007; Pinedo-González, et al., 2015; Moffett & German, 2020; Rafter, et al., 2013), a seemingly ideal recipe for N_2 fixation.

However, the existing data are ambiguous as to the rates of N_2 fixation above and nearby the suboxic zones. Observations from the Arabian Sea support elevated N_2 fixation (Capone, et al., 1998; Bange, et al., 2000; Gandhi, et al., 2011). By contrast, incubation-based measurements in the eastern tropical Pacific suggest negligible to extremely high rates (Knapp, et al., 2016; Jayakumar, et al., 2017; White, et al., 2013; Fernandez, et al., 2011; Moutin, et al., 2008; Dekaezemacker, et al., 2013). Notably, incubation experiments suggest that N_2 fixation occurs in the Costa Rica Dome (Fernandez, et al., 2011), a retentive feature embedded within the eastern tropical Pacific suboxic zone that is characterised by similar hydrography to the Angola Gyre. In the water column of all the suboxic zones, a decrease in nitrate $\delta^{15}N$ is observed above the very high nitrate $\delta^{15}N$ associated with denitrification (Brandes, et al., 1998; Sigman, et al., 2005; Casciotti, et al., 2013; Buchwald, et al., 2015); this upward $\delta^{15}N$ decline has been interpreted as evidence of local N_2 fixation (Brandes, et al., 1998). Coupled nitrate $\delta^{15}N$ and $\delta^{18}O$ measurements from the eastern tropical North Pacific indicated a lower nitrate $\delta^{15}N$ than is expected from nitrate $\delta^{18}O$ in the upper portion of the suboxic zone, also consistent with a role for N_2 fixation (Sigman, et al., 2005). However, N cycling processes occurring within suboxic waters (e.g., nitrite oxidation) provide an alternative explanation for the observed $\delta^{15}N$-$\delta^{18}O$ decoupling (Sigman, et al., 2005; Casciotti, et al., 2013; Buchwald, et al., 2015; Peng, et al., 2015), complicating the use of the nitrate isotopes to evaluate N_2 fixation above and near the major suboxic zones. Importantly, the Angola Gyre is not complicated by the same suboxic zone N cycling processes, allowing us to pinpoint the role of N_2 fixation in this system. Our findings for the Angola Gyre thus suggest that the nitrate $\delta^{15}N$ decline in the shallow subsurface of the suboxic zones may have a similar origin. The nitrate isotope data of the major ocean suboxic zones should be revisited with this new perspective.

2.2.7. Implications of regional N_2 fixation hotspots

N_2 fixation has been proposed to be spatially and/or quantitatively coupled to N loss at the basin scale (Deutsch, et al., 2007; Redfield, et al., 1963; Flohr, et al., 2014). Our estimate of N_2 fixation in the Angola Gyre is notably comparable to N loss from the NBUS (1.4-2.5 Tg $N.a^{-1}$) (Kuypers, et al., 2005; Nagel, et al., 2013). In this regard, the generation and advection of excess-P waters from the NBUS have been hypothesized to fuel N_2 fixation in the vicinity of the Angola Gyre (Flohr, et al., 2014), prompting the suggestion that N sources and sinks in the south-eastern Atlantic are coupled. However, surface P* is perennially elevated across the (sub)tropical South Atlantic, including in Angola Gyre and Brazil subgyre surface waters (Deutsch, et al., 2007; Moore, et al., 2009) (Figure 2.1). Accordingly, it is not clear that the additional flux of excess P from the NBUS, by itself, stimulates N_2 fixation in the Angola Gyre. Rather, N_2 fixation would likely occur in the Angola Gyre regardless of whether it receives excess P from the NBUS, provided that the iron supply is sustained. That is, the greatest influence of the NBUS on N_2 fixation in the Angola Gyre may be through its augmentation of the iron supply. In summary, our findings argue that a P-driven coupling of N_2 fixation to denitrification is contingent on a supply of iron, which is most easily achieved along coastal suboxic zones (Scholz, et al., 2014).

Because the South Atlantic hosts a basin-wide surface P excess, a future increase in the iron supply to the south-eastern Atlantic due to expanding low-oxygen margins (Noble, et al., 2012; Homoky, et al., 2021; Stramma, et al., 2008) and/or a climate change-driven increase in aeolian deposition (Hamilton, et al., 2020) could enhance N_2 fixation in and beyond the Angola Gyre. Consequently, the meridional flux of excess P across the Atlantic could decrease, engendering a shift in the dominance of N_2 fixation from the North to the South.

2.2.8. Lessons for estimating basin-scale N_2 fixation rates

Our observations contradict diagnoses of the regional distribution of N_2 fixation in the South Atlantic computed from nutrient climatologies and velocity fields from ocean general circulation models (GCMs; e.g., P* convergence) (Deutsch, et al., 2007; Wang, et al., 2019). This inconsistency highlights the current inadequacy of nutrient fields to deliver regional representations of N_2 fixation. Modelled distributions suggest that N_2 fixation predominantly occurs in the western and central tropical South Atlantic at a rate of 7.5-8.3 Tg $N.a^{-1}$, yet the nitrate-$\delta^{15}N$ data from these longitudes bear no evidence of the remineralisation of low-$d^{15}N$, diazotroph-derived OM (Figure 2.2d and 2.3b). Thus, while the model diagnoses offer a powerful framework from which to estimate basin-scale N_2 fixation rates and conceptualize the global drivers thereof (Deutsch, et al., 2007), some of the fundamental assumptions inherent to this approach can lead to erroneous diagnoses, potentially underpinning the discrepancy between our observations and existing model solutions. First, coarse resolution (2-4°) GCMs used to simulate current velocities and transports typically resolve only gross circulation features. Although this limitation is widely acknowledged (Deutsch, et al., 2007; Coles & Hood, 2007; Wang, et al., 2019), the implications for estimates of N_2 fixation rates and distributions may be important, particularly at the regional scale. In this regard, such GCMs are unable to reliably simulate ocean-margin environments (Tagliabue, et al., 2016; Weber & Deutsch, 2014; Coles & Hood, 2007). Second, the available South Atlantic nutrient climatologies include few data, particularly in the central basin, such that the choice of dataset can considerably alter the modelled regional distribution of N_2 fixation (Deutsch, et al., 2007). Third, diagnoses of N_2 fixation from inverse models are highly sensitive to the N:P ratios of plankton biomass and exported OM. These properties are difficult to measure and are thought to be dynamic and sensitive to environmental conditions (Weber & Deutsch, 2012; Martiny, et al., 2013; Mills & Arrigo, 2010; Letscher, et al., 2013). Elemental ratios of OM are thus typically parameterized (Deutsch, et al., 2007; Wang, et al., 2019) and may not accurately capture the plasticity of OM stoichiometry. Fourth, to parameterize dissolved OM in models, its production and degradation rates also have to be prescribed. However, few measurements of such rates exist — particularly with respect to dissolved organic phosphorus, which diazotrophs can assimilate when ambient phosphate concentrations are low (Dyhrman, et al., 2006) —, resulting in modelled dissolved OM dynamics that are poorly constrained and potentially erroneous (Letscher, et al., 2015). Finally, the analytical limit of quantification for [PO_4^{3-}] and [NO_3^-] is such that the propagated error on P* is ≥0.1 μM (A.11) (Martiny, et al., 2019). Interpretations of ≤0.1 μM differences in P* may thus inaccurately diagnose the rate and/or distribution of N_2 fixation (Becker, et al., 2020).

Pending enhanced observational coverage and improved model simulations of margin environments, convergent N_2 fixation distributions for the South Atlantic and other dynamic ocean-margin regions will remain elusive. Our work highlights the utility of nitrate isotope ratios for identifying and estimating N_2 fixation, and underscores the importance of regional observations, which are necessary for understanding the regional controls on N_2 fixation that ultimately determine its global distribution.

2.3. Materials and methods

2.3.1. Sample and data provenance

The CoFeMUG nutrient and nitrate isotope data were first published in Noble et al. (2012) and Marconi et al. (2017), respectively. Samples from the CoFeMUG cruise were collected onboard the R/V *Knorr* in November and December 2007 (Figure 2.1). Seawater samples were measured for nitrate isotopes at the Woods Hole Oceanographic Institution using the denitrifier method (Sigman, et al., 2001; Casciotti, et al., 2002). Nitrate concentration and isotope data were first published from the CLIVAR A16N cruise in Marconi et al. (2015; 2019). The samples were collected onboard the NOAA R/V *Ronald H. Brown* between August and October 2013 as part of the GO-SHIP and CLIVAR program. The shipboard-ADCP data from this cruise are provided in Firing & Hummon (2010). The MET131 cruise data have not been previously published. This cruise was undertaken onboard the R/V *Meteor* in October 2016, with nine stations sampled between 6°S-15°S and 7°E-12°E. Twenty-four 12 L Niskin bottles attached to a Sea-Bird rosette with conductivity-temperature-depth (CTD) and oxygen sensors were remotely-fired over the upper 1000 m to collect seawater samples for nutrient and nitrate isotope analysis. Samples were collected in thoroughly-rinsed 30 ml HDPE bottles, filtered (0.4 mm), and immediately frozen at -20°C until analysis.

2.3.2. Analysis of MET131 cruise nutrient concentrations and nitrate isotopes

Nitrate and phosphate concentrations ([NO_3^-], [PO_4^{3-}]) and the dual isotopes of nitrate were analysed at the Helmholtz Zentrum Geesthacht (HZG) in Germany. The concentrations of PO_4^{3-}, nitrite ([NO_2^-]) and nitrate plus nitrite ([NO_3^-]+[NO_2^-]) were measured colourimetrically using an automated continuous flow system (AA3, Seal Analytical, Germany) with a detection limit of 0.01 μM (Grasshoff, 1983); [NO_3^-] was then determined by subtraction. The dual isotopes of nitrate, following nitrite removal (Granger & Sigman, 2009), were measured using the denitrifier method (Sigman, et al., 2001; Casciotti, et al., 2002) whereby nitrate is quantitatively converted to nitrous oxide gas (N_2O) by denitrifying bacteria that lack an N_2O reductase enzyme. The N and O isotope ratios of the N_2O were measured using a Thermo Delta Plus XP isotope ratio mass spectrometer in-line with a GasBench II. The international reference materials, IAEA-N3 (Gonfiantini, 1984) and USGS-34 (Böhlke, et al., 2003), were included in each run to enable post-run calibration of the N_2O measurements to N_2 in air ($\delta^{15}N$) and VSMOW ($\delta^{18}O$). The standard deviation of duplicate measurements of $\delta^{15}N$ and $\delta^{18}O$ was <0.2‰ and <0.4‰, respectively.

2.3.3. Data gridding and interpolation

The CoFeMUG and MET131 data were gridded prior to the generation of section plots and the calculation of mean water-column values (Figure 2.2 and 2.3c,d). The z-grid (pressure) bins focused on the upper 1000 m. Python 3.6 Xarray linear method was used as the interpolation scheme.

2.3.4. Nitrate $\delta^{15}N$ transported into the Angola Gyre

Cruise A16N sampled both the Equatorial Undercurrent (EUC) and South Equatorial Undercurrent (SEUC) at 0.5°S and 3.6°S, respectively, while the CoFeMUG cruise sampled the South Equatorial Countercurrent (SECC) at 27.5-30°E (Figure 2.1; A.6). The mean [NO_3^-]-weighted $\delta^{15}N$ for the EUC, SEUC, and SECC were estimated to be 5.7‰, 6.0‰ and 6.3‰, respectively. To appropriately weight the nitrate flux of each feeder current, two transport volume scenarios were considered due to the uncertainty in the contribution of the EUC to the Angola Gyre (Mercier, et al., 2003). Scenario A considers the net transport across the northern limb of the Angola Gyre, of 8 Sv, to be apportioned between the SEUC (59%) and the SECC (41%), with no contribution from the EUC (Mercier, et al., 2003). Scenario B considers the net transport across the eastern limb of the Angola Gyre, of 11 Sv, to be apportioned between the SEUC (43%), the SECC (30%), and the EUC (27%) (Mercier, et al., 2003). The mean flux-weighted nitrate $\delta^{15}N$ resulting from both transport scenarios was 6.1 ± 0.1‰, this value is used in scenario 2 throughout the study.

2.3.5. Assimilation-corrected, depth-specific fraction of newly-fixed nitrate

Co-occurring nitrate assimilation and nitrification at the base of the euphotic zone raises the δ^{15}N of nitrate, potentially yielding an underestimation of the depth-specific fraction of newly-fixed nitrate inferred from the δ^{15}N data (A.7). During nitrate assimilation, nitrate δ^{18}O and δ^{15}N rise in a 1:1 ratio as nitrate consumption proceeds (Granger, et al., 2004; Granger, et al., 2010) while during nitrification, nitrate δ^{18}O and δ^{15}N become decoupled (Sigman, et al., 2009; Buchwald, et al., 2012; Boshers, et al., 2019). The nitrate δ^{18}O data thus reveal 1) the depth at which nitrate assimilation begins to alter to isotopic composition of the nitrate pool and 2) the magnitude of the nitrate assimilation signal, two insights that are not apparent from the nitrate δ^{15}N data. Assuming that isotopic fractionation associated with nitrate assimilation similarly alters nitrate δ^{15}N and δ^{18}O proceeds (Granger, et al., 2004; Granger, et al., 2010), beginning at the depth where nitrate δ^{18}O starts to rise above its mean deep-ocean value, we quantified the nitrate assimilation signal at each depth in the water column and subtracted it from the nitrate δ^{15}N data. Following the removal of the nitrate assimilation signal, the fraction of newly-fixed nitrate at each depth was calculated.

2.3.6. Statistical analyses

To estimate uncertainty on the mean δ^{15}N of Angola Gyre and western basin nitrate ($\sigma_\theta \leq 27.0$), we calculated the 95% confidence interval associated with a t-distribution (for n <30). The same method was adopted to estimate uncertainty on *f* (equation 2.1) for scenarios 1 and 2. To characterize the uncertainty associated with the Angola Gyre N_2 fixation rates, we ran a Monte Carlo simulation of 100k steps assuming a normal probability distribution. We report the standard deviation of the output as the error associated with the rates.

Appendix A

This appendix has been published as the supplementary information for chapter 2, "*The Angola Gyre is a hotspot of dinitrogen fixation in the South Atlantic Ocean*" as:

Marshall, T. A., Granger, J., Casciotti, K. L., Dähnke, K., Emeis, K. C., Marconi, D., McIlvin, M.E., Noble, A.E., Saito, M.A., Sigman, D.M. and Fawcett, S.E., (2022). The Angola Gyre is a hotspot of dinitrogen fixation in the South Atlantic Ocean. Nature Communications Earth & Environment, 3(151), 151. https://doi.org/10.1038/s43247-022-00474-x

Table A1. Published N_2 fixation rate estimates for the Atlantic Ocean. Estimates of N_2 fixation rates for the Atlantic Ocean derived from both geochemical (i.e., nutrient ratios or nitrate isotopes) and direct (i.e., $^{15}N_2$ addition and acetylene reduction) methods. Note that the domain ranges are not always the same. Table adapted from Marconi et al. (2017).

	Domain	Method	Rate [Tg N.a^{-1}]	Reference
Whole Atlantic	25°S - 65°N	N:P plus circulation model	47.6	(Coles & Hood, 2007)
	35°S - 35°N	N:P plus ventilation rates	22 [b]	(Hansell, et al., 2007)
	45°S - 45°N	N:P plus circulation model	28 [b]	(Deutsch, et al., 2007)
	45°S - 45°N	Nitrate isotopes plus circulation model	15 - 24	(Knapp, et al., 2008)
	35°S - 50°N	N:P plus volume flux	21	(Moore, et al., 2009)
	40°S - 55°N	Direct rate measurements	34 ± 7 [c]	(Luo, et al., 2012)
	45°S - 50°N	Direct rate measurements	27.6 ± 10.4 [c]	(Fonseca-Batista, et al., 2017)
	30°S - 61°N	Nitrate isotopes plus volume flux	30.5 ± 4.9	(Marconi, et al., 2017)
	30°S - 61°N	N:P plus circulation model	36.2	(Wang, et al., 2019)
North Atlantic	10°N - 50°N	N:P plus water age	28	(Gruber & Sarmiento, 1997)
	0°N - 65°N	N:P plus circulation model	39.2	(Coles & Hood, 2007)
	0°N - 55°N	Direct rate measurements	32 ± 7.4 [c]	(Luo, et al., 2012)
	10°S - 50°N	Direct rate measurements	22.6 ± 10.2 [c]	(Fonseca-Batista, et al., 2017)
	11°S - 61°N	Nitrate isotopes plus volume flux	27.1 ± 4.3	(Marconi, et al., 2017)
	11°S - 61°N	N:P plus circulation model	27.9	(Wang, et al., 2019)
South Atlantic	0°S - 25°S	N:P plus circulation model	8.4	(Coles & Hood, 2007)
	0°S - 40°S	N:P plus circulation model	7.5 [a]	(Deutsch, et al., 2007)
	0°S - 40°S	Direct rate measurements	1.8 ± 0.6 [c]	(Luo, et al., 2012)
	10°S - 45°S	Direct rate measurements	5 ± 2 [c]	(Fonseca-Batista, et al., 2017)
	11°S - 30°S	Nitrate isotopes plus volume flux	3 ± 0.5	(Marconi, et al., 2017)
	11°S - 30°S	N:P plus circulation model	8.3	(Wang, et al., 2019)
	6°S - 15°S	Nitrate isotopes plus residence time	2.0-4.1	This study

[a] Estimated from a homogenised rate for the South Atlantic (area= 27 x 10^{12} m^2 for 0-40°S; (Luo, et al., 2012)).

[b] As per Knapp et al. (2008) where estimates are extrapolated from the references cited to yield an estimate representative of the whole Atlantic.

[c] Compilation of direct measurements made by others.

A1. Upper-ocean water masses in the tropical South Atlantic

Tropical Surface Water (TSW) occupies the shallowest depths in the study region (potential density anomaly (σ_θ in kg.m^{-3}) <26.2; Table A2). Thermocline Water (TW) in the tropical South Atlantic occupies the σ_θ range of 26.2-27.0 (Table A2) and includes contributions from multiple types of South Atlantic Subtropical Mode Water (SASTMW), all of which are formed in the higher latitude subtropical South Atlantic (30°S to 45°S at σ_θ=26.2-26.7) (Sloyan & Rintoul, 2001; McCartney, 1982; Roden, 1986; Tsuchiya, et al., 1994; Sato & Polito, 2014; Donners, et al., 2005; Azar, et al., 2020; Talley, et al., 2011). Underlying TW is Subantarctic Mode Water (SAMW), which forms in the Subantarctic Zone of the Southern Ocean. In the tropical South Atlantic, SAMW is typically denser than at formation and in the subtropics (σ_θ=27.0-27.25 vs. σ_θ=26.6-27.0). Since SAMW supplies the Atlantic thermocline with nutrients(Sarmiento, et al., 2004), we consider it the ultimate "source" to the tropical South Atlantic thermocline (i.e., it is the sub-thermocline water mass; Table A2). South Atlantic Central Water (SACW; σ_θ=26.2-27.0), a commonly defined upper-ocean water mass in the South Atlantic, encompasses both thermocline and sub-thermocline waters (Talley, et al., 2011) i.e., SASTMWs and SAMW (Donners, et al., 2005; Mohrholz, et al., 2008; Lamont, et al., 2015; Talley, et al., 2011). Intermediate Water (IW) underlies SAMW, occupying the σ_θ range of 27.25-27.5, and is dominated by Antarctic Intermediate Water (Table A2).

Table A2. Upper-ocean water mass definitions for the tropical South Atlantic. Upper and lower potential density anomaly and depth limits for tropical South Atlantic water masses.

Water mass	Potential density (σ_θ) range [kg.m^{-3}]	Depth range [m]
Tropical Surface Water	< 26.2	0 to 50-150
Thermocline Water	26.2 to 27.0	50-150 to 400
Subantarctic Mode Water (sub-thermocline water)	27.0 to 27.25	400 to 690
Intermediate Water	27.25 to 27.5	690 to 1100

A1.1. Modification of northward-flowing central waters in the Atlantic

As SAMW flows northward from its formation region in the Southern Ocean towards the North Atlantic, it entrains relatively saline thermocline waters from above (Figure A1a). The entrainment produces a clear latitudinal modification in absolute salinity (S_{abs}), the nutrients N:P ratio, and nitrate δ^{15}N for the σ_θ range of 26.6-27.1. This density range, hereafter "central waters", includes contributions from SAMW and overlying thermocline waters. In the tropical South Atlantic, these central waters (S_{abs} of 35.11 g.kg^{-1} for this study at 12°S; Figure A1a) experience the second largest increase in mean nutrient N:P ratios, with the largest occurring in the tropical North Atlantic (Marconi, et al., 2017) (S_{abs} of 35.25-36.18 g.kg^{-1} for 9-25°N; Figure

A1a). A coincident but inverse trend is observed for nitrate $\delta^{15}N$ in the central waters (Figure A1b). Both of these changes result from N_2 fixation (Hoering & Ford, 1960; Minagawa & Wada, 1986; Carpenter, et al., 1997; Knapp & Sigman, 2005; Letelier & Karl, 1998; White, et al., 2006). In the tropical South Atlantic, the sub-thermocline source (SAMW) nitrate $\delta^{15}N$ of 6.3‰ is remarkably similar to the $\delta^{15}N$ of central waters in the subtropical South Atlantic of 6.5‰ (Marconi, et al., 2017; Flynn, et al., 2020) (Figure A1b) suggesting a minor contribution of N_2 fixation to central water nitrate across the South Atlantic subtropical gyre.

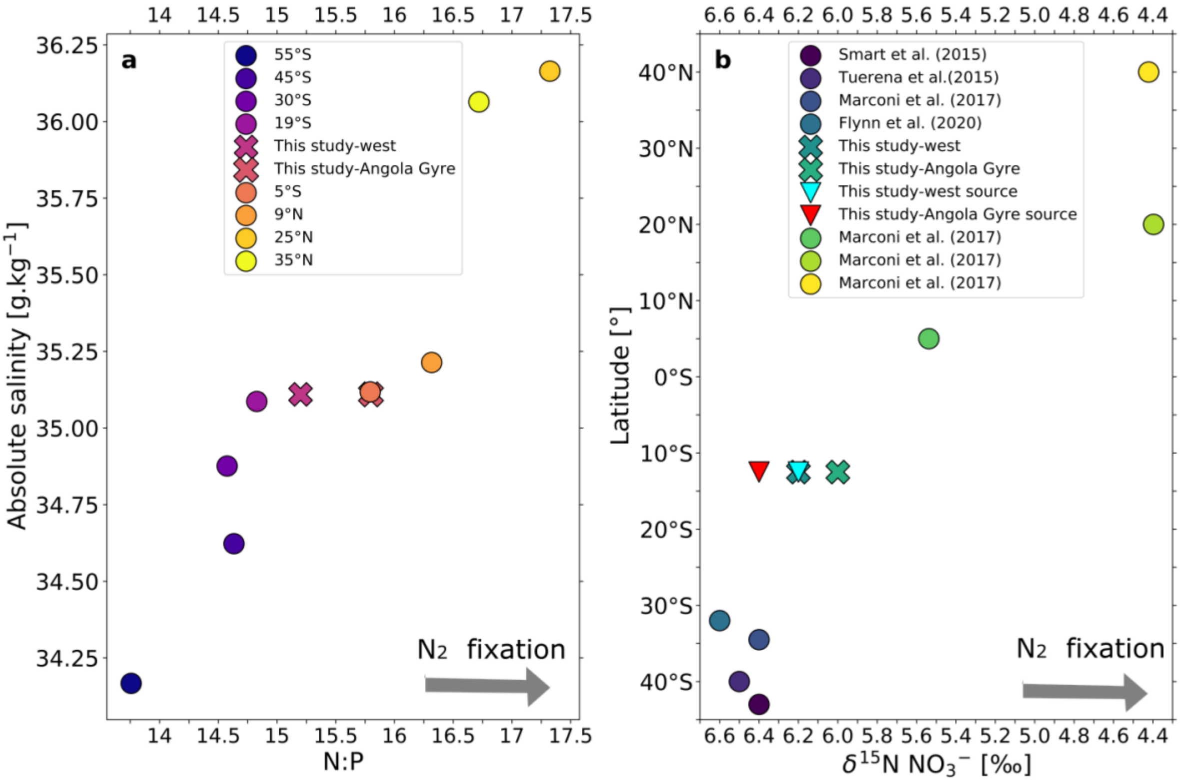

Figure A1. Biogeochemical characteristics of central waters across the Atlantic. Mean nutrient N:P ratios versus absolute salinity (g.kg^{-1}) (**a**) and nitrate $\delta^{15}N$ (‰) versus latitude (°) (**b**) for central waters across the Atlantic (note that the nitrate $\delta^{15}N$ scale is reversed). Here, the density range for all data points is 26.6-27.1 kg.m^{-3}. Data in panel **a** are sourced from numerous WOCE Atlantic transects (https://doi.org/10.21976/C6RP4Z). Triangular markers in panel **b** show the $\delta^{15}N$ of SAMW nitrate that is supplied to the overlying thermocline in the tropical South Atlantic (this study).

A2. Nutrient ratios as geochemical tracers of N_2 fixation

A2.1. The geochemical tracer N*

The geochemical tracer N* (in μM), first defined as ($[NO_3^-] - 16 \times [PO_4^{3-}] + 2.9) \times 0.87$, is used to discern additions or losses of N relative to P to/from the inorganic nutrient pool (Gruber & Sarmiento, 1997). As such, it is a useful tool for diagnosing N_2 fixation, which introduces N in excess of the stoichiometric quantity expected from P (Letelier & Karl, 1998; White, et al., 2006; Gruber & Sarmiento, 1997). N* is now more commonly defined as $[NO_3^-] - 16 \times [PO_4^{3-}]$

(Hansell, et al., 2007; Hansell, et al., 2004; Deutsch & Weber, 2012; Rafter, et al., 2013), which is more appropriate for regional applications of the tracer since it disregards the global PO_4^{3-} excess (intercept) (Mahaffey, et al., 2005; Deutsch & Weber, 2012). In any case, absolute values of N* matter far less than the vertical (and at times, horizontal) gradients in its concentration. The constant, 16, is the expected mean photosynthetic uptake and remineralization ratio of nitrate to phosphate (Redfield, 1958), which, over sufficiently large temporal and spatial scales, is probably reasonable despite the mounting evidence of significant local variability (e.g., (Weber & Deutsch, 2012; Martiny, et al., 2013; Weber & Deutsch, 2010)). However, when employing the N* tracer at a regional scale (i.e., not globally or for a system at steady-state), vertical and/or horizontal changes in N and P should be evaluated relative to the source N:P ratio supplied to the thermocline rather than relative to the mean global uptake and remineralisation ratio of ~16:1. This is because the mean global N:P ratio of 16:1 reflects contributions from both diazotrophic and non-diazotrophic OM, where diazotrophic OM N:P ratios are much higher than 16:1 (typically ~40:1) (White, et al., 2006). Non-diazotrophic N:P ratios may thus be lower than ~16:1, possibly on the order of 15:1 as proposed by Deutsch et al. (2007) and used in the original definition of P* (see A2.2 below). Therefore, in regions that do not host significant rates of N_2 fixation, the mean nutrient N:P ratio supplied to the thermocline is likely <16:1.

The subtropical South Atlantic is one such region. Here, recently formed SAMW sets the thermocline nutrient ratio (Sarmiento, et al., 2004). As expected, mean SAMW N:P ratios are <16:1, as low as 13.75:1 at formation (Figure A1a). It is thus necessary to derive a regionally-appropriate nutrient uptake and remineralisation N:P ratio that can be used to define N* for our study region. We set the N:P ratio constant to the mean *in situ* SAMW nitrate-to-phosphate ratio derived for our dataset, 15.5:1 (Table A3). This means that any changes we report in the thermocline N* values are relative to the underlying source waters that supply the thermocline with nutrients. We define N* as: $[NO_3^-] - 15.5 \times [PO_4^{3-}]$.

Table A3. Mean source-to-thermocline changes in geochemical tracers in the western versus eastern tropical South Atlantic. Changes in nutrient N:P ratios, [NO_3^-]-weighted $\delta^{15}N$ (in ‰), and N* and P* (in μM) between SAMW (i.e., the source) and the thermocline for the western tropical South Atlantic basin (west of 7.5°W) and the Angola Gyre in the eastern basin (east of 7.5°W). We define the thermocline as the region not impacted by surface biological processes such as nutrient assimilation, typically σ_θ=26.5-27.0 kg.m^{-3}, while the source waters are defined as σ_θ=27.0-27.25 kg.m^{-3} (Table A2). The value in brackets under "Western basin N:P / Thermocline (TW)" is the mean regenerated nutrient N:P ratio for the western basin thermocline (addressed in A4).

	Western basin				Angola Gyre			
Water mass	**N:P**	**NO_3^- $\delta^{15}N$**	**N***	**P***	**N:P**	**NO_3^- $\delta^{15}N$ [a]**	**N***	**P***
Thermocline (TW)	15.0:1 (15.2:1)	6.3 ±0.1	-0.43	0.03	15.8:1	5.7 ±0.7	0.71	-0.04
Source (SAMW)	15.4:1	6.2 ±0.1	-0.10	0.01	15.5:1	6.4 ±0.1	0.05	0.00
Difference	**-0.4**	**+0.1**	**-0.33**	**+0.02**	**+0.3**	**-0.7**	**+0.66**	**-0.04**

[a] The Angola Gyre [NO_3^-]-weighted $\delta^{15}N$ includes stations from cruise MET131 and CoFeMUG (Figure 2.1).

A2.2. The geochemical tracer P*

Changes in nutrient stoichiometry have long been used to diagnose N_2 fixation (Gruber & Sarmiento, 1997; Deutsch, et al., 2007). Surface waters hosting an excess of P relative to N (i.e., high P* values, where P* = [PO_4^{3-}] – [NO_3^-] ÷ 15.5) should favour N_2 fixation, and surface P* convergence (i.e., the drawdown of P in the absence of N) has thus been used to diagnose the rate and distribution of N_2 fixation (Deutsch, et al., 2007; Palter, et al., 2011; Eugster & Gruber, 2012). The subsurface remineralisation of OM fuelled by newly-fixed N will act to lower thermocline P* relative to the surface due to the introduction of newly-fixed N in excess of P (Deutsch, et al., 2007).

A2.3. Surface P* concentrations across the South Atlantic

Surface P* distributions derived from earlier editions of the World Ocean Atlas (WOA) will reveal slightly different trends from one another due to the increased data availability over time. For example, Deutsch et al. (2007) use WOA 2001, Moore et al. (2009) use WOA 2007 and this study uses WOA 2018 (Figure 1.1). However, the WOA 2018 surface P* distribution across the tropical South Atlantic is different from that derived from the CoFeMUG cruise data collected in 2007 (inside versus immediately outside the black box in Figure 1.1). For this reason, we show surface P* derived from the CoFeMUG dataset over the region of the transect instead of data from WOA 2018. In the western tropical basin, the CoFeMUG and WOA 2018 surface P* concentrations are fairly indistinguishable. However, in the Angola Gyre in the eastern basin, P* is higher in the CoFeMUG dataset than the value derived from WOA 2018.

These differences have implications for accurately diagnosing N_2 fixation from inverse-model methods (Deutsch, et al., 2007) (see main text discussion). Annual climatologies require averaging across multiple datasets that sample across different seasons, which likely increases uncertainty around the mean (e.g., standard deviation) associated with each grid cell. However, the number of data observations per grid cell in the Angola Gyre in the WOA 2018 dataset is typically not greater than one (thus artefactually reducing uncertainty around the mean; Figure A2), the same as the number of surface measurements for the CoFeMUG dataset. While we expect both datasets to include some degree of uncertainty, the fact that the zonal trends — or the lack thereof — in the WOA 2018 surface P* annual climatology are inconsistent with zonal trends in N_2 fixation and contrast those of the CoFeMUG dataset, highlights the need for increased, high-quality nutrient sampling across the tropical South Atlantic.

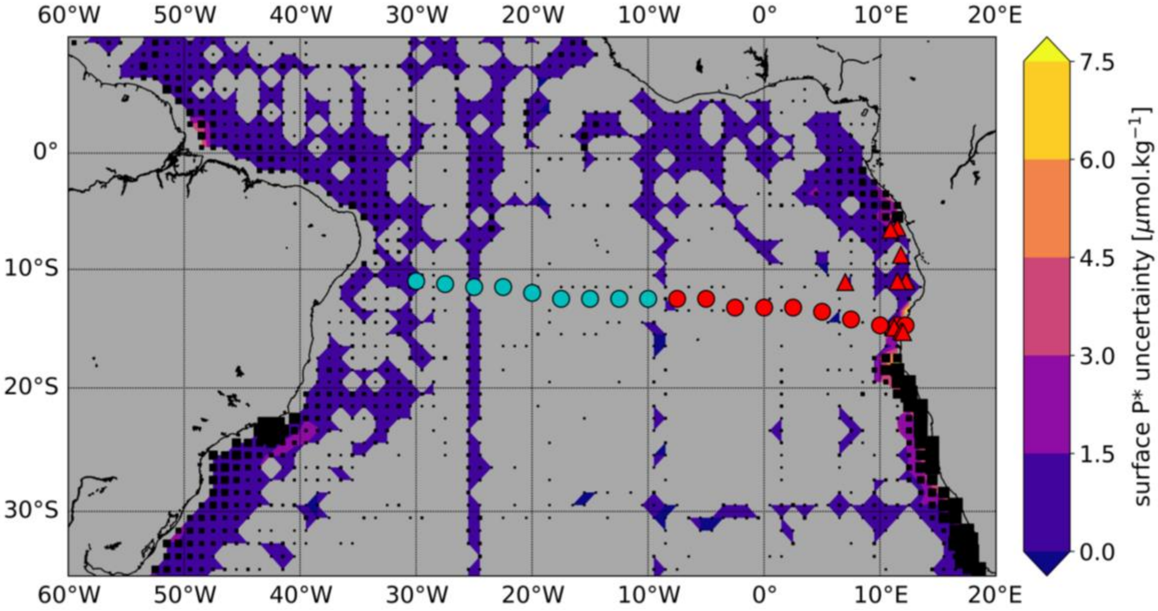

Figure A2. Surface P* uncertainty across the surface South Atlantic Ocean. Surface P* uncertainty calculated as propagated error (A10) for WOA 2018. Grey shading represents grid cells where there are insufficient data to calculate propagated error. Black squares represent the number of nitrate observations per grid cell in the WOA 2018 dataset, where the smallest square represents only one observation per grid cell and the largest square represents 413.

A2.4. Vertical trends in P* support N_2 fixation in the Angola Gyre

The mean tropical Atlantic SAMW P* concentration derived from the CoFeMUG dataset is 0.0 μM (Table A3). In the western tropical basin thermocline, P* increases to 0.03 μM while in the Angola Gyre thermocline, it decreases to -0.04 μM (Table A3, Figure A3a). The source-to-thermocline changes in P* are within the analytical uncertainty associated with phosphate and nitrate concentration measurements and should therefore be interpreted with caution (A10); nonetheless, the vertical trend in P* in the Angola Gyre is consistent with the subsurface remineralization of OM with an higher N:P ratio (>15.5:1, lowering P*) than that supplied by underlying SAMW or available in the overlying surface waters, as would be expected for N_2 fixation (Gruber & Sarmiento, 1997; Deutsch, et al., 2007). Additionally, as with N*, the observation of a source-to-thermocline change in P* supports the notion that partial nitrate assimilation in TSW is not the primary cause of the low-δ^{15}N nitrate in the Angola Gyre thermocline (see main text).

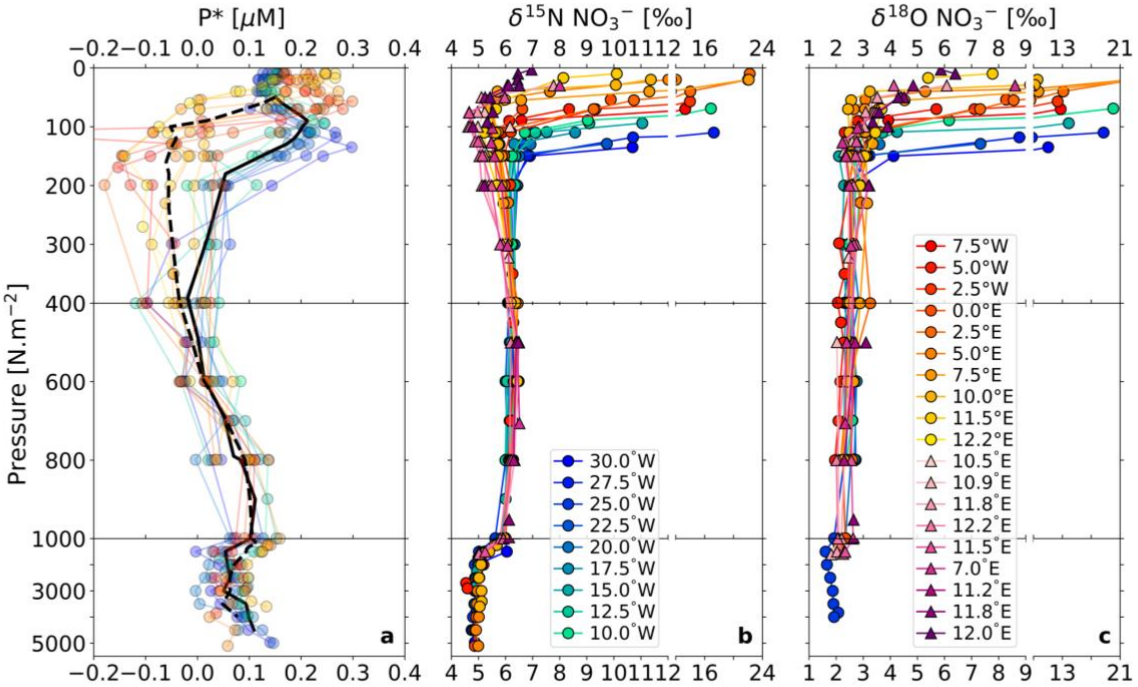

Figure A3. Dual N and O isotopes of nitrate and P* for the tropical South Atlantic. Full depth profiles of P* (= $[PO_4^{3-}] - [NO_3^-] \div 15.5$; A2) in μM (**a**), nitrate δ^{15}N in ‰ vs. N_2 in air (**b**) and δ^{18}O in ‰ vs. VSMOW (discussed in A3) (**c**). Warm (cool) coloured profiles show stations from the Angola Gyre (western basin) in the tropical South Atlantic. The legend provides station longitude. In panel **a**, the dashed (solid) black line indicates the gridded mean P* for the Angola Gyre (western basin) stations. Panel **a** includes only CoFeMUG data because of the high depth-resolution of this sample set. The approximate depth of the TW and SAMW interface is 400 m.

A3. Nitrate δ^{18}O across the tropical South Atlantic

Interpreting changes in N and O isotope ratios together provides insight into the different N cycle processes acting on the nitrate pool. The equivalent rise in nitrate δ^{15}N and δ^{18}O in the upper ~100 m of the tropical South Atlantic is the result of nitrate assimilation by phytoplankton, which imparts near-equal isotopic fractionation on the N and O isotopes of nitrate (Granger, et al., 2004; Granger, et al., 2010) (Figure A3b and c). In the subsurface (below 50-150 m), the processes acting on nitrate decouple the N and O isotopes — nitrate δ^{15}N declines to values lower that the source (SAMW) while nitrate δ^{18}O remains fairly constant (at 2-3‰). This decoupling occurs because the δ^{15}N of newly nitrified nitrate is set by the δ^{15}N of the OM plus ammonium being remineralised and oxidized (which, in the case of the Angola Gyre, is low because of the influence of N_2 fixation), while its $\delta^{18}O$ is set by the $\delta^{18}O$ of seawater (i.e., the $\delta^{18}O$ of newly nitrified nitrate = $\delta^{18}O$ of water (~0‰) + ~1.15‰) (Sigman, et al., 2009a; Buchwald, et al., 2012; Boshers, et al., 2019).

Following Knapp et al. (2008) and Fawcett et al. (2015), a salinity correction was applied to the CoFeMUG and MET131 cruise nitrate $\delta^{18}O$ data ($\delta^{18}O_{NO3\_salcorr} = \delta^{18}O_{NO3} - (0.5 \times (sal - sal_m)$, where $\delta^{18}O_{NO3}$ is the measured $\delta^{18}O$ of nitrate, the constant 0.5 is the slope describing the relationship between salinity and the $\delta^{18}O$ of seawater in the Atlantic, sal is the measured salinity for a given sample, and sal_m is the mean salinity at 1000 m (34.8 g.kg^{-1})). This correction is necessary because of the empirical relationship between salinity and the $\delta^{18}O$ of seawater (Craig & Gordon, 1965); in the (sub)tropical Atlantic, seawater $\delta^{18}O$ increases by 0.5‰ for every 1 unit rise in salinity (Bigg & Rohling, 2000). Between 1000 m and the surface along our transect, salinity increases by 1.2 to 2.2. g.kg^{-1} and nitrate $\delta^{18}O$ rises by 3.9‰ to 18.9‰; 0.6‰ to 1.2‰ of this rise can be explained by the salinity-seawater $\delta^{18}O$ relationship. Because the $\delta^{18}O$ of nitrate is set by the $\delta^{18}O$ of water (Sigman, et al., 2009a; Buchwald, et al., 2012; Boshers, et al., 2019), OM remineralised in shallower waters where seawater $\delta^{18}O$ is higher will yield nitrate with an elevated $\delta^{18}O$ compared to that produced in deeper waters where seawater $\delta^{18}O$ (and salinity) is lower. The data shown in Figure A3c are the salinity-corrected values.

A4. Nutrient stoichiometry in the Tropical South Atlantic

A4.1. The impact of partial nitrate assimilation on nutrient stoichiometry

Non-diazotrophic nutrient uptake and remineralisation ratios are thought to fall just below the Redfield ratio of 16:1 (to balance the high-N:P input from diazotrophs), possibly on the order of ~15:1 (Deutsch, et al., 2007). Even though flexible N:P ratios have been observed for non-diazotrophic OM across the global ocean (Weber & Deutsch, 2012; Martiny, et al., 2013; Wang, et al., 2019), whether phytoplankton consume the available nutrient pool partially or completely in a particular region should yield a negligible change in thermocline N* and surface P*. By contrast, the $\delta^{15}N$ of thermocline nitrate can be considerably altered if nitrate is only partially consumed in overlying TSW.

If partial nitrate assimilation is the sole cause of the low-$\delta^{15}N$ nitrate in the Angola Gyre thermocline, we expect there to be no increase in the regenerated thermocline N* relative to the underlying source, SAMW. By this logic, where the N:P ratio of the regenerated nutrient pool is greater than that expected of non-diazotrophic OM (i.e., in the western tropical basin where there is no isotopic evidence for N_2 fixation), we attribute the increase to N_2 fixation introducing high-N:P OM (Gruber & Sarmiento, 1997; Weber & Deutsch, 2012; Deutsch & Weber, 2012).

A4.2. Regenerated nutrient stoichiometry is consistent with N_2 fixation in the Angola Gyre

Assuming that N_2 fixation is responsible for the low $\delta^{15}N$ of nitrate in the Angola Gyre thermocline, the N:P ratio of regenerated nutrients in this water mass should be higher than that of both the regenerated nutrient pool in the western tropical basin and the underlying source waters. Likewise, if partial nitrate assimilation were the cause of the low-$\delta^{15}N$ thermocline nitrate, we would expect no increase in the N:P ratio of regenerated nutrients in the Angola Gyre thermocline relative to the western tropical basin and underlying source waters.

To derive the N:P ratio of Angola Gyre thermocline regenerated nutrients (equation A1) we make two assumptions. First, we assume that the remineralisation of P occurs in a constant P:AOU ratio of 1:140. This ratio is taken from an ensemble of global mean P:AOU ratios, constrained to the latitudinal domain of the Angola Gyre (DeVries & Deutsch, 2014). Using the P:AOU ratio and the measured [PO_4^{3-}], we can estimate the fraction of regenerated nutrients for the whole water column (Angola Gyre thermocline mean of $f_{regenerated} = 0.7$). Second, we assume that the N:P ratio of preformed nutrients (i.e., the N:P ratio of nutrients supplied to the Angola Gyre prior to alteration by N_2 fixation) is equal to that of SAMW prior to this water mass entering the tropical South Atlantic. We calculate the mean SAMW N:P ratio from WOCE transect A09 data at 19°S to be 15.0:1 (https://cchdo.ucsd.edu/cruise/06M T15 _3). This ratio is lower than published estimates for the subtropical thermocline that converge on ~20:1 (Weber & Deutsch, 2012; Martiny, et al., 2013). However, these high N:P ratios are strongly biased towards the northern hemisphere, and thus reflect a contribution of high-N:P OM that is generated by N_2 fixation, which is low in the subtropical South Atlantic (Table A1 and Figure A1) (Coles & Hood, 2007; Deutsch, et al., 2007; Marconi, et al., 2017; Wang, et al., 2019; Luo, et al., 2012; Fonseca-Batista, et al., 2017). Published subtropical N:P ratios cannot therefore be taken as representative of the subtropical South Atlantic, which is furthermore not represented in the published estimates since there are no measurements of OM N:P ratios from this basin(Martiny, et al., 2013).

We estimate the N:P of regenerated nutrients in the Angola Gyre thermocline as:

$$N{:}P_{regenerated} = [N{:}P_{measured} - (N{:}P_{preformed} * (1 - f_{regenerated}))] / f_{regenerated} \tag{A1}$$

The $\text{N:P}_{\text{regenerated}}$ in the Angola Gyre thermocline is on average 16:1, reaching as high as 17.2:1, while for the western tropical basin thermocline, we calculate an $\text{N:P}_{\text{regenerated}}$ of 15.2:1 (Figure A4). The fact that $\text{N:P}_{\text{regenerated}}$ in the western tropical basin is lower than the N:P ratios of the SAMW supply of 15.4:1 explains the observed decrease in TW N* (Table A3). Our calculated values of $\text{N:P}_{\text{regenerated}}$ are consistent with the remineralisation of high-N:P OM influenced by N_2 fixation in the Angola Gyre (White, et al., 2006; Mahaffey, et al., 2005), with no evidence for N_2 fixation in the western tropical basin.

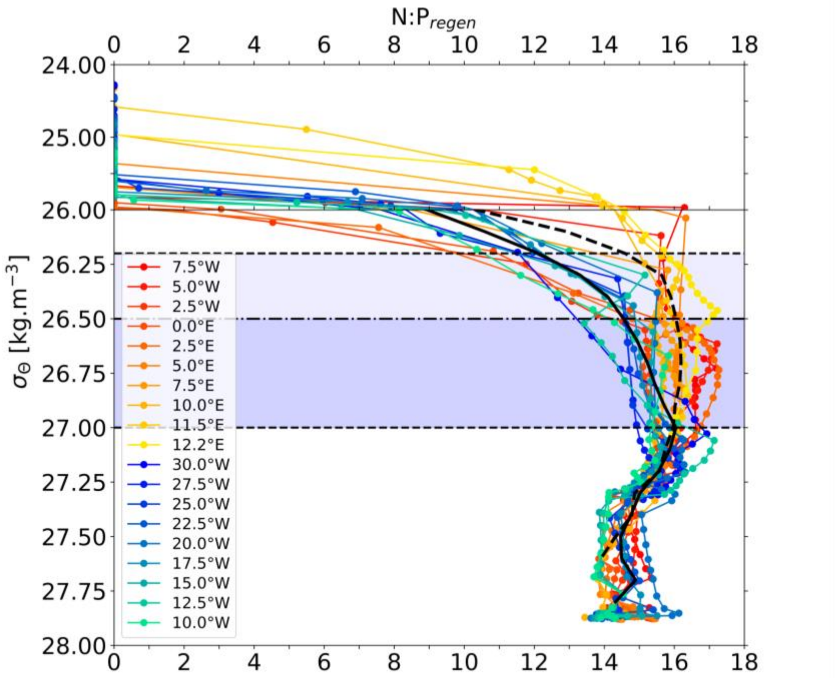

Figure A4. N:P ratios of the regenerated nutrient pool in the thermocline of the tropical South Atlantic. Density profiles of $\text{N:P}_{\text{regenerated}}$ (equation A1) calculated for all CoFeMUG stations. Warm (cool) coloured profiles represent stations from the Angola Gyre (western basin) in the tropical South Atlantic. The density increments change above and below 26 kg.m^3. The legend provides station longitude. The dashed (solid) black profile indicates the mean gridded N:P ratio of regenerated nutrients for the Angola Gyre (western basin) stations. The horizontal black dashed lines show the density range of TW (Table A2) and the dot-dashed line indicates the density below which TW is unaffected by nutrient consumption.

A5. Evaluating the potential for anthropogenic atmospheric N deposition to the Angola Gyre

Estimates of total inorganic nitrogen (TIN) deposition to the South Atlantic converge on an arithmetic mean of 259 ± 16 mol N.a^{-1} (or 3.6 ± 0.22 x 10^{-9} Tg N.a^{-1}) (Dentener, 2006; Luo, et al., 2007; Baker, et al., 2010) over an area of 29.7 x 10^{12} m^2 (5-50°S) (Baker, et al., 2010). Applying this deposition rate to the areal extent of the Angola Gyre (2.6 x 10^{12} m^2) yields a hypothetical deposition rate of 22.7 mol N.a^{-1} (or 3.2 x 10^{-10} Tg N.a^{-1}).

The δ^{15}N of anthropogenically-sourced atmospheric N is similar to and sometimes lower than that of N_2 fixation (-14‰ to 2‰) (Hastings, et al., 2003; Morin, et al., 2009; Knapp, et al., 2010; Altieri, et al., 2013; Altieri, et al., 2014; Altieri, et al., 2021). In addition, atmospheric deposition is typically characterized by a very high N:P ratio (450:1 to 2200:1, median of 910:1) (Baker, et al., 2010; Baker, et al., 2007). It is thus possible that atmospheric deposition could be the cause of the high-N*, low-δ^{15}N nitrate observed in the Angola Gyre thermocline.

To evaluate the likelihood of this scenario, we first estimate the fraction of atmospherically-derived N ($f_{\mathrm{atm\_dep}}$) required to explain the low-δ^{15}N nitrate signal observed in the Angola Gyre thermocline. Then, after multiplying $f_{\mathrm{atm\_dep}}$ by the Angola Gyre nitrate inventory, we estimate the deposition rate required to yield $f_{\mathrm{atm\_dep}}$ and compare this to existing estimates of the N deposition rate for the tropical South Atlantic. $f_{\mathrm{atm\_dep}}$ is derived as:

$$f_{\mathrm{atm\_dep}} = \frac{\delta^{15}\mathrm{N}_{\mathrm{AG\_mean}} - \delta^{15}\mathrm{N}_{\mathrm{SAMW\_source}}}{\delta^{15}\mathrm{N}_{\mathrm{atm\_dep}} - \delta^{15}\mathrm{N}_{\mathrm{SAMW\_source}}} \qquad \text{(A2)}$$

where $\delta^{15}\mathrm{N}_{\mathrm{AG\_mean}}$ is the mean concentration-weighted δ^{15}N of Angola Gyre nitrate for the upper water column where $\sigma_\theta \leq 27.0$ kg.m^{-3}, estimated to be 5.7‰; $\delta^{15}\mathrm{N}_{\mathrm{SAMW\_source}}$ is the δ^{15}N of SAMW nitrate (6.4‰); and $\delta^{15}\mathrm{N}_{\mathrm{atm\_dep}}$ is the δ^{15}N of atmospheric N deposition. We compute $f_{\mathrm{atm\_dep}}$ using both the minimum and maximum δ^{15}N reported for anthropogenically-derived atmospheric N, -13.9‰ and 1.8‰ (Hastings, et al., 2003; Morin, et al., 2009; Knapp, et al., 2010; Altieri, et al., 2013; Altieri, et al., 2014; Altieri, et al., 2021). Our estimates of $f_{\mathrm{atm\_dep}}$ indicate that between 3% and 15% of Angola Gyre thermocline nitrate would need to derive from anthropogenic atmospheric N deposition to account for its low δ^{15}N. As a deposition rate, this amounts to between 0.9 and 8.0 x 10^{11} mol N.a^{-1} (or 1.3 to 11.2 Tg N.a^{-1}), which is ten orders of magnitude higher than the observed deposition rate (Dentener, 2006; Luo, et al., 2007; Baker, et al., 2010). Moreover, the δ^{15}N of fossil foraminifera in sediments underlying the Angola Gyre is ~5‰ (Schiebel, et al., 2018), very similar to modern thermocline nitrate. This observation implies that thermocline nitrate δ^{15}N has not changed in >1000 years, ruling out anthropogenic atmospheric N deposition, relevant over the last 100-150 years only, as a significant source of exogenous N to the Angola Gyre. Atmospheric N deposition cannot, therefore, explain the low δ^{15}N of Angola Gyre thermocline nitrate.

A6. The δ^{15}N of nitrate transported into the Angola Gyre

Three eastward currents feed the Angola Gyre; the Equatorial Undercurrent (EUC), the South Equatorial Undercurrent (SEUC) and the South Equatorial Countercurrent (SECC) (Figure 1.1) (Gordon & Bosley, 1990; Peterson & Stramma, 1991; Stramma & England, 1999; Stramma & Schott, 1999). Since two of these currents (the EUC and SEUC) could transport water from the tropical North Atlantic where N_2 fixation rates are high (Marconi, et al., 2017; Moore, et al., 2009), it is conceivable that low-δ^{15}N nitrate is transported into the Angola Gyre thermocline rather than resulting from local N_2 fixation. To address this possibility, we estimated the flux of nitrate into the gyre by the feeder currents, along with its δ^{15}N.

A6.1. Estimating the contribution of each current feeding the Angola Gyre

To determine the contribution of each current to the Angola Gyre, we use the absolute transport volumes reported by Mercier et al. (2003). This approach is complicated by the fact that the contribution of the EUC is uncertain (Stramma & England, 1999; Mercier, et al., 2003). The EUC bifurcates east of 0°E, with its southward extension merging with the Gabon-Congo Undercurrent (Stramma & Schott, 1999) (GCUC; Figure 1.1). The GCUC is thought to transport EUC-derived waters into the Angola Gyre via the southward-flowing Angola Current (AC). The uncertainty lies in the contribution of the EUC to the GCUC and the GCUC to the Angola Gyre. Measurements across the EUC at ~2°E (just before bifurcation) indicate that its eastward transport is fully accounted for by two westward return currents, the north South Equatorial Current (nSEC) and equatorial South Equatorial Current (eSEC), suggesting that the EUC contribution to the GCUC is weak (proposed to be ~1 Sv (1 Sv = 10^6 $m^3.s^{-1}$); (Mercier, et al., 2003); their table 2). Consequently, we consider two scenarios in order to account for both extrema of the EUC contribution – the first scenario (A) assumes no contribution of the EUC to the Angola Gyre and the second (B) assumes a maximum contribution (Table A4). In scenario A, we assume that the 8 Sv of transport measured in the northern limb of the Angola Gyre represents net transport into the gyre (Mercier, et al., 2003). Across its northern limb at 5°E, the SEUC and SECC transport 4.7 Sv and 3.3 Sv, respectively (Mercier, et al., 2003), which amounts to 59% and 41% of the net transport (Table A4). In scenario B, we consider the transport across the eastern limb of the Angola Gyre of 11 Sv to represent the net transport (Mercier, et al., 2003). The increase in measured transport between the northern and eastern limbs of the gyre has been proposed to reflect the inclusion of the AC (Mercier, et al., 2003). We attribute the difference in transport (3 Sv) to EUC-derived waters feeding the GCUC and AC. In scenario B, therefore, the relative contributions of the SEUC, SECC and EUC to the Angola Gyre are ~43%, 30% and 27%, respectively (Table A4).

A6.2. Estimating the δ^{15}N of the nitrate transported into the Angola Gyre

The EUC and SEUC were sampled at 25°W during the CLIVAR/GO-SHIP A16N cruise (Marconi, et al., 2017; Marconi, et al., 2019) (Figure 1.1). The EUC and SEUC crossed the A16N transect at the 0.3 $m.s^{-1}$ and 0.2 $m.s^{-1}$ eastward velocity contours, respectively (Figure A5)(Firing & Hummon, 2010). The current positions were confirmed by their characteristic relative oxygen and salinity maxima(Mercier, et al., 2003). The EUC core was observed at

0.5°S between 50 m and 150 m while the SEUC core was observed at 3.6°S between 100 m and 300 m (Figure A5). The mean [NO_3^-]-weighted $\delta^{15}N$ for the EUC and SEUC were estimated to be 5.7‰ and 6.0‰, respectively (Table A4). The SECC (centred at ~10°S) was not sampled during the A16N cruise. Instead, we derived the SECC nitrate $\delta^{15}N$ end-member from the two most western stations of the CoFeMUG transect, the positions of which coincide with the formation region of the SECC (a derivation of the sSEC; Figure 1.1). The SECC mean [NO_3^-]-weighted $\delta^{15}N$ is 6.3‰ (Table A4). The flux-weighted nitrate $\delta^{15}N$ end-member for scenario A is thus 6.1‰ and for scenario B is 6.0‰ (Table A4). Given their similarity, we consider the mean nitrate-$\delta^{15}N$ for these two scenarios (6.1±0.1‰) to be representative of the nitrate transported into the Angola Gyre.

Table A4. The $\delta^{15}N$ of nitrate transported into the Angola Gyre. Mean nitrate $\delta^{15}N$ values (derived from gridded and [NO_3^-]-weighted data) and relative transport contributions (as interpreted from Mercier et al. (2003)) of the three currents feeding the Angola Gyre.

Angola Gyre feeder currents	**Mean $\delta^{15}N$ of nitrate [‰]**	**Scenario A**		**Scenario B**	
		Transport [Sv]	**Relative contribution**	**Transport [Sv]**	**Relative contribution**
EUC	5.7	0	0	3	0.27
SEUC	6.0	4.7	0.59	4.7	0.43
SECC	6.3	3.3	0.41	3.3	0.30
Total transport:		**8**	**1**	**11**	**1**
Transported nitrate $\delta^{15}N$ end-member [‰]		**6.1**		**6.0**	

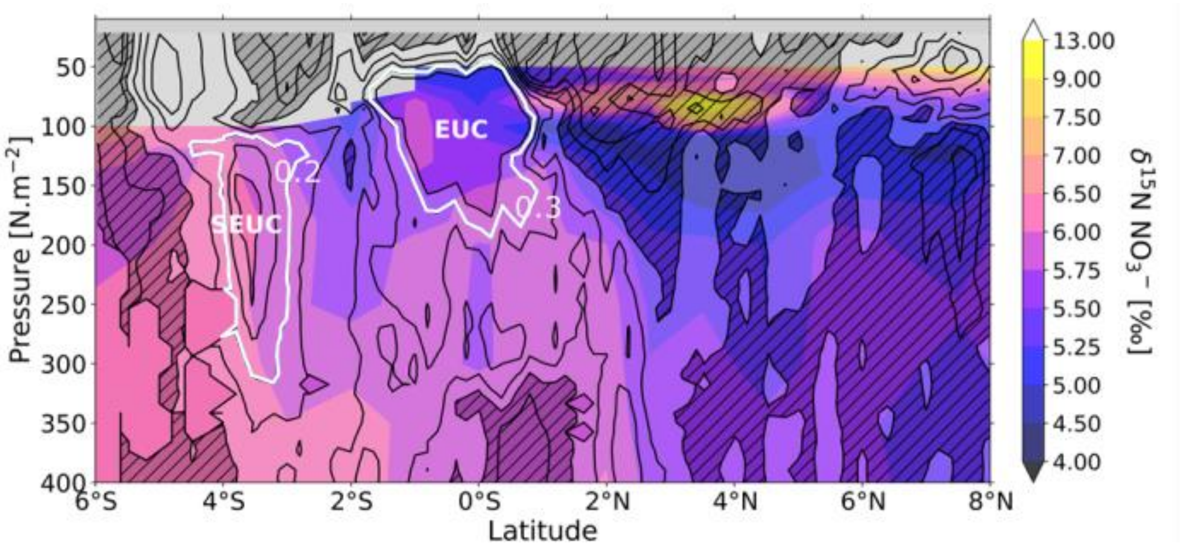

Figure A5. Nitrate $\delta^{15}N$ across the equatorial Atlantic currents. Meridional section (6°S to 8°N) of nitrate $\delta^{15}N$ at 25°W (Marconi, et al., 2017; Marconi, et al., 2019). Contours of the *u*-component of velocity (Firing & Hummon, 2010) indicate equatorial current positions. The unshaded (shaded and hashed) contours denote eastward (westward) currents. The 0.2 $m.s^{-1}$ and 0.3 $m.s^{-1}$ velocity contours that characterize the SEUC and EUC, respectively, are highlighted in white and labelled. Note that the colour bar is non-linear upwards of 7.5‰ in order to more clearly show the thermocline nitrate $\delta^{15}N$.

A7. Assimilation-corrected, depth-specific fraction of newly-fixed nitrate

Overlapping nitrate assimilation and nitrification at the base of the euphotic zone can result in an underestimation of the depth-specific fraction of newly-fixed nitrate inferred from the nitrate δ^{15}N data ($f_{depth\_specific}$; equation A3a), and thus an underestimation of the N_2 fixation rate (Knapp, et al., 2008). As a first approximation, $f_{depth\_specific}$ is calculated as:

$$f_{depth\_specific} = \frac{\delta^{15}\mathrm{N}_{\mathrm{meas}} - \delta^{15}\mathrm{N}_{\mathrm{source}}}{\delta^{15}\mathrm{N}_{\mathrm{N_2fix}} - \delta^{15}\mathrm{N}_{\mathrm{source}}} \qquad \text{(A3a)}$$

where $\delta^{15}N_{meas}$ is the δ^{15}N of nitrate measured at each depth above 400 m (σ_θ~27.0 kg.m^{-3}) in the Angola Gyre, $\delta^{15}N_{N2fix}$ is the δ^{15}N of nitrate produced from the remineralization and nitrification of diazotrophic OM, and $\delta^{15}N_{source}$ is the scenario-specific nitrate-δ^{15}N supplied to the Angola Gyre thermocline. The δ^{15}N of newly-fixed N is low, taken here to be -1‰ (Hoering & Ford, 1960; Minagawa & Wada, 1986; Carpenter, et al., 1997), and distinct from that of the subsurface nitrate that is supplied (through vertical mixing and/or transport by feeder currents) to TSW (δ^{15}N = 6.1-6.4‰ (scenario 2 and 1, respectively, as outlined in the main text); Figure 1.3d). By definition, the formulation above for $f_{depth\_specific}$ considers all nitrate with a δ^{15}N <6.1-6.4‰ to be a mixture of just two end-members: N_2 fixation and the source. Nitrate with a δ^{15}N >6.1-6.4‰ (e.g., in TSW as a result of nitrate assimilation) will yield an $f_{depth\_specific}$ < 0. A negative value of $f_{depth\_specific}$ for a particular sample does not mean, however, that there is no contribution of newly-fixed N to the nitrate pool at that depth. Consider, for example, the situation wherein newly-fixed OM with a δ^{15}N of -1‰ is remineralised and nitrified at the base of the euphotic zone and mixed with the ambient nitrate pool to yield a combined δ^{15}N of 5.5‰. If this nitrate is subsequently assimilated to the degree that its δ^{15}N rises above 6.1-6.4‰, $f_{depth\_specific}$ will be < 0, which implies (according to equation A3a) no input of newly-fixed N even though the initial δ^{15}N of the nitrate being assimilated was lower than the δ^{15}N of the ultimate nitrate source.

Previous workers have attempted to correct for this circumstance using coincident measurements of nitrate δ^{18}O (Knapp, et al., 2008). During nitrate assimilation, fractionation of the O isotopes of nitrate occurs in a 1:1 ratio with that of the N isotopes, such that nitrate δ^{18}O and δ^{15}N rise by the same amount as nitrate consumption proceeds (Granger, et al., 2004; Granger, et al., 2010). By contrast, during nitrification, the δ^{15}N of newly nitrified nitrate is set by the δ^{15}N of the OM plus ammonium being remineralised and oxidized, while its δ^{18}O is equal to the δ^{18}O of seawater plus ~1.15‰ (Sigman, et al., 2009a; Buchwald, et al., 2012; Boshers, et al., 2019). Nitrification is thus the ultimate source of the O atoms in nitrate (while N_2 fixation is the ultimate source of the N atoms) and acts to reset the δ^{18}O of nitrate. In the Angola Gyre, examination of the nitrate $\delta^{18}O$ data yields two useful insights that cannot be gleaned from the $\delta^{15}N$ data: 1) the depth at which nitrate assimilation begins to alter to isotopic composition of the nitrate pool and 2) the magnitude of the nitrate assimilation signal. In theory, if we can quantify the nitrate assimilation signal, we can remove it from the nitrate $\delta^{15}N$ data and then assume that the remaining nitrate $\delta^{15}N$ constitutes a mixture of newly-fixed nitrate and upwelled/transported nitrate.

We assume that isotopic fractionation associated with nitrate assimilation begins to alter the $\delta^{15}N$ of the nitrate pool at the depth at which nitrate $\delta^{18}O$ starts to rise toward the surface (σ_θ~26.5 kg.m^{-3}; Figure A6c). The magnitude of the assimilation signal can then be calculated as the difference between the $\delta^{18}O$ of nitrate at each depth ($\delta^{18}O_z$) and the mean $\delta^{18}O$ of deep nitrate ($\delta^{18}O_{deep}$; for σ_θ=26.5-27.0 kg.m^{-3}), which in the case of the Angola Gyre is ~2.7‰ (Figure A6c). In other words, $\Delta\delta^{18}O_z = \delta^{18}O_z - \delta^{18}O_{deep}$. To remove the assimilation signal from nitrate $\delta^{15}N$, we subtract $\Delta\delta^{18}O_z$ from the measured $\delta^{15}N$ of nitrate at each depth above the initial rise in nitrate $\delta^{18}O$. We refer to these corrected values as $\delta^{15}N_{assim.\_removed}$ (coloured profiles in Figure A6b), and use them to calculate the fraction of newly-fixed nitrate at each depth by amending equation A3a as follows:

$$f_{depth\_specific} = \frac{\delta^{15}N_{assim.\_removed} - \delta^{15}N_{source}}{\delta^{15}N_{N_2fix} - \delta^{15}N_{source}} \qquad \text{(A3b)}$$

At the base of TSW (σ_θ~25-26.2 kg.m^{-3}), $f_{depth\_specific}$ reaches a maximum of >0.4 (Figure A6d) even though the measured nitrate $\delta^{15}N$ has already begun to rise due to nitrate assimilation (grey profiles in Figure A6b). While useful for visualizing the depth distribution of newly-fixed N in the Angola Gyre, these estimates of $f_{depth\_specific}$ (and of the concentration of newly-fixed nitrate, derived by multiplying $f_{depth\_specific}$ by the measured nitrate concentration at each depth; Figure A6d and e) cannot be integrated to yield the inventory of newly-fixed N in the Angola Gyre. This is because low-$\delta^{15}N$ nitrate (i.e., deriving from N_2 fixation) consumed in the surface is ultimately returned to the thermocline when the OM fuelled by that nitrate is exported to the subsurface and remineralised (Knapp, et al., 2008) – integration would thus result in double counting.

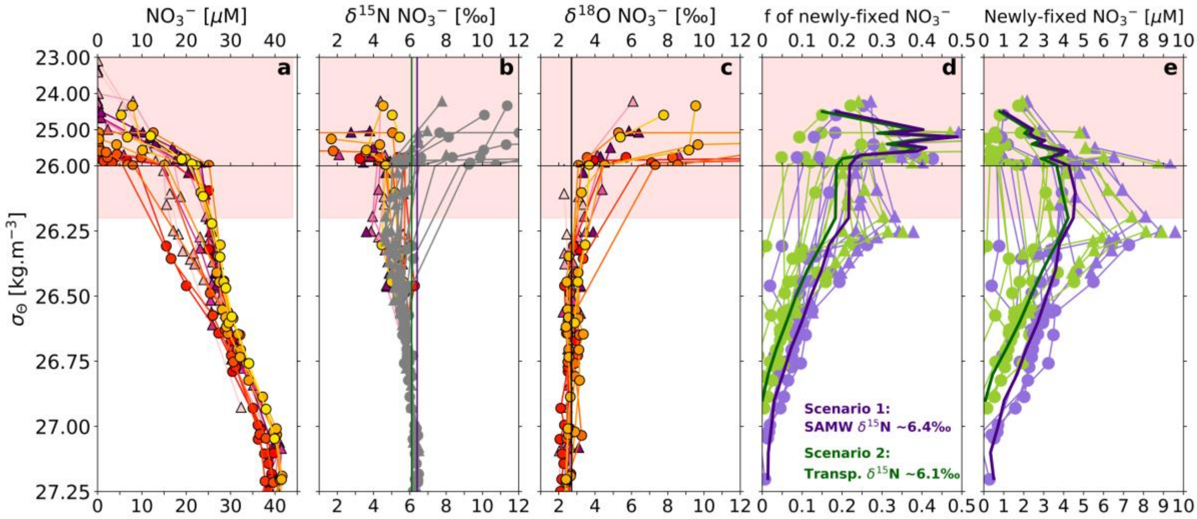

Figure A6. Assimilation-corrected, depth-specific fraction of newly-fixed nitrate in the Angola Gyre. Density profiles of nitrate concentrations in μM (**a**), measured (grey) and assimilation-removed (coloured) nitrate δ^{15}N in ‰ (**b**), measured nitrate δ^{18}O in ‰ (**c**), the depth-specific fraction of newly-fixed nitrate ($f_{depth\_specific}$; equation A3b) (**d**) and the corresponding concentration of depth-specific newly-fixed nitrate in μM (**e**)**.** Red shading indicates the density range of TSW (Table A2). In panels **a** to **c**, profile colours represent station longitude (see Figure A3). In panels **b** and **c**, the solid vertical line indicates the isotopic composition of the source nitrate, 6.1-6.4‰ for **b** and 2.7‰ for **c**. In panels **d** and **e**, purple data show results from scenario 1 while green represents scenario 2 (see main text for details). The mean of each scenario is shown by the bold line of corresponding colour.

A8. Method for estimating the N_2 fixation rate in the Angola Gyre

To estimate the N_2 fixation rate in the Angola Gyre, we first calculate the amount of newly-fixed nitrate in the thermocline reservoir ($\sigma_\theta \leq 27.0$ kg.m^{-3}) to be 641 mmol N.m^{-2} for scenario 1, which considers all low-δ^{15}N thermocline nitrate to be generated by *in situ* N_2 fixation, and 313 mmol N.m^{-2} for scenario 2, which considers an input of N_2 fixation from the North Atlantic via Angola Gyre feeder currents (see main text and SI.6). We take the areal extent of the Angola Gyre to be 2.6 x 10^{12} m^2 given the following boundaries: The northern boundary of the Angola Gyre appears to be at 6°S, coincident with a southward shift in the SEUC (Mercier, et al., 2003). The eastern and southern boundaries are commonly defined as the Angola Current (~12.2-12.5°E) and Angola-Benguela Front (~15-18°S), respectively (Stramma & Schott, 1999; Mercier, et al., 2003). The western boundary is less well-defined. Since the Angola Gyre feeds the westward-flowing central South Equatorial Current (cSEC), its physical properties can extend to the mid-Atlantic Ridge at 15°W(Mercier, et al., 2003; Reid, 1989). We define the western boundary at 7.5°W however, based on the shoaling of the 12°C isotherm (Figure 1.2b) and the distribution of salinity and oxygen concentrations at the time of sampling (Gordon & Bosley, 1990; Mercier, et al., 2003). The residence time of the Angola Gyre ranges between 4.4 and 8.5 years (Gordon & Bosley, 1990). Under scenario 1, we estimate the N_2 fixation rate to be 2.8 ± 1.3 Tg N.a^{-1} to 5.4 ± 2.5 Tg N.a^{-1}, with a mean of 4.1 ± 2.8 Tg N.a^{-1}. Under scenario

2, we estimate the N_2 fixation rate to be 1.4 ± 1.4 Tg $N.a^{-1}$ to 2.6 ± 2.7 Tg $N.a^{-1}$, with a mean of 2.0 ± 3.0 Tg $N.a^{-1}$. The rates are calculated as follows, using a 4.4 year residence time under scenario 2 as an example:

$$\left[\left[\left[\left[\frac{313\ \text{mmol N.m}^{-2}}{10^{3}\ \text{mol}}\right] \div 4.4\ \text{years}\right] \times\ 2.6 \times 10^{12}\ \text{m}^{2}\right] \times 14.0067\ \text{g N}\ \right] \div 10^{12}\ \text{Tg N} = 2.6\ \text{Tg N.a}^{-1}$$

We quantify the uncertainty associated with our N_2 fixation estimates by running a normal probability distribution Monte Carlo simulation of 100k steps, considering the mean and standard deviation of the amount of newly-fixed nitrate for each scenario and each residence time. We take the standard deviation of the output as indicative of the uncertainty.

As per the new production paradigm, euphotic zone primary production fuelled by new N (one form of which is N_2 fixation) must be balanced on an annual basis by the export of organic carbon from the euphotic zone (Dugdale & Georing, 1967). Multiplying our N_2 fixation rate estimates by the molar carbon (C) to N stoichiometry of ~6.63:1 typical of remineralised OM (Redfield, 1958; Anderson & Sarmiento, 1994), implies that N_2 fixation in the Angola Gyre supports the net removal of between 8.0 Tg $C.a^{-1}$ and 30.7 Tg $C.a^{-1}$.

A9. Comparison of the nitrate isotope-derived Angola Gyre N_2 fixation rate and direct N_2 fixation measurements

There are 18 direct measurements of N_2 fixation from in and near the Angola Gyre that range from undetectable to 170 μmol $N.m^{-2}.d^{-1}$ (Sohm, et al., 2011; Fonseca-Batista, et al., 2017; Subramaniam, et al., 2013). To compare our nitrate isotope-based rates with these values, we scale our Angola Gyre N_2 fixation rate in Tg $N.a^{-1}$ to a daily N_2 fixation rate. Considering the residence time extrema of 4.4 and 8.5 years, the maximum daily N_2 fixation rate implied by scenario 1 is 390.2 μmol $N.m^{-2}.d^{-1}$ and the minimum daily N_2 fixation rate implied by scenario 2 is 102.1 μmol $N.m^{-2}.d^{-1}$ (e.g., (641 mmol $N.m^{-2} \times 10^{3}$ mol N) ÷ 4.4 yr) × 365 days = 390.2 μmol $N.m^{-2}.d^{-1}$). Our nitrate isotope-based rates are thus comparable to the limited number of published N_2 fixation rate measurements.

A10. Potential hotspots of N_2 fixation controlled by the overlapping biogeography of excess P relative to N and bioavailable iron

The controls on N_2 fixation have been under investigation since the mid-1970s with early work concluding that oxygen (linked to turbulence) and temperature limit diazotroph (*Trichodesmium* spp.) blooms (Carpenter & Price, 1976; Carpenter, 1983b). Today, excess P relative to N (Deutsch, et al., 2007) and iron availability (Moore, et al., 2009) are considered the dominant controls, with field- and lab-based support for each (Sohm, et al., 2011a; Garcia, et al., 2015; Held, et al., 2020). In the South Atlantic, where surface waters host excess P, N_2 fixation is thought to be limited by iron (Moore, et al., 2009; Sohm, et al., 2011a; Wang, et al., 2019; Marconi, et al., 2017). A similar case has been made for the eastern tropical Pacific (15-21°S) (Knapp, et al., 2016; Sohm, et al., 2011a; Wang, et al., 2019).

We hypothesize the overlapping biogeography of excess P and bioavailable iron control N_2 fixation in the Angola Gyre. Co-occurring limitation of P and iron have been observed in diazotrophs (*Trichodesmium* spp.) across the tropical North Atlantic (Mills, et al., 2004; Held, et al., 2020). As such, we hypothesize that other regions of overlapping high P* and iron may also constitute N_2 fixation hotspots (Table A5). High P* waters are inherently linked to oxygen-deficient zones (ODZs) where significant denitrification occurs (Deutsch, et al., 2007), and these shadow zones occur proximate to continental margins where low oxygen environments generate narrow redox windows that enhance sedimentary iron fluxes (Scholz, et al., 2014). We thus hypothesize that eastern tropical margins are likely to be N_2 fixation hotspots. For surface waters overlying ODZs, N_2 fixation likely does not offset N loss, as in the Arabian Sea (Devol, et al., 2006), but the controls on the distribution of N_2 fixation nonetheless remain valid.

Table A5. Potential hotspots of N_2 fixation controlled by the overlapping biogeography of excess P relative to N and bioavailable iron. Regional hotspot locations where available data suggest the presence of both excess P relative to N (high P*) and bioavailable iron. Domain range is approximated based on data available for the region. References providing evidence for each control, excess P and iron, are included. Eastern basin hotspots appear to always be proximal to low oxygen environments.

Region	**Domain**	**Excess P availability**	**Dissolved iron availability**	**Supportive data**	**Proximal to OMZ/ODZ**
Brazil Current System subgyre	30-40°S 40-55°W	Deutsch et al. (2007)	Geotraces A02 and A10; Homoky et al. (2021)	**δ^{15}N nitrate**: Tuerena et al. (2015) **Trichodesmium**: Lima et al. (2019)	No
Guinea Dome	10-15°N 18-25°E	Moore et al. (2009); Boyer et a. (2018)	Geotraces A03 east and west; Conway & John (2014)	**δ^{15}N nitrate**: Marconi et al. (2015) **Direct rates**: Fonseca-Batista et al. (2017); **Trichodesmium:** Benavides & Voss (2015); Landolfi et al. (2018)	Yes
Costa Rica Dome	10-15°N 86-92°W	Deutsch et al. (2007); Boyer et a. (2018)	Pinedo-González et al. (2015); Moffett et al. (2020)	**δ^{15}N nitrate**: Casciotti et al. (2013); Buchwald et al. (2015) **Direct rates:** Landolfi et al. (2018)	Yes
Eastern tropical South Pacific	10-15°N 75-81°W	Deutsch et al. (2007); Boyer et a. (2018)	Geotraces P16	**δ^{15}N nitrate**: Casciotti et al. (2013) **Direct rates**: Bonnet et al. (2013)	Yes
Arabian Sea	10-25°N 60-75°E	Deutsch et al. (2007); Boyer et a. (2018)	Geotraces I04; Moffett et al. (2020)	**δ^{15}N nitrate**: Martin & Casciotti et al. (2017); Gaye et al. (2013) **Direct rates:** Landolfi et al. (2018)	Yes
Agulhas Current System subgyre	30-38°S 30-60°E	Deutsch et al. (2007); Boyer et a. (2018)	WOCE I05 and I06; Grand et al. (2015c)	**Trichodesmium:** Poulton et al. (2009)	No

A11. Analytical error associated with derivations of N* and P*

The error associated with calculations of N* and P* is most appropriately propagated as:

$$\text{N*}_{\text{propagated error}} = \sqrt{[NO_3^-]_{uncertainty}{}^2 + [PO_4^{3-}]_{\%\,uncertainty}{}^2} \quad \text{(A4)}$$

$$\text{P*}_{\text{propagated error}} = \sqrt{[PO_4^{3-}]_{uncertainty}{}^2 + [NO_3^-]_{\%\,uncertaity}{}^2} \quad \text{(A5)}$$

where $[NO_3^-]_{\text{uncertainty}}$ and $[PO_4^{3-}]_{\text{uncertainty}}$ are the standard deviations of replicate measurements of the same sample, typically 0.1 µM for the WOCE datasets (Joyce, et al., 1991; Becker, et al., 2013; Becker, et al., 2020; Martiny, et al., 2019). $[NO_3^-]_{\%\ uncertainty}$ and $[PO_4^{3-}]_{\%\ uncertainty}$ is the percent measurement uncertainty, necessary for propagating error when dividing or multiplying by a constant (in this case, 15.5; A2). Percent uncertainty is the same as relative uncertainty, calculated as the error (in this case, standard deviation) divided by the mean of all replicate measurements of a particular sample. The WOCE data reporting manual stipulates a 1% error for $[NO_3^-]$ and 1-2% for $[PO_4^{3-}]$ datasets (Joyce, et al., 1991; Becker, et al., 2013; Becker, et al., 2020). The resulting propagated error (equations A4 and A5) associated with both N* and P* is 0.1 µM. The implication is that changes in P* and N* of ≤0.1 µM should be interpreted with caution as they could easily lead to inaccurate diagnoses of the rate and/or distribution of N_2 fixation.

Chapter 3: The Agulhas Current Transports Signals of Local and Remote Indian Ocean Nitrogen Cycling

This chapter has been published as:

Marshall, T. A., Sigman, D. M., Beal, L. M., Foreman, A., Martínez-García, A., Blain, S., Campbell, E., Fripiat, F., Granger, R., Harris, E., Haug, G.H., Marconi, D., Oleynik, S., Rafter, P.A., Roman, R., Sinyanya, K., Smart, S.M., and Fawcett, S.E. (2023). The Agulhas Current transports signals of local and remote Indian Ocean nitrogen cycling. Journal of Geophysical Research: Oceans, 128, e2022JC019413. https://doi.org/10.1029/2022JC019413

Abstract

The greater Agulhas Current region is an important component of the climate system, yet its influence on carbon and nutrient cycling is poorly understood. Here, we use nitrate isotopes (δ^{15}N, δ^{18}O, Δ(15-18) = δ^{15}N – δ^{18}O) to trace regional water mass circulation and investigate nitrogen cycling in the Agulhas Current and adjacent recirculating waters. The deep and intermediate waters record processes occurring remotely, including partial nitrate assimilation in the Southern Ocean and denitrification in the Arabian Sea. In the thermocline and surface, tropically-sourced waters are biogeochemically distinct from adjacent subtropically-sourced waters, confirming inhibited lateral mixing across the current core. (Sub)tropical thermocline nitrate δ^{15}N is lower (4.9-5.8‰) than the sub-thermocline source, Subantarctic Mode Water (6.9‰); we attribute this difference to local N_2 fixation. Using a one-box model to simulate the newly-fixed nitrate flux, we estimate a local N_2 fixation rate of 7-25 Tg N.a^{-1}, with the upper limit likely biased high. In the mixed layer, nitrate δ^{15}N and δ^{18}O rise in unison, indicating that phytoplankton nitrate assimilation dominates in surface waters, with nitrification restricted to deeper waters. Because nitrate assimilation and nitrification are vertically decoupled, the rate of nitrate assimilation plus N_2 fixation can be used to approximate carbon export. Thermocline and mixed-layer nitrate Δ(15-18) is low, due to both N_2 fixation and coupled partial nitrate assimilation and nitrification. Similarly low-Δ(15-18) nitrate in Agulhas rings indicates leakage of low-δ^{15}N nitrogen into the South Atlantic, which should be recorded in the organic matter sinking to the seafloor, providing a potential tracer of past Agulhas leakage.

Plain Language Summary

The Agulhas Current is known to transport heat and salt from the warm tropics to the cooler (sub-)polar regions, but little is known of its nutrient fluxes. Here we use new measurements of the essential phytoplankton nutrient, nitrate, and its isotope ratios to better characterize

water circulation and the nitrogen cycle in the Agulhas Current and adjacent waters. Below 500 m, we see evidence of processes that occurred in other remote ocean basins. Above 500 m, we find that the nearby tropical and subtropical waters that feed the current have different chemistries and do not mix across its fast-flowing core. In the sunlit surface layer, the dominant nitrogen cycle process is nitrate uptake by phytoplankton, while nitrification, which produces nitrate from organic matter, occurs only in the dark waters below the surface. Additionally, the Agulhas Current and adjacent waters host significant rates of N_2 fixation, the process by which atmospheric N_2 gas is converted to nitrogen forms usable by phytoplankton. This N_2 fixation imprints a unique isotopic signature on the nitrate pool below the surface layer, which remains evident in Agulhas waters that enter the South Atlantic, potentially providing a tool to track Agulhas leakage, today and in the past.

3.1. Introduction

The role that western boundary currents (WBCs) play in Earth's climate system by transporting heat and salt from low- to higher latitudes is well-known (Bryden & Beal, 2001; Yu & Weller, 2007; Imawaki, et al., 2013; Talley, et al., 2011). The resultant net heat loss observed across WBCs strengthens the solubility pump leading to enhanced dissolution of atmospheric CO_2 in surface waters (Imawaki, et al., 2013; Takahashi, et al., 2009; Cronin, et al., 2010; Yu & Weller, 2007). WBCs also transport nutrients from the low-latitude tropics to the subtropical and subpolar gyres in subsurface "nutrient streams" (Pelegrí & Csanady, 1991). The eventual induction of these nutrients into the mixed layer of the gyres fuels biological production (Pelegrí & Csanady, 1991; Williams, et al., 2006; Guo, et al., 2012). While recent measurements have quantified heat and salt properties and fluxes in and near the Agulhas Current, the WBC of the South Indian Ocean (McMonigal, et al., 2020; Gunn, et al., 2020), the sources and cycling of nutrients in Agulhas waters have yet to be investigated.

The Agulhas Current flows south-west along the steep southern African continental slope between 27°S and 37°S (Figure 3.1). Its transport volume is approximately 77 ± 5 Sv (1 Sv = 1×10^6 $m^3.s^{-1}$) (Beal, et al., 2015), which makes it the strongest boundary current for its latitude (Bryden, et al., 2005). The Agulhas Current derives its waters from three source regions; the Mozambique Channel, the South East Madagascar Current, and recirculating subtropical gyre waters (Stramma & Lutjeharms, 1997; Donohue & Toole, 2003; Beal, et al., 2006). Toward the southern tip of Africa, the Agulhas Current makes an abrupt anticlockwise retroflection to flow eastward toward the Indian Ocean as the Agulhas Return Current (Gordon, 2003; Lutjeharms, 1980; Bang, 1970b). By 70°E, the majority of the waters in the Agulhas Return Current have recirculated into the subtropical southwest Indian Ocean, implying that the

Return Current contributes significantly to the recirculation that ultimately supplies the Agulhas Current (Stramma & Lutjeharms, 1997; Lutjeharms & Ansorge, 2001; Grand, et al., 2015c). At the Agulhas Retroflection, 9 ± 4 Sv of Indian Ocean waters "leak" into the South Atlantic each year (de Ruijter, et al., 1999; Richardson, 2007; Souza, et al., 2011). This Agulhas leakage plays a role in maintaining the Atlantic Meridional Overturning Circulation (AMOC) through the addition of heat and salt to the Atlantic Ocean (Gordon, 1985; Beal, et al., 2011).

WBC systems (i.e., the WBC and adjacent subtropical gyre waters) are regions of high eddy kinetic energy (Bryden, et al., 2005; Imawaki, et al., 2013; Schubert, et al., 2019a; Lévy, et al., 2012; Krug, et al., 2017; Thomas, et al., 2013; Ducet, et al., 2000) and their eddies are often associated with increased mixing. However, the strong cross-stream potential vorticity gradient and kinematic steering typical of WBCs tend to inhibit lateral mixing across the current core (Bower, et al., 1985; Beal, et al., 2006; Howe, et al., 2009). In the Agulhas Current, a consequence of this inhibited lateral mixing is a clear, physical partitioning of tropical waters from subtropical waters at the dynamical front (Beal, et al., 2006). Along the inshore side of the Agulhas Current, tropical waters are warmer, fresher, and older than subtropical waters, which are cooler, more saline, and younger (Figure 3.2a and b) (Beal, et al., 2006; Gordon, 1987). Mixing can and does occur elsewhere in the current, such as across the current edges, within the mixed layer, and in the deep waters below the potential vorticity gradient and kinematic steering level near 2000 m (Bower, 1991; Palter, et al., 2013; Leber & Beal, 2015; Beal, et al., 2006). How the dynamical front in the Agulhas Current impacts the distribution of nutrients is yet to be explored.

The surface waters of WBC systems are typically nitrogen (N) limited (Smith, 1984; Voss, et al., 2013). The availability of this nutrient thus exerts a dominant control on primary productivity and carbon export. In subtropical gyres, winter convective mixing supplies subsurface nitrate (NO_3^-) to the euphotic zone, with strong stratification during the remainder of the year impeding the upward mixing of nitrate (Williams & Follows, 2003; Williams, et al., 2006; Palter, et al., 2005; Lomas, et al., 2013). Nitrogen can also be supplied via N_2 fixation, a process mediated by diazotrophs (i.e., specialized plankton capable of transforming atmospheric N_2 gas into bioavailable or "fixed" N) that typically occurs in the warm, sunlit surface layer (Landolfi, et al., 2018). Incidences of N_2 fixation have been diagnosed in subtropical waters adjacent to and within WBCs (Shiozaki, et al., 2015; Wu, et al., 2018; Palter, et al., 2020; Detoni, et al., 2016; Wen, et al., 2022; Armbrecht, et al., 2015), although the Agulhas Current remains unstudied in this regard.

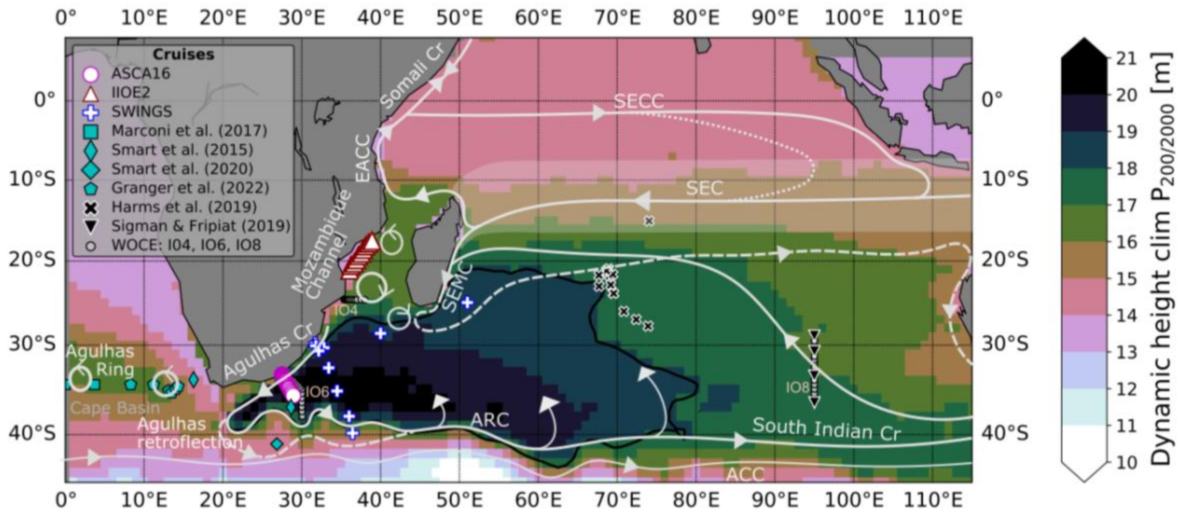

Figure 3.1. Thermocline circulation in the South Indian Ocean. Map showing the station locations (symbols) and thermocline circulation of the South Indian Ocean overlaid on an annual climatology of mean dynamic height for $P_{200/2000}$, which represents the mean circulation at 200 dbar referenced to 2000 dbar. Open pink circles show stations sampled during the ASCA16 cruise, open maroon triangles indicate stations sampled during the IIOE2 cruise, and open blue pluses show stations sampled during the SWINGS cruise. Cyan symbols show the locations of earlier studies that measured nitrate isotopes in Agulhas features (Marconi, et al., 2017; Smart, et al., 2015; Smart, et al., 2020; Granger, et al., 2023), while black symbols indicate the locations of published nitrate isotope data from the South Indian Ocean (Sigman & Fripiat, 2019; Harms, et al., 2019). Small white circles show the three WOCE lines; IO4 along 24°S, IO6 along ~30°E, and IO8 along 95°E. The white arrows represent the approximate thermocline circulation and circles with arrows indicate eddies. The black line shows the 18 m dynamic height contour that encompasses the region of retentive subtropical recirculation, and the dashed arrows represent the surface and seasonal currents. SEC: South Equatorial Current (the opaque shading around the SEC represents its broad meridional extent; (Talley, et al., 2011)); SECC: South Equatorial Countercurrent; EACC: East African Coastal Current; SEMC: South East Madagascar Current; ARC: Agulhas Return Current; ACC: Antarctic Circumpolar Current. To derive the mean dynamic height climatology for 2004-2018, we used data from the updated Roemmich-Gilson Argo Climatology (Roemmich & Gilson, 2009). These data were collected and made freely available by the International Argo Program and the national programs that contribute to it (https://argo.ucsd.edu, https://www.ocean-ops.org). The Argo Program is part of the Global Ocean Observing System (Argo, 2021).

Both newly-fixed N and nitrate supplied from depth are considered “new” N sources to the mixed layer, fueling phytoplankton growth termed “new production” (Dugdale & Goering, 1967). On an annual timescale, new production must be balanced by the export of organic matter from the surface layer (i.e., “export production”), and can thus be used to infer carbon export potential (Eppley & Peterson, 1979). This mass balance approach for estimating export production is complicated if nitrification, the microbial oxidation of ammonium to nitrite and then nitrate, occurs in the euphotic zone coincident with nitrate assimilation. If so, it yields regenerated (rather than new) nitrate, the assimilation of which supports “regenerated production" (Dugdale & Goering, 1967). Failing to account for surface-layer nitrification, if significant relative to the upward supply of subsurface nitrate, will cause carbon export potential to be overestimated (Yool, et al., 2007; Mdutyana, et al., 2020).

In the Indian Ocean, model-based mean estimates of N_2 fixation and denitrification (i.e., the removal of fixed N) are approximately 26 Tg N.a^{-1} and 40 Tg N.a^{-1}, respectively (Landolfi, et al., 2018; Wang, et al., 2019; DeVries, et al., 2013; Deutsch, et al., 2007; Bianchi, et al., 2012). The imbalance between these two fluxes implies that N loss is not completely offset by N gain in the Indian Ocean. N_2 fixation measured in the euphotic zone of the Arabian Sea, a region that supports high rates of denitrification, contributes only ~10% of the basin-wide N gain (2.3 Tg N.a^{-1}; (Capone, et al., 1998; Bange, et al., 2000; Gandhi, et al., 2011)). Therefore, N_2 fixation must be significant elsewhere in the Indian Ocean (Gruber & Sarmiento, 1997; Deutsch, et al., 2007; Wang, et al., 2019; Grand, et al., 2015c), yet there are almost no observations of this process, particularly from the southern basin (cf. Poulton, et al. 2009; Harms, et al., 2019; Karlusich, et al., 2021; Metzl, et al., 2022).

Here, we use measurements of hydrography, nutrients, and the N and oxygen (O) isotopes of nitrate across the southwest Indian Ocean to investigate circulation and N cycling. Our goals are to 1) biogeochemically characterize the regional water masses to better understand their sources and circulation and 2) diagnose regional N cycle processes such as N_2 fixation, nitrate assimilation, and nitrification. The nitrate isotopes are well suited for investigating circulation and N cycling for three main reasons. First, nitrate isotope ratios in the waters beneath the thermocline record preformed signals that can be used to trace water masses and their subsequent modification between formation and our study site (e.g., (Rafter, et al., 2013; Marconi, et al., 2017)). Second, any (de)coupling of the N and O isotope ratios in the thermocline and mixed layer allows us to disentangle nitrate assimilation from nitrification and thus to evaluate the relative importance of nitrate supplied to the mixed layer from the subsurface (which fuels new production) versus nitrate regenerated within the mixed layer (which fuels regenerated production). Third, the nitrate isotopes record and integrate the signal of N_2 fixation and as such, can be used to evaluate the proportion of locally-produced versus transported newly-fixed nitrate in the southwest Indian Ocean (Knapp, et al., 2005; Knapp, et al., 2008; Marconi, et al., 2017; Marshall, et al., 2022).

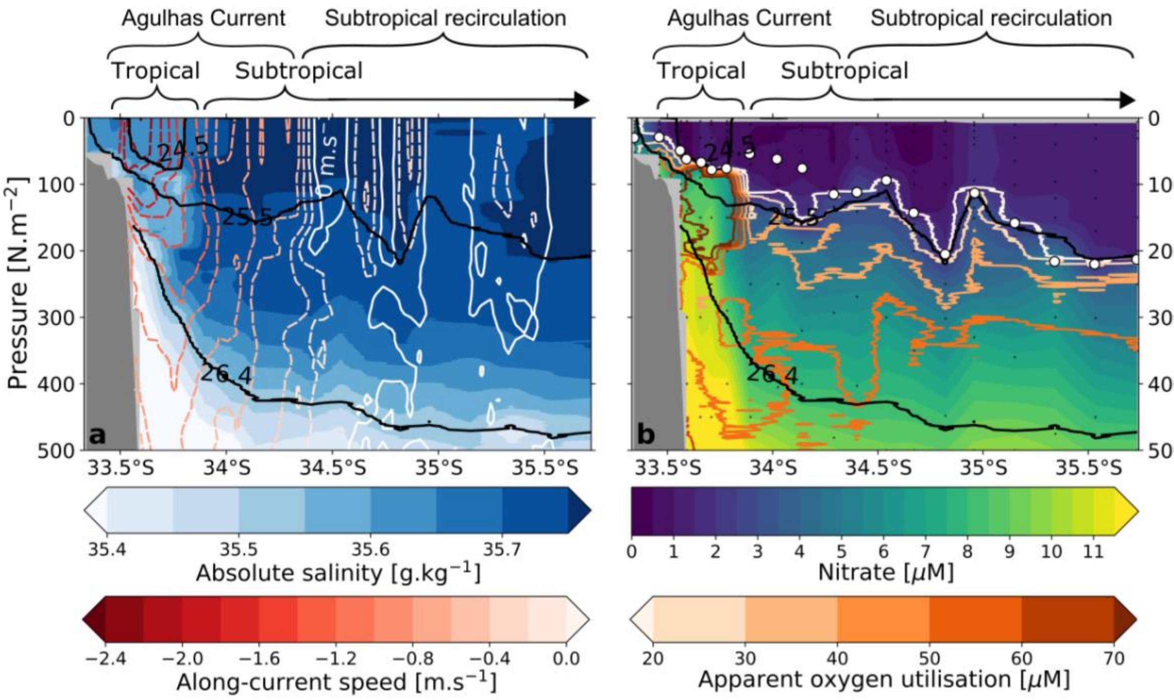

Figure 3.2. Structure of the Agulhas Current and recirculating waters. a) Gridded depth section of absolute salinity [g.kg^{-1}] over the upper 500 m of the ASCA16 transect. Overlaid in shades of red are contours of along-current speed [m.s^{-1}] measured from a shipboard acoustic Doppler current profiler. **b**) Gridded depth section of nitrate concentration [μM] over the upper 500 m of the ASCA16 transect. Overlaid in shades of orange are contours of apparent oxygen utilisation (AOU) [μM]. Small white circles indicate the mixed layer depth at each station. In both **a** and **b**, black contours show the isopycnal boundaries of the major water masses (see Table 3.1). The top row of brackets indicates the position of the fast-flowing Agulhas Current and adjacent subtropical recirculation. The bottom row of brackets distinguishes the fresh, high-AOU, high-nitrate, tropically-sourced waters along the inshore side of the Agulhas Current from the saline, lower-AOU, lower-nitrate, subtropically-sourced waters along the offshore side of the Agulhas Current. The shoaling isopycnals that uplift nutrient-rich waters within the Agulhas Current are consistent with observations of subsurface nutrient streams reported in other WBCs (Pelegrí & Csanady, 1991).

3.2. Methods

3.2.1. Field sampling

During three cruises to the southwest Indian Ocean, we collected full-depth hydrographic data and seawater samples for nutrient and nitrate isotope analysis. Twenty stations were occupied across the Agulhas Current and adjacent recirculating waters along the Agulhas System Climate Array near ~34°S in austral winter, July 2016 (ASCA16), onboard the R/V *SA Agulhas II* (circles outlined in pink in Figure 3.1). Ten stations were occupied along the western slope of the Mozambique Channel along ~37°E (which sampled to ~1500 m) in austral spring, October 2017, as part of a larger study of the African continental shelf (IIOE2; iioe-2.incois.gov.in), also onboard the R/V *SA Agulhas II* (triangles outlined in red in Figure 3.1).

Finally, ten stations were occupied across the southwest Indian Ocean, with four stations in the Agulhas Current (near ~30°S) and six in the subtropical recirculation, in austral summer, January 2021, as part of the GEOTRACES SWINGS cruise (swings.geotraces.org) onboard the R/V *Marion-Dufresne* (pluses outlined in blue in Figure 3.1).

All hydrographic measurements were made using a Conductivity-Temperature-Depth-Oxygen (CTDO) sensor attached to a Seabird 9/11+ rosette equipped with 12 L Niskin bottles. Potential density anomalies referenced to 0 dbar (σ_θ), 2000 dbar (σ_2), and 4000 dbar (σ_4) pressure levels were derived from conservative temperature and absolute salinity using the Gibbs Seawater Oceanographic package in Python. Apparent oxygen utilization (AOU) was calculated as the difference between the derived oxygen saturation concentration at a given salinity and temperature and the observed oxygen concentration (i.e., AOU, in μM, = $[O_{2saturated}] - [O_{2observed}]$). Duplicate seawater samples were collected throughout the water column for nutrients and nitrate isotopes in thoroughly rinsed 50 ml Falcon tubes and high-density polyethylene bottles, respectively. All nitrate isotope samples and the nutrient samples from ASCA16 and IIOE2 were frozen at -20°C directly after collection while the SWINGS nutrient samples were syringe-filtered (0.45 µm) shipboard, then poisoned with mercuric chloride (20 mg.L^{-1} final concentration) and stored at room temperature until analysis.

During the ASCA16 cruise, a ship-mounted 75 kHz Teledyne RD acoustic Doppler current profiler collected velocity data from 45 m to ~850 m. These data were rotated normal to the Agulhas Current and extended from 45 m to the surface.

3.2.2. Nutrient analyses

Samples were measured for nitrate, silicic acid ($Si(OH)_4$), and nitrite (NO_2^-) concentrations in the Marine Biogeochemistry Lab at the University of Cape Town (UCT-MBL; for ASCA16 and IIOE2) and in the Microbial Oceanography Laboratory at the Sorbonne Université (for SWINGS). Full-depth distributions of nitrate, nitrite, and silicic acid concentrations for ASCA16 are shown in Figure B1, for SWINGS in Figure B2, and for IIOE2 in Figure B3. In the UCT-MBL, nitrate+nitrite and silicic acid concentrations were measured using a Lachat QuickChem® Flow Injection Analysis platform (Grasshoff, 1976; Diamond, 1994) with a precision of 0.2 μM and detection limit of 0.1 μM. Nitrite concentrations were measured manually using standard colorimetric methods (Grasshoff, 1976; Strickland & Parsons, 1972) and a Genesys 30 Visible spectrophotometer, with a precision of 0.1 μM and a detection limit of 0.05 μM. In the Microbial Oceanography Laboratory, nitrate+nitrite, nitrite, and silicic acid concentrations were determined using a Skalar segmented flow analyser (Blain, et al., 2015) with a precision of 1-4% and detection limits of 0.02 μM for nitrate+nitrite and nitrite and 0.1 μM for silicic acid. Certified reference materials (JAMSTEC for ASCA16 and IIOE2 and Certipur for SWINGS) were included in all runs to ensure measurement accuracy. Nitrate concentrations were calculated as the difference between the nitrate+nitrite and nitrite concentrations. Hereafter, all references to nitrate concentration are to the nitrate-only data.

3.2.3. Nitrate N and O isotope analyses

All nitrate isotope samples were syringe-filtered (0.2 μm) to remove organic matter. Prior to isotopic analysis, samples with nitrite concentrations >0.5% of the nitrate+nitrite concentrations were treated with sulfamic acid to remove nitrite, followed by 2 M sodium hydroxide to return the sample pH to between 7 and 8 (Granger & Sigman, 2009). The removal of nitrite is necessary because its isotopic composition can differ greatly from that of nitrate, such that even when present at low concentrations, nitrite can have a significant effect on the δ^{15}N and δ^{18}O of the nitrate+nitrite pool (Fawcett, et al., 2015; Granger & Sigman, 2009; Casciotti & McIlvin, 2007; Kemeny, et al., 2016).

The natural abundance N and O isotope ratios of nitrate are reported in delta (δ) notation as δ^{15}N, in ‰ versus N_2 in air, = $[(^{15}N/^{14}N)_{sample}/(^{15}N/^{14}N)_{reference}-1]\times10^3$ and δ^{18}O, in ‰ versus VSMOW, = $[(^{18}O/^{16}O)_{sample}/(^{18}O/^{16}O)_{reference}-1]\times10^3$. The nitrate isotopes were measured at Princeton University (ASCA16; δ^{15}N and δ^{18}O) and the Max Planck Institute for Chemistry (IIOE2 and SWINGS, with only δ^{15}N data available for SWINGS) using the "denitrifier" method (Sigman, et al., 2001; Casciotti, et al., 2002). This method relies on the bacterial reduction of nitrate to nitrous oxide gas (N_2O), after which a Thermo MAT 253 isotope ratio mass spectrometer interfaced with a custom-built online N_2O extraction and purification system was used to measure the N and O isotopic composition of the N_2O (Sigman, et al., 2001; Casciotti, et al., 2002; Weigand, et al., 2016). International reference materials, IAEA-N3 and USGS-34 (Gonfiantini, 1984; Böhlke, et al., 2003), as well as an in-house N_2O standard, were run in parallel with the samples. The pooled standard deviation of replicate measurements of nitrate δ^{15}N and δ^{18}O for the ASCA16 samples was 0.10‰ and 0.20‰ (n = 281; all samples with nitrate concentrations >0.35 μM were measured), for the IIOE2 samples was 0.12‰ and 0.15‰ (n = 103, all samples with nitrate concentrations >1.76 μM were measured), and for the SWINGS samples was 0.17‰ (δ^{15}N only, n = 172, all samples with nitrate concentrations >0.96 μM were measured). The nitrate δ^{18}O data were not corrected for depth-related changes in salinity (Knapp, et al., 2008) as the vertical salinity gradients were relatively minor and there is considerable uncertainty associated with the $\delta^{18}O_{H2O}$/salinity relationship in the subtropical Indian Ocean (Schmidt, G.A., G. R. Bigg and E. J. Rohling. 1999. "Global Seawater Oxygen-18 Database-v1.22"; https://data.giss.nasa.gov /o18data/; B1).

3.2.3.1. The dual isotopes of nitrate

Nitrate $\delta^{15}N$ and $\delta^{18}O$ can separately yield insights into oceanic N cycling; however, their dual measurement increases their utility, allowing overlapping processes to be disentangled (e.g., (Sigman, et al., 2005; Rafter, et al., 2013; Fawcett, et al., 2015). During nitrate assimilation, phytoplankton preferentially consume the lighter ^{14}N and ^{16}O isotopes, causing the $\delta^{15}N$ and $\delta^{18}O$ of the ambient nitrate pool to increase as its concentration declines (Wada & Hattori, 1976; Sigman, et al., 1999; Casciotti, et al., 2002). This increase occurs in a ratio of ~1:1 (i.e., the rise in nitrate $\delta^{15}N$ is coupled to that of $\delta^{18}O$; (Granger, et al., 2004; Granger, et al., 2010)). Denitrification also raises the $\delta^{15}N$ and $\delta^{18}O$ of nitrate in tandem (Granger, et al., 2008). By contrast, during nitrification, the $\delta^{15}N$ and $\delta^{18}O$ of nitrate are decoupled because the $\delta^{15}N$ of newly nitrified nitrate is set by the $\delta^{15}N$ of the organic matter plus ammonium being remineralised and oxidized while its $\delta^{18}O$ is strongly controlled by the $\delta^{18}O$ of seawater (i.e., the $\delta^{18}O$ of newly nitrified nitrate has been shown to equal $\delta^{18}O_{H2O}$, = ~0‰, plus an isotopic offset of ~1.1‰; (Sigman, et al., 2009a; Buchwald, et al., 2012; Boshers, et al., 2019; Marconi, et al., 2019)).

The parameter nitrate $\Delta(15\text{-}18)$ (= $\delta^{15}N - \delta^{18}O$) leverages the (de)coupling of nitrate $\delta^{15}N$ and $\delta^{18}O$ and as such, is useful for identifying overlapping N cycle processes (Sigman, et al., 2005; Rafter, et al., 2013). In surface waters where photosynthetic nitrate assimilation is dominant, we expect nitrate $\Delta(15\text{-}18)$ to remain constant (e.g., (DiFiore, et al., 2009; Fawcett, et al., 2015)) as nitrate $\delta^{15}N$ and $\delta^{18}O$ rise in unison (Granger, et al., 2004; Granger, et al., 2010). In the underlying thermocline where organic matter deriving from surface productivity is remineralised, nitrate $\Delta(15\text{-}18)$ may increase or decrease depending on the $\delta^{15}N$ of the remineralized organic matter relative to the $\delta^{18}O$ of newly nitrified nitrate. Since N_2 fixation introduces organic matter with a $\delta^{15}N$ of approximately -1‰ (Hoering & Ford, 1960; Minagawa & Wada, 1986; Carpenter, et al., 1997), which is low relative to subsurface nitrate (which ranges in $\delta^{15}N$ from roughly 3‰ to 7‰ (Sigman, et al., 1999; Knapp, et al., 2008; Rafter, et al., 2013; Fripiat, et al., 2021; Rafter, et al., 2019)), its remineralization yields nitrate with a low $\delta^{15}N$ and $\Delta(15\text{-}18)$ (Rafter, et al., 2013; Knapp, et al., 2008; Knapp, et al., 2005; Lehmann, et al., 2018; Sigman, et al., 2005; Sigman, et al., 2009a). Co-occurring partial nitrate assimilation and nitrification also yields low-$\Delta(15\text{-}18)$ nitrate (Sigman, et al., 2005; Sigman, et al., 2009a;

Rafter, et al., 2013; Fawcett, et al., 2015; Deman, et al., 2021). This is because the cycling of N between nitrate assimilation and nitrification has little effect on the δ^{15}N of nitrate as in net, N is neither lost nor gained. Contrastingly, nitrate assimilation is a sink for the O atoms of nitrate and nitrification is the ultimate source, such that the δ^{18}O of nitrate is “reset” by nitrification. In the case of co-occurring partial nitrate assimilation and nitrification, the δ^{18}O of the combined partially assimilated and newly nitrified nitrate pool ends up higher than the δ^{18}O of the nitrate initially removed by phytoplankton (Sigman, et al., 2005; Sigman, et al., 2009a; Rafter, et al., 2013; Fawcett, et al., 2015).

3.3. Results and interpretation

We report our findings in the context of the regional water masses, presenting their biogeochemical properties for the first time. Mean values of measured hydrographic and biogeochemical properties for the Agulhas Current and adjacent recirculating waters are included in Table 3.1 (ASCA16 plus SWINGS) and for the western Mozambique Channel (IIOE2), in Table 3.2. The divide created by the dynamical front in the Agulhas Current is most apparent in the upper ocean (σ_θ < 26.4 kg.m^{-3}) water mass properties (Figure 3.3). Subtropical waters are present at ASCA16 stations south of 33.78°S and at SWINGS stations east of ~33°E (circles and pluses in Figure 3.3; blue circles and green pentagons in Figure 3.4), while tropical waters occur at ASCA16 stations north of and including 33.78°S and at SWINGS stations west of and including 33°E (stars and diamonds in Figure 3.3; pink circles and purple pentagons in Figure 3.4). We treat the subtropical waters in the Agulhas Current and the adjacent recirculating waters from the subtropical gyre collectively (Table 3.1) since the Agulhas Current sources the majority of its water from the recirculation. Because ASCA16 was sampled at higher resolution and the dataset includes nitrate δ^{18}O (and therefore Δ(15-18)), we focus our analysis on the nitrate dual isotope data from the ASCA16 cruise, incorporating the nitrate concentration and δ^{15}N data from the SWINGS cruise only where relevant.

Table 3.1. Water mass characteristics in the subtropical southwest Indian Ocean. Mean values (± 1 SD) of absolute salinity [g.kg^{-1}], conservative temperature [°C], oxygen concentration [μM], apparent oxygen utilization (AOU) [μM], nitrate concentration [μM], and concentration-weighted nitrate δ^{15}N [‰], δ^{18}O [‰], and Δ(15-18) [‰] for the water masses identified in the ASCA16 and SWINGS datasets. Nitrate δ^{18}O and Δ(15-18) are included for the ASCA16 dataset only. For the other parameters, values from the SWINGS dataset are provided in soft brackets. Water masses are defined by potential density anomalies, σ_θ [kg.m^{-3}], with the core properties of Subantarctic Mode Water, the ultimate source water to the region, listed in square brackets. The narrow density range occupied by the surface and thermocline waters condenses the data in density space (B3); we thus report surface and thermocline water mass properties averaged over

depth rather than density (the density-defined values are provided separately in Tables B1 (for ASCA16) and B2 (for SWINGS)). The row subheadings *Tropical* and *Subtropical* refer to the waters inshore and offshore of the Agulhas Current core, respectively. Tropical (subtropical) waters occur at ASCA16 stations north (south) of 33.78°S and at SWINGS stations west (east) of ~33°E. The two most coastal ASCA16 stations (33.34°S and 33.46°S) are excluded from the inshore means as both are influenced by shelf upwelling, which is evident in their elevated density, nitrate concentration, and nitrate-Δ(15-18) values that resemble deeper waters. The column headed *Abbrev.* lists the abbreviations for the various water masses used throughout this study.

Table 3.2. Water mass characteristics in the western Mozambique Channel. Mean values (± 1 SD) of absolute salinity [g.kg^{-1}], conservative temperature [°C], oxygen concentration [uM], apparent oxygen utilization (AOU) [µM], nitrate concentration [µM], and concentration-weighted nitrate δ^{15}N [‰], δ^{18}O [‰], and Δ(15-18) [‰] for the water masses identified in the IIOE2 dataset. Water masses are defined by potential density anomalies, σ_θ [kg.m^{-3}], and the core properties of Subantarctic Mode Water are listed in square brackets.

Table 3.1

	Water mass	Abbrev.	Potential density, σ_θ [kg.m^{-3}]	Absolute salinity [g.kg^{-1}]	Conservative temperature, θ [°C]	Oxygen [μM]	AOU [μM]	NO_3^- [μM]	$\delta^{15}N$ NO_3^- [‰]	$\delta^{18}O$ NO_3^- [‰][1]	Δ(15-18) [‰][1]
Tropical	Tropical Surface Water	TSW	<24.5	35.6 ± 0.51	22.8 ± 1.37	200.8 ± 9.3	12.9 ± 4.8	1.1± 0.9 (0.2 ± 0.1)	6.5 ± 1.2 (NA)	4.0 ± 1.2	2.5 ± 1.2
	Tropical Thermocline Water	TTW	24.5 - 26.4	35.6 ± 0.05	17.4 ± 2.26	179.8 ± 27.7	73.4 ± 13.6	7.8 ± 1.8 (9.6 ± 2.5)	5.8 ± 0.3 (6.2 ± 0.4)	2.7 ± 0.4	3.2 ± 0.3
Subtropical	Subtropical Surface Water	STSW	24.5 - 25.5	35.7 ± 0.11	20.1 ± 1.47	212.2 ± 14.1	10.2 ± 7.6	1.0 ± 0.5 (0.4 ± 0.6)	8.0 ± 0.7 (6.0 ± 1.9)	6.7 ± 0.7	1.3 ± 0.8
	Subtropical Thermocline Water	STTW	25.5 - 26.4	35.7 ± 0.03	18.3 ± 0.99	199.4 ± 16.5	28.3 ± 11.3	3.0 ± 1.4 (3.0 ± 1.4)	4.9 ± 0.7 (5.1 ± 0.7)	2.8 ± 0.8	2.1 ± 0.8
Subantarctic Mode Water		SAMW	26.4 - 27.0	35.1 ± 0.23 [35.1 ± 0.05]	11.0 ± 1.86 [11.3 ± 0.38]	203.6 ± 8.6 [209.4 ± 4.7]	65.4 ± 16.3 [57.4 ± 4.4]	15.2 ± 4.3 (15.3 ± 3.9) [13.8 ± 1.1]	6.7 ± 0.4 (6.6 ± 0.5) [6.9 ± 0.1]	3.3 ± 0.4 [3.5 ± 0.1]	3.4 ± 0.4 [3.4 ± 0.1]
Antarctic Intermediate Water		AAIW	27.0 - 27.4	34.6 ± 0.06	5.4 ± 1.06	177.8 ± 14.9	128.4 ± 18.0	28.3 ± 2.4 (31.6 ± 2.4)	6.0 ± 0.1 (6.0 ± 0.1)	2.6 ± 0.1	3.4 ± 0.1
Red Sea Water lenses		RSW	27.45 - 27.55	34.8 ± 0.04	4.1 ± 0.28	150.3 ± 8.8	166.8 ± 7.0	31.9 ± 0.7 (31.5 ± 2.0)	6.0 ± 0.0 (5.9 ± 0.1)	2.6 ± 0.1	3.4 ± 0.0
Upper Circumpolar Deep Water		UCDW	27.4 - σ_2 =36.9	34.8 ±0.07	3.1 ± 0.46	164.3 ± 10.5	160.1 ± 7.6	30.7 ± 1.3 (31.7 ± 2.0)	5.5 ± 0.1 (5.5 ± 0.1)	2.2 ± 0.1	3.4 ± 0.1
Indian Deep Water		IDW	*27.45 - σ4 = 45.9*	(34.9 ± 0.00)	(1.8 ± 0.04)	(211.9 ± 0.3)	(177.3 ± 0.4)	(35 ± 0.1)	(5.4 ± 0.0)		
North Atlantic Deep Water		NADW	σ_2=36.9 - σ4 = 45.9	35.0 ± 0.02	2.1 ± 0.31	202.2 ± 8.4	129.1 ± 6.7	27.4 ± 0.8 (29.1 ± 1.4)	5.0 ± 0.00 (5.1 ± 0.1)	1.9 ± 0.1	3.1 ± 0.1
Lower Circumpolar Deep Water		LCDW	σ_4 > 45.9	34.9 ± 0.02	0.9 ± 0.32	208.2 ± 2.5	134.7 ± 2.8	29.3 ± 0.8 (30.9 ± 1.0)	4.9 ± 0.0 (4.9 ± 0.0)	1.8 ± 0.1	3.0 ± 0.0

Footnotes: [1] Data from ASCA16 only

Table 3.2

Water mass	**Abbrev.**	**Potential density, σ_θ [kg.m^{-3}]**	**Absolute salinity [g.kg^{-1}]**	**Conservative temperature, θ [°C]**	**Oxygen [µM]**	**AOU [µM]**	**NO_3^- [µM]**	**$\delta^{15}N$ NO_3^- [‰]**	**$\delta^{18}O$ NO_3^- [‰]**	**Δ(15-18) [‰]**
Tropical Surface Water	TSW	<24.5	35.4 ± 0.05	25.0 ± 1.36	180.2 ± 14.5	25.9 ± 19.0	2.2 ± 2.0	6.5 ± 1.3	3.0 ± 1.3	3.6 ± 1.3
Tropical Thermocline Water	TTW	24.5 - 26.4	35.5 ± 0.05	16.8 ± 2.28	139.1 ± 8.4	99.7 ± 10.1	10.9 ± 2.2	6.0 ± 0.4	2.8 ± 0.4	3.2 ± 0.4
Southeast Indian Subantarctic Mode Water	SEISAMW	26.4 - 26.9	35.1 ± 0.13 (35.1 ± 0.07)	11.2 ± 1.28 (11.2 ± 0.58)	169.0 ± 7.0 (173.2 ± 4.1)	98.9 ± 8.2 (94.3 ± 4.6)	16.9 ± 3.6 (16.4 ± 2.4)	6.7 ± 0.3 (6.8 ± 0.2)	3.2 ± 0.3 (3.3 ± 0.2)	3.5 ± 0.3 (3.5 ± 0.2)
Antarctic Intermediate Water	AAIW	26.9 - 27.1	34.9 ± 0.02	8.5 ± 0.44	146.1 ± 10.9	138.6 ± 13.4	24.6 ± 2.7	6.6 ± 0.1	3.0 ± 0.1	3.6 ± 0.1
Red Sea Water	RSW	27.1 - σ_2 =36.6	35.0 ± 0.03	6.2 ± 0.83	95.6 ± 11.9	204.3 ± 15.9	32.9 ± 2.8	6.6 ± 0.1	2.9 ± 0.1	3.7 ± 0.1
Upper Circumpolar Deep Water	UCDW	$\sigma_2 > 36.6$	34.9 ± 0.03	4.0 ± 0.37	115.5 ± 10.7	200.0 ± 8.1	34.6 ± 1.3	6.1 ± 0.1	2.5 ± 0.1	3.5 ± 0.1

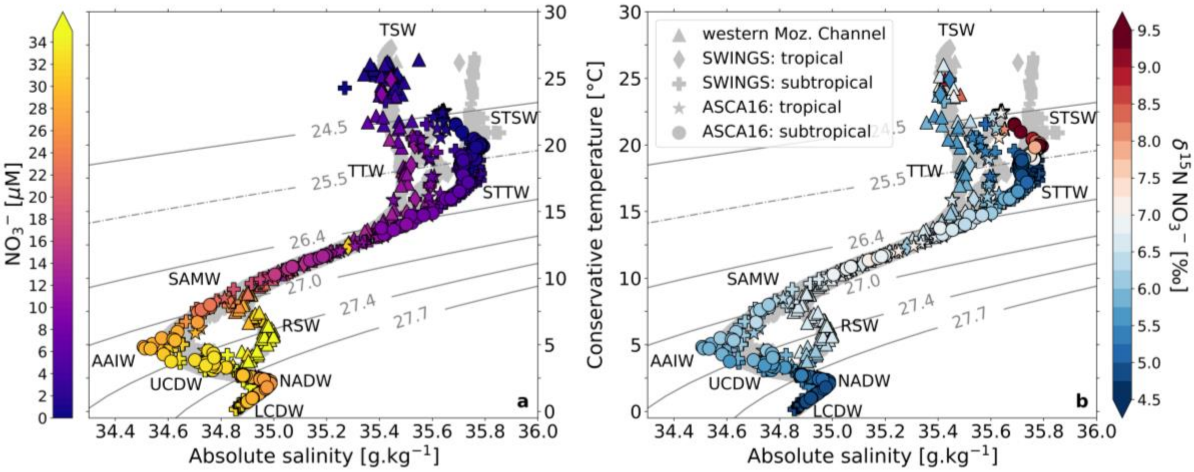

Figure 3.3. Biogeochemical characteristics of water masses in the southwest Indian Ocean. Conservative temperature [°C] versus absolute salinity [g.kg^{-1}] for the ASCA16 (circle and star symbols), IIOE2 (triangle symbols), and SWINGS (plus and diamond symbols) cruises. Symbol colours indicate **a**) nitrate concentration [µM] and **b**) nitrate δ^{15}N [‰]. ASCA16 and SWINGS stations that sampled tropical versus subtropical waters are indicated in the legend. The coloured symbols show discrete samples and the underlying grey symbols show the high resolution CTDO-derived values of temperature and salinity. Grey contours indicate the potential density anomalies (labeled on the panels, in kg.m^{-3}) that form the boundaries of water masses (see Table 3.1). TSW: Tropical Surface Water; STSW: Subtropical Surface Water; TTW: Tropical Thermocline Water; STTW: Subtropical Thermocline Water; SAMW: Subantarctic Mode Water; AAIW: Antarctic Intermediate Water; RSW: Red Sea Water; UCDW: Upper Circumpolar Deep Water; NADW: North Atlantic Deep Water; LCDW: Lower Circumpolar Deep Water.

3.3.1. Source waters of the southwest Indian Ocean

Our biogeochemical measurements yield new insights into the origins and modifications of water masses in the southwest Indian Ocean. The Agulhas Current water masses were first defined by Beal et al. (2006) based on salinity, potential vorticity, and oxygen concentrations. By also considering the biogeochemistry, we can refine the original water masses definitions and identify additional water masses from their distinctive biogeochemical properties (Figure 3.3 and 3.4). For example, we distinguish between thermocline and sub-thermocline waters, which are often collectively described as “central waters” (~25.0 kg.m^{-3} < σ_θ < 27.0 kg.m^{-3}). Thermocline waters (σ_θ <26.4 kg.m^{-3}) are influenced by the remineralization of organic matter produced in the overlying surface waters as well as by the upward supply of nutrients from below (e.g., during deep winter/spring mixing), while sub-thermocline waters (σ_θ >26.4 kg.m^{-3}) constitute the ultimate source of nutrients to the overlying thermocline and surface layer. Additionally, we use knowledge of water mass biogeochemistry at the sites of formation to infer modifications, and the processes responsible therefor, along the circulation pathways to our study site (Figure 3.5).

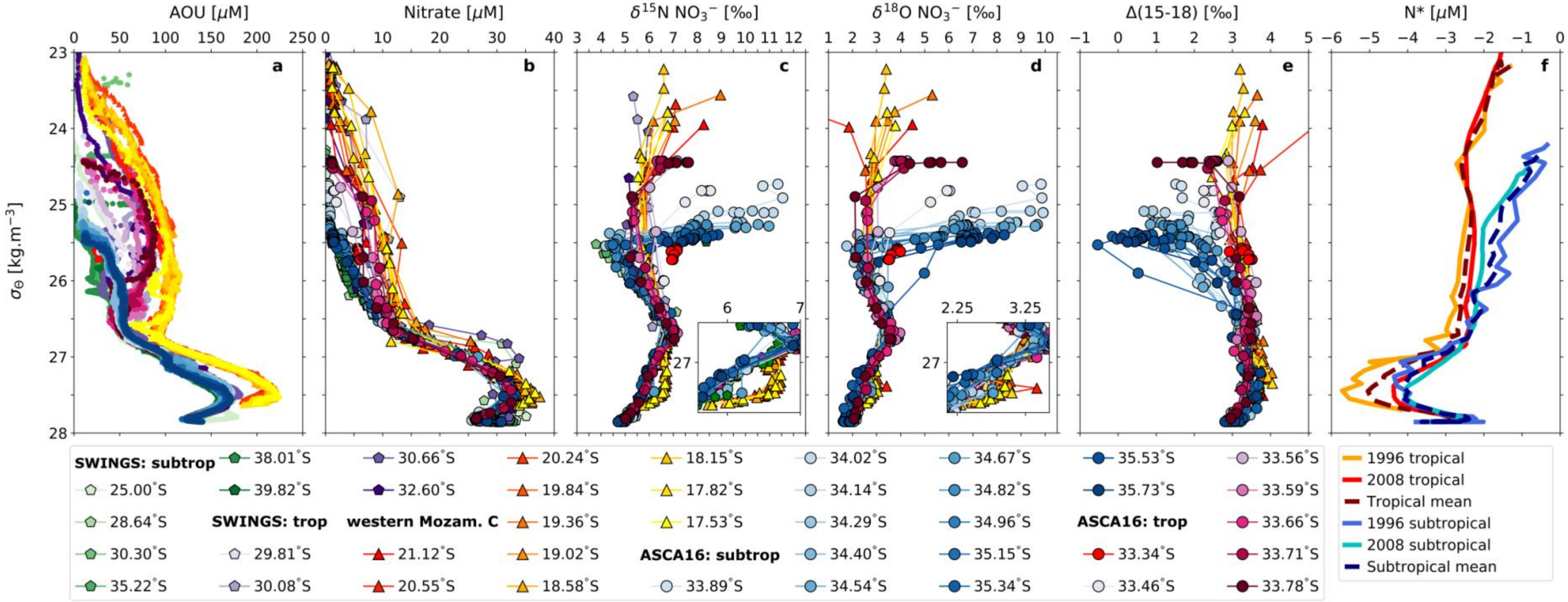

Figure 3.4. Biogeochemistry of the southwest Indian Ocean. Density profiles of **a**) apparent oxygen utilization (AOU) [μM], **b**) nitrate concentration [μM], **c**) nitrate δ^{15}N [‰], **d**) nitrate δ^{18}O [‰], **e**) nitrate Δ(15-18) [‰], and **f**) mean gridded N* [μM] (= $[NO_3^-] - 16 \times [PO_4^{3-}]$; (Gruber & Sarmiento, 1997)). The legend provides station latitude with subheadings indicating sample region. Subtropical and tropical SWINGS data are represented by green and purple pentagons, respectively, IIEO2 data are shown by the triangle symbols and represent the western Mozambique Channel, and subtropical and tropical ASCA16 data are represented by blue and pink circles, respectively. The AOU values are derived from measurements made during CTDO deployments and as such, are available at higher vertical resolution than the discrete measurements shown in panels **b**-**e**. The inset boxes in panels **c** and **d** provide a zoomed-in view of the intermediate waters. The N* data shown in panel **f** are from two occupations (1996 and 2008; solid lines) of WOCE IO6 line (near-meridional line at ~30°E). Tropical (subtropical) means for each cruise are shown in warm (cool) colours, with the inter-cruise means indicated by the dashed profile.

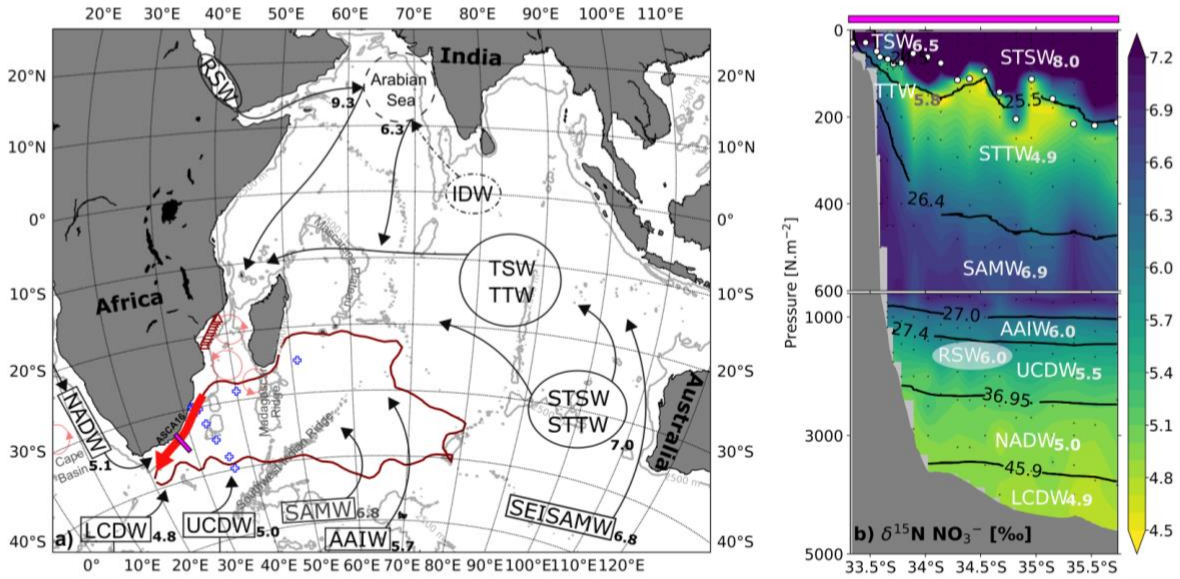

Figure 3.5. Source water circulation and modification in the southwest Indian Ocean. a) Schematic of the source regions and pathways followed by the water masses that enter the southwest Indian Ocean, along with their nitrate-δ^{15}N endmembers, and **b**) gridded full-depth section of nitrate δ^{15}N [‰] across the ASCA16 transect. On both panels, water mass abbreviations are as in Figure 3.3 and Table 3.1. The bold subscripted values indicate the mean nitrate δ^{15}N [‰] for each water mass, with the panel **b** values from ASCA16 (Table 3.1). In panel **a**, water masses formed within the Indian Ocean are outlined with ovals while water masses formed outside the basin are outlined with squares. The nitrate-δ^{15}N values, where available, are those measured either at formation or prior to entering the Agulhas Current (see section 3.1 for details). Nitrate δ^{15}N values are not provided for the (sub)tropical surface waters (i.e., σ_θ <25.5 kg.m^{-3}, or upper 50 to 100 m; Tables 3.1 and 3.2) at formation because repeated cycles of nitrate supply and assimilation in these waters alter their preformed δ^{15}N. As such, the nitrate δ^{15}N subscript associated with STSW/STTW is for Subtropical Thermocline Water only. Additionally, there are no nitrate-δ^{15}N data available for Tropical Thermocline Water at formation. Indian Deep Water (IDW) has a dot-dashed line to indicate that it forms throughout the north Indian Basin and not only at the location of the circle. The grey contours represent the bathymetry at 2500 m, with the Mascarene Plateau, Madagascar Ridge, Southwest Indian Ridge, and Cape Basin labeled in grey (data from the GEBCO Compilation Group (2022) GEBCO_2022 Grid (doi:10.5285/e0f0bb80-ab44-2739-e053-6c86abc0289c)). The thin black arrows approximate the pathways by which the water masses enter the southwest Indian Ocean. The thick red arrow indicates the Agulhas Current and the bold maroon contour encompasses the subtropical recirculation. Thin light-red circles indicate eddies in the Mozambique Channel, south of Madagascar, and in the Cape Basin. The pink line indicates the location of the ASCA16 transect, the open maroon triangles indicate the IIEO2 stations, and open blue pluses indicate the SWINGS stations. This panel is adapted from Beal et al. (2006), their Figure 3.5. In panel **b**, black contours indicate the isopycnal boundaries of water masses (see Table 3.1) and small white circles show the mixed layer depth. The white opaque oval represents a Red Sea Water lens, and the black dots indicate discrete sampling depths. The y-axis is broken at 600 m in order to adequately resolve both the upper- and deep water masses.

3.3.1.1. Deep waters

Four deep water masses occupy the southwest Indian Ocean; from deepest to shallowest these are Lower Circumpolar Deep Water (LCDW; σ_4 ≥45.9 kg.m^{-3}), North Atlantic Deep Water

(NADW; σ_2 = 36.9 kg.m^{-3} to σ_4 = 45.9 kg.m^{-3}), Indian Deep Water (IDW; σ_θ = 27.45 kg.m^{-3} to σ_4 = 45.9 kg.m^{-3}, with its core at σ_2 = ~37.0 kg.m^{-3}), and Upper Circumpolar Deep Water (UCDW; σ_θ = 27.4 kg.m^{-3} to σ_2 = 36.9 kg.m^{-3}) (Figure 3.3-5 and Table 3.1 and 3.2). These deep water masses exchange properties via the global overturning circulation. Following the mixing of NADW with IDW (as well as Pacific Deep Water) in the ocean interior, the deep waters upwell in the Southern Ocean to form Upper and Lower CDW, eventually circulating back to the northern basins to be incorporated into newly-forming deep waters (Talley, et al., 2011; Talley, 2013). Here, we identify the two limbs of CDW in the Agulhas Current for the first time.

NADW is formed by deep convection in the subarctic North Atlantic where it has a mean nitrate concentration of 17.5 μM and δ^{15}N of 4.8‰ (Sigman, et al., 2000; Marconi, et al., 2015). Its relatively low nitrate δ^{15}N derives from N_2 fixation in the (sub)tropical North Atlantic (Marconi, et al., 2015; Marconi, et al., 2017; Knapp, et al., 2008; Deman, et al., 2021). By the time NADW reaches the southwest Indian Ocean, its mean nitrate concentration has increased to 27.4 ± 0.8 μM and its δ^{15}N to 5.0 ± 0.0‰, similar to observations from the Cape Basin (26.0 μM and 5.1‰, respectively; (Campbell, 2016; Marconi, et al., 2017)). The higher nitrate concentration and δ^{15}N are likely due to NADW mixing with CDW during its southward transit towards the Southern Ocean.

IDW forms in the Indian basin through diapycnal diffusion and subsurface upwelling of NADW, Upper and Lower CDW, and deep North Indian basin waters (Talley, et al., 2011; Donohue & Toole, 2003; Talley, 2013). Deep waters from the North Indian basin carry a strong remineralization and denitrification signal that is reflected in their high AOU (>230 μM) and elevated nitrate δ^{15}N (mean of 6.3 ± 0.2‰) (Martin & Casciotti, 2017; Harms, et al., 2019). We observe IDW to the east of Madagascar in one profile from the SWINGS cruise (at 25°S) where AOU reaches 177.3 ± 0.4 μM and nitrate δ^{15}N is 5.4 ± 0.0‰. The eroded properties likely result from mixing with younger deep waters that have a lower nitrate δ^{15}N (Harms, et al., 2019). IDW is not found in the Agulhas Current and adjacent recirculating waters because the Mozambique and Madagascar Ridges block the south-westward flow of deep waters from the basin interior (Figure 3.5a).

Where LCDW upwells, typically at >60°S, it has a relatively low nitrate δ^{15}N of 4.8‰ and δ^{18}O of 1.8‰, reflecting a large contribution of low-δ^{15}N NADW nitrate (Sigman, et al., 1999; Smart, et al., 2015; Fripiat, et al., 2019). In the Agulhas Current region, LCDW nitrate is similarly characterised by a δ^{15}N of 4.9 ± 0.0‰ and δ^{18}O of 1.8 ± 0.1‰ owing to the proximity to its formation region in the Southern Ocean. Where UCDW upwells, at approximately 55°S-60°S, it has a relatively high AOU and nitrate concentration, and nitrate δ^{15}N of 5.0‰ and δ^{18}O of 2.1‰, reflecting contributions of both low-δ^{15}N NADW nitrate and high-δ^{15}N IDW and Pacific Deep Water nitrate (Sigman, et al., 1999; Talley, et al., 2011; Smart, et al., 2015; Fripiat, et al., 2019; Sigman, et al., 2000). In the Agulhas Current, the mean AOU and nitrate concentration in UCDW are 160.1 ± 7.6 μM and 30.7 ± 1.3 μM, respectively, and nitrate δ^{15}N and δ^{18}O are 5.5 ± 0.1‰ and 2.2 ± 0.1‰. The elevated nitrate δ^{15}N but similar δ^{18}O relative to UCDW at formation suggests the remineralisation of organic matter with a relatively high δ^{15}N in the Subantarctic Zone where UCDW directly underlies Subantarctic Surface Water (Fripiat, et al., 2019). In the western Mozambique Channel, the upper limit of UCDW has a slightly higher density than UCDW in the Agulhas Current (σ_2 = 36.6 kg.m^{-3} vs 36.5 kg.m^{-3}, the former being ~100 m deeper). In the channel, UCDW has a mean AOU, nitrate concentration, and nitrate δ^{15}N and δ^{18}O of 200.0 ± 8.1 μM, 34.6 ± 1.3 μM, 6.1 ± 0.1‰, and 2.5 ± 0.1‰, respectively. These values are higher than those measured for UCDW in the Agulhas Current, although we note that the Mozambique Channel samples were collected down to 1500 m only (σ_2 = 36.7 kg.m^{-3}). Regardless, the higher AOU, nitrate concentration and isotope ratios suggest that UCDW in the Mozambique Channel has mixed with the overlying intermediate waters, which carry remineralization and denitrification signals generated in the Arabian basin (see section 3.1.2). The presences of two overlying intermediate waters may also explain why UCDW in the channel occurs slightly deeper than in the Agulhas Current.

3.3.1.2. Intermediate waters

There are two intermediate water masses in the southwest Indian Ocean, Antarctic Intermediate Water (AAIW) and Red Sea Water (RSW), which occupy a similar density range (27.0 kg.m^{-3} < σ_θ < 27.4 kg.m^{-3}; (Toole & Warren, 1993; Beal, et al., 2006; Roman & Lutjeharms, 2007; Roman & Lutjeharms, 2009)). The stark differences in the salinity and AOU of AAIW and RSW evince their disparate formation histories (Figure 3.3-5; Table 3.1 and 3.2).

AAIW is formed in the Polar Frontal Zone (at approximately 50°S-55°S) where surface waters are relatively fresh (Reid, 2003; Talley, et al., 2011) and partial nitrate assimilation by phytoplankton produces relatively high δ^{15}N and δ^{18}O nitrate (Sigman, et al., 1999; Sigman, et al., 2000; Smart, et al., 2015). In the Indian sector of the Southern Ocean, AAIW has a nitrate concentration of 27.5 μM and δ^{15}N and δ^{18}O of 5.7‰ and 2.7‰, respectively (Fripiat, et al., 2019). This water mass enters the Indian basin at around 60°E, its northward passage aided by the bathymetry of the Southwest Indian ridge (Fine, 1993). AAIW circulates within the subtropical gyre and subsequently enters the Agulhas Current, primarily through recirculation of the subtropical waters and to a lesser extent, through the South East Madagascar Current and Mozambique Channel (Fine, 1993; Beal, et al., 2006). In the Agulhas Current and adjacent recirculating waters, mean AAIW salinity, nitrate concentration, and δ^{15}N and δ^{18}O are 34.6 ± 0.06 g.kg^{-1}, 28.3 ± 2.4 μM, 6.0 ± 0.1‰ and 2.6 ± 0.1‰, respectively. Thus, AAIW still bears the salinity minimum and high nitrate δ^{18}O imparted at formation, while its nitrate δ^{15}N is even higher. In the western Mozambique Channel, AAIW occupies a slightly lower and narrower density range (26.9 kg.m^{-3} < σ_θ < 27.1 kg.m^{-3}), sandwiched between two high-salinity and high-δ^{15}N nitrate water masses (Figure 3.3 and 3.4c inset). Here, its mean salinity, δ^{15}N, and δ^{18}O (of 34.9 ± 0.02 g.kg^{-1}, 6.6 ± 0.1‰, and 3.0 ± 0.1‰, respectively) are considerably higher than in AAIW at formation and slightly higher than in the Agulhas Current and adjacent recirculating waters, while its nitrate concentration is lower (24.6 ± 2.7 μM). The higher δ^{15}N of AAIW nitrate in the southwest Indian Ocean compared to at formation is likely due to both mixing with RSW (see below) and remineralization of high-δ^{15}N organic matter produced in the subtropical surface waters overlying equatorward-flowing AAIW. In the latter case, the high-δ^{15}N organic matter derives from complete consumption of mode-water nitrate that is higher in δ^{15}N than AAIW nitrate (Rafter, et al., 2013; Fripiat, et al., 2019).

RSW is formed by strong evaporation over the northwest Indian Red Sea, where salinity is 40 g.kg^{-1} (Bower, et al., 2000; Beal, et al., 2000). This water mass is thus discernible throughout the Indian Ocean by a relative salinity maximum (Talley, et al., 2011). RSW flows through the Arabian Sea oxygen deficient zone and upon exiting, carries the elevated nitrate δ^{15}N and δ^{18}O imparted by denitrification (mean of 9.3‰ and 7.9‰, respectively, at times reaching 16‰; Figure 3.5a), along with a strong remineralization signal (AOU >250 μM) (Brandes, et al., 1998; Gaye, et al., 2013; Martin & Casciotti, 2017). RSW enters the Agulhas Current primarily through the Mozambique Channel, with a purity of 30-40% and transport volume of 1.4 Sv (Roman & Lutjeharms, 2009), as well as via the South East Madagascar Current at a significantly reduced purity and volume (~15% and 0.3 Sv) (Roman & Lutjeharms, 2009; Donohue & Toole, 2003). In the western Mozambique Channel, RSW (σ_θ = 27.1 kg.m^{-3} to σ_2 = 36.6 kg.m^{-3}) is discernible by a salinity maximum of 35.0 ± 0.03 g.kg^{-1}, AOU of 204.3 ± 15.9 μM, nitrate concentration of 32.9 ± 2.8 μM, and nitrate δ^{15}N and δ^{18}O of 6.6 ± 0.1‰ and 2.9 ± 0.1‰, respectively. Downstream in the Agulhas Current, the distribution of RSW is patchy due to seasonally variable transport from the Red Sea and Mozambique Channel, and takes the form of lenses and filaments (Roman & Lutjeharms, 2009; Beal, et al., 2000).

In the western Mozambique Channel, RSW bears similarly elevated N and O isotope ratios to AAIW in the Agulhas Current (although generated through different mechanisms). However, we can identify RSW in the Agulhas Current because it occurs at a slightly higher density (i.e., deeper) than AAIW (σ_θ = 27.0-27.4 kg.m^{-3} versus 27.45-27.55 kg.m^{-3}), near-coincident with UCDW that has a lower nitrate δ^{15}N and δ^{18}O than RSW (Table 3.1, Figure 3.4 insets, 3.5b). Two RSW lenses are apparent in our dataset, represented by few discrete measurements (n=5 for the ASCA16 lens and n=2 for the SWINGS lens; B2), which is unsurprising given the reduced purity and volume expected for RSW in this region (Roman & Lutjeharms, 2009). The ASCA16 lens is located between 34.1°S and 34.7°S and is characterized by a salinity of 34.7 ± 0.03 g.kg^{-1}, AOU of 164.3 ± 5.2 μM, nitrate concentration of 32.2 ± 0.3 μM, and nitrate δ^{15}N and δ^{18}O of 6.0 ± 0.0‰ and 2.6 ± 0.1‰, respectively (Table B1), while the SWINGS lens is located between 30.30°S and 30.66°S and has a salinity of 34.8 ± 0.03 g.kg^{-1}, AOU of 172.4 ± 7.5 μM, nitrate concentration of 31.6 ± 2.4 μM, and nitrate δ^{15}N of 5.9 ± 0.1‰ (Table B2).

The nitrate isotope ratios provide a means of identifying and quantifying RSW in the Agulhas Current since the δ^{15}N (and δ^{18}O) of RSW nitrate is elevated relative to that of UCDW, by 0.4-0.5‰ (and by 0.4‰) (Table 3.1 and Figure 3.4 inset). Using a two-endmember mixing model, we can estimate the fraction (i.e., purity) of RSW in the Agulhas Current lenses, which together have a mean nitrate δ^{15}N of 5.9 ± 0.1‰. We set the δ^{15}N of the first endmember to the mean RSW nitrate δ^{15}N of 9.3 ± 0.3‰ measured in the Arabian Sea (Martin & Casciotti, 2017), while the second endmember is the δ^{15}N of UCDW nitrate at formation (5.0 ± 0.0‰; (Smart, et al., 2015; Fripiat, et al., 2019)). By mixing these two endmembers, we estimate the fraction of RSW in the Agulhas Current lenses to be approximately 21%. This value is consistent with the 10-20% purity estimated previously for RSW in the Agulhas Current and adjacent waters using an optimum multi-parameter analysis that considered 15 datasets from the region and required seven input variables (Roman & Lutjeharms, 2009).

3.3.1.3. Sub-thermocline waters

Subantarctic Mode Water (SAMW; σ_θ = 26.4-27.0 kg.m^{-3}) is formed in the deep winter mixed layers north of the Subantarctic Front (approximately 45°S-50°S) and records partial phytoplankton nitrate assimilation in its isotope ratios, similar to AAIW (Sigman, et al., 1999; Sigman, et al., 2000; DiFiore, et al., 2006; Fripiat, et al., 2021; Rafter, et al., 2013). SAMW subducts and flows northwards in the interior of the subtropical gyres to eventually supply nutrients to most of the global ocean thermocline (Sarmiento, et al., 2004; Fripiat, et al., 2021).

Two types of SAMW occur in the South Indian Ocean: 1) SAMW that last ventilated west of 70°E (i.e., west of the Kerguelen Plateau) with a core density of 26.5 kg.m^{-3}, and 2) Southeast Indian SAMW (SEISAMW) that last ventilated east of the Kerguelen Plateau and has a higher core density of 26.8 kg.m^{-3} (McCartney, 1982; Fine, 1993; Wong, 2005; Koch-Larrouy, et al., 2010; Herraiz-Borreguero & Rintoul, 2011). Both SAMW types can be reventilated through interaction with the base of the relatively deep winter mixed layers that occur in the southern reaches of the subtropical gyre, before circulating anticyclonically through the South Indian basin (Wong, 2005; Koch-Larrouy, et al., 2010; Lu, et al., 2021).

In the eastern Indian sector of the Southern Ocean (i.e., in the region where SEISAMW forms), nitrate δ^{15}N is 6.8‰ and δ^{18}O is 3.9‰ (Figure 3.5a; (Fripiat, et al., 2019)). There are currently no nitrate isotope measurements of SAMW formed west of 70°E yet both types of SAMW reach the southwest Indian Ocean. SEISAMW is thought to enter via a longer route through the Mozambique Channel and South East Madagascar Current while SAMW, formed more locally, enters through the subtropical recirculation (Talley, et al., 2011; Toole & Warren, 1993; Donohue & Toole, 2003; Beal, et al., 2006). The SAMW in the western Mozambique Channel is thus likely SEISAMW, with a mean AOU of 94.3 ± 4.6 μM and nitrate δ^{15}N and δ^{18}O of 6.8 ± 0.2‰ and 3.3 ± 0.2‰, respectively. In the Agulhas Current and adjacent recirculating waters, the SAMW is likely more locally formed, with a lower mean AOU (57.4 ± 4.4 μM), near-indistinguishable nitrate δ^{15}N (6.9 ± 0.1‰), and slightly higher nitrate δ^{18}O (3.5 ± 0.1‰) than SEISAMW in the western Mozambique Channel (Figure 3.3; Table 3.1). The higher AOU and lower nitrate δ^{18}O of SEISAMW in the channel evince a larger remineralization signal (i.e., more nitrification) than in the downstream Agulhas waters. This observation corroborates previous work suggesting that due to differences in circulation, SEISAMW in the western Mozambique Channel is older (i.e., has had more time to accumulate the products of remineralization) than SAMW directly supplied to the subtropical recirculation and subsequently, the Agulhas Current (Fine, 1993; Beal, et al., 2006; Fine, et al., 2008; Wong, 2005; Koch-Larrouy, et al., 2010). In our ASCA16 dataset, SAMW is apparent at the shallow shelf station (latitude = 33.34°S; red circles in Figure 3.4) in the high mean shelf nitrate δ^{15}N and δ^{18}O of 7.0‰ and 3.7‰ (Δ(15-18) = 3.4‰), likely due to inshore upwelling (Leber, et al., 2017; Russo, et al., 2019).

3.3.1.4. Thermocline and surface waters

Thermocline waters: We identify two thermocline waters in the southwest Indian Ocean, Tropical Thermocline Water (TTW; σ_θ = 24.5-26.4 kg.m^{-3}) and Subtropical Thermocline Water

(STTW; σ_θ = 25.5-26.4 kg.m^{-3}). These waters occupy a similar density range but have different formation histories, making them easily distinguishable by salinity and AOU, as well as by their physical partitioning across the Agulhas Current core (Figure 3-5; Table 3.1; (Beal, et al., 2006)). TTW underlies Tropical Surface Water (TSW; σ_θ <24.5 kg.m^{-3}), with both water masses forming in the warm, fresh tropical latitudes (approximately 5-25°S) where precipitation exceeds evaporation and fresh Indonesian Through Flow waters are supplied by the South Equatorial Current (SEC; Figure 3.1) (Wyrtki, 1971; Gordon, et al., 1997; Gordon, 1987). STTW underlies Subtropical Surface Water (STSW; σ_θ <25.5 kg.m^{-3}), with both water masses forming in the more saline subtropical gyre (25-35°S, east of 90°E) where evaporation exceeds precipitation (Wyrtki, 1971; Gordon, 1987; Beal, et al., 2006). TTW is thus a comparatively fresh thermocline water mass (salinity of 35.4-35.6 g.kg^{-1}) compared to its subtropical counterpart (salinity >35.7 g.kg^{-1}) (Figure 3.2a and 3.3).

TTW is the only thermocline water mass in the western Mozambique Channel, with a salinity of 35.5 ± 0.05 g.kg^{-1}, AOU of 99.7 ± 10.1 μM, nitrate concentration of 10.9 ± 2.2 μM, and nitrate δ^{15}N and δ^{18}O of 6.0 ± 0.4‰ and 2.8 ± 0.4‰, respectively (Figure 3.3 and 3.4, Table 3.2). By the time TTW reaches the Agulhas Current, it is constrained to the inshore side of the current core (Figure 3.2). Here, it is slightly more saline (mean salinity of 35.6 ± 0.05 g.kg^{-1}), has a lower AOU and nitrate concentration (73.4 ± 13.6 μM and 7.8 ± 1.8 μM), and slightly lower nitrate δ^{15}N and δ^{18}O (5.8 ± 0.3‰ and 2.7 ± 0.4‰) than in the western Mozambique Channel, likely due to lateral entrainment of subtropical water by Mozambique Channel eddies as they propagate southwards. At formation, the nitrate δ^{15}N of STTW is 7.0 ± 0.1‰ and its δ^{18}O is 4.5 ± 0.1‰ (Figure 3.1 and 3.5a; (Sigman & Fripiat, 2019)). STTW enters the Agulhas Current through the subtropical gyre recirculation where it has a mean salinity of 35.7 ± 0.03 g.kg^{-1}, AOU of 28.3 ± 11.3 μM, and nitrate concentration of 3.0 ± 1.4 μM (Table 3.1). Its mean nitrate δ^{15}N and δ^{18}O of 4.9 ± 0.7‰ and 2.8 ± 0.8‰, respectively, are lower than at formation. Indeed, both thermocline waters have a lower nitrate δ^{15}N than their upstream endmembers and the underlying SAMW, suggesting local remineralization of low-δ^{15}N organic matter. This thermocline signal is similarly observed in summer (i.e., SWINGS and B4). STTW nitrate δ^{15}N is on average lower than that of TTW, 4.9‰ versus 5.8‰ (5.1‰ versus 6.2‰ for the SWINGS dataset), reaching a minimum of 4.2‰ versus 5.2‰. Thus, in the Agulhas Current, TTW is biogeochemically different from STTW and is characterized by a higher AOU, nitrate concentration, and nitrate δ^{15}N.

Surface waters: At formation, TSW (σ_θ <24.5 kg.m^{-3}) is particularly fresh (salinity <35.0 g.kg^{-1}). During the westward transit of TSW to the Mozambique Channel, the incorporation of Arabian Sea surface waters increase its salinity, such that in the western channel, TSW is characterized by salinities ≥35.3 g.kg^{-1} (mean of 35.4 ± 0.05 g.kg^{-1}; Figure 3.3 and Table 3.2) (Donohue & Toole, 2003; DiMarco, et al., 2002; Wyrtki, 1971). TSW salinity is further increased to 35.6 ± 0.51 g.kg^{-1} inshore of the Agulhas Current (Figure 3.3 and Table 3.1), likely also due to the lateral entrainment of more saline STSW by southward propagating Mozambique Channel eddies. STSW (σ_θ <25.5 kg.m^{-3}) is transported into the Agulhas Current via the subtropical gyre recirculation (Gründlingh, et al., 1991; DiMarco, et al., 2002). In the Agulhas Current and adjacent recirculating waters, STSW has a relatively high salinity (mean of 35.7 ± 0.03 g.kg^{-1}) compared to TSW. Both TSW and STSW have a relatively low nitrate concentration of ~1.0 μM and elevated nitrate δ^{15}N and δ^{18}O, of >6.5‰ and >4.0‰, respectively, reaching values as high as 11.5‰ and 9.9‰ (Figure 3.3 and 3.4), due to photosynthetic nitrate assimilation (Sigman, et al., 1999; Granger, et al., 2004; Granger, et al., 2010). The depth of the mixed layer, defined by vertical gradients in density and nitrate concentration (Figure 3.2), is largely coincident with the boundary of the surface waters (Figure 3.2b and 3.5b).

3.4. Discussion

We discuss the implications of the nitrate isotope distributions in the upper southwest Indian Ocean (σ_θ <26.4 kg.m^{-3} or shallower than 500 m) in detail below. The southwestern region of the subtropical gyre (20-70°E) is characterized by highly retentive thermocline circulation that is largely dominated by waters from the Agulhas Return Current and is sometimes referred to as the southwest Indian subgyre (Figure 3.1; (Stramma & Lutjeharms, 1997; Lutjeharms & Ansorge, 2001; Grand, et al., 2015c; Ridgway & Dunn, 2007)). Hereafter, we will refer to the Agulhas Current (tropical and subtropical waters) and adjacent recirculating (subtropical) waters collectively as the “greater Agulhas region” (i.e., all stations sampled during ASCA16 and SWINGS).

3.4.1. Nitrogen cycling in the thermocline and mixed layer of the greater Agulhas region

Across the greater Agulhas region, upper thermocline and mixed-layer nitrate Δ(15-18) is low relative to underlying SAMW (Figure 3.4e). Above σ_θ = 26.0 kg.m^{-3}, mean nitrate Δ(15-18) is 1.6‰, reaching as low as -0.5‰, while SAMW nitrate Δ(15-18) is 3.4‰. Two processes can cause the Δ(15-18) of nitrate to decrease. The first is N_2 fixation, which lowers the δ^{15}N of thermocline nitrate more than its $\delta^{18}O$ through the introduction of low-$\delta^{15}N$ (i.e., ~ -1‰) organic matter (Hoering & Ford, 1960; Minagawa & Wada, 1986; Carpenter, et al., 1997). The nitrate generated from the remineralization and nitrification of this newly-fixed organic matter is similarly low in $\delta^{15}N$ while its $\delta^{18}O$, which is set by $\delta^{18}O_{H2O}$ (equal to ~0‰) plus an isotopic offset, is ≥1.1‰ (Rafter, et al., 2013; Knapp, et al., 2008; Sigman, et al., 2005; Lehmann, et al., 2018; Fawcett, et al., 2015; Sigman, et al., 2009a; Marconi, et al., 2019). The second process is partial nitrate assimilation occurring in the same water parcel as nitrification (Fawcett, et al., 2015; Deman, et al., 2021; Smart, et al., 2015; Wankel, et al., 2007). These co-occurring processes generate nitrate that is high in $\delta^{18}O$ relative to that initially removed by phytoplankton but leave nitrate $\delta^{15}N$ unchanged (since in net, N is neither gained nor lost from the water parcel; (Sigman, et al., 2005; Sigman, et al., 2009a; Rafter, et al., 2013; Fawcett, et al., 2015)). The signal of coupled nitrate assimilation and nitrification can be generated in situ (i.e., nitrate assimilation and nitrification co-occurring at the base of the euphotic zone; (Fawcett, et al., 2015)) or as a result of partial nitrate assimilation in surface waters that then subduct and flow laterally along subsurface isopycnals where nitrification occurs (Deman, et al., 2021; Fawcett, et al., 2018). While both N_2 fixation and co-occurring nitrate assimilation and nitrification decrease the $\Delta(15\text{-}18)$ of nitrate, N_2 fixation also lowers its $\delta^{15}N$ (Figure 3.6a versus 3.6b).

3.4.1.1. Drivers of the low nitrate Δ(15-18) in the upper thermocline

Thermocline nitrate $\delta^{15}N$ across the greater Agulhas region, which ranges from 4.2‰ to 5.5‰, is low relative to sub-thermocline SAMW ($\delta^{15}N$ of 6.9‰), while its $\delta^{18}O$ ranges from 2‰ to 3‰ (also lower than the mean SAMW $\delta^{18}O$ of 3.5‰, but not to the same degree as the $\delta^{15}N$) (Figure 3.4c-d). As a result, nitrate $\Delta(15\text{-}18)$ decreases from 3.4 ± 0.1‰ in SAMW to a mean of 3.2 ± 0.3‰ in TTW and 2.1 ± 0.8‰ in STTW, reaching a minimum of -0.5‰ (Figure 3.4e and Table 3.1). The general coincidence of low-$\delta^{15}N$ and low-$\Delta(15\text{-}18)$ nitrate can be explained by N_2 fixation (Sigman, et al., 2005; Knapp, et al., 2008; Rafter, et al., 2013; Lehmann, et al., 2018). Since the dual isotopes of SAMW nitrate are both elevated and N_2 fixation lowers nitrate $\delta^{15}N$ more than its $\delta^{18}O$, the addition of newly-fixed nitrate to the Agulhas thermocline will drive the nitrate data above the 1:1 line in a plot of $\delta^{18}O$ versus $\delta^{15}N$ (i.e., toward a lower $\Delta(15\text{-}18)$; Figure 3.6a). This trend is evident in the subtropical thermocline between $\sigma_\theta = 25.5$ kg.m^{-3} and 26.4 kg.m^{-3} and in the tropical thermocline between $\sigma_\theta = 24.5$ kg.m^{-3} and 26.4 kg.m^{-3} (orange arrow in Figure 3.6c).

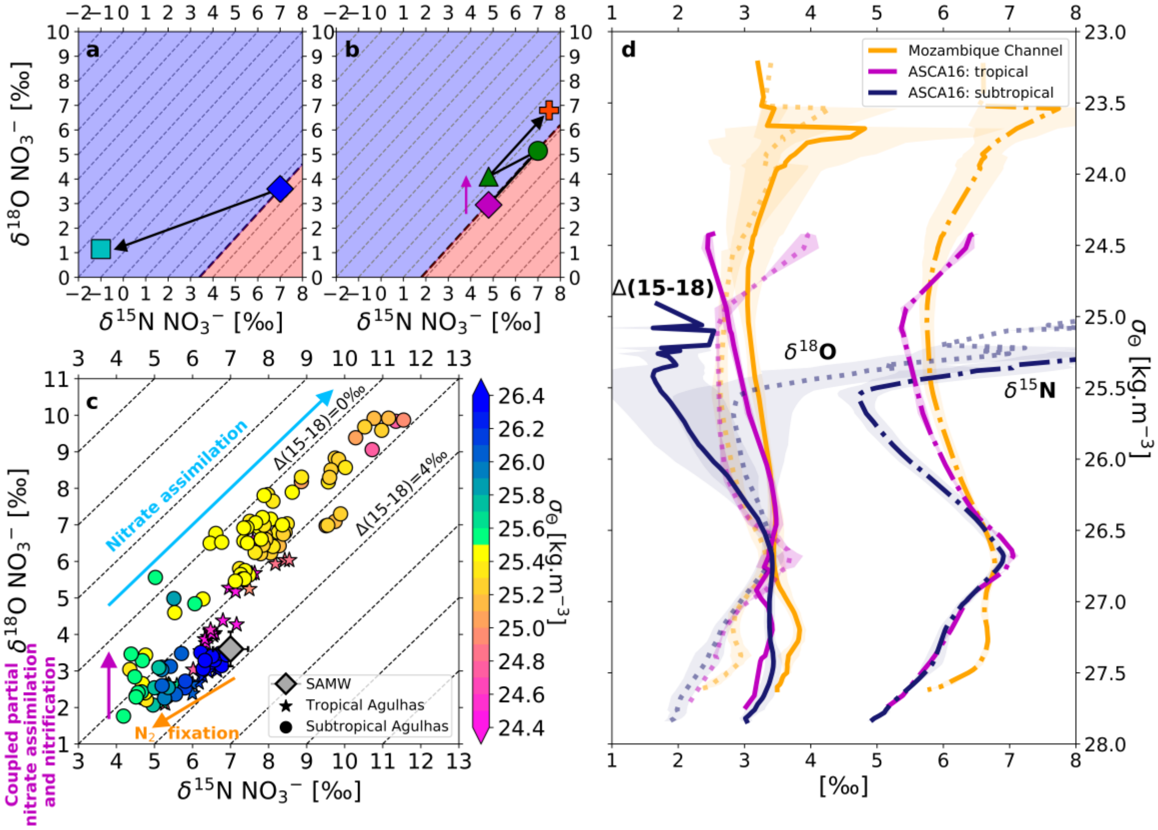

Figure 3.6. Coupled N and O isotope dynamics in the greater Agulhas region. Panels **a**, **b**, and **c** show nitrate δ^{18}O versus δ^{15}N [‰], with dashed diagonal contours indicating nitrate Δ(15-18) [‰]. Panel **a** shows how N_2 fixation lowers thermocline nitrate δ^{15}N more than its δ^{18}O, thereby lowering Δ(15-18). Panel **b** shows how in net, coupled partial nitrate assimilation (magenta diamond to green circle) and nitrification (green circle to green triangle) cause the δ^{18}O of nitrate to rise while its δ^{15}N remains unchanged (net effect indicated by the vertical magenta arrow). This mechanism lowers the Δ(15-18) of nitrate at the base of the greater Agulhas region mixed layer and when that nitrate is subsequently assimilated in surface waters (green triangle to red plus), its Δ(15-18) remains unchanged (i.e., low) even as its δ^{15}N and δ^{18}O rise. In panels **a** and **b**, the blue shading indicates values of nitrate Δ(15-18) that are lower than the source nitrate while the red shading indicates higher nitrate Δ(15-18). Panel **c** shows the ASCA16 data coloured by potential density (σ_θ) [kg.m^{-3}] with arrows and text indicating the effect on the nitrate isotope ratios of the various processes outlined above and discussed in the text. The grey diamond indicates the mean, concentration-weighted δ^{18}O and δ^{15}N of SAMW with propagated error shown by the capped bars. Panel **d** shows mean density profiles of nitrate δ^{15}N (dash-dotted line), δ^{18}O (opaque dotted line), and Δ(15-18) (solid line) [‰], with ± 1 SD represented by the opaque shading. The profile colours indicate the regions from which the data were collected (see legend), with the Mozambique Channel data included to represent the tropical endmember to the Agulhas Current.

Upper thermocline nitrate Δ(15-18) continues to decline towards the base of the mixed layer, which broadly coincides with the 25.5 kg.m^{-3} and 24.5 kg.m^{-3} isopycnals for subtropical and tropical waters, respectively (Figure 3.4e and 3.6c). Here, subtropical water nitrate δ^{18}O rises by ~1.5‰ while its δ^{15}N remains relatively constant between 4.5‰ and 5.0‰ (mean of 4.8 ±

0.3‰). Nitrate Δ(15-18) thus decreases from 2.1 ± 0.5‰ to <0‰ (Figure 3.6c). Analogously, tropical water nitrate Δ(15-18) declines from 3.2 ± 0.3‰ to <2‰. A similar trend was observed at the Bermuda Atlantic Time-series Study (BATS) site where a 3.4‰ rise in nitrate δ^{18}O below the euphotic zone coincident with little change in nitrate δ^{15}N was explained by partial nitrate assimilation and nitrification mainly co-occurring in situ (Fawcett, et al., 2015). We similarly attribute the low nitrate Δ(15-18) at the base of mixed layer in the greater Agulhas region to these co-occurring processes. The coincidence of partial nitrate assimilation and nitrification will drive shallow nitrate vertically above thermocline nitrate in δ^{18}O versus δ^{15}N space (i.e., above the 1:1 line and towards lower Δ(15-18); purple diamond to green triangle in Figure 3.6b and purple arrows in Figure 3.6b and c). The signal is likely generated predominantly in situ, akin to at BATS, with some portion possibly transported from the Subantarctic Southern Ocean (i.e., partial nitrate assimilation in Subantarctic surface waters followed by nitrification that occurs once these waters subduct and flow northwards). The combination of (i) partial nitrate assimilation and nitrification at the base of the mixed layer and (ii) the introduction of newly-fixed nitrate into the thermocline following surface N_2 fixation will vertically decouple the mean nitrate δ^{15}N minimum (deeper) from the mean nitrate Δ(15-18) minimum (shallower), as we observe (Figure 3.6d).

3.4.1.2. Phytoplankton nitrate assimilation dominates the mixed layer nitrogen cycle

In the mixed layer of the greater Agulhas region, the linear relationship of δ^{18}O and δ^{15}N yields an approximately invariant Δ(15-18) that averages 1.2 ± 0.5‰ (green triangle to red cross in Figure 3.6b; blue arrow in Figure 3.6c). This pattern indicates that assimilation by phytoplankton is the dominant process acting on the surface nitrate pool (Granger, et al., 2004; Granger, et al., 2010; Rohde, et al., 2015; Fawcett, et al., 2015). The near-invariant nitrate Δ(15-18) also shows that nitrification does not occur in surface waters at significant rates during winter relative to the upward supply of subsurface nitrate (Fawcett, et al., 2015; Peng, et al., 2018; DiFiore, et al., 2009). A similar condition is expected in spring through autumn when the mixed layer shoals and receives more light, which can directly inhibit nitrification (Olson, 1981; Merbt, et al., 2012) and will favour the growth of phytoplankton that outcompete nitrifiers for ammonium (Ward, 1985; Smith, et al., 2014). Since nitrate produced by mixed layer nitrification constitutes a regenerated rather than a new source of N to phytoplankton (Dugdale & Goering, 1967; Yool, et al., 2007), its restriction to the waters below the mixed layer implies that the combined rate of nitrate assimilation and N_2 fixation can be used to approximate carbon export from Agulhas surface waters.

3.4.2. N_2 fixation in the South Indian Ocean

3.4.2.1. Evidence of N_2 fixation in the greater Agulhas region

We attribute the low $\delta^{15}N$ of thermocline nitrate across the greater Agulhas region to N_2 fixation. However, this signal could theoretically derive from three other processes. The first is the deposition of atmospheric N, which is generally low in $\delta^{15}N$ (-14 to 2‰; (Altieri, et al., 2021)). However, the mean modelled N deposition rate over the southwest Indian Ocean of 0.14 g $N.m^{-2}.a^{-1}$ (Okin, et al., 2011; Somes, et al., 2016; Jickells, et al., 2017) is on average far too low to account for the low $\delta^{15}N$ of its thermocline nitrate (B5).

The second process that could decrease thermocline nitrate $\delta^{15}N$ is the lateral advection of high-$\delta^{15}N$ nitrate and/or dissolved organic N (DON) out of the greater Agulhas region while low-$\delta^{15}N$ organic matter is retained and remineralised in the thermocline (Rafter, et al., 2013; Lehmann, et al., 2018). However, inorganic N is the primary limiting nutrient in Agulhas surface waters, such that any nitrate supplied to the mixed layer should be rapidly consumed by phytoplankton, leaving little opportunity for partially-assimilated, high-$\delta^{15}N$ nitrate to be advected away. Additionally, there is no discernible surface gradient in the DON concentration across the greater Agulhas region (Letscher, et al., 2013), implying that significant lateral advection of DON (regardless of its $\delta^{15}N$, which is unknown) is unlikely. Furthermore, the tendency of the anticyclonic subgyre is to retain and downwell its shallow waters, such that even if nitrate were left unconsumed for a short period and/or high-$\delta^{15}N$ DON were produced, neither N species is likely to be transported out of the greater Agulhas region at significant rates.

The third process that could decrease thermocline nitrate $\delta^{15}N$ involves isotope fractionation during DON degradation. Shallow DON $\delta^{15}N$ profiles from some oligotrophic regions suggest preferential remineralisation of ^{14}N during DON degradation (Knapp, et al., 2018; Zhang, et al., 2020), which could contribute low-$\delta^{15}N$ N to the thermocline (Zhang, et al., 2020). The vertical gradients in the (limited) existing DON $\delta^{15}N$ data are variable and inconsistent however ((Zhang, et al., 2020) and references therein), making estimates of the DON degradation isotope effect uncertain. Nevertheless, the thermocline nitrate-$\delta^{15}N$ minimum observed in the shallowest subsurface (i.e. below the euphotic zone) in many oligotrophic regions is typically held within the low concentration of nitrate that characterizes the top of the nitracline (Figure 3.4b and c). Accordingly, even a relatively small quantity (~1-2 μM) of DON-derived low-$\delta^{15}N$ N, if produced with an isotope effect of ~5‰ (Zhang, et al., 2020), could be important in the shallowest component of the nitrate-$\delta^{15}N$ minimum. However, below the top of the nitracline where the nitrate concentrations rapidly increase with depth, DON degradation is too small of a nitrate source to explain the still-low thermocline nitrate δ^{15}N. N_2 fixation must therefore play a dominant role in decreasing the δ^{15}N of thermocline nitrate. One complementary source of support for this interpretation comes from paleoceanographic records. Foraminifera-bound N isotope measurements suggest that, in both the North Atlantic and the South China Sea, the shallow thermocline nitrate δ^{15}N minimum has undergone proportionally large changes over glacial cycles; such changes are consistent with N_2 fixation, not isotope fractionation during organic N degradation, as the origin of the δ^{15}N minimum (Ren, et al., 2009; Straub, et al., 2013; Ren, et al., 2017). In any case, future work will pursue the role of DON in the greater Agulhas region.

A final consideration is that in subtropical waters, low-δ^{15}N N also resides in the suspended particulate organic nitrogen (PON) pool (Altabet, 1988; Knapp, et al., 2005; Knapp, et al., 2011). Suspended PON can be mixed down into the shallow subsurface where it will be remineralized to low-δ^{15}N nitrate, potentially lowering the δ^{15}N of the thermocline nitrate pool. However, suspended PON represents a very small fraction of the total N pool (Fawcett, et al., 2011) and thus has little capacity to change the δ^{15}N of subsurface nitrate (Knapp, et al., 2005; Zhang, et al., 2020).

Our conclusion that N_2 fixation occurs locally in the greater Agulhas region is consistent with previous observations. First, diazotrophs have been observed during the late-summer bloom that occurs irregularly to the southeast of Madagascar (Poulton, et al., 2009), as well as within and south of the Mozambique Channel (Huggett & Kyewalyanga, 2017; Karlusich, et al., 2021), with surface N_2 fixation rates of 2-18 nM.d^{-1} measured southeast of Madagascar during the most recent (2020) late-summer bloom (Metzl, et al., 2022). Second, one third of the thermocline nitrate at the north-eastern edge of the greater Agulhas region (~23°S, 70°E; Figure 3.1) has previously been estimated to be newly-fixed based on subsurface nutrient N:P ratios (Harms, et al., 2019). Here, the δ^{15}N of thermocline nitrate, which was measured to average 5.2 ± 1.1‰, and the mean AOU and nitrate concentrations of 27.9 ± 10.5 μM and 1.6 ± 1.3 μM, respectively, are remarkably similar to those of STTW in our datasets (Table 3.1) (Harms, et al., 2019), strongly suggesting that newly-fixed nitrate is retained in the greater Agulhas region. Third, the mean N* (= $[NO_3^-] - 16 \times [PO_4^{3-}]$; (Gruber & Sarmiento, 1997)) of -2.0 ± 0.5 μM in the Agulhas thermocline (N* in TTW = -2.3 ± 0.3 μM and in STTW = -1.8 ± 0.4 μM) is higher than that in underlying SAMW (mean N* of -2.7 ± 0.4 μM; data from WOCE IO6; Figure 3.4f), consistent with the addition of N in stoichiometric excess of phosphorus (P), which is characteristic of N_2 fixation (Marconi, et al., 2017; Marshall, et al., 2022; Deutsch, et al., 2007). Importantly, a comparison of the 0-100 m vertical gradient in dissolved organic P recently measured in the greater Agulhas region (Liang, et al., 2022) with that of DON from other regions (0.06-0.08 μM versus 0.5-1 μM; (Zhang, et al., 2020) and references therein) suggests that dissolved organic matter degradation occurs at or below the Redfield ratio (i.e., <16:1). As such, N_2 fixation must be the dominant cause of the elevated N* in the thermocline of the greater Agulhas region even if DON degradation contributes to lowering its nitrate δ^{15}N.

3.4.2.3. Quantifying local N_2 fixation in the greater Agulhas region

We use a one-box model to provide two estimates of the local newly-fixed nitrate flux. Our approach incorporates the flux of nutrients, sinking organic matter, and N isotope ratios into and out of the upper waters (i.e., upper 400 m, which approximately includes the surface and thermocline waters) of the greater Agulhas region. The one-box model is governed by four steady-state equations (Eq. 3.1-4) (Figure 3.7). Eq. 3.1 expresses the water volume fluxes in Sv, with the tropical and subtropical source endmembers denoted as $_{\text{Trop}}$ and $_{\text{Subtrop}}$, and the flux out of the greater Agulhas region denoted as $_{\text{Agulhas}}$. Eqs. 3.2 to 3.4 express the P, N, and δ^{15}N fluxes into and out of the upper Agulhas waters, and include the organic matter sinking fluxes ($_{\text{Sinking}}$; in mmol.m^{-2}.a^{-1}) out of the base of the thermocline at 400 m. The sinking fluxes are independent of the water volume fluxes. Eq. 3.3 and 3.4 additionally include a newly-fixed nitrate flux (denoted as $_{\text{Newly-fixed}}$), which is also independent of the water volume fluxes.

First, we assume that the water volume fluxes into and out of the greater Agulhas region are in steady-state, at least over the residence time of the thermocline (Eq. 3.1). While this residence time is uncertain, proxies for water mass age suggest that the thermocline waters are between two and six years old (Fine, et al., 2008; McDonagh, et al., 2005; Karstensen & Tomczak, 1997); we use a conservative thermocline residence time of four years (i.e., since Agulhas thermocline waters are older than two and younger than six years, the maximum possible residence time is four years (Fine, et al., 2008)). The volume of the upper Agulhas region is estimated by multiplying the surface area, taken to be the highly retentive region within the 18 m climatological dynamic height contour (Figure 3.1) of 7.3×10^{12} m^2, by the depth of the base of the thermocline (i.e., 400 m). The volume flux out of the upper Agulhas region is then computed by dividing its volume by the thermocline residence time (= 23.2 Sv) (Eq. 3.1a). There are no estimates of the relative contributions of the source waters to the greater Agulhas region, so we use the proportions available for the Agulhas Current. The Mozambique Channel supplies only Tropical waters, contributing 22% ± 5% of the Agulhas waters (Ridderinkhof, et al., 2010; Beal, et al., 2015). The South East Madagascar Current contributes largely Subtropical waters, although ~20% of these waters derive from the northern/tropical Indian Ocean (Roman & Lutjeharms, 2009). We therefore assign 20% of the 24% ± 12% that the South East Madagascar Current contributes to the Agulhas waters (Ponsoni, et al., 2016; Beal, et al., 2015) to Tropical waters and the remaining 80% to Subtropical waters. The subtropical recirculation supplies only Subtropical waters and contributes the remaining 54% ± 17% to the Agulhas waters (Ridderinkhof, et al., 2010; Beal, et al., 2015; Ponsoni, et al., 2016). In sum, the greater Agulhas region comprises 26.8% ± 6% Tropical waters (22% + 4.8%) and 73.2% ± 21% Subtropical waters (54% + 19.2%). The Tropical source water flux into the Agulhas region (Eq. 3.1b) is thus 6.2 ± 1.4 Sv and the Subtropical source water flux (Eq. 3.1c) is 17.0 ± 4.9 Sv (grey values in Figure 3.7).

$$\text{Volume flux}_{\text{Agulhas}} = \text{Volume flux}_{\text{Trop}} + \text{Volume flux}_{\text{Subtrop}} \tag{3.1}$$

$$\text{Volume flux}_{\text{Agulhas}} = (\text{Area}_{\text{Agulhas}} \times \text{Thermocline depth}_{\text{Agulhas}}) \div \text{Thermocline residence time}_{\text{Agulhas}} \tag{3.1a}$$

$$\text{Volume flux}_{\text{Trop}} = (26.8\% \times \text{Volume flux}_{\text{Agulhas}}) \tag{3.1b}$$

$$\text{Volume flux}_{\text{Subtrop}} = (73.2\% \times \text{Volume flux}_{\text{Agulhas}}) \tag{3.1c}$$

Second, we balance the P fluxes into and out of the upper Agulhas region (Eq. 3.2). We multiply the mean phosphate concentrations measured in the Agulhas region and the Tropical and Subtropical source regions by their respective volume fluxes (Eq. 3.1) and then solve for the flux of organic P out of the base of the thermocline. We use phosphate concentration data from three WOCE transects that sampled the endmember regions (small grey circles in Figure 1; B6). The mean phosphate concentration measured in the greater Agulhas region (IO6) is 0.54 ± 0.3 μM, at the Tropical source (IO4) is 0.60 ± 0.3 μM, and at the Subtropical source (IO8) is 0.59 ± 0.3 μM. The resulting phosphate flux for the Agulhas water is 54.0 mmol.m^{-2}.a^{-1} (Eq. 3.2a), for the Tropical water is 16.1 mmol.m^{-2}.a^{-1} (Eq. 3.2b), and for the Subtropical water is 43.2 mmol.m^{-2}.a^{-1} (Eq. 3.2c). Using these values, we calculate an organic P sinking flux of 5.3 mmol P.m^{-2}.a^{-1} (pink values in Figure 3.7).

$$\text{Phosphate flux}_{\text{Trop}} + \text{Phosphate flux}_{\text{Subtrop}} = \text{Phosphate flux}_{\text{Agulhas}} + \text{Organic P flux}_{\text{Sinking}} \tag{3.2}$$

$$\text{Phosphate flux}_{\text{Agulhas}} = \text{Phosphate concentration}_{\text{Agulhas}} \times \text{Volume flux}_{\text{Agulhas}} \tag{3.2a}$$

$$\text{Phosphate flux}_{\text{Trop}} = \text{Phosphate concentration}_{\text{Trop}} \times \text{Volume flux}_{\text{Trop}} \tag{3.2b}$$

$$\text{Phosphate flux}_{\text{Subtrop}} = \text{Phosphate concentration}_{\text{Subtrop}} \times \text{Volume flux}_{\text{Subtrop}} \tag{3.2c}$$

Multiplying the organic P sinking flux by 128.6:1, the average measured C:P ratio of particulate organic matter in the greater Agulhas region (Copin-Montegut & Copin-Montegut, 1978; Martiny, et al., 2013), suggests a flux of organic carbon from the base of the thermocline of 0.7 mol C.m^{2}.a^{-1}. For comparison, the mean organic carbon flux out of the seasonal mixed layer (i.e., net community production; NCP) at subtropical sites such as BATS and station ALOHA in the subtropical North Pacific is 2.5-3.8 mol C.m^{-2}.a^{-1} ((Emerson, 2014) and references therein). We expect our sinking flux estimate to be lower than these values of NCP given the greater depth of the Agulhas region thermocline (i.e., 400 m) than the mixed layer at BATS and station ALOHA, along with the fact that a P-based carbon flux excludes sinking material deriving from N_2 fixation. Nonetheless, that our sinking flux is only an order of magnitude lower than NCP at BATS and station ALOHA is reassuring and validates our steady-state assumption and volume flux estimates.

Third, we balance the N fluxes into and out of the upper Agulhas region using the nutrient concentration data to estimate the generation of newly fixed nitrate (i.e., nitrate from the nitrification of organic N that was produced by new N_2 fixation) (Eq. 3.3). We multiply the nitrate concentrations from the three WOCE transects by their respective volume fluxes (Eq. 3.1). The mean nitrate concentration measured in the Agulhas (IO6) is 6.6 ± 5.0 μM, at the Tropical source (IO4) is 7.0 ± 4.7 μM, and at the Subtropical source (IO8) is 6.8 ± 4.2 μM. The resulting nitrate flux for Agulhas waters is 660.0 mmol.m^{-2}.a^{-1} (Eq. 3.3a), for Tropical water is 187.6 mmol.m^{-2}.a^{-1} (Eq. 3.3b), and for Subtropical water is 497.8 mmol.m^{-2}.a^{-1} (Eq. 3.3c). Multiplying the P-based organic sinking flux by the mean measured N:P of particulate organic matter in the region ((average of 18.1:1; (Copin-Montegut & Copin-Montegut, 1978; Martiny, et al., 2013)) yields a flux of organic N out of the thermocline of 95.4 mmol N.m^{-2}.a^{-1} (Eq. 3.3d).

$$\text{Nitrate flux}_{\text{Trop}} + \text{Nitrate flux}_{\text{Subtrop}} + \text{Nitrate flux}_{\text{Newly-fixed}} = \text{Nitrate flux}_{\text{Agulhas}} + \text{Organic N flux}_{\text{Sinking}} \quad (3.3)$$

$$\text{Nitrate flux}_{\text{Agulhas}} = \text{Nitrate concentration}_{\text{Agulhas}} \times \text{Volume flux}_{\text{Agulhas}} \quad (3.3a)$$

$$\text{Nitrate flux}_{\text{Trop}} = \text{Nitrate concentration}_{\text{Trop}} \times \text{Volume flux}_{\text{Trop}} \quad (3.3b)$$

$$\text{Nitrate flux}_{\text{Subtrop}} = \text{Nitrate concentration}_{\text{Subtrop}} \times \text{Volume flux}_{\text{Subtrop}} \quad (3.3c)$$

$$\text{Organic N flux}_{\text{Sinking}} = \text{Organic P flux}_{\text{Sinking}} \times \text{Organic N:P} \quad (3.3d)$$

$$\text{Nitrate flux}_{\text{Newly-fixed}} = (\text{Nitrate flux}_{\text{Agulhas}} + \text{Organic N flux}_{\text{Sinking}}) - (\text{Nitrate flux}_{\text{Trop}} + \text{Nitrate flux}_{\text{Subtrop}}) \quad (3.3e)$$

Substituting Eq. 3.3a-d into Eq. 3.3 (as represented by Eq. 3.3e) yields an estimate of the flux of newly-fixed nitrate into the greater Agulhas region of 70.0 ± 84.7 mmol N.m^{-2}.a^{-1} (orange values in Figure 3.7).

We can alternately estimate the flux of newly fixed nitrate into the greater Agulhas region using the N isotope data (Eq. 3.4). We multiply the N fluxes from Eq. 3.3a-d by their respective δ^{15}N endmembers (B7). The mean concentration-weighted nitrate δ^{15}N for the Agulhas region is

6.0 ± 1.0‰ (taken from ASCA16; Eq. 3.4a), for the Tropical waters is 6.4 ± 0.7‰ (taken from IIEO2; Eq. 3.4b), and for the Subtropical waters is 7.0 ± 0.2‰ (taken from IO8, see B7 (Sigman & Fripiat, 2019); Eq. 3.4c). While N_2 fixation may occur in the South Equatorial Current, between the IO8 sampling site and the greater Agulhas region, there is only one nitrate δ^{15}N profile available in these waters (from 15°S, 74°E, Figure 3.1; (Harms, et al., 2019)) and it shows no evidence of N_2 fixation. The relatively low nitrate δ^{15}N of the Tropical water indicates that N_2 fixation likely occurs in and/or upstream of the Mozambique Channel (i.e., in the northern tropical waters). However, the Tropical water nitrate δ^{15}N (of 6.4‰) is not low enough to yield the low nitrate δ^{15}N measured in the Agulhas waters (of 6.0‰), confirming that some amount of the signal must be generated by in situ N_2 fixation. There are no measurements of the δ^{15}N of sinking organic N in the Agulhas Current region; however, the sub-euphotic zone nitrate δ^{15}N can be used to estimate this term as it records the δ^{15}N of organic matter remineralized immediately below the surface layer (i.e., following its sinking out of the euphotic zone). We thus set the δ^{15}N of sinking organic N to the mean sub-euphotic zone (σ_θ =25.5-25.6 kg.m^{-3}) nitrate δ^{15}N measured across the Agulhas region, of 5.1 ± 0.7‰ (Eq. 3.4d).

$$\delta^{15}\text{N nitrate flux}_{\text{Trop}} + \delta^{15}\text{N nitrate flux}_{\text{Subtrop}} + \delta^{15}\text{N nitrate flux}_{\text{Newly-fixed}} = \delta^{15}\text{N nitrate flux}_{\text{Agulhas}} + \delta^{15}\text{N Organic N flux}_{\text{Sinking}} \tag{3.4}$$

$$\delta^{15}\text{N Nitrate flux}_{\text{Agulhas}} = \text{Nitrate flux}_{\text{Agulhas}} \times \delta^{15}\text{N}_{\text{Agulhas}} \tag{3.4a}$$

$$\delta^{15}\text{N Nitrate flux}_{\text{Trop}} = \text{Nitrate flux}_{\text{Trop}} \times \delta^{15}\text{N}_{\text{Trop}} \tag{3.4b}$$

$$\delta^{15}\text{N Nitrate flux}_{\text{Subtrop}} = \text{Nitrate flux}_{\text{Subtrop}} \times \delta^{15}\text{N}_{\text{Subtrop}} \tag{3.4c}$$

$$\delta^{15}\text{N Organic N flux}_{\text{Sinking}} = \text{Organic N flux}_{\text{Sinking}} \times \delta^{15}\text{N}_{\text{subeuphotic zone}} \tag{3.4d}$$

$$\text{Nitrate flux}_{\text{Newly-fixed}} = \frac{(\delta^{15}\text{N flux}_{\text{Agulhas}} + \delta^{15}\text{N flux}_{\text{Sinking}}) - (\delta^{15}\text{N flux}_{\text{Trop}} + \delta^{15}\text{N flux}_{\text{Subtrop}})}{\delta^{15}\text{N}_{\text{N2 fixation}}} \tag{43.e}$$

Substituting Eq. 3.4a-d into Eq. 3.4 (to yield Eq. 3.4e) and setting the δ^{15}N of newly-fixed nitrate to -1‰ (Hoering & Ford, 1960; Minagawa & Wada, 1986; Carpenter, et al., 1997) provides a second estimate of the newly-fixed nitrate flux into the greater Agulhas region of 238.7 ± 157.5 mmol N.m^{-2}.a^{-1} (red values in Figure 3.7). The sensitivity of this flux to the δ^{15}N of each endmember and the uncertainties associated with all fluxes, derived through error propagation of the volume fluxes, are reported in B8.

Above, we derive two estimates of the newly-fixed nitrate flux to the greater Agulhas region, of 70.0 and 238.7 mmol N.m^{-2}.a^{-1}. We consider the nutrient concentration-based estimate (Eq. 3.3e) to be the lower limit of the N_2 fixation rate and the N isotope-based estimate (Eq. 3.4e) to be the upper limit. In particular, the N isotope-based estimate is likely too high. The subtropical nitrate $\delta^{15}N$ endmember is poorly constrained as the available data are from substantially upstream of the subtropical Agulhas source region (Figure 3.1). As such, the subtropical $\delta^{15}N$ endmember does not include the signal of any N_2 fixation occurring en route to the subtropical source region. Coincident nutrient and N isotope data from the subtropical waters nearer the greater Agulhas region would better constrain our estimate. Additionally, our N isotope budget does not account for DON cycling because the $\delta^{15}N$ of DON in our region is unknown. Since DON degradation has the potential to supply low-$\delta^{15}N$ N to the thermocline nitrate pool (see section 3.4.2.1; (Zhang, et al., 2020)), its exclusion from our budget could lead us to overestimate the N_2 fixation rate from the N isotopes. For its part, the nutrient concentration-based estimate of N_2 fixation may be biased low, for reasons described in section 3.4.2.3.

Notwithstanding these uncertainties, the fluxes of newly-fixed nitrate calculated using the box model scale to an areal N_2 fixation rate for the greater Agulhas region of between 7.2 and 24.5 Tg $N.a^{-1}$, and a daily N_2 fixation rate of between 192 and 654 μmol $N.m^{-2}.d^{-1}$. Our daily rates are comparable to euphotic zone-integrated N_2 fixation rates that we measured along the ASCA transect in winter 2018, of 28-236 μmol $N.m^{-2}.d^{-1}$ (B9), as well as to estimates from other subtropical regions (Landolfi, et al., 2018). Our analysis indicates that N_2 fixation in the greater Agulhas region could contribute 28-94% of the whole Indian Ocean N gain estimated by models (Deutsch, et al., 2007; Wang, et al., 2019; Landolfi, et al., 2018).

3.4.2.2. Controls on N_2 fixation in the South Indian Ocean

N_2 fixation is hypothesized to be controlled by the availability of excess P relative to N (Deutsch, et al., 2007), the supply of bioavailable iron (Moore, et al., 2009; Shiozaki, et al., 2014), or both (Mills, et al., 2004; Held, et al., 2020; Cerdan-Garcia, et al., 2022; Weber & Deutsch, 2014; Sigman, et al., 1999; Singh, et al., 2017). The surface waters of the Indian Ocean host a P excess (>0.1 μM; (Deutsch, et al., 2007; Garcia, et al., 2018)), which is largely generated in the Arabian Sea where denitrification removes fixed N but not P (Deutsch, et al., 2007; DeVries, et al., 2013). More locally, the western Mozambique Channel shelf appears to supply P in stoichiometric excess of N to the overlying waters (P excess of >0.3 μM; Figure B9), potentially augmenting the basin-wide P excess. In calculating the nutrient concentration-based N_2 fixation rate, we are unlikely to have fully accounted for this local P excess (i.e., low N* input) in our P and N budgets, leading to an underestimation of N_2 fixation. Upper ocean dissolved iron measurements from across the Indian basin, albeit limited, reveal generally

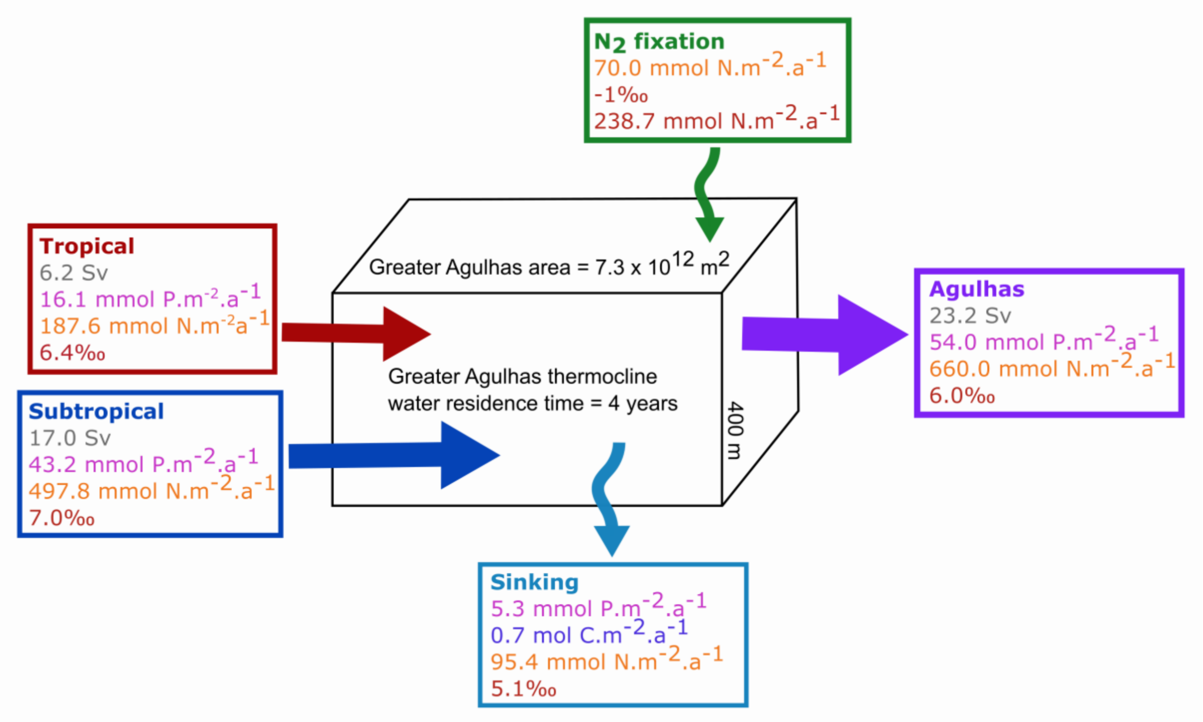

Figure 3.7. Estimating the newly-fixed nitrate flux into the greater Agulhas region. Schematic of our one-box model showing the volume fluxes of water (grey text in Sv), phosphorus (pink text in mmol.m^{-2}.a^{-1}), nitrogen (orange text in mmol.m^{-2}.a^{-1}), and nitrogen δ^{15}N (red text in ‰) into and out of the upper 400 m of the greater Agulhas region (see Discussion 4.2.2 for more detail). The upper water column (mixed layer and thermocline) of the greater Agulhas region is represented by the black box, with a surface area of 7.3 × 10^{12} m^2, residence time of four years, and thermocline depth of 400 m. There are two source water inputs, Tropical (red box and arrow) and Subtropical (blue box and arrow), and one output, the Agulhas waters (purple box and arrow). The sinking flux (cyan box and arrow) at the base of the thermocline represents a non-hydrographic nutrient loss from the upper 400 m of the greater Agulhas region (as organic matter). N$_2$ fixation (green box and arrow) constitutes a non-hydrographic N gain.

higher concentrations in the northern versus southern basin (0.1-1.3 nM versus 0.05-0.5 nM) and near the south-western and south-eastern margins versus the south-central basin (reaching 1.4 nM versus 0.2 nM) (Nishioka, et al., 2013; Shiozaki, et al., 2014; Grand, et al., 2015c; Siefert, et al., 1999; Chinni & Singh, 2022; Grand, et al., 2015a). Dissolved iron concentrations measured during the WOCE IO5 and IO6 expeditions that sampled the Agulhas region were high, >1 nM at the shelf and >0.3 nM in the current, and attributed to the entrainment of sedimentary iron by the Agulhas Current, augmented by local iron deposition (Grand, et al., 2015c). Thus, the supply of both excess P and iron appear to be sufficient to support significant rates of N$_2$ fixation in Agulhas surface waters. Similar conditions likely fuel N$_2$ fixation elsewhere in the basin too, such as north and west of the Mascarene Plateau (i.e., 5-20°S, 50-60°E; Figure 3.5), and at the west Australian margin.

The nitrate isotopes indicate that N_2 fixation occurs predominantly in the greater Agulhas region of the subtropical gyre (as well as in the northern tropics and/or Mozambique Channel) and not in the more sluggish waters of the subtropical gyre's northern and eastern limbs (Sigman & Fripiat, 2019; Harms, et al., 2019). This finding differs from N_2 fixation distributions diagnosed by models, which predict high rates in the southeast Indian basin (Deutsch, et al., 2007; Wang, et al., 2019). The overlap of excess P and iron across the Agulhas region may be enhanced by the retentive nature of the subtropical recirculation (Marshall, et al., 2022), perhaps explaining why N_2 fixation occurs predominantly in the southwest Indian Ocean. Moreover, that the Agulhas Current entrains shelf-derived iron (Grand, et al., 2015c) and transports excess P waters into the greater Agulhas region suggests that the current plays a role in modulating both the rate and distribution of N_2 fixation in the southwest Indian Ocean. The Gulf Stream has similarly been shown to supply the adjacent subtropical North Atlantic with iron and excess P that sustain elevated N_2 fixation rates in the oligotrophic gyre waters (Palter, et al., 2011; Conway, et al., 2018).

3.4.3. Tracking Agulhas leakage using the nitrate isotopes

At the Agulhas Retroflection and in Agulhas eddies leaking into the Cape Basin, rapid heat loss (and thus evaporation) can erode the relatively fresh signal of surface to sub-thermocline Agulhas waters compared to those in the more saline South Atlantic (Gordon, 1987; Olson, et al., 1992). During this modification, convective mixing may ventilate waters down to the 27.0 kg.m^{-3} isopycnal (Gordon, 1987), which weakens upper water column gradients, thus limiting the utility of physical tracers (i.e., temperature and salinity) for identifying Agulhas leakage (Olson, et al., 1992). However, nitrate Δ(15-18) is conserved during mixing (Rafter, et al., 2013), such that it may be useful for tracking Agulhas leakage.

Agulhas leakage first enters the South Atlantic via the Cape Basin (Figure 3.1) where upper water column nitrate Δ(15-18) is relatively high (~2.9‰; squares in Figure 3.8) and indistinct from the underlying SAMW (Campbell, 2016; Marconi, et al., 2017; Flynn, et al., 2020). This high-Δ(15-18) nitrate derives from the complete consumption in subtropical surface waters of high-δ^{15}N nitrate that is laterally advected into the subtropical South Atlantic from the Southern Ocean (Campbell, 2016; Marconi, et al., 2017). In addition, N_2 fixation, which lowers nitrate Δ(15-18), is thought to be negligible across the subtropical South Atlantic, unlike in the North Atlantic and North Pacific subtropical gyres (Marconi, et al., 2017; Moore, et al., 2009; Fernández, et al., 2010; Landolfi, et al., 2018; Shiozaki, et al., 2017). In contrast to the South Atlantic, the Δ(15-18) of nitrate in the upper water column of the greater Agulhas region is low (mean of 1.6‰, with a minimum of -0.5‰) and should persist in Agulhas-derived waters transported into the South Atlantic. While assimilation by phytoplankton of Agulhas thermocline nitrate in Agulhas leakage will raise its δ^{15}N, it will raise its δ^{18}O to the same extent (Granger, et al., 2004; Granger, et al., 2010), leaving the characteristic Δ(15-18) of Agulhas nitrate unchanged. At the same time, mixing of Agulhas and South Atlantic waters at the retroflection will combine low- and high-Δ(15-18) nitrate, yielding a Δ(15-18) for nitrate in Agulhas leakage that is lower than that of the South Atlantic and higher than that of the greater Agulhas region. Continuous mixing (i.e., entrainment and detrainment) with the surrounding Cape Basin waters may further alter the Agulhas nitrate pool. However, given the retentive (and downwelling) nature of Agulhas leakage features (Gordon, 1987; Fine, et al., 1988; Wallschuss, et al., 2022; Arhan, et al., 2011), mixing will not fully erase the low-Δ(15-18) of Agulhas nitrate in Agulhas rings and eddies (Figure B10). As such, Agulhas leakage should retain a nitrate Δ(15-18) that is considerably lower than that of the Cape Basin.

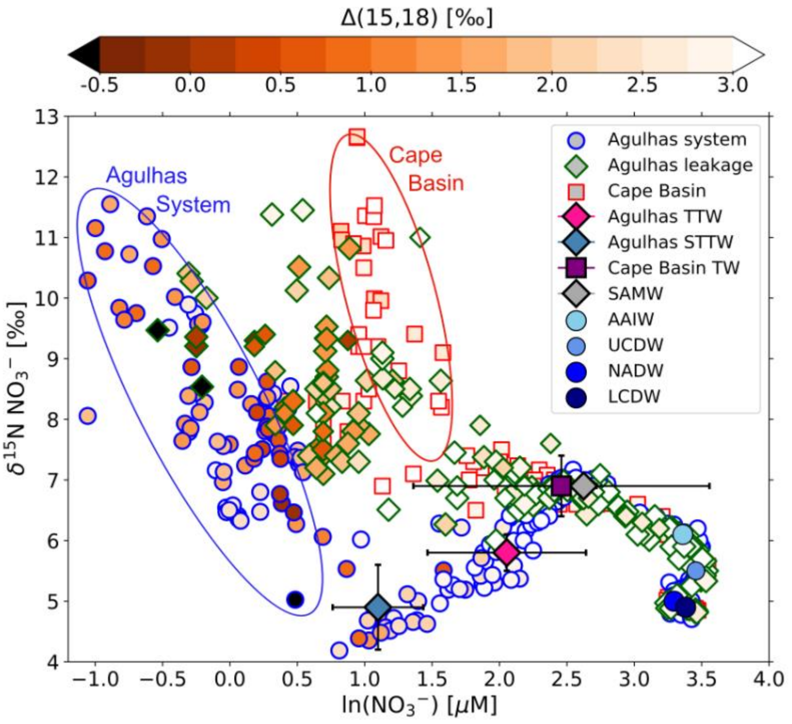

Figure 3.8. Tracking Agulhas leakage into the South Atlantic Ocean. Data from ASCA16 and the subtropical South Atlantic plotted in nitrate δ^{15}N [‰] vs ln([NO_3^-]) [μM] space (i.e., "Rayleigh space"), with symbol colour indicating nitrate Δ(15-18) [‰]. Symbol shape and outline-colour indicate the sampling region, except for the bold diamond markers outlined in black, which show the mean ln([NO_3^-]) and concentration-weighted nitrate δ^{15}N measured for Subantarctic Mode Water (SAMW; grey), Agulhas Subtropical Thermocline Water (STTW; blue), and Agulhas Tropical Thermocline Water (TTW; pink), as well as the purple square, which shows Cape Basin Thermocline Water (TW). In addition, the mean ln([NO_3^-]) and concentration-weighted nitrate δ^{15}N are shown for Antarctic Intermediate Water (AAIW), Upper Circumpolar Deep Water (UCDW), North Atlantic Deep Water (NADW), and Lower Circumpolar Deep Water (LCDW), as measured

in the Agulhas region. Four datasets that sampled both "background" Cape Basin conditions (squares outlined in red) and Agulhas leakage (diamonds outlined in green) are included on the plot: VOY016 cruise (Smart, et al., 2020), SAMBA: South Atlantic MOC Basin-wide Array 2015 (Marconi, et al., 2017) and 2017 (Granger, et al., 2023), and VOY03 cruise (Smart, et al., 2015).

Four nitrate isotope datasets from across the Cape Basin have sampled Agulhas leakage (see Figure 3.1 for sampling locations and Figure 3.8 for data (Smart, et al., 2015; Campbell, 2016; Marconi, et al., 2017; Smart, et al., 2020; Granger, et al., 2023)). Low nitrate Δ(15-18) is observed in the thermocline and mixed layer of these features (mean Δ(15-18) of 2.5 ± 0.6‰ for σ_θ <26.4 kg.m^{-3} and 1.8 ± 0.8‰ for the mixed layer, with values as low as -0.7‰; diamonds outlined in green in Figure 3.8), in contrast to the background Cape Basin (mean Δ(15-18) of 2.9 ± 0.2‰ for σ_θ <26.4 kg.m^{-3} and 2.7 ± 0.6‰ for the mixed layer; squares outlined in red in Figure 3.8). It is likely that Agulhas leakage perennially influences the mean state of the background Cape Basin since leakage features are constantly being eroded and incorporated into Cape Basin waters (Gordon, 2003; Wallschuss, et al., 2022). Nevertheless, our observations of lower nitrate Δ(15-18) in Agulhas leakage support the hypothesis that this parameter retains the imprint of southwest Indian Ocean N cycle processes in the subtropical southeast Atlantic Ocean.

At the same time, the available Agulhas leakage data reveal little evidence of the low-δ^{15}N nitrate characteristic of Agulhas thermocline waters, except perhaps in the slightly lower δ^{15}N measured for similar nitrate concentrations in the leakage versus the background Cape Basin (compare diamonds outlined in green to squares outlined in red at ln([NO_3^-]) = 0.5 to 1.5 μM in Figure 3.8). Instead, the data show that subsurface nitrate δ^{15}N in Agulhas leakage is relatively high, typically >6.6‰ and never lower than 6.0‰ (squares in Figure 3.8; background Cape Basin thermocline nitrate-δ^{15}N averages 6.9‰). The absence of an N_2 fixation signal, as low-δ^{15}N thermocline nitrate, in Agulhas leakage can be explained by isotope fractionation during nitrate assimilation, which raises the δ^{15}N (and δ^{18}O) of nitrate. While the deep convective mixing characteristic of Agulhas rings and eddies will entrain low-δ^{15}N nitrate from the thermocline into the surface layer, its subsequent rapid consumption by phytoplankton will overprint its low δ^{15}N, but because of the equivalent assimilation-driven rise in nitrate δ^{18}O, will not erode its Δ(15-18).

Our findings highlight the potential utility of the dual isotopes of nitrate for tracking Agulhas leakage in the Cape Basin and across the South Atlantic. In the modern ocean, this tracer may be particularly useful for tracking older Agulhas eddies that can no longer be distinguished by sea level height anomalies, sea surface temperature, or salinity. Plankton fueled by nitrate ultimately supplied from the southwest Indian Ocean should preserve the low-δ^{15}N of Agulhas nitrate in their biomass even as this signal is eroded from the thermocline and surface nitrate pool by nitrate assimilation. The eventual sinking to the seafloor of some of these plankton (e.g., planktic foraminifera; single-celled zooplankton with calcite shells that include minute quantities of organic N, protecting it from isotopic alteration) may transfer the low-δ^{15}N of Agulhas nitrate to the sediment record (Ren, et al., 2009; Ren, et al., 2012; Smart, et al., 2018; Martínez-García, et al., 2014). Similarly, plankton fueled by nitrate ultimately sourced from the South Atlantic thermocline should impose a higher δ^{15}N on sedimenting material. The δ^{15}N of fossil foraminifera from the Cape Basin sediment record might thus be used to infer the strength of Agulhas leakage in the past.

3.5. Summary

This study provides the first biogeochemical characterization of the Agulhas Current and adjacent recirculating waters. We identify both Upper and Lower Circumpolar Deep Water in the Agulhas Current for the first time and distinguish between thermocline and sub-thermocline waters, often referred to collectively as central waters. These waters are fundamentally different from one another, both hydrographically (e.g., in salinity) and biogeochemically (e.g., in their nitrate concentration and isotopes). Both the tropical and subtropical thermocline waters in the greater Agulhas region bear the isotopic imprint of N_2 fixation, while underlying SAMW does not. From a one-box model that incorporates water volume, P, N, and N isotope fluxes, we estimate a local N_2 fixation rate for the greater Agulhas region. While a lack of data from the South Indian Ocean introduces significant uncertainties that yield a wide range in the N_2 fixation rate estimates, we nonetheless calculate an N_2 fixation rate of between 7 and 25 Tg N.a^{-1}, the first observations-based estimate for the subtropical southwest Indian Ocean; consideration of various factors causes us to favor the lower portion of this range. Furthermore, the nitrate N and O isotopes indicate that nitrate assimilation is the dominant N cycle process occurring in the mixed layer of the Agulhas Current and adjacent recirculating waters, with nitrification confined to the subsurface. The implication of this finding is that export production in the greater Agulhas region can be estimated from the rate of nitrate assimilation plus N_2 fixation, with no need to account for nitrate regenerated in the mixed layer. Along with coupled partial nitrate assimilation and nitrification that occurs largely at the base of the mixed layer, N_2 fixation generates low Δ(15-18) nitrate in the Agulhas thermocline and mixed layer. As such, we propose that Agulhas leakage into the South Atlantic can be tracked using nitrate Δ(15-18) even as the low-δ^{15}N of Agulhas thermocline nitrate is eroded by isotopic fractionation during in situ nitrate assimilation by phytoplankton. This result may have implications for using the N isotopes in the Cape Basin sediment record to reconstruct past Agulhas leakage.

Appendix B

This appendix has been published as the supplementary information for chapter 3, “*The Agulhas Current Transports Signals of Local and Remote Indian Ocean Nitrogen Cycling*” as:

Marshall, T. A., Sigman, D. M., Beal, L. M., Foreman, A., Martínez-García, A., Blain, S., Campbell, E., Fripiat, F., Granger, R., Harris, E., Haug, G.H., Marconi, D., Oleynik, S., Rafter, P.A., Roman, R., Sinyanya, K., Smart, S.M., and Fawcett, S.E. (2023). The Agulhas Current transports signals of local and remote Indian Ocean nitrogen cycling. Journal of Geophysical Research: Oceans, 128, e2022JC019413. https://doi.org/10.1029/2022JC019413

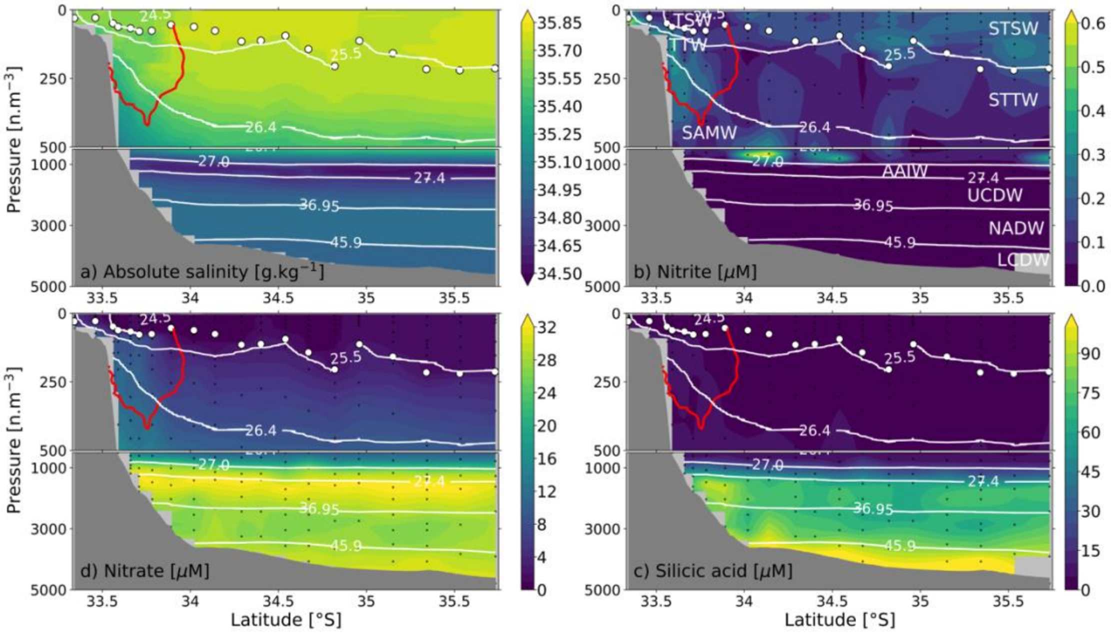

Figure B1. **Full depth nutrient concentrations across the ASCA16 transect**. Gridded section plots from the ASCA16 transect of **a**) absolute salinity [g.kg^{-1}] and **b**) nitrite, **c**) nitrate, and **d**) silicic acid concentrations [μM]. The red contour depicts the 1 m.s^{-1} along-stream current speed, indicating the position of the Agulhas Current core at the time of sampling, and the white contours show the isopycnal boundaries of the water masses along σ_θ, σ_2, and σ_4 (see Table 1). The white circles indicate the depth of the mixed layer at each station and the small black circles show discrete sampling depths. The y-axis of each plot is non-linear to focus on the upper 500 m while still showing the full depth concentrations. TSW: Tropical Surface Water; STSW: Subtropical Surface Water; TTW: Tropical Thermocline Water; STTW: Subtropical Thermocline Water; SAMW: Subantarctic Mode Water; AAIW: Antarctic Intermediate Water; UCDW: Upper Circumpolar Deep Water; NADW: North Atlantic Deep Water; LCDW: Lower Circumpolar Deep Water.

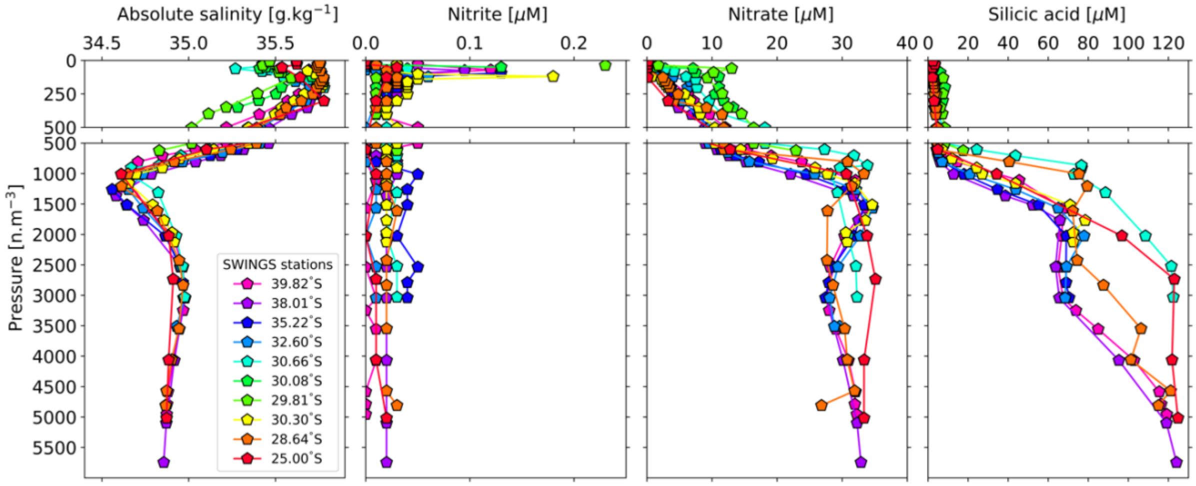

Figure B2. **Full depth profiles of nutrient concentrations across the SWINGS transect**. Discrete depth profiles of **a**) absolute salinity [g.kg^{-1}] and **b**) nitrite, **c**) nitrate, and **d**) silicic acid concentrations [μM] for samples collected during the SWINGS cruise. The legend provides station latitude. Note that the depth (i.e., pressure) axis is shown at two resolutions, with the top panels showing the surface-to-thermocline data and the bottom panels showing the deep-water data.

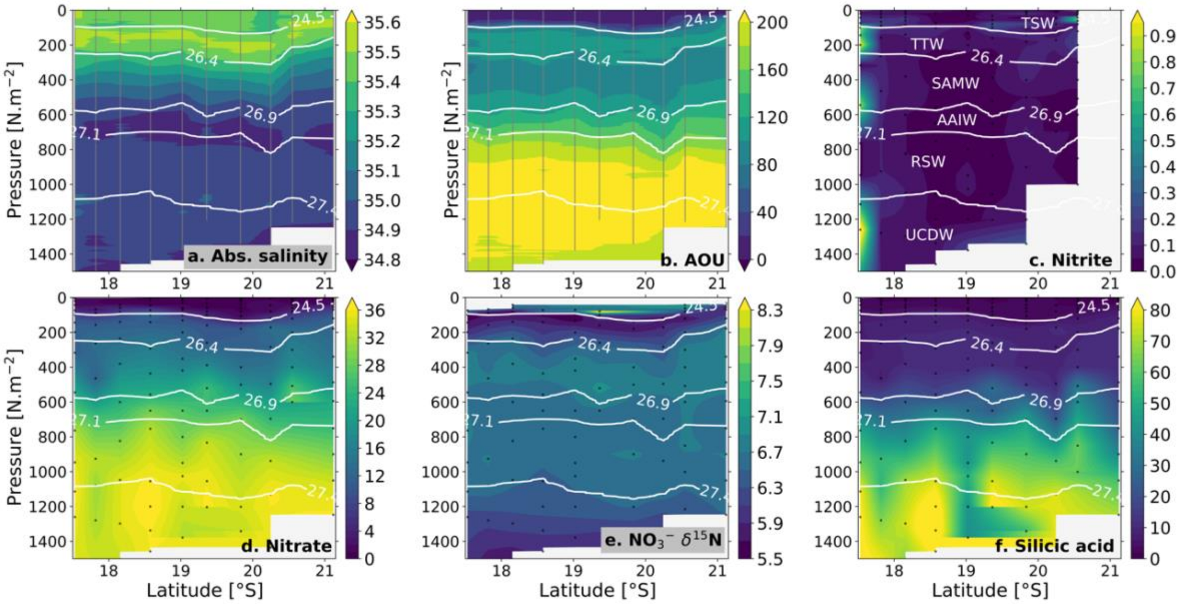

Figure B3. **Biogeochemistry of the western Mozambique Channel.** Gridded section plots from the IIOE2 transect of **a**) absolute salinity [g.kg^{-1}], **b**) apparent oxygen utilization (AOU) [μM], **c**) nitrite concentration [μM], **d**) nitrate concentration [μM], **e**) nitrate δ^{15}N [‰], and **f**) silicic acid concentration [μM]. White contours indicate the isopycnal boundaries of water masses (see Table 2) and small black circles indicate discrete sampling depths. Water mass abbreviations are as in Figure B1 and include RSW: Red Sea Water.

B1. Correcting nitrate $\delta^{18}O$ for changes in salinity. During marine nitrification, the dominant source of the O atoms for nitrate is ambient seawater (Casciotti, et al., 2002; Casciotti, et al., 2010; Boshers, et al., 2019); changes in seawater $\delta^{18}O$ (i.e., $\delta^{18}O_{H2O}$) will thus affect the $\delta^{18}O$ of the nitrate that is produced. Generally, $\delta^{18}O_{H2O}$ varies little over the water column, but in regions characterised by large vertical salinity gradients, the measured $\delta^{18}O$ of nitrate may need to be corrected for changes in $\delta^{18}O_{H2O}$ (Knapp, et al., 2008; Fawcett, et al., 2015). This is because there exists a well-defined relationship between salinity and $\delta^{18}O_{H2O}$, with both parameters typically increasing towards the surface. The remineralization of organic matter in shallower waters where $\delta^{18}O_{H2O}$ is high could thus artefactually increase nitrate $\delta^{18}O$. In the subtropical Indian Ocean, $\delta^{18}O_{H2O}$ increases only slightly with decreasing depth (by 0.25‰ for a 0.42 rise in salinity between 0 and 500 m; Schmidt, G.A., G. R. Bigg and E. J. Rohling. 1999. “Global Seawater Oxygen-18 Database-v1.22”; https://data.giss.nasa.gov/o18data/). Applying a correction for salinity-driven depth variations in $\delta^{18}O_{H2O}$ following Knapp et al. (2008) decreases the nitrate $\delta^{18}O$ by an average of only 0.19‰ for our ASCA16 dataset (depth profiles of absolute salinity and the measured- and salinity-corrected nitrate $\delta^{18}O$ for the ASCA16 dataset are shown in Figure B4). Additionally, the error associated with the subtropical Indian Ocean $\delta^{18}O_{H2O}$/salinity relationship is considerable (r^2 =0.5, n=37). Finally, correcting nitrate $\delta^{18}O$ using coincidentally measured salinity assumes that all the nitrate was regenerated in situ (i.e., no preformed nitrate), which is not the case. We have thus chosen not to apply a salinity-based correction to our nitrate $\delta^{18}O$ dataset.

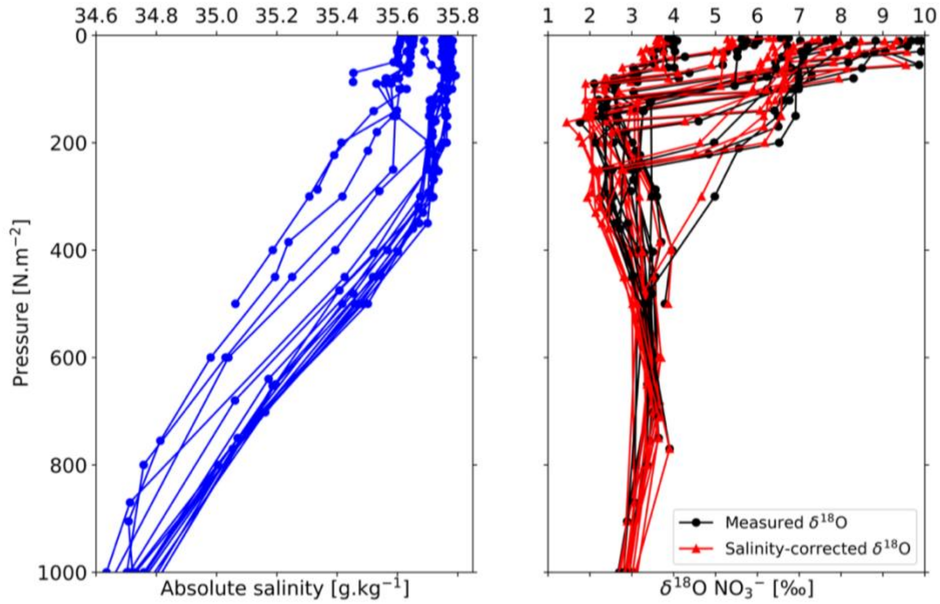

Figure B4. Depth profiles of a) absolute salinity [g.kg^{-1}] and b) nitrate δ^{18}O [‰] from across the Agulhas Current and adjacent recirculating waters. In panel **b**, the black profiles show the measured nitrate δ^{18}O data and the red profiles show the salinity-corrected nitrate δ^{18}O data. This exercise reveals that correcting for salinity-driven changes in $\delta^{18}O_{H2O}$ makes almost no difference to the δ^{18}O of nitrate.

Table B1. Mean values (± 1 SD) of absolute salinity [g.kg^{-1}], conservative temperature [°C], oxygen concentration [μM], apparent oxygen utilization (AOU) [μM], silicic acid, nitrite, and nitrate concentrations [μM], and concentration-weighted nitrate δ^{15}N [‰], δ^{18}O [‰], and Δ(15-18) [‰] for the water masses identified in the ASCA16 dataset. Water masses are defined by potential density anomalies, σ_θ [kg.m^{-3}], and their core properties are listed in brackets. The narrow density range between the surface and thermocline condenses the shallow data in density-space (B3); we thus report surface and thermocline water mass properties averaged over depth rather than density. The row subheadings *Tropical* and *Subtropical* refer to inshore and offshore of the Agulhas Current core, respectively. The two most coastal ASCA16 stations (33.34°S and 33.46°S) are excluded from the inshore mean as they are both influenced by upwelling.

Table B2. Mean values (± 1 SD) of absolute salinity [g.kg^{-1}], conservative temperature [°C], oxygen concentration [μM], apparent oxygen utilization (AOU) [μM], silicic acid, nitrite, and nitrate concentrations [μM], and concentration-weighted nitrate δ^{15}N [‰] for the water masses identified in the SWINGS dataset. Water masses are defined by potential density anomalies, σ_θ [kg.m^{-3}], and their core properties are listed in brackets. The narrow density range between the surface and thermocline condenses the shallow data in density-space (B3); we thus report surface and thermocline water mass properties averaged over depth rather than density. The row subheadings *Tropical* and *Subtropical* refer to inshore and offshore of the Agulhas Current core, respectively. There are no nitrate δ^{18}O measurements (and thus no Δ(15-18)) available for the SWINGS dataset.

Table B1

Water mass		**Abbrev**	**Potential density, σ_θ [kg.m^{-3}]**	**Absolute salinity [g.kg^{-1}]**	**Conservative temperature, θ [°C]**	**Oxygen [μM]**	**AOU [μM]**	**Si(OH)$_4$ [μM]**	**NO$_2^-$ [μM]**	**NO$_3^-$ [μM]**	**δ^{15}N NO$_3^-$ [‰]**	**δ^{18}O NO$_3^-$ [‰]**	**Δ(15-18) [‰]**
Tropical	Tropical Surface Water	TSW	<24.5	35.6 ± 0.54 (35.6 ± 0.49)	22.5 ±0.07 (22.2 ± 0.68)	201.8 ± 2.4 (198.3 ± 10.4)	12.8 ±2.5 (17.3 ± 12.6)	2.6 ± 0.3 (2.7 ± 0.3)	0.1 ± 0.0 (0.1 ± 0.0)	0.8 ± 0.4 (1.1 ± 0.9)	6.7 ± 0.3 (6.5 ± 1.2)	4.4 ± 0.4 (4.0 ± 1.2)	2.3 ± 0.3 (2.5 ± 1.2)
	Tropical Thermocline Water	TTW	24.5 - 26.4	35.6 ±0.04 (35.6 ± 0.03)	16.9 ± 2.10 (17.2 ± 1.82)	172.5 ± 18.5 (162.7± 14.3)	65.5 ± 16.4 (73.9 ± 14.3)	5.5 ± 1.4 (5.6 ± 1.4)	0.2 ± 0.1 (0.2 ±0.1)	8.0 ± 2.1 (7.8 ± 1.8)	6.0 ± 0.3 (5.8 ± 0.3)	2.7 ± 0.4 (2.7 ± 0.4)	3.2 ± 0.3 (3.2 ± 0.3)
Subtropical	Subtropical Surface Water	STSW	24.5 - 25.5	35.8 ±0.25 (35.8 ± 0.05)	19.5 ± 2.17 (19.7 ± 1.59)	213.0 ± 21.8 (214.4 ± 1.8)	13.2 ± 27.2 (11.1 ± 2.7)	2.7 ± 0.5 (2.6 ± 0.4)	0.2 ± 0.1 (0.2 ± 0.0)	1.2 ± 0.6 (1.0 ± 0.5)	7.2 ± 0.7 (8.0 ± 0.7)	5.9 ± 0.7 (6.7 ± 0.7)	1.3 ± 0.9 (1.3 ± 0.8)
	Subtropical Thermocline Water	STTW	25.5 - 26.4	35.7 ± 0.17 (35.7 ± 0.02)	16.5 ± 2.04 (18.4 ± 0.77)	198.7 ± 10.5 (201.8 ± 9.0)	45.8 ± 8.8 (29.9 ± 11.9)	4.1 ± 0.6 (3.3 ± 0.6)	0.1 ± 0.0 (0.1 ± 0.1)	5.9 ± 1.9 (3.0 ± 1.4)	5.7 ± 0.5 (4.9 ± 0.7)	3.0 ± 0.5 (2.8 ± 0.8)	2.7 ± 0.5 (2.1 ± 0.8)
Subantarctic Mode Water		SAMW	26.4 - 27.0	35.1 ± 0.23 (35.1 ± 0.06)	35.1 ± 0.23 (35.1 ± 0.06)	11.1 ± 1.86 (11.3 ± 0.38)	203.5 ± 6.7 (209.3 ± 2.5)	65.3 ± 15.7 (57.7 ± 3.6)	9.9 ± 5.6 (6.9 ± 2.3)	0.1 ± 0.13 (0.2 ± 0.15)	15.2 ± 4.3 (13.8 ± 1.1)	6.7 ± 0.4 (6.9 ± 0.1)	3.3 ± 0.4 (3.5 ± 0.1)
Antarctic Intermediate Water		AAIW	27.0 - 27.4	35.1 ± 0.23 (35.1 ± 0.06)	11.1 ± 1.86 (11.3 ± 0.38)	203.5 ± 6.7 (209.3 ± 2.5)	65.3 ± 15.7 (57.7 ± 3.6)	9.9 ± 5.6 (6.9 ± 2.3)	0.1 ± 0.1 (0.2 ± 0.2)	15.2 ± 4.3 (13.8 ± 1.1)	6.7 ± 0.4 (6.9 ± 0.1)	3.3 ± 0.4 (3.5 ± 0.1)	3.4 ± 0.4 (3.4 ± 0.1)
Red Sea Water lenses		RSW	27.45 - 27.55	34.6 ± 0.06 (34.6 ± 0.06)	5.4 ± 1.05 (5.3 ± 0.63)	178.3 ± 14.1 (181.3 ± 12.4)	128.0 ± 18.2 (125.8± 12.0)	38.3 ± 11.3 (36.9 ± 6.6)	0.0 ± 0.0 (0.0 ± 0.0)	28.3 ± 2.4 (28.6 ± 1.3)	6.0 ± 0.1 (6.0 ± 0.1)	2.6 ± 0.1 (2.6 ± 0.1)	3.4 ± 0.1 (3.4 ± 0.1)
Upper Circumpolar Deep Water		UCDW	27.4 - σ_2 =36.9	34.7 ± 0.03	4.2 ± 0.25	151.0 ± 6.9	164.3 ± 5.2	63.9 ± 2.2	0.0 ± 0.0	32.2 ± 0.3	6.0 ± 0.0	2.6 ± 0.1	3.4 ± 0.0
North Atlantic Deep Water		NADW	σ_2=36.9 - σ_4 = 45.9	35.0 ± 0.02 (35.0 ± 0.00)	2.1 ± 0.31 (2.1 ± 0.14)	202.7 ± 8.1 (207.3 ± 2.6)	128.6 ± 6.3 (124.2 ± 1.9)	75.0 ± 8.1 (72.8 ± 6.6)	0 ±0.00	27.4 ± 0.8 (27.0 ± 0.7)	5.0 ± 0.0 (5.0 ±0.0)	1.9 ± 0.1 (1.9 ± 0.1)	3.1 ± 0.1 (3.1 ± 0.1)
Lower Circumpolar Deep Water		LCDW	σ_4 > 45.9	34.9 ± 0.01 (34.9 ± 0.01)	1.0 ± 0.2 (0.9 ± 0.09)	206.2 ±1.1 (205.7 ± 0.8)	134.5 ± 2.5 (136.5 ± 1.3)	98.8 ± 7.1 (105.5 ± 3.6)	0 ±0.00	29.3 ± 0.8 (30.0 ± 0.4)	4.9 ± 0.0 (4.8 ± 0.0)	1.8 ± 0.1 (1.8 ± 0.1)	3.0 ± 0.0 (3.0 ± 0.0)

Table B2

Water mass		Abbrev	Potential density, σ_θ [kg.m^{-3}]	Absolute salinity [g.kg^{-1}]	Conservative temperature, θ [°C]	Oxygen [μM]	AOU [μM]	$Si(OH)_4$ [μM]	NO_2^- [μM]	NO_3^- [μM]	$\delta^{15}N$ NO_3^- [‰]
Tropical	Tropical Surface Water	TSW	<24.5	35.4 ± 0.05 (35.5 ± 0.06)	25.7 ± 1.76 (27.0 ± 0.59)	203.6 ± 24.0 (195.6 ± 28.4)	14.8 ± 26.0 (5.3± 2.5)	2.4 ± 1.0 (1.7 ± 0.1)	0.1 ± 0.07 (0.0 ± 0.01)	3.9 ± 3.1 (0.2 ± 0.1)	5.6 ± 0.0 (NAN)
	Tropical Thermocline Water	TTW	24.5 - 26.4	35.5 ±0.06 (35.5 ± 0.07)	16.9 ± 2.30 (17.7 ± 2.94)	214.6 ± 6.5 (215.7 ± 6.4)	78.1 ± 26.1 (72.5 ± 19.3)	3.8 ± 0.9 (6.5 ± 1.5)	0.0 ± 0.4 (0.0 ± 0.06)	10.5 ± 1.0 (9.6 ± 2.5)	6.3 ± 0.3 (6.2 ± 0.4)
Subtropical	Subtropical Surface Water	STSW	24.5 - 25.5	35.7 ±0.04 (35.7 ± 0.22)	20.5 ± 0.92 (22.0 ± 2.55)	204.1 ± 29.0 (203.2 ± 30.6)	11.5 ± 16.0 (6.0 ± 16.4)	2.0 ± 0.4 (2.0 ± 0.5)	0.0 ± 0.04 (0.0 ± 0.03)	0.6 ± 0.6 (0.4 ± 0.6)	5.8 ± 0.7 (6.0 ± 1.9)
	Subtropical Thermocline Water	STTW	25.5 - 26.4	35.7 ± 0.08 (35.7 ± 0.04)	16.5 ± 1.23 (18.1 ± 1.60)	192.1 ± 21.9 (188.9 ± 31.0)	32.7 ± 9.2 (24.7 ± 7.4)	3.4 ± 0.5 (3.0 ± 0.5)	0.0 ± 0.02 (0.0 ± 0.02)	5.0 ± 2.0 (3.0 ± 1.4)	5.8 ± 0.6 (5.1 ± 0.7)
Subantarctic Mode Water		SAMW	26.4 - 27.0	35.1 ± 0.23 (35.1 ± 0.06)	10.9 ± 1.84 (11.3 ± 0.37)	203.9 ± 12.8 (207.8 ± 8.9)	65.7 ± 18.2 (57.1 ± 6.6)	12.3 ± 12.9 (8.6 ± 5.9)	0.0 ± 0.01 (0.0 ± 0.01)	16.9 ± 6.5 (15.3 ± 3.9)	6.6 ± 0.5 (6.7 ± 0.4)
Antarctic Intermediate Water		AAIW	27.0 - 27.4	34.7 ± 0.06 (34.6 ± 0.06)	5.5 ± 1.10 (5.4 ± 0.59)	176.4 ± 16.9 (176.7 ± 15.1)	129.7 ± 17.3 (127.0 ± 12.0)	47.0 ± 18.5 (45.8 ± 17.1)	0.0 ± 0.01	30.3 ± 2.4 (30.4 ± 1.5)	6.0 ± 0.1 (6.0 ± 0.1)
Red Sea Water lenses		RSW	27.45 - 27.55	34.8 ± 0.03	3.9 ± 0.25	148.6 ± 11.9	172.4 ± 7.5	81.0 ± 10.8	0.0 ± 0.00	31.6 ± 2.4	5.9 ± 0.1
Upper Circumpolar Deep Water		UCDW	27.4 - σ_2 =36.9	34.8 ± 0.07 (34.8 ± 0.06)	3.1 ± 0.48 (3.2 ± 0.46)	167.3 ± 11.8 (165.4 ± 11.4)	160.0 ± 8.8 (162.2 ± 7.6)	72.8 ± 11.3 (72.5 ± 11.3)	0.0 ± 0.01	31.5 ± 2.0 (31.7 ± 2.0)	5.5 ± 0.1 (5.6 ± 0.1)
Indian Deep Water		IDW	*27.45 - σ_4 = 45.9*	34.9 ± 0.00	1.8 ± 0.04	211.9 ± 0.29	177.3 ± 0.4	122.7 ± 0.3	0.0 ± 0.00	35 ± 0.1	5.4 ± 0.1
North Atlantic Deep Water		NADW	σ_2=36.9 - σ_4 = 45.9	35.0 ± 0.02 (35.0 ± 0.0)	2.1 ± 0.30 (2.0 ± 0.14)	200.7 ± 9.2 (204.9 ± 4.1)	130.7 ± 7.3 (126.7 ± 4.3)	81.3 ± 18.2 (81.0 ± 19.2)	0.0 ± 0.01	29.1 ± 1.4 (28.8 ± 1.5)	5.1 ± 0.1 (5.1 ± 0.1)
Lower Circumpolar Deep Water		LCDW	σ_4 > 45.9	34.9 ± 0.01 (34.9 ± 0.01)	0.7 ± 0.34 (0.5 ± 0.21)	210.2 ± 2.0 (210.5 ± 2.0)	133.4 ± 3.0 (134.6 ± 2.4)	106.0 ± 9.1 (110.0 ± 6.6)	0.0 ± 0.01	30.9 ± 1.0 (31.2 ± 0.9)	4.9 ± 0.0 (4.9 ± 0.0)

B2. Identifying Red Sea Water in the Agulhas Current and adjacent recirculating waters. A Red Sea Water (RSW) lens is apparent in both the ASCA16 and SWINGS transects. RSW is typically most easily identified by its maxima in salinity and AOU relative to young and fresh Antarctic Intermediate Water (AAIW; see water mass labels on Figure 3.3 and B5) that occupies a similar density range (σ_θ = 27.0-27.4 kg.m^{-3}). The low purity of RSW in the Agulhas region, however, coupled with its interleaving with the surrounding water masses, dilutes the signal and makes identifying and quantifying RSW a challenge. Moreover, at the time of our sampling of the ASCA16 and SWINGS transects, RSW occurred coincident with (deeper) Upper Circumpolar Deep Water (UCDW; σ_θ = 27.4-27.7 kg.m^{-3}), which is also characterised by relative salinity and AOU maxima (Table 3.1 and Table B1 and B2 and Figure B5), further complicating the identification of RSW in Agulhas waters. RSW is, however, distinguishable from UCDW by its nitrate δ^{15}N and δ^{18}O that are 0.4-0.5‰ and 0.4‰, respectively, higher than the surrounding deep-water nitrate (Figure 3.4c and d inset and Figure B5b). The ASCA16 RSW lens is apparent as a nitrate-δ^{15}N maximum along the 27.45 kg.m^{-3} isopycnal (Figure 3.4c inset and S5b green-edged circles). These discrete data (n=5) are from offshore of the Agulhas Current core, between 34.1°S and 34.4°S and again at 34.7°S (Figure B5b). The SWINGS RSW lens is similarly apparent as a nitrate-δ^{15}N maximum between the 27.45 and 27.55 kg.m^{-3} isopycnals (Figure 3.4c inset and B5b green-edged pluses) and these discrete data (n=2) are also from offshore of the current core, at stations located at latitudes of 30.66°S; 32.15°E and 30.30°S; 32.80°E (Figure 3.1 and 3.4c).

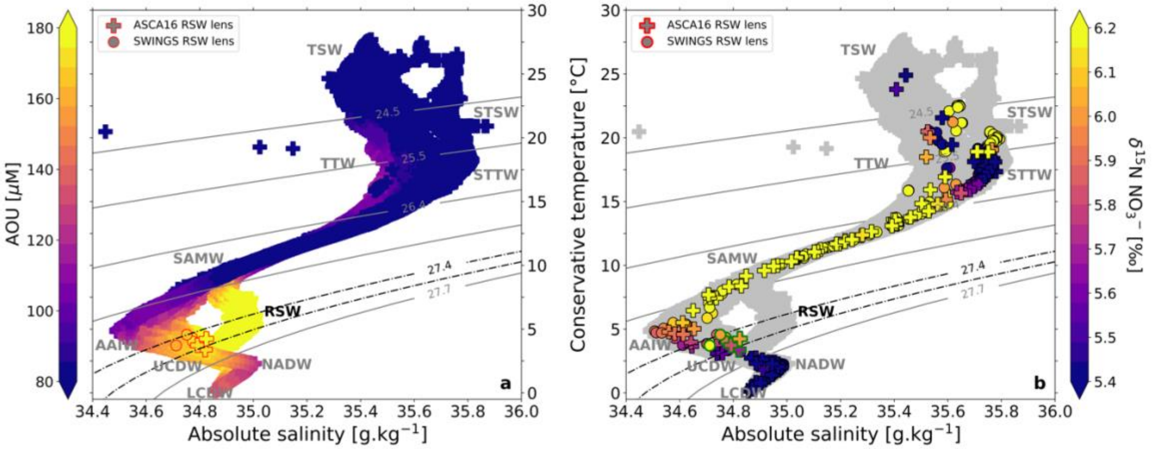

Figure B5. Conservative temperature [°C] versus absolute salinity [g.kg^{-1}] for the ASCA16 (circle symbols), IIEO2 (triangle symbols), and SWINGS (plus symbols) datasets. Symbol colours indicate **a**) apparent oxygen utilisation (AOU) [µM] and **b**) nitrate δ^{15}N [‰]. The symbols outlined in red (on panel **a**) and green (on panel **b**) show discrete samples representing the Red Sea Water (RSW) lenses, as per the legend. In panel **b**, all discrete ASCA16 and SWINGS isotope samples are outlined in black while the underlying grey symbols show the high-resolution CTDO data (including from the IIEO2 cruise, see Figure 3.3). Black and grey contours indicate the potential density anomalies (in kg.m^{-3}) that form the boundaries between water masses (see Table 3.1). TSW: Tropical Surface Water; STSW: Subtropical Surface Water; TTW: Tropical Thermocline Water; STTW: Subtropical Thermocline Water; SAMW: Subantarctic Mode Water; AAIW: Antarctic Intermediate Water; RSW: Red Sea Water; UCDW: Upper Circumpolar Deep Water; NADW: North Atlantic Deep Water; IDW: Indian Deep Water; LCDW: Lower Circumpolar Deep Water.

B3. The biogeochemistry of the southwest Indian Ocean in depth-space. All western boundary currents experience isopycnal shoaling at the position of the current, due to these currents maintaining geostrophic balance (Imawaki, et al., 2013). The water mass properties of such systems are therefore best viewed in density-space. By contrast, processes acting in the surface mixed layer are at times better viewed in depth-space since mixing can homogenize these waters and erode the density gradient across a broad depth interval. In other words, the density gradient across the surface mixed layer (i.e., surface to ~25.5 kg.m^{-3} isopycnal) is narrow, sometimes only 0.1 kg.m^{-3} over a 200 m depth interval, which condenses the data in density-space (for example, the subtropical waters in Figure 3.4). As such, we present the surface mixed layer data in both density (Figure 3.4) and depth space (Figure B6). The shallowest depth down to which surface conservative temperature, salinity, potential density, and nitrate concentrations are near-uniform approximates the depth of the mixed layer for each profile (white circles in Figure B1). Typically, mixed layer depth increases offshore, from as shallow as 29 m over the shelf to 220 m offshore.

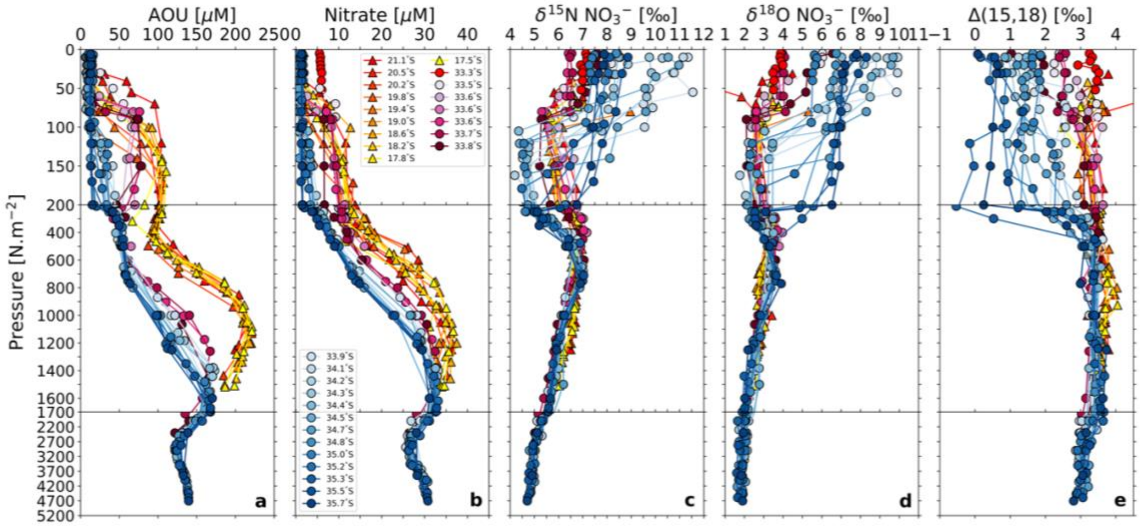

Figure B6. Full depth profiles of **a**) apparent oxygen utilization (AOU) [μM], **b**) nitrate concentration [μM], **c**) nitrate δ^{15}N [‰], **d**) nitrate δ^{18}O [‰], and **e**) nitrate Δ(15-18) [‰] from ASCA16 (circles) and IIEO2 (triangles). The legend provides station latitude. The depth (i.e., pressure) axis is shown at three resolutions to separate the surface, thermocline, and deep waters.

B4. Summertime nitrate isotope ratios in the Agulhas Current. A nearshore summertime transect of the Agulhas Current was sampled in January 2018 onboard the R/V *Nansen*. The transect covers only the seven most shoreward stations of the ASCA16 transect, from 33.34°S to 33.78°S (Figure B7). These data yield two major insights. First, across the transect, thermocline nitrate δ^{15}N is low, between 5‰ and 6‰ (Figure B7c). The δ^{15}N of thermocline nitrate in Tropical Thermocline Water (TTW) is slightly higher than in Subtropical Thermocline Water (STTW) (5.7‰ versus 5.3‰), as is the case for the ASCA16 and SWINGS datasets (Table 3.1, Figure 3.3b and 4c). The similarity of these data to our ASCA16 observations indicates that low-δ^{15}N nitrate is a perennial feature of the Agulhas Current thermocline and that STTW nitrate is consistently lower than TTW nitrate, as similarly demonstrated by the summer SWINGS dataset. Second, high AOU and nitrate concentrations over the shelf break in summer indicate that TTW has been vertically displaced (and compressed) to between 30 and 100 m from between 100 and 200 m where it is typically located (Figure B7a and b versus Figure 3.2a and b). The 26.4 kg.m^{-3} isopycnal (the interface between the thermocline and Subantarctic Mode Water (SAMW); Table 1) is located at 270 m at the most offshore station (33.78°S) and rises to 52 m, the bottom depth at the shelf station (33.34°S). Along the bottom of the shelf and shelf break (33.46°S), nitrate Δ(15-18) is elevated to 3.4-3.5‰, while surface nitrate Δ(15-18) is lower, between -0.1 and 2.7‰. Together, these observations suggests that SAMW upwelled onto the shelf bottom but did not reach the surface to ventilate the shelf. The upwelling of these deeper waters likely explains the vertical displacement of TTW.

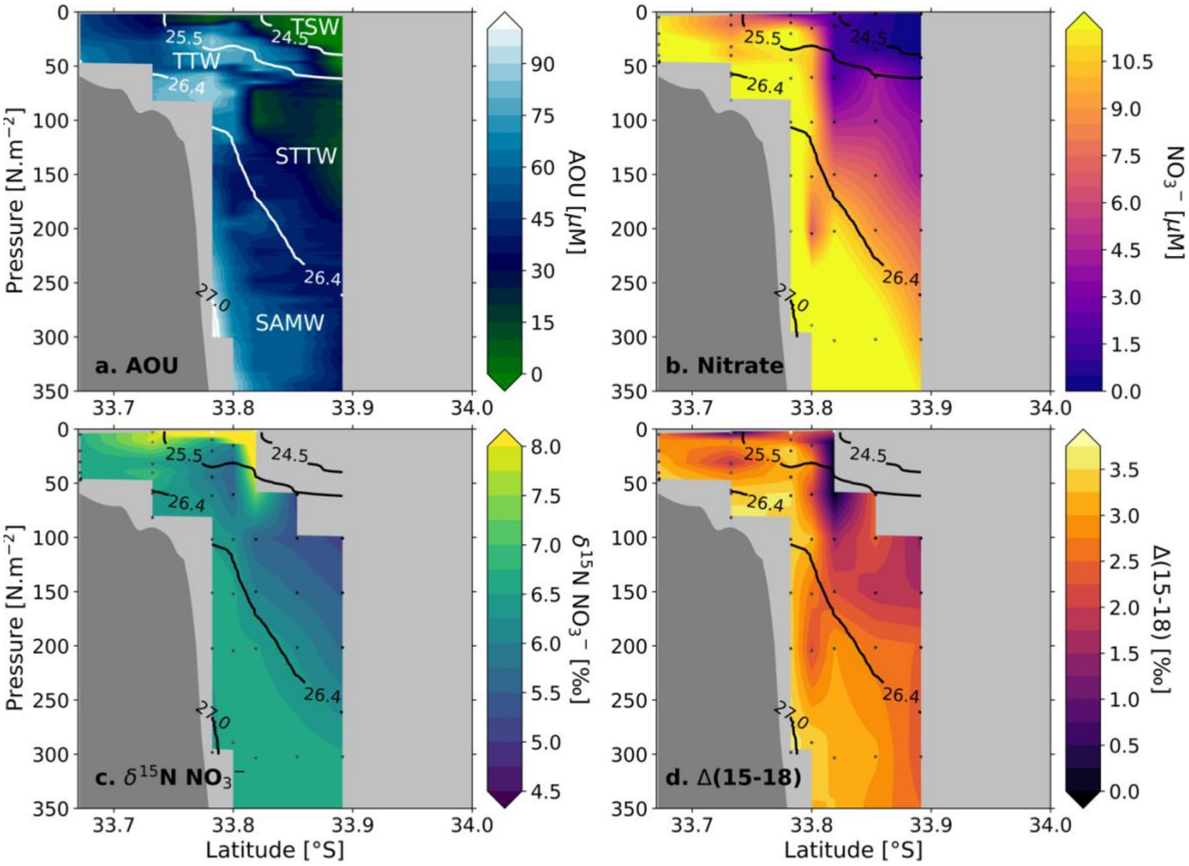

Figure B7. Summertime biogeochemistry across the Agulhas Current. Gridded section plots from the nearshore ASCA 2018 summer transect of **a)** apparent oxygen utilization (AOU) [μM], **b)** nitrate concentration [μM], **c)** nitrate δ^{15}N [‰], and **d)** nitrate Δ(15-18). Black and white contours indicate the isopycnal boundaries of the water masses (Table 3.1). Dark grey points indicate the discrete sampling depths.

B5. Estimating the magnitude of atmospheric nitrogen deposition to the greater Agulhas region. The δ^{15}N of fixed nitrogen (N) in the atmosphere is low, typically ranging between -14‰ and 2‰ (Altieri, et al., 2021). Atmospheric N deposition over the southwest Indian Ocean, if occurring at significant rates, could thus lower thermocline nitrate δ^{15}N and diminish the apparent role of N_2 fixation. The magnitude of the N deposition flux required to lower the Agulhas thermocline nitrate δ^{15}N from 6.9‰, as supplied by Subantarctic Mode Water, to the mean upper water column (σ_θ <26.7 kg.m^{-3}) value of 6.3‰ (also noting the minimum thermocline δ^{15}N of 4.2‰) is 3.0-12.8 Tg N.a^{-1} (this range considers both the minimum and maximum atmospheric N isotope endmembers). This N deposition rate is estimated by first using a two-endmember mixing model to calculate the fraction of atmospheric N required to account for the entirety of the low-δ^{15}N thermocline nitrate in the greater Agulhas region, and then by multiplying this fraction by the water column-integrated nitrate burden. Additionally, we approximate the areal extent of the greater

Agulhas region to be the highly retentive region of thermocline circulation enclosed by the 18 m dynamical height contour (black contour in Figure 3.3.1) of 7.3×10^{12} m^2 and assume a thermocline residence time of four years (i.e., as per the water volume flux estimate in Discussion 4.2.2). Our estimate of the N deposition rate required to lower thermocline nitrate $\delta^{15}N$ from the nitrate source value of 6.9‰ to the mean measured $\delta^{15}N$ of 6.3‰ represents the upper bound of atmospheric deposition. This is because the source waters to the greater Agulhas region likely contribute some amount of low-$\delta^{15}N$ nitrate along with low-nutrient surface waters, neither of which are accounted for by the N isotope mixing model outlined above, thus leading to an overestimation of the required atmospheric N deposition rate. It is nevertheless useful to compare our estimate of the upper bound to modelled N deposition rates.

The available modelled N deposition rates for the region range from 0.02 g $N.a^{-1}$ to 0.42 g $N.m^{-2}.a^{-1}$ and average 0.14 g $N.m^{-2}.a^{-1}$ (Somes, et al., 2016; Jickells, et al., 2017; Okin, et al., 2011), noting that the observational data required to initialize these models are sparse in the greater Agulhas region. This range of N deposition rates equates to an areal rate of 0.1-3.0 Tg $N.a^{-1}$ and a mean of 1.0 Tg $N.a^{-1}$ for the greater Agulhas region. Comparing the N deposition rate required to explain our isotope data to the modelled rates indicates that on average atmospheric N deposition to the greater Agulhas region is too low to account for the $\delta^{15}N$ of thermocline nitrate. This conclusion is consistent with the work of Grand et al. (2015c) that evaluated differences in the N:P ratio of the thermocline and aeolian dust (the latter typically characterized by a very high N:P ratio; (Baker, et al., 2010)) in the southwest Indian Ocean and concluded that the atmospheric deposition rate was far too low to account for the elevated subsurface N* observed in the western subtropical Indian Ocean.

Likewise, the terrestrial nitrogen flux from rivers and/or groundwater also appears to be negligible given the lack of any freshwater signal in our salinity data (Figure 3.3). Additionally, Russo et al. (2019) sampled the southeast African shelf extensively in both summer and winter and found evidence of freshwater input at only one of 38 shelf transects occupied in the summer. The authors attributed this signal to the Mzimvubu River and concluded that its influence penetrated <5 km offshore (i.e., not reaching the Agulhas Current) (Russo, et al., 2019). Moreover, even if there were a significant terrestrial nitrate flux to the Agulhas Current system, its magnitude will be small relative to the volume flux of the Agulhas Current, which transports ~77×10^6 cubic meters of water per second (Beal, et al., 2015). We thus conclude that terrestrial nitrate sourced from the southeast African coastline is highly unlikely to affect the biogeochemistry of the greater Agulhas region.

B6. **WOCE transects sampling the Agulhas region and its source waters.** We use WOCE data to estimate the phosphorus (P) and nitrogen (N) fluxes in the greater Agulhas region (see Discussion 4.2.2 for details and Figure 3.1 for WOCE transect locations).

B6.1. **Tropical source waters**. For the topical source waters, we use the IO4 transect that samples zonally across the southern boundary of the Mozambique Channel along 24°S. Between 32°E and 38°E, a southward propagating Mozambique Channel eddy was sampled (Donohue & Toole, 2003), which represents the tropical source waters entering the greater Agulhas region. To estimate the tropical source water nutrient concentrations, we calculate the mean phosphate and nitrate concentrations over the upper 400 m from across the longitudes that sample the eddy.

B6.2. **Subtropical source waters.** For the subtropical source waters, we use the IO8 transect that samples meridionally across the eastern subtropical gyre along 95°E where the subtropical waters form and are therefore uninfluenced by the greater Agulhas region. To estimate the subtropical source water nutrient concentrations, we calculate the mean phosphate and nitrate concentrations over the upper 400 m from between 29°S and 36°S for the 2007 occupation. During the 2016 occupation of the IO8 transect, strong mesoscale anticyclonic eddies (with u-components of speed >0.4 $m.s^{-1}$) caused downwelling of low-nutrient surface waters to depth, which resulted in low mean nutrient concentrations that unlikely represent the mean condition (see GO-SHIP SADCP repository for details, https://currents.soest.hawaii.edu/go-ship/sadcp/cruises/2016_I08S/index.html). We therefore exclude the 2016 nutrient data from our analysis.

B6.3. **Greater Agulhas region waters.** For the greater Agulhas region waters, we use the IO6 transect that samples meridionally across the Agulhas Current and adjacent recirculating waters along ~30°E. To estimate the Agulhas water nutrient concentrations, we calculate the mean phosphate and nitrate concentrations from between 33°S and 38°S.

B7. The δ^{15}N endmembers and their sensitivity to the N isotope equation in the one-box model. We use the available N isotope data (which are admittedly sparse) from across the South

Indian Ocean to estimate the δ^{15}N of the endmembers that represent the sources and sinks to the upper (<400 m) greater Agulhas region (see Discussion 4.2.2 for details).

B7.1. **Tropical nitrate δ^{15}N**. We set the nitrate δ^{15}N for the Tropical waters to the mean, concentration-weighted nitrate δ^{15}N measured over the upper 400 m of the IIOE2 transect (triangles in Figure 3.1), of 6.4 ± 0.7‰. As there are no measurements of nitrate δ^{15}N from elsewhere in the Mozambique Channel, we take our data as representative of the tropical waters that supply the Agulhas Current. We attribute the low δ^{15}N of this nitrate, relative to underlying Southeast Indian Subantarctic Mode Water (SEISAMW), to N_2 fixation likely occurring both in the channel and in northern tropical waters (i.e., north of the South Equatorial Current). Regardless of where the tropical N_2 fixation signal is generated, it must pass through the Mozambique Channel to enter the Agulhas Current.

B7.2. **Subtropical nitrate δ^{15}N.** We set the nitrate δ^{15}N for the Subtropical waters to the mean, concentration-weighted nitrate δ^{15}N measured over the 26.7-26.85 kg.m^{-3} isopycnal range, which represents SEISAMW in the southeast Indian Ocean (Lu, et al., 2021), of 7.0 ± 0.2‰. These data were collected during the 2016 occupation of IO8 (along ~95E; black, inverted triangles in Figure 3.1) when a mesoscale anticyclonic eddy greatly perturbed the upper 400 m of the water column, reaching down to 800 m. Downwelling and mixing of the low-nutrient (i.e., highly assimilated) surface waters with thermocline water resulted in an anomalously elevated nitrate δ^{15}N, of 7.9‰ (triangle symbols in Figure B8c; (Sigman & Fripiat, 2019)), that is unlikely to be representative of the mean condition (see B6.2). To resolve this, we set the subtropical nitrate δ^{15}N endmember to that of the underlying SEISAMW source that ultimately supplies nitrate to the surface and thermocline (Sarmiento, et al., 2004; Fripiat, et al., 2021).

Only one nitrate δ^{15}N profile exists between IO8 and the greater Agulhas region, along the pathway of the westward South Equatorial Current (15°S, 74°E, Figure 3.1; (Harms, et al., 2019)). Nitrate δ^{15}N from the South Equatorial Current profile and the eastern subtropical gyre profiles show no evidence of N_2 fixation (thermocline nitrate δ^{15}N is >7.0‰). With no available data between the South Equatorial Current and the South East Madagascar Current, we tentatively conclude that the Subtropical waters do not contribute low-δ^{15}N nitrate (i.e., via transport of a remote N_2 fixation signal) into the greater Agulhas region. Data from downstream of the Seychelles-Chagos island chain (i.e., between 50-70°E) would provide a better constraint on the subtropical nitrate δ^{15}N endmember supplied to the greater Agulhas region, but such data do not exist. Additional subtropical (20-27°S) nitrate δ^{15}N measurements from the center of the South Indian basin (black crosses in Figure 3.1; (Harms, et al., 2019)) are remarkably similar to the ASCA16 and SWINGS subtropical profiles and so are not considered source waters to the greater Agulhas region (see B7.3 below).

B7.3. Greater Agulhas nitrate δ^{15}N. We set the nitrate δ^{15}N for the Agulhas waters to the mean, concentration-weighted nitrate δ^{15}N measured over the upper 400 m of the ASCA16 transect (circles in Figure 3.1), of 6.0 ± 1.0‰. The subtropical profiles from the center of the South Indian basin sample between 20°S and 27°S along ~70°E (black crosses in Figure 3.1; (Harms, et al., 2019)). Here, Subtropical Thermocline Water (STTW) is characterised by a mean nitrate δ^{15}N of 5.2 ± 1.1‰ and AOU and nitrate concentration of 27.9 ± 10.5 μM and 1.6 ± 1.3 μM, respectively. These characteristics are similar to STTW sampled during the ASCA16 and SWINGS cruises (Table B1 and B2) and different from STTW in the eastern basin along IO8 (i.e., where nitrate δ^{15}N is >7.0‰; (Sigman & Fripiat, 2019); compare crosses and circles with inverted triangles in Figure B8c). The similar biogeochemical properties measured across the southwest Indian Ocean indicates that the subtropical profiles published by Harms, et al. (2019) cannot provide a source endmember to the greater Agulhas region (i.e., these stations are within the greater Agulhas region) and confirms the retention of subtropical waters in the western basin, extending to 70°E. Moreover, the contrast between eastern and western basin STTW nitrate δ^{15}N highlights basin-scale differences in N cycling.

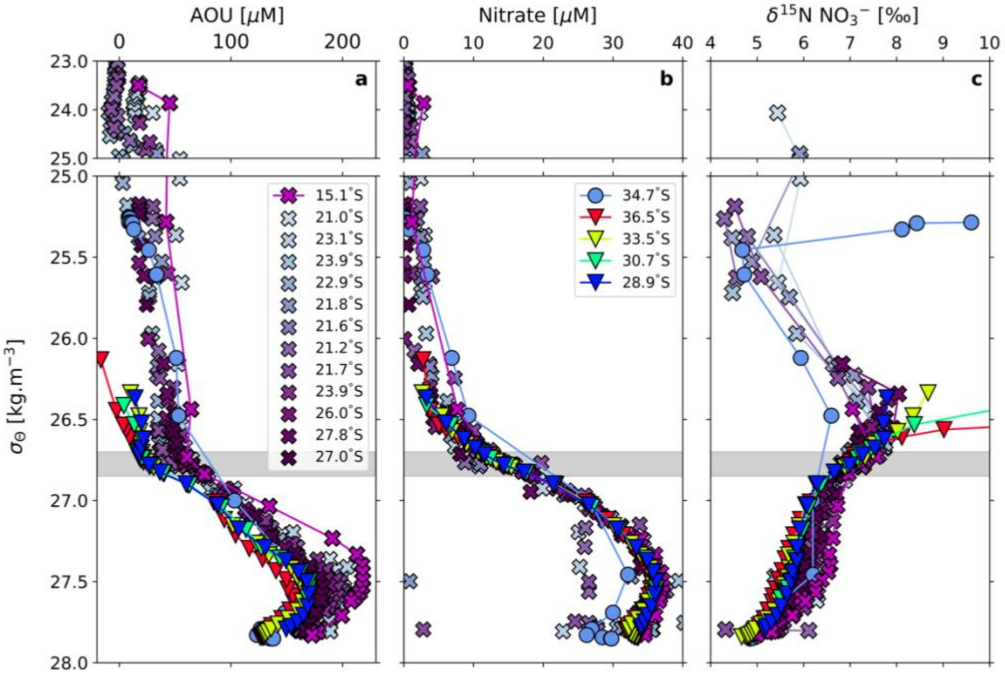

Figure B8. Density profiles of **a)** apparent oxygen utilisation (AOU) [μM], **b)** nitrate concentration [μM], and **c)** nitrate δ^{15}N [‰] for samples collected in the eastern, northern, and central South Indian Ocean (see Figure 3.3.1 for sampling locations). Triangles indicate profiles sampled along 95°E during a WOCE IO8S cruise (Sigman & Fripiat, 2019) and crosses show profiles collected at ~74°E during the MSM-59/2 and SO-259 cruises (Harms, et al., 2019). The light-blue circles show a typical subtropical profile from the greater Agulhas region, included to highlight the difference between the eastern and western basin profiles. Profile latitude is provided in the legend. The y-axis is segmented to highlight the thermocline (σ_θ = 25.0-26.4 kg.m^{-3}). The grey shading indicates the isopycnal range used to calculate the mean properties of Southeast Indian Subantarctic Mode Water (see S7.2). For the eastern basin profiles, no nitrate δ^{15}N data are available for σ_θ <26.2 kg.m^{-3} where the nitrate concentration is <2.65 μM.

B8.1. Calculating uncertainty on the volume, phosphorus, and nitrogen fluxes into and out of the greater Agulhas region. We use a one-box model to estimate the flux of newly-fixed nitrate into the greater Agulhas region (see Discussion 4.2.2). The uncertainty associated with the volume, phosphorus (P), and nitrogen (N) fluxes was calculated by propagating the uncertainty associated with the fluxes of water into and out of the greater Agulhas region and does not include uncertainty associated with the mean nutrient (phosphate and nitrate) concentrations. The volume, P, and N flux uncertainties are provided in Table B3. The mean and uncertainty associated with the organic P sinking flux is 5.3 ± 12.9 mmol.m^{-2}.a^{-1}, the organic N sinking flux is 95.4 ± 233.5 mmol.m^{-2}.a^{-1}, the N flux-based newly-fixed nitrate flux is 70.0 ± 84.7 mmol.m^{-2}.a^{-1}, and the N isotope flux-based newly-fixed nitrate flux is 238.7 ± 157.5 mmol.m^{-2}.a^{-1}.

The uncertainties for the nutrient fluxes are propagated from the volume fluxes. This is because the nutrient concentrations are calculated as an average over the upper 400 m of the water column where the range in phosphate and nitrate concentrations is large.

Table B3. Uncertainty associated with the volume and nutrient fluxes into the greater Agulhas region from the one-box model used to estimate the newly-fixed nitrate flux. Uncertainty is derived through error propagation of the relative volume contributions to the Agulhas Current ± their respective uncertainties (see Discussion 4.2.2 for details).

Box model inputs	**Tropical source waters**	**Subtropical source waters**
Volume fluxes [Sv]	6.2 ± 1.4	17.0 ± 4.9
Phosphate fluxes [mmol.m^{-2}.a^{-1}]	16.1 ± 3.6	43.2 ± 12.4
Nitrate fluxes [mmol.m^{-2}.a^{-1}]	187.6 ± 42.0	497.8 ± 142.8

B8.2. Sensitivity of the newly-fixed nitrate flux to the δ^{15}N of the endmembers. To assess the sensitivity of the newly-fixed nitrate flux to each of the δ^{15}N endmembers, we ran a sensitivity analysis using the standard deviation associated with each endmember. The results are provided in Table B4. The newly-fixed nitrate flux is most sensitive to the δ^{15}N of N_2 fixation, which is unsurprising given the relative magnitude of its uncertainty (of ± 1.0‰) relative to the mean value (of -1‰). The newly-fixed nitrate flux is also sensitive to the δ^{15}N of the greater Agulhas region, which also has a relatively large uncertainty (of 1.0‰) around the mean (of 6.0‰). Surprisingly, the newly-fixed nitrate flux is not particularly sensitive to the δ^{15}N assigned to sinking organic N, which gives us confidence in our choice of value.

Table B4. Sensitivity of the newly-fixed nitrate flux [mmol.m^{-2}.a^{-1}] to the δ^{15}N of the endmembers [‰] used in the nitrogen isotope equation. Each endmember was tested using ± 1 standard deviation around the mean (see B8.2 for details).

δ^{15}N endmember	**Tropical**	**Subtropical**	**Agulhas**	**Sinking**	**N_2 fixation**	**Newly-fixed nitrate flux**
This study	6.4	7.0	6	5.1	-1	238.7
Tropical	6.4 - 0.7	7	6	5.1	-1	107.4
Tropical	6.4 + 0.7	7	6	5.1	-1	370.0
Subtropical	6.4	7.0 - 0.2	6	5.1	-1	139.1
Subtropical	6.4	7.0 + 0.2	6	5.1	-1	388.2
Agulhas	6.4	7	6.0 - 1.0	5.1	-1	898.7
Agulhas	6.4	7	6.0 + 1.0	5.1	-1	-421.3
Sinking	6.4	7	6	5.1 - 0.7	-1	305.4
Sinking	6.4	7	6	5.1 + 0.7	-1	171.9
N_2 fixation	6.4	7	6	5.1	-1 - 1	119.3
N_2 fixation	6.4	7	6	5.1	-1 + 1	2386.7

B9. Euphotic zone-integrated rates of N_2 fixation in the Agulhas Current and adjacent recirculating waters. We directly measured N_2 fixation rates throughout the euphotic zone at select stations across the Agulhas Current and adjacent recirculating waters in winter 2018 (ASCA18; near identical station locations to ASCA16; Figure 3.1). At three euphotic zone depths representing 55%, 10%, and 1% of the photosynthetically available radiation (PAR; measured during CTD down-casts using a PAR sensor), duplicate polycarbonate bottles were filled with 200 µm-prefiltered seawater for direct measurement of the N_2 fixation rate using the "dissolution method" (Mohr, et al., 2010; Klawonn, et al., 2015). Briefly, $^{15}N_2$ gas was added to gas-tight glass bottles that were completely filled with degassed (using helium) 0.2 µm-filtered seawater and agitated to ensure gas dissolution. This $^{15}N_2$-enriched seawater was added to the incubation bottles and an initial subsample was collected in a 20 mL glass vial closed with a gas-tight seal for analysis of $^{15}N_2$ atom % by membrane inlet mass spectrometry (White, et al., 2020). The N_2 fixation bottles were incubated on-deck for 24 hours in a custom-built incubator cooled with continuously running surface seawater and shaded with neutral density filters. Additional 1-L seawater samples were collected from each N_2 fixation depth (but not amended with $^{15}N_2$) and filtered immediately after collection through pre-combusted 0.3 µm glass fibre filters (GF-75s) for analysis of the initial $^{15}N/^{14}N$ ratio of the particulate organic N pool (White, et al., 2020).

The N_2 fixation experiments were terminated by filtration through a 0.3 µm GF-75 filter that was subsequently wrapped in pre-combusted foil and stored frozen at -80°C until analysis. Ashore, filters were oven dried for 24 hours at 45°C, then trimmed with a 20 mm metal punch to remove unused perimeter filter and folded into tin cups. Samples were analysed for PON content and $^{15}N/^{14}N$ using a Thermo Delta V Plus isotope ratio mass spectrometer interfaced with a Flash Elemental Analyser 1112 Series. The volumetric rates of N_2 fixation (nmol L^{-1} d^{-1}) were calculated following (Montoya, et al., 1996), taking into account the initial $^{15}N/^{14}N$ of the PON pool and the measured fractional ^{15}N enrichment of the seawater N_2 at the start of the experiments (White, et al., 2020). The euphotic zone-integrated N_2 fixation rates, computed by integrating between the 55% and 1% PAR rate measurements (with the base of the euphotic zone defined as the penetration depth of 1% of surface PAR (Kirk, 1994)) range from 27.8 to 236.1 μmol N.m^{-2}.d^{-1} (Table B5).

Table B5. Euphotic zone-integrated N_2 fixation rates measured across the ASCA transect in winter 2018 (see B9 for details)**.**

Latitude	Longitude	Euphotic zone depth [m]	N_2 fixation rate [μmol N.m^{-2}.d^{-1}]
33.33°S	27.59°E	20	30.8
33.37°S	27.37°E	20	27.8
33.55°S	27.49°E	45	34.9
33.54°S	27.47°E	80	113.8
35.15°S	28.37°E	80	170.5
34.24°S	28.06°E	70	236.1
34.59°S	28.26°E	120	204.8
35.44°S	28.54°E	120	155.7

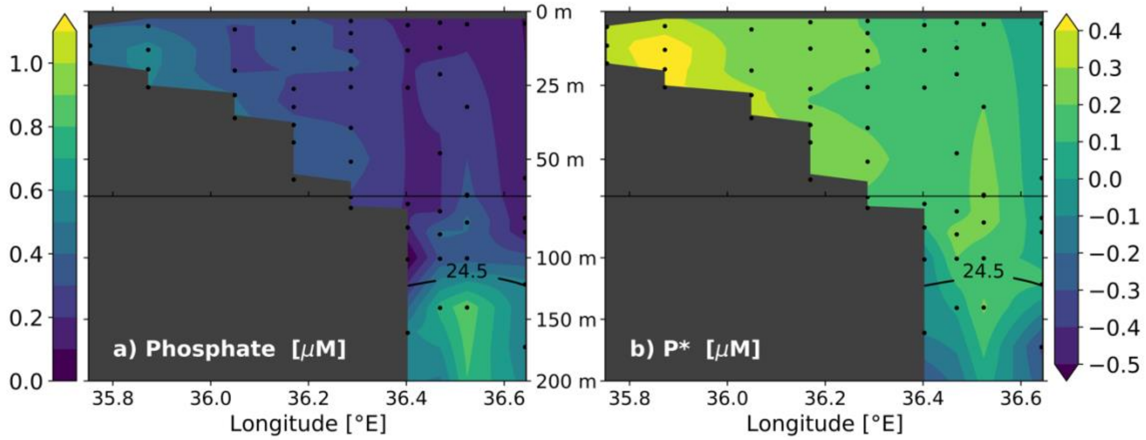

Figure B9. Phosphate and P* concentrations on the western Mozambique Channel shelf. Gridded section plots of a zonal (cross-shelf) transect sampled during the IIEO2 cruise showing **a)** phosphate concentration [μM] and **b)** P* (=[PO_4^{3-}] – [NO_3^-] ÷ 16; (Deutsch, et al., 2007)) [μM]. The y-axis in nonlinear to highlight the shelf concentrations. The black contour indicates the 24.5 kg.m^{-3} isopycnal boundary that separates Tropical Surface Water (above) and Tropical Thermocline Water (below). Dark grey points indicate the discrete sampling depths. Nutrient samples were collected as per those from the Mozambique Channel meridional transect described in Methods 3.2.2 of the main text. Phosphate and nitrate concentrations were measured at the Marine Biogeochemistry Lab at the University of Cape Town (UCT-MBL). Nitrate concentrations were measured using a Lachet QuickChem® Flow Injection Analysis platform with a precision of 0.2 μM and detection limit of 0.12 μM (Grasshoff, et al., 1999). Phosphate concentrations were measured manually using standard colourimetric methods (Grasshoff, et al., 1999; Strickland & Parsons, 1972) and a Genesys 30 Visible spectrophotometer, with a precision of 0.1 μM and a detection limit of 0.05 μM. Aliquots of a certified reference material (JAMSTEC) were included in each autoanalyzer and manual run to ensure measurement accuracy.

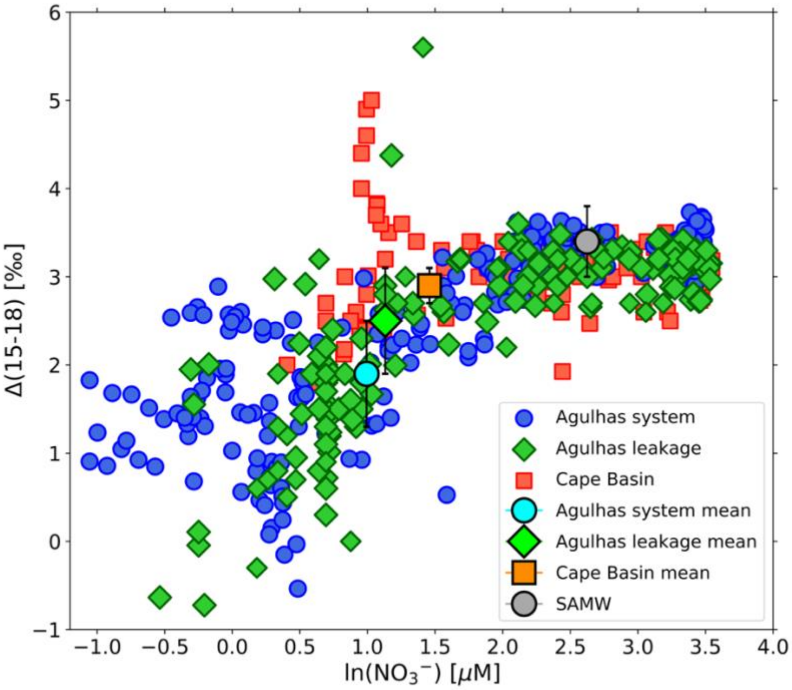

Figure B10. The Δ(15-18) of nitrate in the greater Agulhas region, Agulhas leakage, and background Cape Basin. Nitrate Δ(15-18) [‰] vs ln([NO$_3^-$]) [μM] for the ASCA16 and Cape Basin data. Symbol colour and shape indicate the sampling region. The mean ln([NO$_3^-$]) and concentration-weighted nitrate Δ(15-18) values for each region (for σ_θ<26.4 kg.m^{-3}) are shown in a lighter shade and outlined in black. The bold grey circle outlined in black shows the mean ln([NO$_3^-$]) and concentration-weighted nitrate Δ(15-18) measured for Subantarctic Mode Water (SAMW). The data from the Cape Basin are detailed in Figure 3.8. Figure B10 clearly shows that shallow nitrate in Agulhas leakage retains much of the low-Δ(15-18) signal that is characteristic of the greater Agulhas region even as it mixes with generally higher-Δ(15-18) Cape Basin nitrate.

Chapter 4: Agulhas Current dynamics enhance upward nitrate supply in the southwest subtropical Indian Ocean

Abstract

The Agulhas Current, like other western boundary currents (WBCs), transports nutrients from the tropics to the subtropics in a subsurface “nutrient stream”. Subtropical surface waters receive these nutrients during seasonal convective mixing that fuels a brief period of productivity before phytoplankton become nutrient-limited. Episodic mixing events can temporarily alleviate nutrient scarcity by vertically entraining deep nutrients into surface waters. However, our mechanistic understanding of these nutrient fluxes is limited, due to both the rapidity and small distances over which the fluxes occur. Here, we use a novel application of nitrate Δ(15-18), the difference between the nitrogen and oxygen isotope ratios of nitrate, to characterize three (sub)mesoscale mechanisms of upward nitrate supply across the Agulhas Current in winter: 1) mixing at the edges of an anticyclonic eddy, 2) inshore upwelling likely resulting from submesoscale meanders of the Agulhas Current, and 3) entrainment at the edge of the current core likely driven by coupled mesoscale-submesoscale instabilities. All three events manifest as upward injections of high-Δ(15-18) nitrate into the thermocline and surface where nitrate Δ(15-18) is low; at times, these entrainment events are not apparent in the other co-collected physical and biogeochemical data. The physical dynamics driving the nitrate supply events are common to all WBCs, implying that nitrate entrainment facilitated by WBCs is quantitatively significant and supports productivity in the subtropical gyres. A future rise in energy across WBC systems may increase these nutrient fluxes, partly offsetting the predicted stratification-induced decrease in subtropical ocean fertility.

Plain Language Summary

Strong and fast-flowing currents transport heat, salt, and nutrients from the warm tropical ocean to the cooler subtropics along the western boundary of all ocean basins. Productivity in the subtropics is limited by nutrients such as nitrogen, which are trapped below the sunlit surface layer due to strong temperature differences between the upper layer and the waters beneath. Wind-driven mixing in winter/spring temporarily erodes this temperature gradient, supplying nutrients to the surface that are rapidly consumed by phytoplankton. Short-lived and small-scale mixing events may significantly enhance the seasonal nutrient supply in and around highly energetic western boundary currents, although such events have proven difficult to observe. Here, we use nitrate isotope ratios to identify three mechanisms of deep nutrient supply to the surface waters of the Agulhas Current, the western boundary current of the South Indian Ocean. These mechanisms include upward mixing of nutrients at the edges of an eddy, upwelling of deep,

nutrient-rich water onto the continental shelf inshore of the current, and subsurface mixing of nutrient-rich water at the edge of the current's rapidly-flowing core. It is likely that similar nutrient supply events occur in all western boundary current systems, thereby enhancing subtropical ocean productivity.

4.1. Introduction

The ocean's major western boundary currents (WBCs) form the poleward limb of subtropical gyre circulation (Figure 4.1). WBCs transport significant volumes of water (30-100 Sv; 1 Sv = 10^6 $m^3.s^{-1}$) from the warm low-latitude ocean to the cooler high latitudes, thereby redistributing heat and regulating climate (Yu & Weller, 2007; Imawaki, et al., 2013). WBCs also transfer high concentrations of nutrients from the low- to high latitudes via subsurface "nutrient streams", a phenomenon that has been observed in the Gulf Stream, the Kuroshio Current, and recently, the Agulhas Current (Pelegrí & Csanady, 1991; Guo, et al., 2012; Marshall, et al., 2023). Thermal stratification of the upper subtropical water column confines these nutrients below the surface mixed layer such that physical processes such as turbulent mixing and diffusion are required to deliver them into sunlit waters where they fuel biological productivity (Williams & Follows, 2003; Palter, et al., 2013).

The surface waters of the subtropical gyres receive nutrients such as nitrate via deep convective mixing in winter and/or spring (Williams & Follows, 2003; Williams, et al., 2006; Lomas, et al., 2013). In summer through autumn when stratification impedes the upward nitrate supply, phytoplankton growth is thought to be predominantly supported by nutrients that are recycled within the mixed layer (e.g., ammonium) (Menzel & Ryther, 1960; Lipschultz, et al., 2002; Brix, et al., 2006). However, geochemical estimates of primary production in subtropical systems are higher than can be supported by the nutrients supplied by seasonal mixing and N_2 fixation, the latter process referring to the biologically mediated conversion of N_2 gas to bioavailable nitrogen (N) (Jenkins & Goldman, 1985; Emerson, et al., 2001; Stanley, et al., 2015). This discrepancy has led to the discovery that (sub)mesoscale mixing events (scales 1-100 km, hours to months), in addition to other microbially-mediated processes (Johnson, et al., 2010; Fawcett, et al., 2018), are quantitatively important for nutrient supply in the subtropics (Jenkins, 1988a; Falkowski, et al., 1991; McGillicuddy, et al., 1998; Lipschultz, et al., 2002). Yet, the mechanisms and magnitudes of these episodic nutrient fluxes remain uncertain, largely because of the difficulties associated with observing and modeling at this scale (Lévy, et al., 2018).

WBC systems are characterised by high velocity shears and elevated eddy kinetic energy (Figure 4.1) (Ducet, et al., 2000; Imawaki, et al., 2013; Martínez-Moreno, et al., 2021). Both horizontal and vertical mixing at the mesoscale (10-100 km) and submesoscale (1-10 km) have been observed in these systems (D'Asaro, et al., 2011; Lévy, et al., 2012; Gula, et al., 2016). The horizontal flux of nutrients from WBC streams to adjacent subtropical gyres via eddies, advection, and diffusion is significant (Palter, et al., 2013; Yamamoto, et al., 2018). These lateral nutrient fluxes increase basin-scale productivity and at times even enhance carbon export to the deep ocean (Palter, et al., 2011; Letscher, et al., 2016; Conway, et al., 2018; Yamamoto, et al., 2018; Williams & Follows, 1998). For example, the Gulf Stream has been shown to laterally advect iron and phosphorus into the adjacent North Atlantic subtropical gyre where their entrainment into the mixed layer stimulates N_2 fixation (Palter, et al., 2011; Conway, et al., 2018). The vertical nutrient flux from WBC subsurface nutrient streams to overlying oligotrophic surface waters has received less attention (cf. (Nagai, et al., 2019; Liao, et al., 2022)). Numerous characteristics of WBCs favour upward nutrient supply, such as 1) strong cross-stream isopycnal shoaling of nutrient-rich thermocline waters (Pelegrí & Csanady, 1991; Guo, et al., 2012; Marshall, et al., 2023), 2) the occurrence of upwelling-favourable winds and wind curl (Imawaki, et al., 2013; Leber, et al., 2017), 3) high (sub)mesoscale eddy and frontal activity driven by strong density and velocity gradients (Imawaki, et al., 2013; Lévy, et al., 2018; Tedesco, et al., 2019; Lazaneo, et al., 2020), and 4) steep bathymetry and boundary effects (Schaeffer, et al., 2013; Liao, et al., 2022).

One challenge to understanding upward nitrate supply at the (sub)mesoscale is the paucity of nutrient data collected at the spatial- and/or temporal resolution of such patchy and intermittent events (Palter, et al., 2013; Lévy, et al., 2018). Another challenge is the short timescales (hours to days) of the various and often overlapping biological processes that act on the nitrate pool (Lévy, et al., 2018), as well as mixing and advection of different nitrate sources. The parameter nitrate Δ(15-18), defined as the difference between the N and oxygen (O) isotope ratios of nitrate (i.e., Δ(15-18) = δ^{15}N – δ^{18}O (Sigman, et al., 2005; Rafter, et al., 2013); where $\delta^{15}N = [(^{15}N/^{14}N)_{sample}/(^{15}N/^{14}N)_{reference}-1]\times10^3$ vs. N_2 in air and $\delta^{18}O = [(^{18}O/^{16}O)_{sample}/(^{18}O/^{16}O)_{reference}-1]\times10^3$ vs. VSMOW, both in ‰) may offer a novel solution to these challenges. During mixing, the concentration-weighted nitrate Δ(15-18) is conserved (Rafter, et al., 2013). Mixing of waters with different nitrate Δ(15-18) values will yield a combined water parcel with a Δ(15-18) that is the nitrate concentration-weighted mean of the source waters. Phytoplankton assimilation of nitrate in surface waters also conserves its Δ(15-18) even as its concentration declines (to an analytical

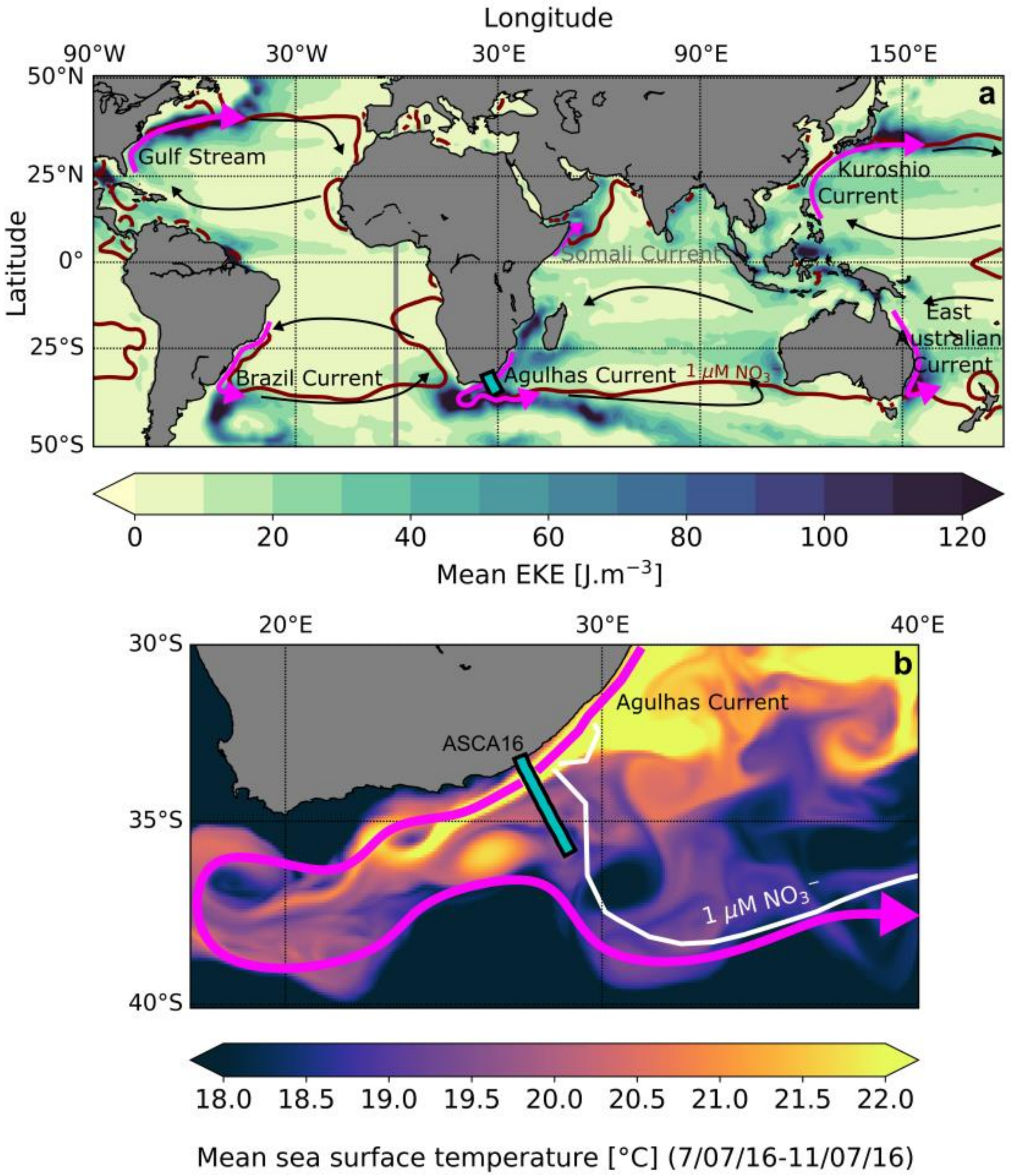

Figure 4.1. High mixing potential and strong nutrient fronts along the ocean's western boundaries. a) Mean eddy kinetic energy (EKE; shading) [J.m^{-3}] derived from monthly-averaged Aviso^{+} altimetry products from 1993-2019 (Martínez-Moreno, et al., 2021). The five major western boundary currents are labelled; Gulf Stream, Brazil Current, Agulhas Current, Kuroshio Current, and the East Australian Current. The seasonal (i.e., monsoon-influenced) Somali Current, the western boundary current of the North Indian Ocean, is shown with a dashed arrow. **b**) Sea surface temperature for the Agulhas Current region averaged over the sampling period, 7-11 July 2016 (shading; data from CMEMS; https://doi.org/10.48670/moi-00021). In both panels, the location of the ASCA16 sampling line is shown in blue. The maroon and white contours indicate the 1 μM surface nitrate concentration in panel **a** and **b**, respectively, with surface nitrate concentrations increasing poleward (data from World Ocean Atlas 2018; (Garcia, et al., 2018)).

limit for measurements of nitrate isotope ratios of ~0.3 μM nitrate) because assimilation raises nitrate δ^{15}N and δ^{18}O in unison (Granger, et al., 2004; Granger, et al., 2010). In other words, the Δ(15-18) of nitrate mixed up into a low-nutrient surface layer will not change during the period of nitrate drawdown by phytoplankton (hours to days in an oligotrophic setting), even as the concentration of nitrate declines and its δ^{15}N and δ^{18}O rise. Other biological processes, such as organic matter remineralisation back to nitrate, do not conserve nitrate Δ(15-18) (Rafter, et al., 2013). As such, nitrate Δ(15-18) can reveal information about events of upward nitrate supply over small to large spatial and temporal scales.

Here we use measurements of nitrate concentration and isotope ratios along with hydrographic data from a transect of the Agulhas Current and adjacent subtropical waters (ASCA16; Figure 4.1) sampled in winter to characterize local events of vertical nitrate supply. We focus our discussion on the nitrate Δ(15-18) data and the application of nitrate Δ(15-18) as a tracer of upward nitrate supply. A more detailed discussion of Agulhas Current nitrate δ^{15}N and δ^{18}O, including their use for diagnosing local and remote Indian Ocean N cycling, can be found in (Marshall, et al., 2023). Our high-resolution dataset reveals evidence of three physical mechanisms of recent and ongoing nitrate supply occurring at the (sub)mesoscale across the Agulhas Current: 1) eddy-edge entrainment, 2) inshore upwelling, and 3) (sub)mesoscale overturning at the edge of the current core. All three mechanisms may contribute significantly to fueling productivity in the Agulhas Current system.

4.2. Methods

Hydrographic data (i.e., absolute salinity, density, oxygen concentrations) and samples for nitrate concentrations and isotope ratios were collected in winter (July) 2016 during an Agulhas System Climate Array occupation (ASCA16) onboard the R/V *SA Agulhas II* (Marshall, et al., 2023). Twenty full-depth stations (4-25 km apart) were sampled between 33.3°S and 35.7°S along ~28°E (Figure 4.1). The hydrographic data were measured using Conductivity-Temperature-Depth-Oxygen (CTDO) sensors attached to a Seabird 9/11+ rosette. Apparent oxygen utilisation (AOU; $= O_{2\text{saturated}} - O_{2\text{observed}}$) was derived from the CTDO data. Velocity data were collected using a ship-mounted 75 kHz Teledyne RD acoustic Doppler current profiler (ADCP). The ADCP data were rotated to acquire the along-shore current speed and binned into 10 m depth intervals, except over the upper 45 m where the values are an extension of the shallowest measurements available. Inferred vertical velocity was estimated as the depth integration (in 10 m bins) of along-track horizontal convergence, assuming that gradients in the along-track flow were small (i.e., $\frac{\partial \mathrm{u}}{\partial \mathrm{x}} = -\frac{\partial \mathrm{w}}{\partial \mathrm{z}}$; where $\frac{\partial \mathrm{v}}{\partial \mathrm{y}}$ is negligible). This assumption is valid in the Agulhas Current because variance in the along-stream flow during non-meandering (i.e., geostrophic flow) conditions is particularly low (~11%; (Elipot & Beal, 2015)). However, the error associated with ship-mounted ADCP data is between 0.03 and 0.1 m.s^{-1} (e.g., (Beal, et al., 2008)), which is the same order of magnitude as the maximum vertical velocities previously measured in the current (Leber & Beal, 2015). As such, our inferred vertical velocities cannot be taken as an accurate measure of the magnitude of upwelling or downwelling, but can instead be used alongside our other data as an indication of the patterns in upwelling and downwelling (i.e., sign changes). Because of this limitation, the vertical velocity data cannot be used to quantify the upward nitrate fluxes. Stratification was quantified by the buoyancy frequency squared (N^2). The mixed layer depth (white circles in Figure 4.2) was determined as the depth at which both potential density (binned to 1 m resolution) and nitrate concentration (discrete measurements) first showed a sharp change in gradient.

Seawater samples for nitrate concentrations and isotope ratios were collected throughout the water column in thoroughly rinsed 60 ml high-density polyethylene bottles. Nitrate+nitrite concentrations were measured shipboard using a Lachat QuickChem® flow injection autoanalyzer (Grasshoff, 1976) with a precision of 0.2 μM and detection limit of 0.1 μM. Nitrite concentrations were measured manually using standard colorimetric methods (Grasshoff, 1976; Strickland & Parsons, 1972) with a precision of 0.1 μM and a detection limit of 0.05 μM. Aliquots of certified reference materials (JAMSTEC) were included in each run to ensure measurement accuracy. The nitrate concentrations were calculated by subtraction. Hereafter, all references to nitrate concentrations are to the nitrate-only data.

After collection, the nitrate isotope samples were immediately frozen at -20°C. Nitrate isotope ratios, following nitrite removal (Granger & Sigman, 2009), were measured using the denitrifier method (Sigman, et al., 2001; Casciotti, et al., 2002) and a Thermo MAT 253 isotope ratio mass spectrometer interfaced with a custom-built online N_2O extraction and purification system (Weigand, et al., 2016). International reference materials, IAEA-N3 and USGS-34 (Gonfiantini, 1984; Böhlke, et al., 2003), as well as an in-house N_2O standard, were run in parallel with the samples. The pooled standard deviations of replicate measurements of nitrate $\delta^{15}N$ and $\delta^{18}O$ (for all samples with a nitrate concentration >0.35 μM) were 0.1‰ and 0.2‰, respectively.

4.3. Observations

4.3.1. The dynamics of the Agulhas Current

During our sampling of the ASCA16 transect, the Agulhas Current is located immediately offshore of the continental slope, with south-westward along-shore speeds reaching 2.1 $m.s^{-1}$ (Figure 4.2a). We delineate the core of the current by the -1 $m.s^{-1}$ isotach, which reaches ~300 m depth (red contour in Figure 4.2). The current core is characterised by strong horizontal velocity and density shears (Figure 4.2a-d; (Beal & Bryden, 1999; Beal, et al., 2006)), and a shallow mixed layer depth (mean of 59 m; Figure 4.2). The sharp velocity gradients indicate regions of potential horizontal convergence and divergence and/or along-shore variability (see Methods). Given the typically limited variance in the along-shore flow (~11%) of the Agulhas Current (Elipot & Beal, 2015), we infer upwelling and downwelling cells only where our other data (e.g., density, AOU, and nitrate Δ(15-18)) are consistent with this interpretation (see below).

The surface layer is well-mixed, as indicated by low values of N^2, while the thermocline is characterised by elevated stratification, particularly immediately below the mixed layer (Figure 4.2c). The strongest stratification is apparent just below the mixed layer within the core of the Agulhas Current where density surfaces slope upward most sharply. Across the upper Agulhas Current (σ_θ <26.4 $kg.m^{-3}$ or <180-480 m), warm, fresh, low-density, high-nutrient waters sourced from the tropics dominate the inshore side of the current, while offshore are cooler, saltier, denser, lower-nutrient subtropical waters (Figure 4.2; (Beal, et al., 2006; Marshall, et al., 2023)). These inshore and offshore waters are constrained from lateral mixing by a strong horizontal potential vorticity gradient across the upper Agulhas Current (Beal & Bryden, 1999; Beal, et al., 2006).

4.3.2. Biogeochemical signals in the water masses of the upper Agulhas Current

Across the southwest Indian Ocean, Subantarctic Mode Water (SAMW; $26.4<\sigma_\theta<27.0$) is the ultimate source of nutrients to the overlying thermocline and surface layer (Sarmiento, et al., 2004; Fripiat, et al., 2021; Marshall, et al., 2023). Due to the geostrophic balance typically maintained by the Agulhas Current, isopycnals shoal toward the coast. At the time of our sampling, SAMW rises from 460 m at the most offshore station of the transect to 160 m on the continental slope (Figure 4.2d). Here, this water mass is characterised by a relatively high mean nitrate concentration of 13.8 μM, $\delta^{15}N$ of 6.9‰, $\delta^{18}O$ of 3.5‰, and Δ(15-18) of 3.4‰ (Marshall, et al., 2023), which distinguish it from the overlying surface and thermocline waters that are lower in all these variables (Figure 4.2g-j).

Two thermocline waters overlie SAMW. Tropical Thermocline Water ($24.5<\sigma_\theta<26.4$, <33.78°S; Figure 4.2d) occupies the inshore side and most of the core of the Agulhas Current and is easily identifiable by a well-conserved subsurface signal of high AOU (>60 μM) generated by intense remineralisation in and upstream of the Mozambique Channel (Figure 4.2f) (Marshall, et al., 2023). Tropical Thermocline Water is fresh and nutrient-rich, with a mean salinity, AOU, and nitrate concentration of 35.6 $g.kg^{-1}$, 73.9 μM, and 7.8 μM, respectively (Figure 4.2e-g). By contrast, the Subtropical Thermocline Water ($25.5<\sigma_\theta<26.4$, >33.78°S; Figure 4.2d) that dominates the offshore side of the Agulhas Current is relatively salty and nutrient-poor, with a mean salinity, AOU, and nitrate concentration of 35.7 $g.kg^{-1}$, 29.9 μM, and 3.0 μM, respectively (Figure 4.2e-g). Both thermocline waters are low in nitrate $\delta^{15}N$ (and $\delta^{18}O$), with the lower $\delta^{15}N$ of subtropical than tropical thermocline nitrate (4.9‰ vs. 5.8‰) yielding a lower Δ(15-18) (2.1‰ vs. 3.2‰, with a combined mean of 2.6‰) (Figure 4.2h-j). The low $\delta^{15}N$ and Δ(15-18) of Agulhas thermocline nitrate are generated mainly by local N_2 fixation (Marshall, et al., 2023). Newly-fixed organic matter has a $\delta^{15}N$ of ~-1‰ (Hoering & Ford, 1960; Minagawa & Wada, 1986; Carpenter, et al., 1997), which is low compared to the $\delta^{15}N$ of subsurface nitrate (typically 3-7‰; (Sigman, et al., 1999; Knapp, et al., 2008; Fripiat, et al., 2021)). Remineralisation of this organic matter in the thermocline will yield newly nitrified nitrate that is similarly low in $\delta^{15}N$ (Knapp, et al., 2005). The $\delta^{18}O$ of the remineralised nitrate will be ~1.1‰ because it is set by the $\delta^{18}O$ of seawater (of ~0‰) plus an isotopic offset of ~1.1‰ (Sigman, et al., 2009a; Buchwald, et al., 2012; Boshers, et al., 2019). As such, N_2 fixation lowers the $\delta^{15}N$ of nitrate more than it lowers the $\delta^{18}O$, thus also decreasing nitrate Δ(15-18).

Near the base of the mixed layer at the top of the thermocline ($\sigma_\theta \approx 25.5$), nitrate $\delta^{15}N$ and $\delta^{18}O$ begin to rise yet Δ(15-18) decreases further. This trend can be explained by co-occurring partial nitrate assimilation and nitrification (Marshall, et al., 2023), which approximately conserves the $\delta^{15}N$ of nitrate while raising its $\delta^{18}O$, thereby decreasing Δ(15-18) (Fawcett, et al., 2015; Deman, et al., 2021).

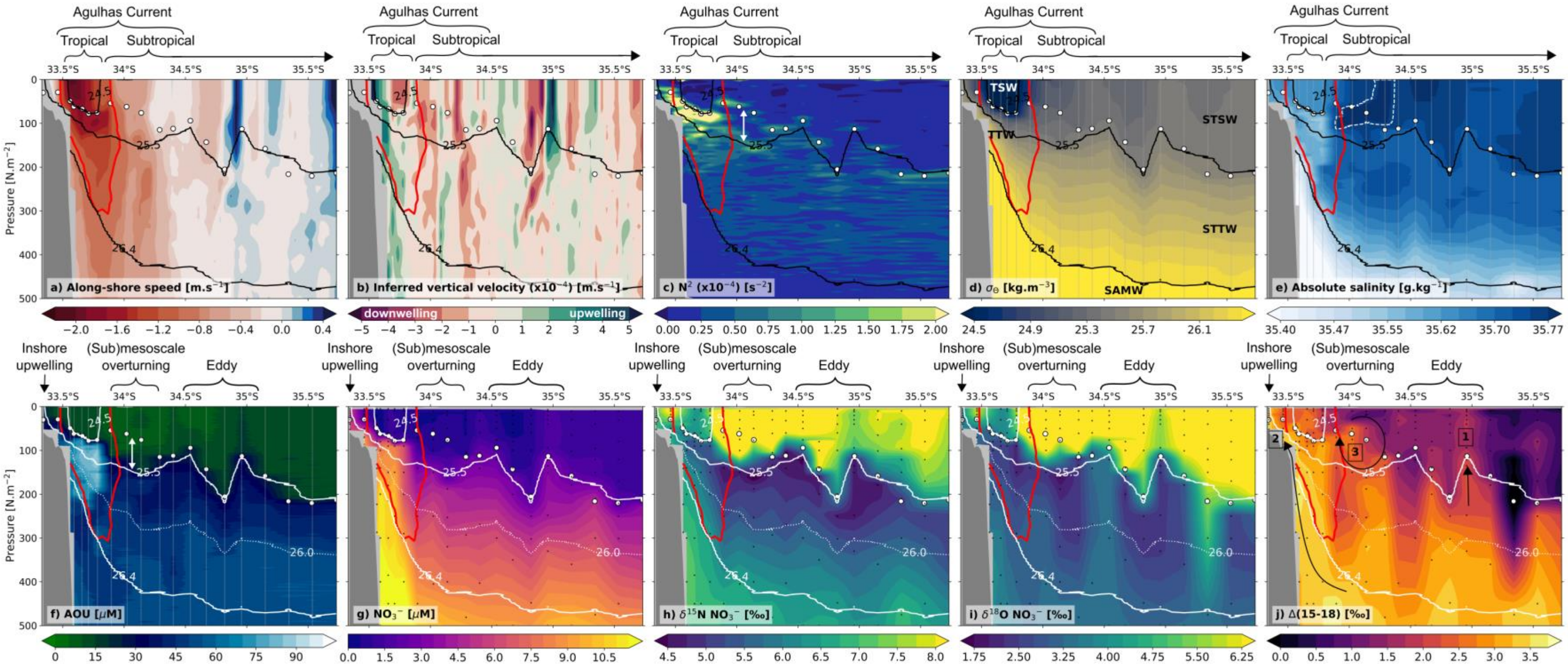

Figure 4.2. Cross-stream features of the Agulhas Current. Gridded section plots from the ASCA16 transect showing **a)** along-shore speed [m.s^{-1}] from shipboard ADCP, **b)** inferred vertical velocity ($\times 10^{-4}$) [m.s^{-1}], **c)** stratification (N^2; $\times 10^{-4}$) [s^{-2}], **d)** potential density anomaly (σ_θ) [kg.m^{-3}], **e)** absolute salinity [g.kg^{-1}], **f)** apparent oxygen utilization (AOU) [μM], **g)** nitrate concentration [μM], **h)** nitrate δ^{15}N [‰], **i)** nitrate δ^{18}O [‰], and **j)** nitrate Δ(15-18) [‰]. Above the top panels, the positions of the Agulhas Current and tropically- and subtropically sourced waters are annotated. The red contour represents the -1 m.s^{-1} isotach and indicates the position of the Agulhas Current core. White circles show the mixed layer depth, and where relevant, black points indicate discrete water sample depths. White and black solid contours denote the isopycnal boundaries of water masses [kg.m^{-3}], as labelled on panel **d**. TSW: Tropical Surface Water; STSW: Subtropical Surface Water; TTW: Tropical Thermocline Water; STTW: Subtropical Thermocline Water; SAMW: Subantarctic Mode Water. The white dotted contour included in the bottom panels shows the position of 26.0 kg.m^{-3} isopycnal, the approximate divide between the upper and lower subtropical thermocline waters. The bold numbers (1-3) and black arrows on panel **j** indicate the three nitrate supply events discussed in the text, which are also annotated above the bottom row of panels and represented in Figure 4.3

In the surface layer, the Agulhas Current swiftly transports well-mixed fresh Tropical Surface Water (σ_θ<24.5) alongside salty Subtropical Surface Water (σ_θ<25.5) (Figure 4.2a, c-e; (Beal, et al., 2006; Marshall, et al., 2023)). The mixed layer depth roughly coincides with the base of these surface waters, except near the offshore edge of the current core at ~34°S (Figure 4.2d). Both surface waters are characterised by low nitrate concentrations (mean of <1.0 μM) and high nitrate δ^{15}N and δ^{18}O, of >7.7‰ and >6.2‰, respectively (Figure 4.2g-i), due to phytoplankton assimilation of nitrate. This process raises nitrate δ^{15}N and δ^{18}O in unison, thus conserving the Δ(15-18) of the nitrate source as the nitrate concentration declines (Granger, et al., 2004; Granger, et al., 2010; Rohde, et al., 2015; Sigman, et al., 1999). Compared to the whole thermocline, surface water nitrate Δ(15-18) is low (mean of 1.5‰) because partial nitrate assimilation and nitrification overlap at the top of the thermocline, which is also the isopycnal that represents the immediate nitrate supply to surface waters (Figure 4.2j).

Across the transect, nitrate Δ(15-18) is not uniform, particularly in the mixed layer (Figure 4.2j). The horizontal distribution of nitrate Δ(15-18) cannot be fully attributed to the lateral advection of source waters, nor in situ biological processes. For example, upstream of the transect, thermocline nitrate Δ(15-18) is similarly lowbecause the multi-year residence time of thermocline water in the greater Agulhas Current system (Karstensen & Tomczak, 1997; Fine, et al., 2008)means that the signal of N_2 fixation is imprinted on its nitrate across the region (Harms, et al., 2019; Marshall, et al., 2023). As such, anomalously high-Δ(15-18) nitrate in the surface and subsurface, some incidences of which protrude through isopycnal surfaces (bold numbers on Figure 4.2j), signals a local upward supply of higher-Δ(15-18) nitrate from below the mixed layer.

4.4 Events of upward nitrate supply into the sunlit waters of the Agulhas Current

4.4.1. A mesoscale eddy injects nitrate into the surface waters at its edges

We observe evidence of upward nitrate supply to the surface waters at the periphery of a mesoscale anticyclonic eddy that was present just offshore of the Agulhas Current during our sampling (box 1 on Figure 4.2j). Satellite-derived SST data indicate that we sampled the trailing-edge of this south-westward propagating eddy (Figure 1b). The eddy is located between 34.5°S and 35°S (i.e., ~50 km in diameter) and perturbs the isopycnals from the surface to ~400 m depth (Figure 4.2d). The mixed layer depth at the core of the eddy is 100 m deeper than at its edges, forming a bolus of lower-density well-mixed surface waters surrounded by strongly stratified thermocline waters (Figure 2c). Convergence at the core of the eddy (negative values of vertical velocity in Figure 4.2b) downwells surface-water properties to ~200 m. This convergence is balanced by divergence at the edges of the eddy, particularly at the offshore edge (at 35°S) where there is a narrow northward jet reaching >0.4 m.s^{-1} (Figure 4.2a and b). The upward vertical velocities coincide with elevated mixed-layer nitrate concentrations of 1.7 μM, compared to 0.9 μM outside the eddy (Figure 4.2b and g). Nitrate supplied to N-limited, light-replete surface waters will be rapidly consumed by phytoplankton (i.e., within hours of supply). The elevated mixed-layer nitrate concentrations at the eddy edges thus indicate ongoing upward nitrate supply. The strong upwelling at the offshore edge of the eddy is also where the 25.4 kg.m^{-3} isopycnal surfaces (not shown) and mixed layer AOU, nitrate concentration, and nitrate Δ(15-18) are high (while nitrate δ^{15}N and δ^{18}O are low) compared to in the adjacent surface waters (box 1 on Figure 4.2j). These signals are consistent with ongoing upward entrainment of higher-nitrate waters from the thermocline.

Anticyclonic eddies have been shown through observed and modeled fields (typically of chlorophyll-a distributions) to enhance local productivity (Moore, et al., 2007; Kolasinski, et al., 2012; Dufois, et al., 2016; He, et al., 2017; Lovecchio, et al., 2022). However, observations of elevated nitrate concentrations at the surface of solitary anticyclonic eddy edges (i.e., not eddy dipoles) are scarce. Using nitrate Δ(15-18) as a tracer, we show that nitrate can be injected upwards from as deep as 100 m below the mixed layer at the edge of an eddy. We expect that cyclonic eddies would similarly induce an upward nitrate flux into the mixed layer at their cores. Given the ubiquity of eddies in the Agulhas Current system, the annual eddy-driven nitrate flux to surface waters is likely significant. We thus expect this nitrate supply to fuel considerable regional productivity, as has been observed for Agulhas eddies that have “leaked” into the South Atlantic (Wallschuss, et al., 2022).

4.4.2. Inshore upwelling entrains deep nitrate onto the continental shelf

We observe elevated nitrate concentrations throughout the water column at the most inshore shelf station at the time of sampling (mean nitrate concentration of 5.9 μM, bottom depth of 52 m) (box 2 on Figure 4.2j). Concurrently, isopycnals located at 200-400 m offshore rise steeply towards the surface at the inshore stations, even outcropping in the case of the 25.5 kg.m^{-3} isopycnal (Figure 4.2d), which is necessary for the Agulhas Current to maintain geostrophic balance. The upwelling of relatively nitrate-rich (3-10 μM) thermocline waters can explain the elevated on-shelf nitrate concentration, indicating entrainment of nitrate from below the mixed layer. The inferred upward vertical velocities against the continental margin (Figure 4.2b), driven by an onshore component of the current's flow during our occupation (not shown), are consistent with ongoing inshore upwelling.

The nitrate isotope ratios at the shelf station yield further information about the source and intensity of the upwelling that cannot be gleaned from our other data (box 2 on Figure 4.2j). While the elevated nitrate concentrations and tilted isopycnals suggest upwelling of thermocline waters, the nitrate δ^{15}N, δ^{18}O, and Δ(15-18) — with means of 7.0‰, 3.7‰, and 3.4‰, respectively — more closely resemble the SAMW that underlies the thermocline (Figure 4.2h-j). Indeed, the on-shelf nitrate δ^{15}N and δ^{18}O are 1.2-2.1‰ and 0.9-1.0‰ higher than the thermocline values. Partial assimilation on the shelf of upwelled thermocline nitrate could explain the elevated δ^{15}N and δ^{18}O and lower nitrate concentration but not the higher Δ(15-18) of the on-shelf- versus thermocline nitrate (3.4‰ vs. a mean of 2.6‰). We thus conclude that the shelf was being actively flushed at the time of our sampling with SAMW, which has a nitrate Δ(15-18) of 3.4‰ (and δ^{15}N of 6.9‰ and δ^{18}O of 3.5‰). On-shelf mixing of upwelled SAMW with the extant low-density and low-nitrate water (likely Tropical Surface Water) would lower the density and nitrate concentration of the mixture without noticeably changing its isotopic composition, consistent with our observations.

Inshore upwelling events along the Agulhas Current are a well-known phenomenon (Walker, 1986; Lutjeharms, et al., 2000; Goschen, et al., 2015) and are primarily driven by wind and/or current meanders (Leber, et al., 2017). Before and during our occupation of the ASCA16 transect, the winds were weak and variable (not shown), and the current did not meander, such that neither mechanism could have facilitated the upwelling. Moreover, given that the Agulhas Current is stronger during austral summer (Beal, et al., 2015), we did not expect upwelling of SAMW during our sampling (Braby, et al., 2022). While we cannot fully characterize the dynamics responsible for the inshore upwelling from our single occupation, we hypothesize that it was driven by small cross-shore oscillations of the current (Elipot & Beal, 2015). These 10-km scale meanders account for ~12% of the variance of the Agulhas Current at the latitude of our transect and are associated with anomalous cross-shore flow that impinges on the deep continental slope for periods of days (Elipot & Beal, 2015). These meanders can generate submesoscale frontal eddies, which have recently been observed in the Agulhas Current (Krug, et al., 2017; Tedesco, et al., 2019).

Regardless of whether the on-shelf nitrate derives from the thermocline or the underlying SAMW, it constitutes a new N source to the mixed layer that will fuel regional productivity. However, deeper upwelling that entrains SAMW (which has a higher nitrate concentration than thermocline water), as revealed by our nitrate Δ(15-18) data, would support more production.

4.4.3. Coupled mesoscale-submesoscale instabilities cause upward nitrate entrainment at the offshore edge of the Agulhas Current core

The edges of the Agulhas Current core are regions of maximum horizontal velocity and density gradients (Figure 4.2a-d; (Beal & Bryden, 1999; Beal, et al., 2006)). These gradients are established by a stream of fast-flowing, low-density Tropical Surface Water positioned between slower moving, denser Subtropical Surface Water offshore and upwelled (modified) SAMW inshore (Figure 4.2d). The offshore horizontal density gradient along our winter transect is far sharper than that observed in previous summertime occupations of the Agulhas Current (Beal & Bryden, 1999; Leber & Beal, 2015) because the offshore winter mixed layer is two- to four-times deeper than in summer.

The sharp horizontal velocity and density gradients and weak stratification characteristic of persistent fronts like the Agulhas Current (and other WBCs) in winter prime the current for submesoscale instabilities (i.e., ageostrophic circulation), which draw their energy from the front (D'Asaro, et al., 2011; Lévy, et al., 2012; Thomas, et al., 2013). Small perturbations to these persistent fronts can generate instabilities that drive vertical velocities (~50-100 m.d^{-1}; (Mahadevan & Tandon, 2006; Klein & Lapeyre, 2009)) along the current that can extend below the mixed layer into nutrient-rich waters (Lévy, et al., 2001; D'Asaro, et al., 2011; Ramachandran, et al., 2014). Particular to deep and persistent fronts, mesoscale-submesoscale coupling has been shown in models to entrain nutrients from deep within the thermocline (Ramachandran, et al., 2014). Additionally, mixed layer instabilities in frontal regions can generate submesoscale eddies that induce lateral stirring and subsequent vertical water mass interleaving (i.e., generating diapycnal mixing) (Shcherbina, et al., 2009; Jaeger, et al., 2020; Gula, et al., 2022), which together could result in upward mixing of nutrients. However, observational evidence for an upward nutrient flux, as well as its impact on productivity, is difficult to acquire given the spatio-temporal scales at which (sub)mesoscale processes operate (Lévy, et al., 2018).

The Agulhas Current favours two types of instabilities in winter, 1) baroclinic instabilities and 2) symmetric instabilities. Lighter waters adjacent to denser waters within the mixed layer are subject to submesoscale baroclinic instabilities that can cause slumping and overturning of the front. The weak vertical density gradients within the wintertime mixed layer, combined with the strong horizontal potential vorticity gradients across the front, can generate symmetric instabilities that cause slantwise convection (i.e., mixing along tilted isopycnal surfaces) (Thomas, et al., 2013; Le Bras, et al., 2022). Slantwise convection can entrain thermocline water through the base of the mixed layer, yielding weak re-stratification and a shoaling of the mixed layer. The precise identification of types of instability in observations is challenging. Given the available data, we cannot conclusively identify the dominant mechanism responsible for the upward injection of deep nitrate at the offshore edge of the Agulhas Current. Nevertheless, the upward velocities associated with such instabilities and/or eddies could mix nutrient-rich waters from below the mixed layer into the sunlit surface, fueling productivity.

We observe a submesoscale overturning cell in the upper 100 m of the water column at the offshore edge of the current core (box 3 on Figure 4.2j). Active overturning is apparent in a tongue of salty Subtropical Surface Water (>35.78 g.kg^{-1}) subducting 50-100 m beneath fresher Tropical Surface Water between 33.78°S and 34.29°S (dashed white contour on Figure 4.2e), which could result from baroclinic instabilities. Additionally, the strong shoaling of the mixed layer and its decoupling from the top of the thermocline at σ_θ = 25.5 kg.m^{-3} (by ~75 m; white arrow on Figure 4.2c), as well as the local elevation of N^2 coincident with the shoaled mixed layer, indicate recent re-stratification (Figure 2c and d), which could result from slantwise convection following symmetric instability. Immediately below the mixed layer, the biogeochemical properties should reflect those of thermocline water (e.g., high AOU and low nitrate δ^{15}N). Instead, we observe surface-water biogeochemical properties, including low AOU, which indicates recent subduction of ventilated surface waters (white arrow on Figure 4.2f).

Elevated nitrate Δ(15-18) immediately below the mixed layer is evidence of an upward flux of deep nitrate into shallower waters, likely generated by vertical velocities associated with the mesoscale-submesoscale instabilities (box 3 on Figure 24.j). More specifically, between the mixed layer and top of the thermocline at 33.78°S to 34.29°S, nitrate Δ(15-18) is relatively high (mean of 2.5‰) compared to in the overlying shallow mixed layer (mean of 1.0‰) and offshore upper thermocline (mean of 1.9‰; σ_θ=25.5-26.0 for >34.29°S), and is instead more similar to the Δ(15-18) measured in the lower thermocline (2.9‰; σ_θ=26.0-26.4; Figure 4.2j). If upper thermocline nitrate was the source of the vertical nitrate flux, its low Δ(15-18) would be evident between the mixed layer and the top of the thermocline. Instead, the high nitrate Δ(15-18) of this layer must originate from the lower thermocline where Δ(15-18) is similarly high (Δ(15-18)=3.3‰ for σ_θ=26.0-27.0, a density range that includes SAMW). That the Δ(15-18) of nitrate in the overlying mixed layer remains low indicates that the upward nitrate flux did not reach the surface. Nevertheless, the high δ^{15}N and δ^{18}O and low concentration of nitrate within the euphotic waters immediately below the mixed layer indicate that this deep nitrate supply was consumed by phytoplankton, revealing that our sampling occurred after and not during the supply event (Figure 4.2g-j). As such, accurately diagnosing the physical mechanism that entrained lower thermocline nitrate into shallower waters is more challenging, however, we use the available data to hypothesize the likely drivers.

In sum, we find evidence for a mesoscale-submesoscale overturning cell along the offshore edge of the Agulhas Current core. Our nitrate Δ(15-18) data reveal a substantial upward supply of nitrate into the sunlit layer from as deep as 250 m (σ_θ>26.0 kg.m^{-3}), which was consumed, fueling primary productivity. To our knowledge, this is the first time that observations show an upward injection of nutrients, as well as the response of phytoplankton, driven by mesoscale-submesoscale instabilities.

4.4.5. Ambiguous features of the nitrate Δ(15-18) tracer field

Since Δ(15-18) is a tracer of (sub-)thermocline nitrate, other positive excursions in nitrate Δ(15-18) in the mixed layer (e.g., at 35.53°S) may also indicate recent entrainment of deep nitrate that is not apparent in our other data. Downwelling is also suggested at some locations across the transect (e.g., at 34.54°S and 35.34°S) in the low values of nitrate Δ(15-18) observed in the thermocline. However, these putative signals of downwelling are not corroborated by other observations. For example, at both 34.54°S and 35.34°S the thermocline waters were highly-stratified (Figure 2 c and d), thermocline AOU was relatively high (Figure 2f), and the inferred vertical velocity gradients were weak (Figure 2b). As such, we are reluctant to ascribe any certainty to these potential downwelling signals.

4.4.6. Implications for vertical nitrate entrainment across western boundary currents

Our diagnosis of episodic upward nitrate supply events in the Agulhas Current has implications for vertical nitrate fluxes in WBC systems globally. First, the high eddy kinetic energy characteristic of all WBC systems (Figure 4.1; (Martínez-Moreno, et al., 2021)) implies that annually, the eddy-driven vertical nitrate flux is quantitatively significant (point 1 in Figure 4.3). Second, the upwelling of nitrate-rich waters carried in subsurface nutrient streams along steep western boundaries, whether in response to frontal eddies as suggested here or to wind events and meanders as observed previously, likely enhances WBC productivity (point 2 in Figure 4.3). Third, strong horizontal velocity and density shears are inherent to all WBCs as warm, low-salinity tropical waters flow rapidly alongside cool, high-salinity subtropical waters. The resultant high shear region along the length of these currents (often >1600 km), combined with weak stratification in the winter mixed layer, primes the current edges for repeated entrainment of deep nitrate via (sub)mesoscale instabilities (point 3 in Figure 4.3). Repeated sampling of the Agulhas region, including in other seasons and when other entrainment mechanisms are active (e.g., coastal trapped waves, internal gravity- and near-inertial waves), should eventually allow for a more complete characterization of Agulhas Current-induced (sub)mesoscale nitrate fluxes. While the available data cannot be reliably used to quantify the vertical nitrate fluxes observed in our dataset (see Methods), the diffusive nitrate flux has been estimated for the Kuroshio and Brazil WBCs, with values of order 1-10 $mmol.m^{-2}.d^{-1}$ (Nagai, et al., 2019; Lazaneo, et al., 2020). These WBC-facilitated nitrate fluxes are at least double those associated with episodic mixing driven by eddies in stratified subtropical gyres (McGillicuddy, et al., 1998; Johnson, et al., 2010).

The recurring upward supply of nitrate across WBCs implies that these features may significantly augment the primary productivity fueled by seasonal mixing of nutrients and N_2 fixation. We note, however, that enhanced vertical mixing of nitrate (and its consumption by phytoplankton) will not necessarily increase atmospheric CO_2 removal. Upwelling also supplies a stoichiometric quantity of dissolved inorganic carbon to the surface, which will outgas as CO_2. Thus, the increased biological productivity fuelled by the additional nutrients will largely balance this CO_2 flux, preventing significant biologically induced air-sea CO_2 transfer. However, it is possible that these nutrient entrainments have implications for the carbon-to-nutrient and calcite-to-organic carbon ratios of sinking organic matter associated with the WBCs and the gyres that they support, for example, through their impacts on the plankton assemblage (Bode, et al., 2020; Bonino, et al., 2021; Inomura, et al., 2022). Regardless, nitrate-based phytoplankton production is central to the ocean's biological pump, which maintains the atmospheric concentration of CO_2 (Volk & Hoffert, 1985). The greater the supply of subsurface nitrate to N-limited surface waters, the more fertile the region, with implications for sustaining higher trophic levels and fisheries.

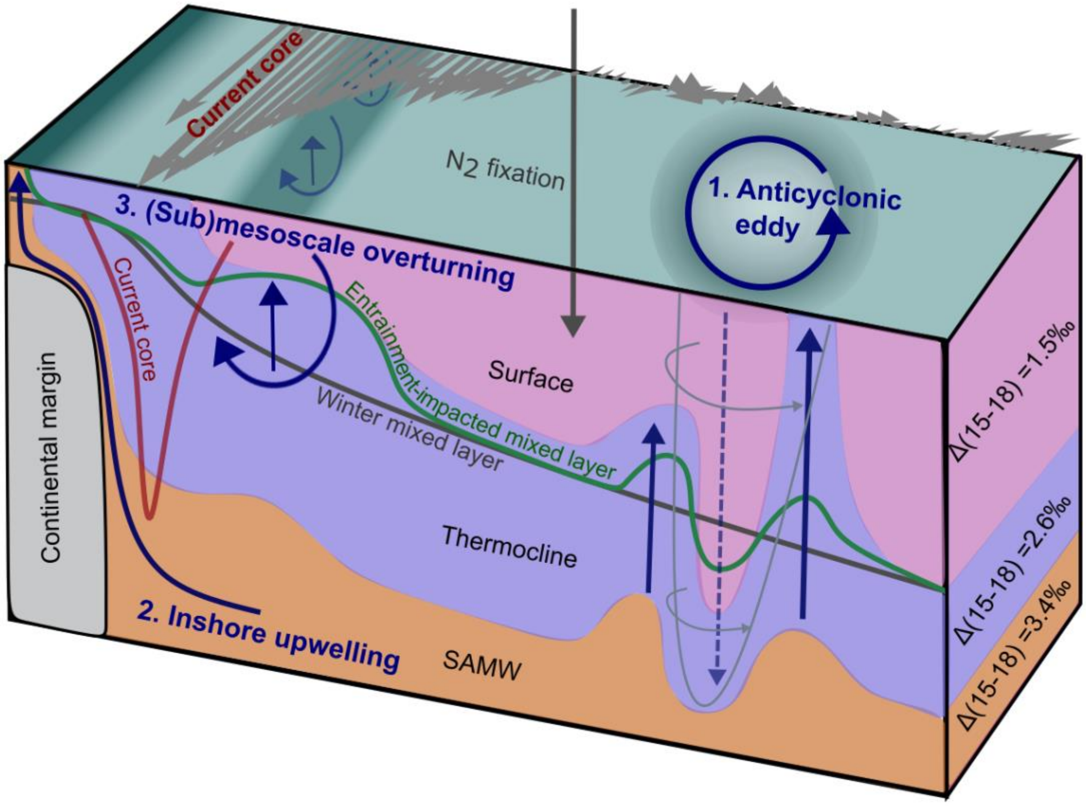

Figure 4.3. A visual abstract showing the three observed mechanisms of upward nitrate supply. A schematized depth section of nitrate Δ(15-18) across the Agulhas Current system based on our ASCA16 dataset. Nitrate Δ(15-18) is highest in deep Subantarctic Mode Water (SAMW) (mean of 3.4‰; orange shading), lower in the thermocline waters (mean of 2.6‰; purple shading), and lowest at the top of the thermocline and in the surface mixed layer (mean of 1.5‰; pink shading). The Agulhas Current core (southwest speeds >1 m.s^{-1}) is shown as a red V-shaped contour and its horizontal shear at the surface by grey velocity vectors from the shipboard ADCP. The horizontal dark grey contour represents the typical depth of the winter mixed layer, which generally follows the top of the thermocline, while the green contour shows how entrainment events can shoal the mixed layer. The vertical grey arrow represents N_2 fixation, which lowers thermocline nitrate Δ(15-18) through the production and remineralisation of low-δ^{15}N organic matter; this Δ(15-18) decrease is augmented by co-occurring partial nitrate assimilation and nitrification at the top of the thermocline (Marshall, et al., 2023). The navy blue arrows show the (sub)mesoscale processes that supply deep nitrate to shallow waters: 1) An anticyclonic eddy entrains thermocline nitrate into the mixed layer and surface at its edges. Cyclonic eddies should similarly entrain thermocline nitrate at their cores; 2) Inshore upwelling entrains high-Δ(15-18) SAMW nitrate onto the shelf. Inshore upwelling of thermocline waters, which also occurs in this system, would supply lower-Δ(15-18) nitrate; 3) Large horizontal density and velocity shears at the edges of the current core generate (sub)mesoscale instabilities, temporarily shoaling the mixed layer relative to its mean wintertime depth and inducing secondary vertical velocities that entrain nitrate into sunlit waters. The increase in nitrate availability that results from all three (sub)mesoscale mechanisms is indicated by the darker green shading at the surface.

4.5 Concluding remarks

This study highlights the important role of high-energy WBC systems in driving upward nutrient supply into the mixed layer of otherwise oligotrophic subtropical waters. Additionally, we demonstrate the remarkable utility of nitrate Δ(15-18) as a tracer of dynamically-driven and biologically-influenced vertical nitrate fluxes at the (sub)mesoscale. The dual isotopes of nitrate record both surface and subsurface upwelling, provide insights into upwelling source and intensity, and retain the signal of upward nitrate supply for some time after an event because the provenance of the nitrate supplied to the surface is preserved in its Δ(15-18). As such, using high-resolution nitrate Δ(15-18) measurements, combined with hydrographic and velocity data, we can resolve three dynamical processes that facilitate upward nitrate supply. Notably, nutrient supply associated with coupled mesoscale-submesoscale instabilities (point 3 in Figure 4.3) has been theorized but not previously observed in a WBC system.

We conclude that the (sub)mesoscale dynamics operating in the Agulhas Current system facilitate upward nutrient fluxes to overlying surface waters, thereby enhancing the productivity of the subtropical southwest Indian Ocean relative to that fueled by seasonal convection and N_2 fixation. We suggest that similar dynamics occur in all major WBC systems, which may collectively increase ocean fertility and aid in sustaining higher trophic levels. With climate change, eddy kinetic energy across WBCs is increasing at a rate of ~2.5% per decade (Martínez-Moreno, et al., 2021); for example, observations show an increase in eddies and current meanders in the Agulhas Current since the 1990s (Beal & Elipot, 2016). The related increase in (sub)mesoscale nutrient supply may have already enhanced regional fertility. A continued rise in WBC-facilitated nutrient supply may partially offset the decline in productivity expected for subtropical gyres due to enhanced thermal stratification of the upper water column (Fu, et al., 2016; Moore, et al., 2018).

Chapter 5: Concluding remarks and future work

Chapters 2-4 of this thesis each include comprehensive implications and conclusions sections. To avoid repetition, the conclusions provided in chapters 2-4 will not be re-examined here. Instead, this chapter provides some remarks on the broad contributions made by the entirety of the work detailed in this thesis, comments on the remaining gaps in our knowledge, and suggestions of future directions that could aid in bridging these gaps. As a reminder, the goal of this thesis is to characterise N cycling in the South Atlantic and South Indian Oceans by examining nutrient supply, ocean fertility, and carbon export potential, with the broad purpose of better understanding the biogeochemical functioning of two historically understudied ocean basins.

The biogeochemical functioning of the South Atlantic and South Indian Oceans

The biogeochemical functioning of the South Atlantic and South Indian Oceans displays strong regionality and is not meridionally or zonally homogeneous as some models suggest (e.g., (Somes & Oschlies, 2015; Wang, et al., 2019)). While both these basins suffer from severe biogeochemical data paucity, the distributions of macro- and micro-nutrients and geochemical tracers such as nitrate $\delta^{15}N$ and N* reveal spatial heterogeneity. For example, the coincidence of iron and excess P relative to N supplied to both the Angola Gyre and Agulhas Current system appear to control N_2 fixation therein, while their absence in other regions of these basins suggest that N_2 fixation is not a basin-wide feature of either the South Atlantic or South Indian Oceans. Additionally, signals of local and remote N cycling converge in both ocean basins, making the separation of locally generated signals from transported signals important for characterising the functioning of their subsystems and the controls on key ocean processes regulating fertility and carbon export. For example, in chapter 3 (section 3.4.2.2), including transported nutrient and nitrate $\delta^{15}N$ fluxes from the tropical and subtropical source regions to the Agulhas Current in the one-box model prevented a gross overestimation of the N_2 fixation rate for the greater Agulhas region. Similarly, in chapter 2 (section 2.2.3), computation of the nitrate-$\delta^{15}N$ flux transported to the Angola Gyre by feeder currents revealed that some N_2 fixation must occur locally, and also prevented overestimating the local N_2 fixation rate. More accurate estimates of N_2 fixation rates gives confidence to diagnosing the controls thereof. Moreover, the distinct subtropical and tropical gyre systems of the South Atlantic and South Indian Oceans, along with the smaller recirculation cells and highly turbulent subsystems, appear to play a crucial role in shaping nutrient supply to the surface waters of these basins. For example, the (sub)mesoscale instabilities characteristic of the greater Agulhas region drive upward nitrate supply to the surface waters of an otherwise oligotrophic southwest Indian

Ocean. The implication is that without these additional physical nutrient fluxes, productivity in the region would be significantly lower.

In sum, the work detailed in the thesis shows that N cycling in the South Atlantic and South Indian Oceans is regionally dependent, and strongly coupled to the local physical dynamics. These findings can be applied to other ocean basins. Indeed, very recent observation-based results from across the subtropical North Pacific and in the western tropical North Pacific indicate the strong regionality of the controls on N_2 fixation (Wen, et al., 2022; Horii, et al., 2023). Investigating ocean biogeochemistry at the regional scale may provide insights into global ocean processes that impact productivity and climate at the planetary scale.

The spatial distribution of N_2 fixation in the South Atlantic and South Indian Oceans

The spatial distribution of N_2 fixation implied by observations from the South Atlantic and South Indian Oceans demonstrates strong regional variability. Local hotspots of N_2 fixation contrast the basin-wide distributions predicted by some models (Somes & Oschlies, 2015; Wang, et al., 2019). This discrepancy suggests that the controls on N_2 fixation vary regionally, and that models cannot accurately predict N_2 fixation if observations of P* and iron are not made at appropriate (i.e., regional and basin) scales. Additionally, the apparent coincidence of P* generation via denitrification and iron dissolution via reducing margin sediments, both of which require low-oxygen environments (i.e., ODZs and shallow continental shelves), strongly argues for the spatial, but not necessarily quantitative, coupling of N_2 fixation to N loss, as similarly suggested by Deutsch et al. (2007) and Weber and Deutsch (2014). That is, the flux of P* and iron (and thus N_2 fixation) are spatially coupled to low oxygen environments, but N_2 fixation does not have to offset N loss. However, evidence of this spatial coupling, especially along eastern boundaries, is inconsistent (Brandes, et al., 1998; Sigman, et al., 2005; Moutin, et al., 2008; Fernandez, et al., 2011; Dekaezemacker, et al., 2013; White, et al., 2013; Knapp, et al., 2016; Jayakumar, et al., 2017). This inconsistency is perhaps owing to the spatial coupling itself, in that the overlap of N_2 fixation and N loss overprints, at times completely erases, the N_2 fixation signal. In other words, greater regional N loss will in net raise nitrate $\delta^{15}N$ and lower N* in the subsurface, eroding low-$\delta^{15}N$ nitrate and elevated N* resulting from N_2 fixation. Additionally, the advection and mixing of waters along eastern boundaries that have undergone more N loss than gain will further erode signals of N_2 fixation.

The occurrence of N_2 fixation in recirculation features such as the Angola Gyre and southwest Indian subgyre (whether cyclonic or anticyclonic; see section 2.2.6 and A10 for more examples) suggests that the retention of iron and excess P may play a role in maintaining N_2 fixation. That said, it should be noted that strong (thermocline) water retention assists in the accumulation of geochemical tracers of N_2 fixation, such as low-δ^{15}N nitrate and elevated N*, which should not be misinterpreted as indicative of the magnitude of N_2 fixation. For example, a large flux of remotely-generated low-δ^{15}N nitrate and/or elevated N* transported into a retentive system could accumulate in the thermocline and progressively alter its biogeochemistry without local modification. As such, the lateral transport of N_2 fixation signals over large distances should be carefully accounted for when estimating regional N_2 fixation rates.

Rates of N_2 fixation in the South Atlantic and South Indian Oceans, and beyond

Convergent estimates of N_2 fixation rates for the South Atlantic and South Indian Oceans remain elusive. While some reasons therefor are discussed in Chapter 2 (e.g., the coarse resolution of general circulation models that miss regional circulation features and modelling the N:P plasticity of exported organic matter; section 2.2.8), another contributing factor is the difficulty associated with measuring, and thus modelling, fluxes of P*, N*, iron, and nitrate δ^{15}N. Oftentimes the absolute magnitude of P* and/or dissolved iron concentrations, and especially N_2 fixation rates from incubation experiments, are taken as representative of the seasonal-, and at times even annual-, steady state of a system, which is problematic. Ambient dissolved iron concentrations are not necessarily indicative of iron availability, nor more importantly, of the iron flux. Relatedly, the time- and depth-scales over which iron and N* or nitrate δ^{15}N integrate are different. In the upper ocean, recycling of iron (i.e., complexation, scavenging, and remineralisation) is more rapid than the remineralisation and accumulation of newly-fixed organic matter in the thermocline (i.e., days to weeks versus years to decades; (Gruber & Sarmiento, 1997; Boyd & Ellwood, 2010; Tagliabue, et al., 2019; Rafter, et al., 2017). The differing time- and depth-scales over which iron, P, and N are cycled make the combined prediction of their concentrations and fluxes challenging. Some researchers have explored the implications of the temporal (and spatial) variability associated with P and iron limitation on N_2 fixation at intra- and inter-basin scales (Weber & Deutsch, 2014; Wen, et al., 2022). Their findings suggest that iron exerts the dominant control on regional N_2 fixation rates and that P excess relative to N exerts the dominant control on global (i.e., inter-basin) N_2 fixation rates (Weber & Deutsch, 2014; Wen, et al., 2022). In this thesis, the overlapping biogeography of excess P and iron that is proposed to control N_2 fixation, is broadly consistent with the ideas of others (Weber & Deutsch, 2014; Wen, et al., 2022). However, the implications of smaller scale, instantaneous fluxes of P and iron for N_2 fixation rates have yet to be explored.

Lateral fluxes of nutrients also play an important role in nutrient cycling and N_2 fixation (Palter, et al., 2005; Palter, et al., 2011; Letscher, et al., 2016; Conway, et al., 2018). Quantifying accurate rates of N_2 fixation requires the partitioning of locally and remotely generated signals. For example, the lateral advection of newly fixed nitrate and/or DON across ocean basins can cause the overestimation of N_2 fixation from geochemical tracers if not accounted for correctly (see section 2.2.3 and 3.4.2). Additionally, N cycling between transported and local N pools further complicates the extraction of a locally generated N_2 fixation signal (Knapp, et al., 2018; Zhang, et al., 2020). At present, observation-based estimates of N_2 fixation require that assumptions be made about transported N pools, and their subsequent recycling, particularly in the case of DON. However, measurements of DON and other N pools alone may not provide enough information on their fluxes to allow for an accounting of transported signals. Instead, incorporating more quantitative frameworks like general circulation models, which can simulate both advection and mixing as well as cycling between N pools, may yield better constraints on locally operating processes.

Suggested directions for future work on globally significant nitrogen fluxes

Estimates of N fluxes, and ultimately the global ocean N budget, provide a means for inferring ocean fertility and carbon export potential. While efforts have recently been made (and continue to be made) to generate more accurate, or at least more convergent, estimates of N_2 fixation (Wang, et al., 2019; Tang, et al., 2019; Shiozaki, et al., 2020), other N fluxes also require constraining if we are to better estimate N budgets. New methods for characterising and quantifying physical N fluxes at the mesoscale and below are being developed, including equipping ocean gliders and floats with nutrient sensors (Johnson, et al., 2009; Chai, et al., 2020) that provide high spatio-temporal resolution data, as well as coupling vertical micro-profilers with discrete nitrate concentration measurements, which provide high resolution data on the microstructure of the water column (Nagai, et al., 2019; Lazaneo, et al., 2020). Together, these approaches have the potential to quantify N fluxes that have traditionally remained beyond our reach.

Some of the key questions troubling the (sub)mesoscale ocean science community relate to the magnitude of the vertical velocities associated with secondary recirculations following submesoscale instabilities, the magnitude of the nutrient fluxes driven by these velocities, and the impact that these nutrient fluxes have on ocean productivity and plankton diversity ((Lévy, et al., 2012; Lévy, et al., 2018), and references therein). In this thesis, the biogeochemical tracer nitrate Δ(15-18) was coupled with information on physical ocean dynamics to identify and characterise lateral and vertical N fluxes (sections 3.4.3 and 4.4.1). The demonstrated efficacy of this approach motivates for the continued exploration of this and other biogeochemical tools to investigate physical ocean processes, particularly at the (sub)mesoscale. With sustained sampling efforts (i.e., (sub)seasonal timeseries data) from strategic regions of the ocean, the fluxes of the various N pools can be better understood, and thus modelled. The inclusion of additional N fluxes in models should improve our understanding of both the magnitude and distribution of ocean fertility and carbon export, and how these parameters might change in the future.

Under increasingly warm climate conditions, subtropical gyres will continue to stratify and expand, both of which are projected to reduce the upward nutrient supply (Fu, et al., 2016; Moore, et al., 2018; Yang, et al., 2020). If biogeochemical processes are regionally dependent and strongly coupled to physical ocean dynamics, the impact of climate change on ocean fertility and carbon export will also vary regionally and in conjunction with changes to the physical dynamics. As such, determining the impact of climate change on ocean productivity and carbon export will require coincident high spatio-temporal resolution sampling of biogeochemical and physical processes. Improving our understanding of ocean biogeochemistry at the regional scale ultimately improves our ability to quantify key processes regulating global ocean fertility and climate at the global scale.

References

Agawin, N. et al., 2011. Low water column nitrogen fixation in the Mediterranean Sea: basin-wide experimental evidence. Aquatic Microbial Ecology, Volume 64, p. doi:10.3354/ame01511.

Altabet, M. & Francois, R., 1994. Sedimentary nitrogen isotopic ratio as a recorder for surface ocean nitrate utilization. Global Biogeochemical Cycles, 8(1), pp. 103-116.

Altabet, M., 1988. Variations in nitrogen isotopic composition between sinking and suspended particles: Implications for nitrogen cycling and particle transformation in the open ocean. Deep-Sea Research, Volume 35, pp. doi.org/10.1016/0198-0149(88)90130-6.

Altabet, M., 2001. Nitrogen isotopic evidence for micronutrient control of fractional NO utilization in the equatorial Pacific. Limnology and Oceanography, Volume 46, p. doi.org/10.4319/lo.2001.46.2.0368.

Altabet, M., Francois, R., Murray, D. & Prell, W., 1995. Climate-related variations in denitrification in the Arabian Sea from sediment 15N/14N ratios. Nature , Volume 373, p. doi.org/10.1038/373506a0.

Altieri, K. et al., 2013. Isotopic composition of rainwater nitrate at Bermuda: The influence of air mass source and chemistry in the marine boundary layer. Journal of Geophysical Research: Atmospheres, Volume 118, pp. 11304-11316.

Altieri, K. et al., 2014. Isotopic evidence for a marine ammonium source in rainwater at Bermuda. Global Biogeochemical Cycles.

Altieri, K., Fawcett, S. & Hastings, M., 2021. Reactive Nitrogen Cycling in the Atmosphere and Ocean. Annual Reviews of Earth and Planetary Sciences.

Amberger, A. & Schmidt, H., 1987. Natürliche isotopengehalte von Nitrat als Indikatoren für dessen Herkunft. Geochemica et Cosmochimica Acta, Volume 51, pp. 2699-2705.

An, C., 1971. Atlantic Ocean phytoplankton south of the Gulf of Guinea on profiles along 11 and 14 degrees S. Oceanology, Volume 6, pp. 896-901.

Anderson, L. & Sarmiento, J., 1994. Redfield ratios of remineralization determined by nutrient data analysis. Global Biogeochemical Cycles, 8(1), pp. 65-80.

Andersson, K. & Hooper, A., 1983. O2 and H2O are each the source of one O in NO-2 produced from NH3 by Nitrosomonas: 15N-NMR evidence. FEBS Letters, 164(2), pp. 236-240.

Argo, 2021. Argo float data and metadata from Global Data Assembly Centre (Argo GDAC). SEANOE, p. doi.org/10.17882/42182.

Arhan, M. et al., 2011. Anticyclonic and cyclonic eddies of subtropical origin in the subantarctic zone south of Africa. Journal of Geophysical Research, Volume 116, p. doi:10.1029/2011JC007140.

Armbrecht, L., Schaeffer, A., Roughan, M. & Armand, L., 2015. Interactions between seasonality and oceanic forcing drive the phytoplankton variability in the tropical-temperate transition zone (~30°S) of Eastern Australia. Journal of Marine Systems, Volume 144, p. doi.org/10.1016/j.jmarsys.2014.11.008.

Available at: Dataset. https://accession.nodc.noaa.gov/NCEI-WOA18

Azar, E., Piñango, A., Waller-Kersanach, M. & Kerr, R., 2020. Source waters contribution to the tropical Atlantic central layer: New insights on the Indo-Atlantic exchanges. Deep-Sea Research Part I, p. doi.org/10.1016/j.dsr.2020.103450..

Baker, A. et al., 2007. Dry and wet deposition of nutrients from the tropical Atlantic atmosphere: Links to primary productivity and nitrogen fixation. Deep Sea Research Part I, Volume 54, pp. 1704-1720.

Baker, A. et al., 2010. Estimation of atmospheric nutrient inputs to the Atlantic Ocean from 50°N to 50°S based on large-scale field sampling: Fixed nitrogen and dry deposition of phosphorus. Global Biogeochemical Cycles, Volume 24.

Baker, C., Martin, A., Yool, A. & Popova, E., 2022. Biological Carbon Pump Sequestration Efficiency in the North Atlantic: A Leaky or a Long-Term Sink?. Global Biogeochemical Cycles, Volume 36, p. doi.org/10.1029/2021GB007286.

Bang, N., 1970. Dynamic interpretations of a detailed surface temperature chart of the Agulhas Current retroflexion and fragmentation area. South African Geographical Journal, Volume 52, pp. 67-76.

Bang, N., 1970b. Dynamic interpretations of a detailed surface temperature chart of the Agulhas Current retroflexion (sic) and fragmentation area. Journal of South African Geography, Volume 52, pp. 67-76.

Bange, H., Rixen, T., Johansen, A. & Siefert, R., 2000. First direct measurements of N2 fixation during a Trichodesmium bloom in the eastern Arabian Sea. Global Biogeochemical Cycles, 14(4), pp. 1283-1297.

Barnola, J., Raynaud, D., Korotkevich, Y. & Lorius, C., 1987. Vostok ice core provides 160,000-year record of atmospheric CO2. Nature, Volume 329, pp. 408-414.

Beal, L. & Bryden, H., 1999. The velocity and vorticity structure of the Agulhas Current at 328S. Journal of Geophysical Research, Volume 104, pp. 5151-5176.

Beal, L. & Elipot, S., 2016. Broadening not strengthening of the Agulhas Current since the early 1990s. Nature Letter, Volume 540, pp. 570-573.

Beal, L. et al., 2011. On the role of the Agulhas system in ocean circulation and climate. Nature Review, Volume 472.

Beal, L., Chereskin, T., Lenn, Y. & Elipot, S., 2006. The Sources and Mixing Characteristics of the Agulhas Current. Journal of Physical Oceanography, Volume 36, pp. 2060-2074.

Beal, L. et al., 2008. Five years of Florida Current structure and transport from the Royal Caribbean Cruise Ship Explorer of the Seas. Journal of Geophysical Research: Oceans, 113(C6), p. doi.org/10.1029/2007JC004154.

Beal, L., Elipot, S., Houk, A. & Leber, G., 2015. Capturing the Transport Variability of a Western Boundary Jet: Results from the Agulhas Current Time-Series Experiment (ACT). Journal of Physical Oceanography, Volume 45, pp. doi:10.1175/JPO-D-14-0119.1.

Beal, L., Elipot, S., Houk, A. & Leber, G., 2015. Capturing the Transport Variability of a Western Boundary Jet: Results from the Agulhas Current Time-Series Experiment (ACT)*. Journal of Physical Oceanography, Volume 45, pp. doi:10.1175/JPO-D-14-0119.1.

Beal, L., Ffield, A. & Gordon, A., 2000. Spreading of Red Sea overflow waters in the Indian Ocean. Journal of Geophysical Research, 105(C4), p. doi.org/10.1029/1999JC900306C.

Becker, S. et al., 2013. Use of reference materials for nutrients in seawater and comparability of nutrients in the world's oceans. San Diego, IEEE.

Becker, S. et al., 2020. GO-SHIP Repeat Hydrography Nutrient Manual: The Precise and Accurate Determination of Dissolved Inorganic Nutrients in Seawater, Using Continuous Flow Analysis Methods. Frontiers in Marine Science, Volume 7, p. doi:10.3389/fmars.2020.581790.

Becker, S. et al., 2020. GO-SHIP Repeat Hydrography Nutrient Manual: The Precise and Accurate Determination of Dissolved Inorganic Nutrients in Seawater, Using Continuous Flow Analysis Methods. Frontiers in Marine Science: Methods, Volume 7, p. doi:10.3389/fmars.2020.581790.

Benavides, M. & Voss, M., 2015. Five decades of N2 fixation research in the North Atlantic Ocean. Frontiers in Marine Sciences, 2(40), p. doi:0.3389/fmars.2015.00040.

Benson, B. & Krause, D., 1980. The concentration and isotopic fractionation of gases dissolved in freshwater in equilibrium with the atmosphere. Limnology and Oceanography, Volume 25, pp. 662-671.

Berger, W., 1989. Productivity of the Ocean: Present and past. Global maps of ocean productivity. New York, Chichester, pp. 429-455.

Berman-Frank, I. et al., 2001. Iron availability, cellular iron quotas, and nitrogen fixation in Trichodesmium. Limnology and Oceanography, 46(6), pp. 1249-1260.

Bianchi, D., Dunne, J., Sarmiento, J. & Galbraith, E., 2012. Data-based estimates of suboxia, denitrification, and N2O production in the ocean and their sensitivities to dissolved O2. Global Biogeochemical Cycles, 26(GB2009), p. doi:10.1029/2011GB004209.

Bigg, G. & Rohling, E., 2000. An oxygen isotope dataset for marine waters. Journal of Geophysical Research, Volume 105, pp. 8527-8535.

Blain, S. et al., 2015. Distributions and stoichiometry of dissolved nitrogen and phosphorus in the iron-fertilized region near Kerguelen (Southern Ocean). Biogeosciences, Volume 12, pp. doi:10.5194/bg-12-623-2015.

Bode, A., Lamas, A. & Mompeán, C., 2020. Effects of Upwelling Intensity on Nitrogen and Carbon Fluxes through the Planktonic Food Web off A Coruña (Galicia, NW Spain) Assessed with Stable Isotopes. Diversity: Marine Nitrogen Cycling Food Webs, Volume 12, p. doi.org/10.3390/d12040121.

Böhlke, J., S, M. & Coplen, T., 2003. Oxygen isotopes in nitrate: new reference materials for 18O:17O:16O measurements and observations on nitrate-water equilibration. Rapid Communications in Mass Spectrometry, p. doi.org/10.1002/rcm.1123.

Bonino, G. et al., 2021. Drivers and impact of the seasonal variability of the organic carbon offshore transport in the Canary upwelling system. Biogeosciences, Volume 18, pp. doi.org/10.5194/bg-18-2429-2021.

Bonnet, S. et al., 2013. Aphotic N2 fixation in the Eastern Tropical South Pacific Ocean. PLoS one, 8(12), p. doi:10.1371/journal.pone.0081265.

Bonnet, S., Caffin, M., Berthelot, H. & Moutin, T., 2017. Hot spot of N2 fixation in the western tropical South Pacific pleads for a spatial decoupling between N2 fixation and denitrification. PNAS Letter, p. doi/10.1073/pnas.1619514114.

Bonnet, S. et al., 2023. Natural iron fertilization by shallow hydrothermal sources fuels diazotroph blooms in the ocean. Science, Volume 380, p. doi:10.1126/science.abq4654.

Boshers, D. et al., 2019. Constraining the Oxygen Isotopic Composition of Nitrate Produced by Nitrification. Environmental Science and Technology, 53(3), p. DOI: 10.1021/acs.est.8b03386.

Bower, A., 1991. A simple kinematic mechanism for mixing fluid parcels across a meandering jet. Journal or Physical Oceanography, Volume 21, pp. 173-180.

Bower, A., Hunt, H. & Price, J., 2000. Character and dynamics of the Red Sea and Persian Gulf outflows. Journal of Geophysical Research, 105(C3), p. doi.org/10.1029/1999JC900297.

Bower, A., Rossby, H. & Lillibridge, J., 1985. The Gulf Stream- barrier or blender?. Journal of Physical Oceanography, Volume 15, pp. 24-32.

Boyer, T. P. et al., 2018. World Ocean Atlas 2018. [Online]

Braby, L. et al., 2022. First Observations of Seasonal Variability in Water Mass Properties Across the Agulhas Current. Journal of Geophysical Research: Oceans, Volume 127, p. doi.org/10.1029/2021JC018107.

Brandes, J. & Devol, A., 1997. Isotopic fractionation of oxygen and nitrogen in coastal marine sediments. Geochemica et Cosmochimca Acta, Volume 61, pp. doi:10.1016/S0016-7037(97)00041-0.

Brandes, J. & Devol, A., 2002. A global marine-fixed nitrogen isotopic budget: Implications for Holocene nitrogen cycling. Global Biogeochemical Cycles, 16(4), p. 1120.

Brandes, J. et al., 1998. Isotopic composition of nitrate in the central Arabian Sea and eastern tropical North Pacific: A tracer for mixing and nitrogen cycles. Limnology and Oceanography, 43(7), pp. 1680-1689.

Brix, H., Gruber, N., Karl, D. & Bates, N., 2006. On the relationships between primary, net community, and export production in subtropical gyres. Deep Sea Research Part II, Volume 53, p. doi.org/10.1016/j.dsr2.2006.01.024.

Broecker, W. & Henderson, G., 1998. The sequence of events surrounding Termination II and their implications for the cause of glacial-interglacial CO2 changes. Paleoceanography and Paleoclimatology, 13(4), pp. 352-364.

Broecker, W. & Peng, T., 1982. Tracers in the Sea, NY: Palisades.

Bronk, D., Glibert, P. & Ward, B., 1994. Nitrogen Uptake, Dissolved Organic Nitrogen Release, and New Production. Science, Volume 265, p. doi:10.1126/science.265.5180.1843.

Browning, T. et al., 2017. Nutrient co-limitation at the boundary of an oceanic gyre. Nature Letters, Volume 551, p. doi:10.1038/nature24063.

Bryden, H. & Beal, L., 2001. Role of the Agulhas Current in Indian Ocean circulation and associated heat and freshwater fluxes. Deep-Sea Research, Volume 48, pp. 1821-1845.

Bryden, H., Beal, L. & Duncan, L., 2005. Structure and Transport of the Agulhas Current and Its Temporal Variability. Journal of Oceanography, Volume 61, pp. 479-492.

Buchwald, C. & Casciotti, K., 2013. Isotopic ratios of nitrite as tracers of the sources and age of oceanic nitrite. Nature Geoscience, Volume 6, p. doi:10.1038/NGEO1745.

Buchwald, C., Santoro, A., McIlvin, M. & Casciotti, K., 2012. Oxygen isotopic composition of nitrate and nitrite produced by nitrifying cocultures and natural marine assemblages. Limnology and Oceanography, 57(5), pp. 1361-1375.

Buchwald, C., Santoro, A., McIlvin, M. & Casciotti, K., 2012. Oxygen isotopic composition of nitrate and nitrite produced by nitrifying cocultures and natural marine assemblages. Limnology and Oceanography, Volume 57, pp. 1361-1375.

Buchwald, C., Santoro, A., Stanley, R. & Casciotti, K., 2015. Nitrogen cycling in the secondary nitrite maximum of the eastern tropical North Pacific off Costa Rica. Global Biogeochemical Cycles, Volume 29, p. doi:10.1002/ 2015GB005187.

Buckingham, C. et al., 2019. The Contribution of Surface and Submesoscale Processes to Turbulence in the Open Ocean Surface Boundary Layer. Journal of Advances in Modeling Earth Systems, Volume 11, p. doi.org/10.1029/ 2019MS001801.

Busquets-Vass, G. et al., 2017. Estimating blue whale skin isotopic incorporation rates and baleen growth rates: Implications for assessing diet and movement patterns in mysticetes. PLoS ONE, Volume 12, p. doi: 10.1371/journal.pone.0177880.

Campbell, E., 2016. Where three oceans meet: nitrate isotope measurements from the South Atlantic along 34.5S. Senior thesis: Princeton University, US.

Capone, D. et al., 1998. An extensive bloom of the N2-fixing cyanobacterium Trichodesmium erythraeum in the central Arabian Sea. Marine Ecology Progress Series, Volume 172, pp. 281-292.

Carpenter, E. & Price, C., 1976. Marine Oscillatoria (Trichodesmium): explanation for aerobic nitrogen fixation without heterocysts. Science, Volume 191, pp. 1278-1280.

Carpenter, E., 1983b. Physiology and ecology of marine Oscillatoria (Trichodesmium). Marine Biology Letters, Volume 4, pp. 65-85.

Carpenter, E., Harvey, H., Fry, B. & Capone, D., 1997. Biogeochemical tracers of the marine cyanobacterium Trichodesmium. Deep Sea Research I, 44(1), pp. 27-38.

Carpenter, E., Harvey, H., Fry, B. & D, C., 1997. Biogeochemical tracers of the marine cyanobacterium Trichodesmium. Deep Sea Research I, 44(1), pp. 27-38.

Carr, M., 2001. Estimation of potential productivity in the Eastern Boundary Currents using remote sensing.. Deep Sea Research II, Volume 49, pp. doi.org/10.1016/S0967-0645(01)00094-7.

Casciotti, K. & McIlvin, M., 2007. Isotopic analyses of nitrate and nitrite from reference mixtures and application to Eastern Tropical North Pacific waters. Marine Chemistry, Volume 107, p. doi.org/10.1016/j.marchem.2007.06.021.

Casciotti, K. et al., 2002. Measurement of the oxygen isotopic composition of nitrate in seawater and freshwater using the denitrifier method. Analytical Chemistry, 74(19), pp. 4905-4912.

Casciotti, K. et al., 2007. Oxygen Isotopes in Nitrite: Analysis, Calibration, and Equilibration. Analytical Chemistry, Volume 79, p. doi.org/10.1021/ac061598h.

Casciotti, K., 2009. Inverse kinetic isotope fractionation during bacterial nitrite oxidation. Geochimica et Cosmochimica Acta, Volume 73, p. doi.org/10.1016/j.gca.2008.12.022.

Casciotti, K., 2016. Nitrogen and oxygen isotopic studies of the marine nitrogen cycle. Annual Review of Marine Science, Volume 8, pp. doi:10.1146/annurev-marine-010213-135052.

Casciotti, K., Buchwald, C. & McIlvin, M., 2013. Implications of nitrate and nitrite isotopic measurements for the mechanisms of nitrogen cycling in the Peru oxygen deficient zone. Deep-Sea Research I, Volume 80, p. doi.org/10.1016/j.dsr.2013.05.017.

Casciotti, K., Buchwald, C., Santoro, A. & Frame, C., 2011. Assessment of nitrogen and oxygen isotopic fractionation during nitrification and its expression in the marine environment. Methods in Enzymology, Volume 486, pp. doi:10.1016/B978-0-12-381294-0.00011-0.

Casciotti, K., McIlvin, M. & Buchwald, C., 2010. Oxygen isotopic exchange and fractionation during bacterial ammonia oxidation. Limnology and Oceanography, Volume 55, pp. 753-762.

Casciotti, K., Sigman, D. & Ward, B., 2003. Linking diversity and stable isotope fractionation in ammonia-oxidizing bacteria. Geomicrobiology Journal, Volume 20, p. doi:10.1080/01490450390241035.

Cerdan-Garcia, E. et al., 2022. Transcriptional responses of Trichodesmium to natural inverse gradients of Fe and P availability. ISME J, Volume 16, pp. doi.org/10.1038/s41396-021-01151-1.

Checkley, D. & Miller, C., 1989. Nitrogen isotope fractionation by oceanic zooplankton. Deep-Sea Research, Volume 36, pp. doi.org/10.1016/0198-0149(89)90050-2.

Chen, M. et al., 2019. Biogeographic drivers of diazotrophs in the western Pacific Ocean. Limnology and Oceanography, Volume 64, p. doi.org/10.1002/lno.11123.

Chinni, V. & Singh, S., 2022. Dissolved iron cycling in the Arabian Sea and sub-tropical gyre region of the Indian Ocean. Geochimica et Cosmochimica Acta, Volume 317, p. doi.org/10.1016/j.gca.2021.10.026.

Church, M. et al., 2009. Physical forcing of nitrogen fixation and diazotroph community structure in the North Pacific subtropical gyre. Global Biogeochemical Cycles, Volume 23, p. doi.org/10.1029/2008GB003418.

Cline, J. & Kaplan, I., 1975. Isotopic fractionation of dissolved nitrate during denitrification in the eastern tropical North Pacific Ocean. Marine Chemistry, Volume 3, pp. doi.org/10.1016/0304-4203(75)90009-2.

Codispoti, L., 1989. Phosphorus vs nitrogen limitation of the new and export production. In: W. Berger, V. Smetacek & G. Wefer, eds. Productivity of the Ocean: Present and Past. New York: s.n., pp. 377-394.

Codispoti, L., 1995. Is the ocean losing nitrate?. Nature, 376(724).

Codispoti, L., 2007. An oceanic fixed nitrogen sink exceeding 400 Tg N a-1 vs the concept of homeostasis in the fixed-nitrogen inventory. Biogeosciences, Volume 4, pp. 233-253.

Coles, V. & Hood, R., 2007. Modeling the impact of iron and phosphorus limitations on nitrogen fixation in the Atlantic Ocean.. Biogeosciences, Volume 4, pp. 455-479.

Conway, T. & John, S., 2014. Quantification of dissolved iron sources to the North Atlantic Ocean. Nature Letters, Volume 0, p. doi:10.1038/nature13482.

Conway, T., Palter, J. & Souza, G. d., 2018. Gulf Stream rings as a source of iron to the North Atlantic subtropical gyre. Nature Geoscience, Volume 11, pp. 594-598.

Copin-Montegut, C. & Copin-Montegut, G., 1978. The chemistry of particulate matter from the south Indian and Antarctic oceans. Deep Sea Research, 25(10), pp. doi.org/10.1016/0146-6291(78)90633-1.

Craig, H. & Gordon, L., 1965. Deuterium and oxygen 18 variations in the ocean and the marine atmosphere. In: s.l.:Laboratorio di geologia nucleare, pp. 9-131.

Cronin, M. et al., 2010. Monitoring ocean-atmosphere interactions in western boundary current extensions. Venice, ESA Publication WPP-306.

D'Asaro, E. et al., 2011. Enhanced turbulence and energy dissipation at ocean fronts. Science, Volume 332, p. doi:10.1126/science.1201515.

de Ruijter, W. et al., 1999. Indian-Atlantic interocean exchange: Dynamics, estimation and impact. Journal of Geophysical Research, 104(C9), pp. 20885-20910.

de Ruijter, W. et al., 2002. Observations of the flow in the Mozambique Channel. Geophysical Research Letters, 29(10), p. dio:10.1029/2001GL013714.

Dekaezemacker, J. et al., 2013. Evidence of active dinitrogen fixation in surface waters of the eastern tropical South Pacific during El Niño and La Niña events and evaluation of its potential nutrient controls. Global Biogeochemical Cycles, 27(3), p. doi.org/10.1002/gbc.20063.

Deman, F. et al., 2021. Nitrate Supply Routes and Impact of Internal Cycling in the North Atlantic Ocean Inferred From Nitrate Isotopic Composition. Global Biogeochemical Cycles, Volume 35, p. doi.org/10.1029/2020GB006887.

Dentener, F., 2006. Nitrogen and Sulphur Deposition on Regional and Global Scales: A Multimodel Evaluation. Global Biogeochemical Cycles, Volume 20.

Detoni, A. M. S. et al., 2016. Trichodesmium latitudinal distribution on the shelf break in the southwestern Atlantic Ocean during spring and autumn. Global Biogeochemical Cycles, Volume 30, p. doi:10.1002/ 2016GB005431.

Deutsch, C. & Weber, T., 2012. Nutrient Ratios as a Tracer and Driver of Ocean Biogeochemistry. Marine Science Annual Reviews, Volume 4, pp. 113-141.

Deutsch, C. et al., 2007. Spatial coupling of nitrogen inputs and losses in the ocean. Nature Articles, Volume 445.

Deutsch, K. et al., 2002. Dinitrogen fixation in the World's oceans. Biogeochemistry, Volume 57, pp. 47-98.

Devol, A. et al., 2006. Denitrification rates and excess nitrogen gas concentrations in the Arabian Sea oxygen deficient zone. Deep-Sea Research Part I, Volume 53, pp. 1533-1547.

DeVries, T. & Deutsch, C., 2014. Large-scale variations in the stoichiometry of marine organic matter respiration. Nature Geoscience, Volume 7, pp. 890-894.

DeVries, T., Deutsch, C., Rafter, P. & Primeau, F., 2013. Marine denitrification rates determined from a global 3-D inverse model. Biogeosciences, Volume 10, pp. 2481-2496.

Diamond, D., 1994. QuikChem Method 10-114-21-1-B: Silicate by flow injection analysis, s.l.: Lachat Instruments.

DiFiore, P. et al., 2006. Nitrogen isotope constraints on subantarctic biogeochemistry. Journal of Geophysical Research, 111(C08016), p. doi:10.1029/2005JC003216.

DiFiore, P. et al., 2006. Nitrogen isotope constraints on subantarctic biogeochemistry. Journal of Geophysical Research, Volume 111.

DiFiore, P., Sigman, D. & Dunbar, R., 2009. Upper ocean nitrogen fluxes in the Polar Antarctic Zone: Constraints from the nitrogen and oxygen isotopes of nitrate. Geochemistry Geophysics Geosystems, Volume 10, p. doi:10.1029/ 2009GC002468.

Dilmahamod, A. F. et al., 2019. A New Definition of the South-East Madagascar Bloom and Analysis of Its Variability. Journal of Geophysical Research: Oceans, Volume 124, p. doi.org/10.1029/2018JC014582.

Dilmahamod, A. F. et al., 2020. A Model Investigation of the Influences of the South-East Madagascar Current on the South-East Madagascar Bloom. Journal of Geophysical Research: Oceans, Volume 125, p. doi.org/10.1029/2019JC015761.

DiMarco, S. et al., 2002. Volume transport and property distributions of the Mozambique Channel. Deep-Sea Research II, Volume 49, pp. 1481-1511.

Donners, J., Drijfhout, S. & Hazeleger, W., 2005. Water Mass Transformation and Subduction in the South Atlantic. Journal of Physical Oceanography, Volume 35, pp. 1841-1861.

Donohue, K. & Toole, J., 2003. A near-synoptic survey of the Southwest Indian Ocean. Deep-Sea Research II, Volume 50, pp. 1893-1931.

Duce, R. A. et al., 1991. The atmospheric input of trace species to the world ocean. Global Biogeochemical Cycles, Volume 5, p. doi.org/10.1029/91GB01778.

Ducet, N., Le Traon, P. & Reverdin, G., 2000. Global high-resolution mapping of ocean circulation from TOPEX/Poseidon and ERS-1 and -2. Journal of Geophysical Research, Volume 105, pp. 19477-19498.

Dufois, F. et al., 2014. Impact of eddies on surface chlorophyll in the South Indian Ocean. Journal of Geophysical Research: Oceans, Volume 119, p. doi:10.1002/2014JC010164.

Dufois, F. et al., 2016. Anticyclonic eddies are more productive than cyclonic eddies in subtropical gyres because of winter mixing. Science Advances, Volume 2.

Dugdale, R. & Georing, J., 1967. Uptake of new and regenerated forms of nitrogen in primary productivity. Limnology and Oceanography, 12(2), pp. 196-206.

Dyhrman, S. et al., 2006. Phosphonate utilization by the globally important marine diazotroph Trichodesmium. Nature Letters, Volume 439, p. doi:10.1038/nature04203.

Elipot, S. & Beal, L., 2015. Characteristics, Energetics, and Origins of Agulhas Current Meanders and Their Limited Influence on Ring Shedding. Journal of Physical Oceanography, Volume 45, pp. doi:10.1175/JPO-D-14-0254.1.

Emerson, S., 2014. Annual net community production and the biological carbon flux in the ocean. Global Biogeochemical Cycles, Volume 28, p. doi:10.1002/2013GB004680.

Emerson, S., Mecking, S. & Abell, J., 2001. The biological pump in the subtropical North Pacific Ocean' Nutrient sources, Redfield ratios, and recent changes. Global Biogeochemical Cycles, 15(3).

Eppley, R. & Peterson, B., 1979. Particulate organic matter flux and planktonic new production in the deep ocean. Nature Articles, Volume 282.

Eugster, O. & Gruber, N., 2012. A probabilistic estimate of global marine N-fixation and denitrification. Global Biogeochemical Cycles, 26(GB4013), p. doi:10.1029/2012GB004300.

Falkowski, P., 1997. Evolution of the nitrogen cycle and its influence on the biological sequestration of CO2 in the ocean. Nature, Volume 387, p. doi.org/10.1038/387272a0.

Falkowski, P., 2012. Ocean Science: The power of plankton. Nature, Volume 483, p. doi.org/10.1038/483S17a.

Falkowski, P., Barber, R. & Smetacek, V., 1998. Biogeochemical Controls and Feedbacks on Ocean Primary Production. Science, Volume 281, p. doi:10.1126/science.281.5374.200.

Falkowski, P., Ziemann, D., Kolber, Z. & Bienfang, P., 1991. Role of eddy pumping in enhancing primary production in the ocean. Nature, Volume 352, pp. 55-58.

Fawcett, S. et al., 2011. Assimilation of upwelled nitrate by small eukaryotes in the Sargasso Sea. Nature Geoscience, p. DOI: 10.1038/NGEO1265.

Fawcett, S. et al., 2018. Low-nutrient organic matter in the Sargasso Sea thermocline: A hypothesis for its role, identity, and carbon cycle implications. Marine Chemistry, Volume 207, p. doi.org/10.1016/j.marchem.2018.10.008.

Fawcett, S., Ward, B., Lomas, M. & Sigman, D., 2015. Vertical decoupling of nitrate assimilation and nitrification in the Sargasso Sea. Deep-Sea Research I, Volume 103, pp. 64-72.

Fernández-Castro, B., Mouriño-Carballido, B. & Álvarez-Salgado, X., 2019. Non-redfieldian mesopelagic nutrient remineralization in the eastern North Atlantic subtropical gyre. Progress in Oceanography, Volume 171, pp. 136-153.

Fernández, A. et al., 2010. Latitudinal distribution of Trichodesmium spp. and N2 fixation in the Atlantic Ocean. Biogeosciences, Volume 7, pp. doi:10.5194/bg-7-3167-2010.

Fernandez, C., Farías, L. & Ulloa, O., 2011. Nitrogen Fixation in Denitrified Marine Waters. PLoS ONE, Volume 6, p. doi:10.1371/journal.pone.0020539.

Ferrari, R. & Wunsch, C., 2009. Ocean Circulation Kinetic Energy: Reservoirs, Sources, and Sinks. Annual Review of Fluid Mechanics, Volume 41, p. doi:10.1146/ANNUREV.FLUID.40.111406.102139.

Fine, R. et al., 2008. Decadal ventilation and mixing of Indian Ocean waters. Deep-Sea Research Part I, Volume 55, pp. 20-37.

Fine, R., 1993. Circulation of Antarctic Intermediate Water in the South Indian Ocean. Deep-Sea Research I, Volume 40, pp. 2021-2042.

Fine, R., Warner, M. & Weiss, R., 1988. Water mass modification at the Agulhas Retroflection: chlorofluoromethane studies. Deep-Sea Research, Volume 35, pp. doi.org/10.1016/0198-0149(88)90013-1.

Firing, E. & Hummon, J., 2010. The GO-SHIP Repeat Hydrography Manual: A Collection of Expert Reports and Guidelines: Shipboard ADCP measurements, Honolulu: IOCCP.

Fitzsimmons, J., Boyle, E. & Jenkins, W., 2014. Distal transport of dissolved hydrothermal iron in the deep South Pacific Ocean. PNAS, Volume 111, p. doi.org/10.1073/pnas.1418778111.

Flohr, A. et al., 2014. Spatio-temporal patterns of C:N: P ratios in the northern Benguela upwelling system. Biogeosciences, Volume 11, pp. 885-897.

Flynn, R. et al., 2020. On-Shelf Nutrient Trapping Enhances the Fertility of the Southern Benguela Upwelling System. Journal of Geophysical Research: Oceans, Volume 125, p. doi.org/10.1029/2019JC015948.

Fonseca-Batista, D. et al., 2017. Nitrogen fixation in the eastern Atlantic reaches similar levels in the Southern and Northern Hemisphere. Journal of Geophysical Research: Oceans.

Foster, R., Subramaniam, A. & Zehr, J., 2009. Distribution and activity of diazotrophs in the Eastern Equatorial Atlantic. Environmental Microbiology, 11(4), pp. 741-750.

Friedlingstein, P. et al., 2022. Global Carbon Budget 2021. Earth System Science Data, Volume 14, pp. doi.org/10.5194/essd-14-1917-2022.

Fripiat, F. et al., 2019. The isotope effect of nitrate assimilation in the Antarctic Zone: Improved estimates and paleoceanographic implications. Geochimica et Cosmochimica Acta, Volume 247, pp. 261-279.

Fripiat, F. et al., 2021. Nitrogen isotopic constraints on nutrient transport to the upper ocean. Nature Geoscience, Volume 14, pp. doi.org/10.1038/s41561-021-00836-8.

Fripiat, F. et al., 2023. The impact of incomplete nutrient consumption in the Southern Ocean on global mean ocean nitrate δ15N. Global Biogeochemical Cycles, Volume 37, p. doi:org/10.1029/2022GB007442.

Fu, W., Randerson, J. & Moore, K., 2016. Climate change impacts on net primary production (NPP) and export production (EP) regulated by increasing stratification and phytoplankton community structure in the CMIP5 models. Biogeosciences, Volume 13, pp. doi:10.5194/bg-13-5151-2016.

Gandhi, N. et al., 2011. First direct measurements of N2 fixation during a Trichodesmium bloom in the eastern Arabian Sea. Global Biogeochemical Cycles, 25(GB4014), p. doi:10.1029/2010GB003970.

Ganeshram, R., Pedersen, T., Calvert, S. & Murray, J., 1995. Large changes in oceanic nutrient inventories from glacial to interglacial periods. Nature, Volume 376, p. doi.org/10.1038/376755a0.

Garcia, H. E. et al., 2018. World Ocean Atlas 2018, Volume 3: Dissolved Oxygen, Apparent Oxygen Utilization, and Oxygen Saturation, s.l.: NOAA Atlas NESDIS 83, 38pp.

Garcia, H. E. et al., 2019. World Ocean Atlas 2018, Volume 4: Dissolved Inorganic Nutrients (phosphate, nitrate, nitrate+nitrite, silicate), Silver Spring: NOAA Atlas NESDIS 84, 35pp.

Garcia, N., Fu, F., Sedwick, P. & Hutchins, D., 2015. Iron deficiency increases growth and nitrogen-fixation rates of phosphorus-deficient marine cyanobacteria. ISME, Volume 9, p. doi.org/10.1038/ismej.2014.104.

Garzoli, S. et al., 2013. South Atlantic meridional fluxes. Deep-Sea Research I, Volume 71, p. doi.org/10.1016/j.dsr.2012.09.

Gaube, P., Chelton, D., Strutton, P. & Behrenfeld, M., 2013. Satellite observations of chlorophyll, phytoplankton biomass, and Ekman pumping in nonlinear mesoscale eddies. Journal of Geophysical Research: Oceans, Volume 118, p. doi:10.1002/2013JC009027.

Gaye, B. et al., 2013. Evidence of parallel denitrification and nitrite oxidation in the ODZ of the Arabian Sea from paired stable isotopes of nitrate and nitrite. Global Biogeochemical Cycles, Volume 27, pp. 1059-1071.

Gill, E., Green, J. & Simmons, A., 1974. Energy partition in the large-scale ocean circulation and the production of mid-ocean eddies. Deep-Sea Research, Volume 21, pp. 499-528.

Gonfiantini, R., 1984. Stable isotope reference samples for geochemical and hydrological investigations. International Journal of Applied Radiation and Isotopes, 35(5), pp. doi.org/10.1016/0020-708X(84)90059-0.

Gordon, A. & Bosley, K., 1990. Cyclonic gyre in the tropical South Atlantic. Deep-Sea Research, Volume 38, pp. S323-S343.

Gordon, A. et al., 1997. Advection and diffusion of Indonesian Throughflow water within the Indian Ocean South Equatorial Current. Geophysical Research Letters, Volume 24, p. doi.org/10.1029/97GL01061.

Gordon, A., 1985. Indian-Atlantic Transfer of Thermocline Water at the Agulhas Retroflection. Science, Volume 277, pp. 1030-1033.

Gordon, A., 1986. Interocean Exchange of Thermocline Water. Journal of Geophysical Research, 91(C4), pp. 5037-5046.

Gordon, A., 1987. Stratification and circulation at the Agulhas Retroflection. Deep-Sea Research, Volume 34, pp. 565-599.

Gordon, A., 2003. The brawniest retroflection. Nature, Volume 421, pp. 904-905.

Goschen, W., Bornman, T., Deyzel, S. & Schumann, E., 2015. Coastal upwelling on the far eastern Agulhas Bank associated with large meanders in the Agulhas Current. Continental Shelf Research, Volume 101, pp. 34-46.

Grand, M. et al., 2015a. Dust deposition in the eastern Indian Ocean: The ocean perspective from Antarctica to the Bay of Bengal. Global Biogeochemical Cycles, Volume 29, p. doi:10.1002/2014GB004898.

Grand, M. et al., 2015c. The impact of circulation and dust deposition in controlling the distributions of dissolved Fe and Al in the south Indian subtropical gyre. Marine Chemistry, Volume 176, pp. 110-125.

Granger, J. & Sigman, D., 2009. Removal of nitrite with sulfamic acid for nitrate N and O isotope analysis with the denitrifier method. Rapid Communications in Mass Spectrometry, Volume 23, p. doi.org/10.1002/rcm.4307.

Granger, J. et al., 2010. N and O isotope effects during nitrate assimilation by unicellular prokaryotic and eukaryotic plankton cultures. Geochimica et Cosmochimica Acta, 74(3), pp. 1030-1040.

Granger, J. et al., 2011. Coupled nitrification-denitrification in sediment of the eastern Bering Sea shelf leads to 15N enrichment of fixed N in shelf waters. Journal of Geophysical Research, Volume 116, p. doi:10.1029/2010JC006751.

Granger, J., Sigman, D., Lehmann, M. & Tortell, P., 2008. Nitrogen and oxygen isotope fractionation during dissimilatory nitrate reduction by denitrifying bacteria. Limnology and Oceanography, 53(6), pp. 2533-2545.

Granger, J., Sigman, D., Needoba, J. & Harrison, P., 2004. Coupled nitrogen and oxygen isotope fractionation of nitrate during assimilation by cultures of marine phytoplankton. Limnology and Oceanography, Volume 49, pp. 1763-1773.

Granger, R. et al., 2023. Southeast Atlantic nitrate isotope data from winter 2017. doi:10.5281/zenodo.7648606.

Grasshoff, K., 1983. Methods of seawater analysis. In: K. Grasshoff, K. Ehrhardt & K. Kremling, eds. Verlag Chemie. 2nd ed. Weinheim: s.n., pp. 21-30.

Grasshoff, K., Kremling, K. & Ehrhardt, M., 1999. Methods of seawater analysis, Third edition. In: K. Grasshoff, K. Ehrhardt & K. Kremling, eds. Verlag Chemie. 2nd ed. Weinheim: Wiley-VCH, p. 419.

Gruber, N. & Sarmiento, J., 1997. Global patterns of marine nitrogen fixation and denitrification. Global Biogeochemical Cycles, 11(2), pp. 235-266.

Gründlingh, M., Carter, R. & Stanton, R., 1991. Circulation and water properties of the southwest Indian Ocean, Spring 1987. Progress in Oceanography, Volume 28, pp. doi.org/10.1016/0079-6611(91)90031-G.

Gula, J., Molemaker, M. & McWilliams, J., 2016. Topographic vorticity generation, submesoscale instability and vortex street formation in the Gulf Stream. Geophysical Research Letters, Volume 42, p. doi.org/10.1002/2015GL063731.

Gula, J., Taylor, J., Shcherbina, A. & Mahadevan, A., 2022. Chapter 8: Submesoscale processes and mixing. In: M. Meredith & A. Garabato, eds. Ocean Mixing: Drivers, Mechanisms and Impacts. s.l.: Elsevier, pp. doi.org/10.1016/B978-0-12-821512-8.00015-3

Gunn, K. L. et al., 2020. Mixing of Subtropical, Central, and Intermediate Waters Driven by Shifting and Pulsing of the Agulhas Current. Journal of Physical Oceanography, 50(12), pp. doi:10.1175/JPO-D-20-0093.1.

Guo, X., Zhu, X., Wu, Q. & Huang, D., 2012. The Kuroshio nutrient stream and its temporal variation in the East China Sea. Journal of Geophysical Research, 117(C01026), p. doi:10.1029/2011JC007292.

Hamilton, D. et al., 2020. Impact of Changes to the Atmospheric Soluble Iron Deposition Flux on Ocean Biogeochemical Cycles in the Anthropocene. Global Biogeochemical Cycles, Volume 34, p. DOI:10.1029/2019GB006448.

Hansell, D., Bates, N. & Olson, D., 2004. Excess nitrate and nitrogen fixation in the North Atlantic. Marine Chemistry, Volume 84, pp. 243-265.

Hansell, D., Olson, D., Dentener, F. & Zamora, L., 2007. Assessment of excess nitrate development in the subtropical North Atlantic. Marine Chemistry, 106(3-4), pp. 562-576.

Harada, Y. et al., 2022. Compound-Specific Nitrogen Isotope Analysis of Amino Acids in Eye Lenses as a New Tool to Reconstruct the Geographic and Trophic Histories of Fish. Frontiers in Marince Science, p. doi.org/10.3389/fmars.2021.796532.

Harms, N. et al., 2019. Nutrient distribution and nitrogen and oxygen isotopic composition of nitrate in water masses of the subtropical South Indian Ocean. Biogeosciences, pp. doi.org/10.5194/bg-2018-511.

Hastings, M., Sigman, D. & Lipschultz, F., 2003. Isotopic evidence for source changes f nitrate in rain at Bermuda. Journal of Geophysical Research, 108(D24), p. 4790.

Hauck, J. et al., 2020. Consistency and Challenges in the Ocean Carbon Sink Estimate for the Global Carbon Budget. Frontiers in Marine Science, Volume 7, p. doi.org/10.3389/fmars.2020.571720.

He, Q. et al., 2017. Phytoplankton bloom triggered by an anticyclonic eddy: The combined effect of eddy-Ekman pumping and winter mixing. Journal of Geophysical Research: Oceans, Volume 122, p. doi:10.1002/ 2017JC012763.

Held, N. et al., 2020. Co-occurrence of Fe and P stress in natural populations of the marine diazotroph Trichodesmium. Biogeosciences, Volume 17, pp. 2537-2551.

Hermes, J. & Reason, C., 2008. Annual cycle of the South Indian Ocean (Seychelles-Chagos) thermocline ridge in a regional ocean model. Journal of Geophysical Research, Volume 113, p. doi:10.1029/2007JC004363.

Herraiz-Borreguero, L. & Rintoul, S., 2011. Subantarctic mode water: Distribution and circulation. Ocean Dynamics, Volume 61, pp. doi:10.1007/s10236-010-0352-9.

Hoch, M., Fogel, M. & Kirchman, D., 1992. Isotope fractionation associated with ammonium uptake by marine bacterium. Limnology and Oceanography, Volume 37, p. doi.org/10.4319/lo.1992.37.7.1447.

Hoering, T. & Ford, H., 1960. The isotope effect in the fixation of nitrogen by Azotobacter. Journal of the American Chemical Society, 82(2), pp. 376-378.

Homoky, W. et al., 2021. Iron colloids dominate sedimentary supply to the ocean interior. PNAS, 118(13), p. doi.org/10.1073/pnas.2016078118.

Horii, S. et al., 2023. East-West Variabilities of N2 Fixation Activity in the Subtropical North Pacific Ocean in Summer: Potential Field Evidence of the Phosphorus and Iron Co-Limitation in the Western Area. Journal of Geophysical Research: Oceans, Volume 128, p. doi.org/10.1029/2022JC019249.

Horstmann, C. et al., 2021. Hydrographic fronts shape productivity, nitrogen fixation, and microbial community composition in the southern Indian Ocean and the Southern Ocean. Biogeosciences, Volume 18, pp. doi.org/10.5194/bg-18-3733-2021.

Howe, P., Donohue, K. & Watts, D., 2009. Stream-coordinate structure and variability of the Kuroshio Extension. Deep Sea Research Part I: Oceanographic Research Papers, Volume 56, p. doi.org/10.1016/j.dsr.2009.03.007.

Huggett, J. & Kyewalyanga, M., 2017. Chapter 5: Ocean productivity. In: J. Groeneveld & K. Koranteng, eds. The RV Dr Fridtjof Nansen in the Western Indian Ocean: Voyages of marine research and capacity development. Rome, Italy: FAO, p. 55:80.

Hutchings, L. et al., 2009. The Benguela Current: An ecosystem of four components.. Progress in Oceanography, Volume 83, p. doi.org/10.1016/j. pocean.2009.07.046.

Imawaki, S., Bower, A., Beal, L. & Qui, B., 2013. Chapter 13- Western Boundary Currents. In: G. Siedler, S. Griffies, J. Gould & J. Church, eds. Ocean Circulation and Climate: A 21st century perspective. s.l.: International Geophysics, pp. 305-338.

Inomura, K., Deutsch, C., Jahn, O. et al., 2022. Global patterns in marine organic matter stoichiometry driven by phytoplankton ecophysiology. Nat. Geosci. Volume 15, doi.org/10.1038/s41561-022-01066-2

Jaeger, G., Lucas, A. & Mahadevan, A., 2020. Formation of interleaving layers in the Bay of Bengal. Deep-Sea Research Part II, Volume 172, p. doi.org/10.1016/j.dsr2.2019.104717.

Jayakumar, A. et al., 2017. Biological nitrogen fixation in the oxygen-minimum region of the eastern tropical North Pacific ocean. Nature ISME, Volume 11, p. doi:10.1038/ismej.2017.97.

Jenkins, W. & Goldman, J., 1985. Seasonal oxygen cycling and primary production in the Sargasso Sea. Journal of Marine Research, 43(2), p. doi.org/10.1357/002224085788438702.

Jenkins, W., 1988. Nitrate flux into the euphotic zone near Bermuda. Nature, Volume 331, pp. 521-523.

Jickells, T. et al., 2005. Global Iron Connections Between Desert Dust, Ocean Biogeochemistry, and Climate. Science Review.

Jickells, T. et al., 2017. A re-evaluation of the magnitude and impacts of anthropogenic atmospheric nitrogen inputs on the ocean: Duce et al revisited. Global Biogeochemical Cycles, Volume 31, p. doi:10.1002/2016GB005586.

Johnson, K., Riser, S. & Karl, D., 2010. Nitrate supply from deep to near-surface waters of the North Pacific subtropical gyre. Nature Letters, Volume 465, p. doi:10.1038/nature09170.

Joyce, T., Corry, C. & Stalcup, M., 1991. Requirements for WOCE Hydrographic Programme data reporting, Woods Hole: Unpublished manuscript.

Karlusich, J. et al., 2021. Global distribution patterns of marine nitrogen fixers by imaging and molecular methods. Nature Communications, 12(4160), pp. doi.org/10.1038/s41467-021-24299-y.

Karsh, K. et al., 2014. The contributions of nitrate uptake and efflux to isotope fractionation during algal nitrate assimilation. Geochimica et Cosmochimica Acta, Volume 132, p. doi.org/10.1016/j.gca.2013.09.030.

Karsh, K., Granger, J., Kritee, K. & Sigman, D., 2012. Eukaryotic assimilatory nitrate reductase fractionates N and O isotopes with a ratio near unity. Environmental Science & Technology, Volume 5, p. doi:10.1021/es204593q.

Karstensen, J. & Tomczak, M., 1997. Ventilation processes and water mass ages in the thermocline of the southeast Indian Ocean. Journal of Geophysical Research, 24(22), pp. 2777-2780.

Kemeny, P. et al., 2016. Enzyme-level interconversion of nitrate and nitrite in the fall mixed layer of the Antarctic Ocean. Global Biogeochemical Cycles, Volume 30, p. doi:10.1002/ 2015GB005350.

Kirk, J., 1994. Light and Photosynthesis in Aquatic Ecosystems. second ed. s.l.: Cambridge University Press.

Klar, J. et al., 2018. Sources of dissolved iron to oxygen minimum zone waters on the Senegalese continental margin in the tropical North Atlantic Ocean: Insights from iron isotopes. Geochimica et Cosmochimica, Volume 236, p. doi.org/10.1016/j.gca.2018.02.031.

Klawonn, I. et al., 2015. Simple approach for the preparation of 15−15N2-enriched water for nitrogen fixation assessments: Evaluation, application and recommendations. Fontiers in Microbiology, 6(769), p. doi:10.3389/ fmicb.2015.00769.

Klein, P. & Lapeyre, G., 2009. The oceanic vertical pump induced by mesoscale and submesoscale turbulence,. Annual Review in Marine Science, Volume 1, p. doi.org/10.1146/annurev.marine.010908.163704.

Knapp, A. et al., 2010. The flux and isotopic composition of reduced and total nitrogen in Bermuda rain. Marine Chemistry, 120(1-4), pp. 83-89.

Knapp, A. et al., 2011. Interbasin isotopic correspondence between upper-ocean bulk DON and subsurface nitrate and its implications for marine nitrogen cycling. Global Biogeochemical Cycles, Volume 25, p. doi:10.1029/2010GB003878.

Knapp, A. et al., 2016. Low rates of nitrogen fixation in eastern tropical South Pacific surface waters. PNAS, 113(16), pp. 4398-4403.

Knapp, A. et al., 2018b. Distribution and rates of nitrogen fixation in the western tropical South Pacific Ocean constrained by nitrogen isotope budgets. Biogeosciences, Volume 15, pp. doi.org/10.5194/bg-15-2619-2018.

Knapp, A., 2012. The sensitivity of marine N2 fixation to dissolved inorganic nitrogen. Frontiers in Microbiology, Volume 3, p. doi.org/10.3389/fmicb.2012.00374.

Knapp, A., Casciotti, K. & Prokopenko, M., 2018a. Dissolved organic nitrogen production and consumption in Eastern Tropical South Pacific surface waters. Global Biogeochemical Cycles, Volume 32, p. doi.org/10.1029/2017GB005875.

Knapp, A., DiFiore, P., Deutsch, C. & Sigman, D., 2008. Nitrate isotopic composition between Bermuda and Puerto Rico: Implications for N2 fixation in the Atlantic Ocean. Global Biogeochemical Cycles, Volume 22.

Knapp, A., Sigman, D. & Lipschultz, F., 2005. N isotopic composition of dissolved organic nitrogen and nitrate at the Bermuda Atlantic Time-series Study site. Global Biogeochemical Cycles, Volume 19.

Knox, F. & McElroy, M., 1984. Changes in atmospheric CO2 influence of the marine biota at high latitude. Journal of Geophysical Research, Volume 89, p. doi.org/10.1029/JD089iD03p04629.

Koch-Larrouy, A., Morrow, R., Penduff, T. & Juza, M., 2010. Origin and mechanism of Subantarctic Mode Water formation and transformation in the Southern Indian Ocean. Ocean Dynamics, Volume 60, pp. DOI10.1007/s10236-010-0276-4.

Kolasinski, J., Kaehler, S. & Jaquemet, S., 2012. Distribution and sources of particulate organic matter in a mesoscale eddy dipole in the Mozambique Channel (south-western Indian Ocean): Insight from C and N stable isotopes. Journal of Marine Systems, Volume 96-97, pp. 112-131.

Kritee, K. et al., 2012. Reduced isotope fractionation by denitrification under conditions relevant to the ocean.. Geochimica et Cosmochimica Acta, Volume 92, p. doi.org/10.1016/j.gca.2012.05.020.

Krug, M., Swart, S. & Gula, J., 2017. Submesoscale cyclones in the Agulhas current. Geophysical Research Letters, Volume 44, p. doi:10.1002/2016GL071006.

Kulk, G. et al., 2020. Primary Production, an Index of Climate Change in the Ocean: Satellite-Based Estimates over Two Decades. Remote Sensing, Volume 12, p. doi.org/10.3390/rs12050826.

Kumar, S., Nicholas, D. & Williams, E., 1983. Definitive 15N NMR evidence that water serves as a source of “O” during nitrite oxidation by Nitrobacter agilis. FEBS Letters, 152(1), pp. 71-74.

Kuypers, M. et al., 2005. Massive nitrogen loss from the Benguela upwelling system through anaerobic ammonium oxidation. PNAS, 102(18), p. doi.org/10.1073/pnas.0502088102.

Lamont, T. et al., 2015. Hydrographic variability in the St. Helena Bay region of the southern Benguela ecosystem. Journal of Geophysical Research: Oceans.

Lamont, T., Barlow, R. & Brewin, R., 2018. Variations in Remotely-Sensed Phytoplankton Size Structure of a Cyclonic Eddy in the Southwest Indian Ocean. Remote Sensing, 10(7), p. 1143.

Landolfi, A., Kähler, P., Koeve, W. & Oschlies, A., 2018. Global Marine N2 Fixation Estimates: From Observations to Models. Frontiers in Microbiology: Mini review, Volume 9, p. doi:10.3389/fmicb.2018.02112.

Lazaneo, C. et al., 2020. On the Role of Turbulent Mixing Produced by Vertical Shear Between the Brazil Current and the Intermediate Western Boundary Current. Journal of Geophysical Research: Oceans, Volume 125, p. doi.org/10.1029/2019JC015338.

Le Bras, I. et al., 2022. Slantwise Convection in the Irminger Sea. Journal of Geophysical Research: Oceans, Volume 127, p. doi.org/10.1029/2022JC019071.

Leber, G. & Beal, L., 2015. Local water mass modifications by a solitary meander in the Agulhas Current. Journal of Geophysical Research: Oceans, Volume 120, pp. 4503-4515.

Leber, G., Beal, L. & Elipot, S., 2017. Wind and Current Forcing Combine to Drive Strong Upwelling in the Agulhas Current. Journal of Physical Oceanography, Volume 47, pp. 123-134.

Ledgard, S., Woo, K. & Bergersen, F., 1985. Isotopic fractionation during reduction of nitrate to nitrite by extracts of spinach leaves. Journal of Plant Physiology, Volume 12, pp. 613-640.

Lehmann, M. et al., 2007. The distribution of nitrate 15N/14N in marine sediments and the impact of benthic nitrogen loss on the isotopic composition of oceanic nitrate,. Geochimica et Cosmochimica Acta, Volume 71, p. doi:10.1016/j.gca.2007.07.025.

Lehmann, N. et al., 2018. Isotopic Evidence for the Evolution of Subsurface Nitrate in the Western Equatorial Pacific. Journal of Geophysical Research: Oceans, Volume 123, p. DIO:10.1002/2017JC013527.

Letelier, R. & Karl, D., 1998. Trichodesmium spp. physiology and nutrient fluxes in the North Pacific subtropical gyre. Aquatic Microbial Ecology, Volume 15, pp. 265-276.

Letscher, R. & Moore, K., 2015b. Preferential remineralization of dissolved organic phosphorus and non-Redfield DOM dynamics in the global ocean: Impacts on marine productivity, nitrogen fixation, and carbon export. Global Biogeochemical Cycles, Volume 29, p. doi.org/10.1002/2014GB004904.

Letscher, R. et al., 2013. Dissolved organic nitrogen in the global surface ocean: Distribution and fate. Global Biogeochemical Cycles, Volume 27, pp. 141-153.

Letscher, R., Moore, J., Teng, J. & Primeau, F., 2015. Variable C : N : P stoichiometry of dissolved organic matter cycling in the Community Earth System Model. Biogeosciences, Volume 12, pp. 209-221.

Letscher, R., Primeau, F. & Moore, K., 2016. Nutrient budgets in the subtropical ocean gyres dominated by lateral transport. Nature Geoscience, Volume 9, p. DOI:10.1038/NGEO2812.

Lévy, M. et al., 2012. Bringing physics to life at the submesoscale. Geophysical Research Letters, 39(L14602), p. doi:10.1029/2012GL052756.

Lévy, M., Franks, P. & Smith, S., 2018. The role of submesoscale currents in structuring marine ecosystems. Nature Communications, Volume 9, pp. doi:10.1038/s41467-018-07059-3.

Lévy, M., Klein, P. & Treguier, A., 2001. Impacts of sub-mesoscale physics on production and subduction of phytoplankton in an oligotrophic regime. Journal of Marine Research, Volume 59, p. doi:10.1357/002224001762842181.

Liang, Z. et al., 2022. A global ocean dissolved organic phosphorus concentration database (DOPv2021). Nature Scientific Data, Volume 9, pp. doi.org/10.1038/s41597-022-01873-7.

Liao, F., Liang, X., Li, Y. & Spall, M., 2022. Hidden Upwelling Systems Associated With Major Western Boundary Currents. Journal of Geophysical Research: Oceans, Volume 127, p. doi.org/10.1029/2021JC017649.

Lima, C. et al., 2019. Chemotaxonomy-based mapping of phytoplankton communities in the subtropical Southwestern Atlantic Ocean, with emphasis on the marine cyanobacterium Trichodesmium. Progress in Oceanography, Volume 172, pp. 77-88.

Lipschultz, F., Bates, N., Carlson, C. & Hansell, D., 2002. New production in the Sargasso Sea: History and current status. Global Biogeochemical Cycles, Volume 12, p. doi:10.1029/2000GB001319.

Liu, K. & Kaplan, I., 1989. The eastern tropical Pacific as a source of 15N-enriched nitrate in seawater off southern California. Limnology and Oceanography, Volume 34, p. doi.org/10.4319/lo.1989.34.5.0820.

Liu, K. et al., 2013. Concentration dependent nitrogen isotope fractionation during ammonium uptake by phytoplankton under an algal bloom condition in the Danshuei estuary, northern Taiwan. Marine Chemistry, Volume 157, p. doi.org/10.1016/j.marchem.2013.10.005.

Liu, K., Su, M., Hsueh, C. & Gong, G., 1996. The nitrogen isotopic composition of nitrate in the Kuroshio Water northeast of Taiwan: Evidence for nitrogen fixation as a source of isotopically light nitrate. Marine Chemistry, Volume 54, pp. doi.org/10.1016/0304-4203(96)00034-5.

Lomas, M. et al., 2013. Two decades and counting: 24-years of sustained open ocean biogeochemical measurements in the Sargasso Sea. Deep-Sea Research II, Volume 93, pp. 16-32.

Longhurst, A., 2001. A major seasonal phytoplankton bloom in the Madagascar Basin. Oceanographic Research Paper, 48(11), pp. 2413-2422.

Lovecchio, E., Gruber, N., Münnich, M. & Frenger, I., 2022. On the Processes Sustaining Biological Production in the Offshore Propagating Eddies of the Northern Canary Upwelling System. Journal of Geophysical Research: Oceans, Volume 127, p. doi.org/10.1029/2021JC017691.

Lu, Y., Liu, Q. & Xie, S., 2021. Covariability of Subantarctic Mode Water and the Southern Branch of the Subtropical Indian Ocean Countercurrent in Argo Observations. Journal of Ocean University of China, Volume 20, pp. doi.org/10.1007/s11802-021-4677-4.

Lueders-Dumont, J. A. et al., 2022. Controls on the nitrogen isotopic composition of fish otolith organic matter: Lessons from a controlled diet switch experiment. Geochimica et Cosmochimica Acta, Volume 316, p. doi:10.1016/j.gca.2021.09.030.

Lueders-Dumont, J. et al., 2018. Nitrogen isotopic analysis of carbonate-bound organic matter in modern and fossil fish otoliths. Geochimica et Cosmochimica Acta, Volume 224, p. doi.org/10.1016/j.gca.2018.01.001.

Luo, C., Zender, C., Bian, H. & Metzger, S., 2007. Role of ammonia chemistry and coarse mode aerosols in global climatological inorganic aerosol distributions. Atmospheric Environment, 41(12), pp. 2510-2533.

Luo, Y. et al., 2012. Database of diazotrophs in global ocean: abundance, biomass and nitrogen fixation rates. Earth Science Data, Volume 4, pp. 47-73.

Lüthi, D. et al., 2008. High-resolution carbon dioxide concentration record 650,000–800,000 years before present. Nature, Volume 453, p. doi.org/10.1038/nature06949.

Lutjeharms, J. & Ansorge, I., 2001. The Agulhas Return Current. Journal of Marine Systems, Volume 30, pp. 115-138.

Lutjeharms, J., 1980. Retroflection; When the current turns. Oceans, 13(31).

Lutjeharms, J., Cooper, J. & Roberts, M., 2000. Upwelling at the inshore edge of the Agulhas Current. Continental Shelf Research, Volume 20, pp. doi:10.1016/S0278-4343(99)00092-8.

Mahadevan, A. & Tandon, A., 2006. An analysis of mechanisms for submesoscale vertical motion at ocean fronts. Ocean Modelling, Volume 14, p. doi.org/10.1016/j.ocemod.2006.05.006.

Mahaffey, C., Michaels, A. & Capone, D., 2005. The conundrum of marine N2 fixation. American Journal of Science, 305(6-8), pp. 546-595.

Mahowald, N. et al., 2005. Atmospheric global dust cycle and iron inputs to the ocean. Global Biogeochemical Cycles, Volume 19, p. doi.org/10.1029/2004GB002402.

Mara, P. et al., 2009. Isotopic composition of nitrate in wet and dry atmospheric deposition on Crete in the eastern Mediterranean Sea. Global Biogeochemical Cycles, Volume 23, p. doi.org/10.1029/2008GB003395.

Marconi, D. et al., 2015. Nitrate isotope distributions on the US GEOTRACES North Atlantic cross-basin section: Signals of polar nitrate sources and low latitude nitrogen cycling. Marine Chemistry, 177(1), p doi.org/10.1016/j.marchem.2015.06.007

Marconi, D. et al., 2017. Tropical Dominance of N2 Fixation in the North Atlantic Ocean. Global Biogeochemical Cycles, Volume 31, doi:10.1002/2016GB005613

Marconi, D., Kopf, S., Rafter, P. & Sigman, D., 2017. Aerobic respiration along isopycnal leads to overestimation of the isotope effect of denitrification in the ocean water column. Geochimica et Cosmochimica Acta, Volume 197, p. doi.org/10.1016/j.gca.2016.10.012.

Marconi, D., Weigand, M. & Sigman, D., 2019. Nitrate isotopic gradients in the North Atlantic Ocean and the nitrogen isotopic composition of sinking organic matter. Deep-Sea Research Part I, Volume 145, doi.org/10.1016/j.dsr.2019.01.010

Mariotti, A. et al., 1981. Experimental determination of nitrogen kinetic isotope fractionation: Some principles; illustration for the denitrification and nitrification processes. Plant and Soil, 62(3), p. doi.org/10.1007/BF02374138.

Marshall, T. et al., 2022. The Angola Gyre is a hotspot of dinitrogen fixation in the South Atlantic Ocean. Nature Communications Earth & Environment, 3(151), pp. doi.org/10.1038/s43247-022-00474-x.

Marshall, T. et al., 2023. The Agulhas Current transports local and remote signals of Indian Ocean nitrogen cycling. Journal of Geophysical Research: Oceans, volume 128, doi:10.1029/2022JC019413

Martin, J., 1990. Glacial-interglacial CO2 change: the iron hypothesis. Paleoceanography, Volume 5, pp. 1-13.

Martin, T. & Casciotti, K., 2017. Paired N and O isotopic analysis of nitrate and nitrite in the Arabian Sea oxygen deficient zone. Deep-Sea Research I, Volume 121, pp. 121-131.

Martínez-García, A. et al., 2022. Laboratory Assessment of the Impact of Chemical Oxidation, Mineral Dissolution, and Heating on the Nitrogen Isotopic Composition of Fossil-Bound Organic Matter. Geochemistry; Geophysics, Geosystems, Volume 23, p. doi.org/10.1029/2022GC010396.

Martínez-Moreno, J. et al., 2021. Eddy Kinetic Energy and SST gradients global datasets and trends. Additionally, this dataset includes ocean basins and ocean processes masks. Zenodo, p. doi.org/10.5281/zenodo.3993823.

Martínez-Moreno, J. et al., 2021. Global changes in oceanic mesoscale currents over the satellite altimetry record. Nature Climate Change, Volume 11, pp. doi.org/10.1038/s41558-021-01006-9.

Martínez-García, A. et al., 2014. Iron fertilization of the Subantarctic ocean during the last ice age. Science, Volume 343, p. doi.org/10.1126/science.1246848.

Martiny, A. et al., 2013. Strong latitudinal patterns in the elemental ratios of marine plankton and organic matter. Nature Geoscience Letters.

Martiny, A. et al., 2019. Biogeochemical controls of surface ocean phosphate. Science Advances, 5(eaax0341), pp. 1-10.

Matiatos, I. et al., 2021. Global patterns of nitrate isotope composition in rivers and adjacent aquifers reveal reactive nitrogen cascading. Nature Communications Earth & Environment, Volume 2, pp. doi.org/10.1038/s43247-021-00121-x.

McCarthy, M., Benner, R., Lee, C. & Fogel, M., 2007. Amino acid nitrogen isotopic fractionation patterns as indicators of zooplankton and microbial heterotrophy in plankton, dissolved and particulate organic matter in the central Pacific ocean. Geochimica et Cosmochimica Acta, Volume 71, p. doi.org/10.1016/j.gca.2007.06.061.

McCartney, M., 1982. The subtropical recirculation of mode waters. Journal of Marine Research, 40(Supplement), pp. 427-464.

McDonagh, E. et al., 2005. Decadal Changes in the South Indian Ocean Thermocline. Journal of Climate, Volume 18, pp. 1575-1590.

McGillicuddy, D. et al., 1998. Influence of mesoscale eddies on new production in the Sargasso Sea. Letters to Nature, Volume 394, pp. 263-265.

McIlvin, M. & Casciotti, K., 2011. Technical Updates to the Bacterial Method for Nitrate Isotopic Analyses. Analytical Chemistry Technical Note, Volume 83, pp. 1850-1856.

Mcmahon, K., Hamady, L. & Thorrold, S., 2013. A review of ecogeochemistry approaches to estimating movements of marine animals. Limnology and Oceanography, Volume 58, p. doi:10.4319/lo.2013.58.2.0697.

McMonigal, K. et al., 2020. The impact of meanders, deepening and broadening, and seasonality on Agulhas Current temperature variability. Journal of Physical Oceanography, 50(12), pp. doi.org/10.1175/JPO-D-20-0018.1.

Mdutyana, M. et al., 2020. The Seasonal Cycle of Nitrogen Uptake and Nitrification in the Atlantic Sector of the Southern Ocean. Global Biogeochemical Cycles, Volume 34, p. doi.org/10.1029/2019GB006363.

Meckler, N. et al., 2007. Detailed sedimentary N isotope records from Cariaco Basin for Terminations I and V: Local and global implications. Global Biogeochemical Cycles, Volume 21, p. doi:10.1029/2006GB002893.

Menzel, D. & Ryther, J., 1960. The annual cycle of primary production in the Sargasso Sea off Bermuda. Deep-Sea Research, Volume 6, pp. doi.org/10.1016/0146-6313(59)90095-4.

Merbt, S. et al., 2012. Differential photoinhibition of bacterial and archaeal ammonia oxidation. FEMS Microbiology Letters, 327(1), pp. doi:10.1111/j.1574-6968.2011.02457.x..

Mercier, H., Arhan, M. & Lutjeharms, J., 2003. Upper-layer circulation in the eastern Equatorial and South Atlantic Ocean in January–March 1995. Seep-Sea Research I, Volume 50, pp. 863-887.

Metzl, N. et al., 2022. The impact of the South-East Madagascar Bloom on the oceanic CO2 sink. Biogeosciences, Volume 19, pp. doi.org/10.5194/bg-19-1451-2022.

Michaels, A. F. et al., 1994. Seasonal patterns of ocean biogeochemistry at the U.S. JGOFS Bermuda Atlantic time-series study site. Deep Sea Research Part I: Oceanographic Research Papers, 41(7), pp. doi.org/10.1016/0967-0637(94)90016-7.

Mills, M. & Arrigo, K., 2010. Magnitude of oceanic nitrogen fixation influenced by the nutrient uptake ratio of phytoplankton. Nature Geoscience letters.

Mills, M. et al., 2004. Iron and phosphorus co-limit nitrogen fixation in the eastern tropical North Atlantic. Nature Letters, Volume 429, pp. 292-294.

Minagawa, M. & Wada, E., 1986. Nitrogen isotope ratios of red tides organisms in the East China Sea: A characterisation of biological nitrogen fixation. Marine Chemistry, Volume 19, pp. 245-259.

Möbius, J., 2013. Isotope fractionation during nitrogen remineralization (ammonification): Implications for nitrogen isotope biogeochemistry. Geochimica et Cosmochimica Acta, Volume 105, p. doi.org/10.1016/j.gca.2012.11.048.

Moffett, J. & German, C., 2020. Distribution of iron in the Western Indian Ocean and the Eastern tropical South pacific: An inter-basin comparison. Chemical Geology, 532(199334), p. doi.org/10.1016/j.chemgeo.2019.119334.

Mohr, W., Grosskopf, T., Wallace, D. & LaRoche, J., 2010. Methodological underestimation of oceanic nitrogen fixation rates. PLoS ONE, Volume 8, p. doi:10.1371/journal.pone.0012583.

Mohrholz, V., Barthlomomae, C., van der Plas, A. & Lass, H., 2008. The seasonal variability of the northern Benguela undercurrent and its relation to the oxygen budget on the shelf. Continental Shelf Research, Volume 28.

Monteiro, P. et al., 2006. Variability of natural hypoxia and methane in a coastal upwelling system: Oceanic physics or shelf biology?. Geophysical Research Letters, Volume 33, p. doi:10.1029/2006GL026234.

Montoya, J. & McCarthy, J., 1995. Isotopic fractionation during nitrate uptake by marine phytoplankton grown in continuous culture. Journal of Plankton Research, Volume 17, p. doi.org/10.1093/plankt/17.3.439.

Montoya, J., Voss, M., Kahler, P. & Capone, D., 1996. A simple, high-precision, high-sensitivity tracer assay for N2 fixation. Application of Environmental Microbiology, Volume 62, pp. doi:10.1128/AEM.62.3.986-993.1996.

Moore, C. et al., 2009. Large-scale distribution of Atlantic nitrogen fixation controlled by iron availability. Nature Geoscience Letters.

Moore, C. M. et al., 2013. Processes and patterns of oceanic nutrient limitation. Nature Geoscience, Volume 6, p. doi.org/10.1038/ngeo1765.

Moore, K. et al., 2018. Sustained climate warming drives declining marine biological productivity. Science, Volume 359, p. doi.org/10.1126/science.aao6379.

Moore, K., Doney, S., Glover, D. & Fung, I., 2002. Iron cycling and nutrient-limitation patterns in surface waters of the World Ocean. Deep-Sea Research II, Volume 49, pp. doi.org/10.1016/S0967-0645(01)00109-6.

Moore, T., Matear, R., Marra, J. & Clementson, L., 2007. Phytoplankton variability off the Western Australian Coast: Mesoscale eddies and their role in cross-shelf exchange. Deep-Sea Research II, Volume 54, pp. 943-960.

Morin, S. et al., 2009. Comprehensive isotopic composition of atmospheric nitrate in the Atlantic Ocean boundary layer from 65°S to 79°N. Journal of Geophysical Research: Atmospheres, 114(D5).

Moroshkin, K., Bubnov, V. & Bulatov, R., 1970. Water circulation in the eastern South Atlantic. Oceanography and Oceanology, Volume 10, pp. 27-34.

Moutin, T. et al., 2008. Phosphate availability and the ultimate control of new nitrogen input by nitrogen fixation in the tropical Pacific Ocean. Biogeosciences, Volume 5, pp. doi.org/10.5194/bg-5-95-2008.

Nagai, T. et al., 2019. How the Kuroshio Current Delivers Nutrients to Sunlit Layers on the Continental Shelves With Aid of Near-Inertial Waves and Turbulence. Geophysical Research Letters, Volume 46, p. doi.10.1029/2019GL082680.

Nagel, B. et al., 2013. N-cycling and balancing of the N-deficit generated in the oxygen minimum zone over the Namibian shelf—An isotope based approach. Journal of Geophysical Research: Biogeosciences, Volume 118, pp. 1-11.

Naqvi, S. & Sen Gupta, R., 1985. 'NO', a useful tool for the estimation of nitrate deficits in the Arabian Sea. Deep Sea Research Part I, Volume 32, pp. doi.org/10.1016/0198-0149(85)90071-8.

Needoba, J., Sigman, D. & Harrison, P., 2004. The mechanism of isotope fractionation during algal nitrate assimilation as illuminated by the 15N/14N of intracellular nitrate. Journal of Phycology, Volume 40, pp. doi.org/10.1111/j.1529-8817.2004.03172.x.

Nishioka, J., Obata, H. & Tsumune, D., 2013. Evidence of an extensive spread of hydrothermal dissolved iron in the Indian Ocean. Earth and Planetary Science Letters, Volume 361, pp. 26-33.

Noble, A. et al., 2012. Basin-scale inputs of cobalt, iron, and manganese from the Benguela-Angola front to the South Atlantic Ocean. Limnology and Oceanography.

Okin, G. S. et al., 2011. Impacts of atmospheric nutrient deposition on marine productivity: Roles of nitrogen, phosphorus, and iron. Global Biogeochemical Cycles, 25(GB2022), p. doi:10.1029/2010GB003858.

Olson, D., Fine, R. & Gordon, A., 1992. Convective modifications of water masses in the Agulhas. Deep-Sea Research, Volume 39, pp. doi:org/10.1016/S0198-0149(11)80010-5.

Olson, R., 1981. Differential photoinhibition of marine nitrifying bacteria: a possible mechanism for the formation of the primary nitrite maximum. Journal of Marine Research, Volume 39, pp. 227-238.

Orcutt, K. et al., 2001. A seasonal study of the significance of N2 fixation by Trichodesmium spp. at the Bermuda Atlantic Time-series Study (BATS) site. Deep-Sea Research II, Volume 48, pp. doi.org/10.1016/S0967-0645(00)00157-0.

Palter, J. B. et al., 2020. High N2 Fixation in and Near the Gulf Stream Consistent with a Circulation Control on Diazotrophy. Geophysical Research Letters, Volume 47, p. doi.org/10.1029/2020GL089103.

Palter, J., Lozier, M. & Barber, R., 2005. The effect of advection on the nutrient reservoir in the North Atlantic subtropical gyre. Nature , 437(29), p. doi:10.1038/nature03969.

Palter, J., Lozier, S., Sarmiento, J. & Williams, R., 2011. The supply of excess phosphate across the Gulf Stream and the maintenance of subtropical nitrogen fixation. Global Biogeochemical Cycles, 25(GB4007), pp. doi:10.1029/2010GB003955,.

Palter, J., Marinov, I., Sarmiento, J. & Gruber, N., 2013. Large-Scale, Persistent Nutrient Fronts of the World Ocean: Impacts on Biogeochemistry. In: I. Belkim, ed. Chemical Oceanography of Frontal Zones. Heidelberg: Hdb Env Chem.

Pan, H. et al., 2023. N2O Emissions from Aquatic Ecosystems: A Review. Atmosphere, Volume 14, p. doi.org/10.3390/atmos14081291.

Pantoja, S., Repeta, D., Sachs, J. & Sigman, D., 2002. Stable isotope constraints on the nitrogen cycle of the Mediterranean Sea water column. Deep-Sea Research, Volume 49, pp. doi.org/10.1016/S0967-0637(02)00066-3.

Pelegrí, J. & Csanady, G., 1991. Nutrient transport and mixing in the Gulf Stream. Journal of Geophysical Research, Volume 96, pp. 2577-2583.

Peng, X. et al., 2015. Ammonia and nitrite oxidation in the Eastern Tropical North Pacific. Global Biogeochemical Cycles, Volume 29, p. doi:10.1002/2015GB005278.

Peng, X. et al., 2018. Nitrogen uptake and nitrification in the subarctic North Atlantic Ocean. Limnology and Oceanography, Volume 00, p. doi:10.1002/lno.10784.

Pennock, J. et al., 1996. Isotopic fractionation of ammonium and nitrate during uptake by Skeletonema costatum: Implications for δ15N dynamics under bloom conditions. Limnology and Oceanography, Volume 41, p. doi:10.4319/lo.1996.41.3.0451.

Peters, B. et al., 2018. Estimating fixed nitrogen loss and associated isotope effects using concentration and isotope measurements of NO3 –, NO2 –, and N2 from the Eastern Tropical South Pacific oxygen deficient zone. Deep-Sea Research Part I, Volume 156, p. doi.org/10.1016/j.dsr2.2018.02.011.

Peterson, R. & Stramma, L., 1991. Upper-level circulation in the South Atlantic. Progress in Oceanography, Volume 26, pp. 1-73.

Petit, J. et al., 1999. Climate and atmospheric history of the past 420,000 years from the Vostok ice core, Antarctica.. Nature, Volume 399, pp. 429-436.

Pinedo-González, P. et al., 2015. Surface distribution of dissolved trace metals in the oligotrophic ocean and their influence on phytoplankton biomass and productivity. Global Biogeochemical Cycles, Volume 29, p. doi:10.1002/ 2015GB005149.

Ponsoni, L., Aguiar-González, B., Ridderinkhof, H. & Maas, L., 2016. The East Madagascar Current: Volume Transport and Variability Based on Long-Term Observations. Journal of Physical Oceanography, 46(4), pp. doi:10.1175/JPO-D-15-0154.1.

Popp, B. et al., 2007.) Insight into the trophic ecology of yellowfin tuna, Thunnus albacares, from compound-specific nitrogen isotope analysis of protenaceous amino acids. In: T. Dawson & R. Siegwolf, eds. Terrestrial Ecology Series. s.l.:s.n., pp. 173-190.

Poulton, A., Stinchcombe, M. & Quartly, G., 2009. High numbers of Trichodesmium and diazotrophic diatoms in the southwest Indian Ocean. Geophysical Research Letters, 36(L15610), p. doi:10.1029/2009GL039719.

Rafter, P., Bagnell, A., Marconi, D. & DeVries, T., 2019. Global trends in marine nitrate N isotopes from observations and a neural network based climatology. Biogeosciences: Discussions, pp. doi.org/10.5194/bg-2018-525.

Rafter, P., DiFiore, P. & Sigman, D., 2013. Coupled nitrate nitrogen and oxygen isotopes and organic matter remineralization in the Southern and Pacific Oceans. Journal of Geophysical Research: Oceans, Volume 118, p. doi:10.1002/jgrc.20316.

Rahmstorf, S. et al., 2015. Exceptional twentieth-century slowdown in Atlantic Ocean overturning circulation. Nature Climate Change, Volume 5, p. doi.org/10.1038/nclimate2554.

Raj, R., Peter, B. & Pushpadas, D., 2010. Oceanic and atmospheric influences on the variability of phytoplankton bloom in the Southwestern Indian Ocean. Journal of Marine Systems, Volume 82, p. doi:10.1016/j.jmarsys.2010.05.009.

Ramachandran, S., Randon, A. & Mahadevan, M., 2014. Enhancement in vertical fluxes at a front by mesoscale-submesoscale coupling. Journal of Geophysical Research: Oceans, Volume 119, p. doi:10.1002/2014JC010211.

Redfield, A., 1934. On the proportions of organic derivatives in sea water and their relation to the composition of plankton. James Johnstone Memorial Volume.

Redfield, A., 1958. The Biological Control of Chemical Factors in the Environment. American Scientist, September, 46(3), pp. 205-221.

Redfield, A., Ketchum, B. & Richards, F., 1963. The Influence of Organisms on the Composition of the Sea Water. In: M. Hill, ed. New York: s.n., pp. 26-77.

Reid, J., 1989. On the total geostrophic circulation of the South Atlantic Ocean: Flow patterns, tracers, and transports. Progress in Oceanography, 23(3), pp. 149-244.

Reid, J., 2003. On the total geostrophic circulation of the Indian Ocean: flow patterns, tracers, and transports. Progress in Oceanography, Volume 56, pp. 137-186.

Ren, H. et al., 2009. Foraminiferal isotope evidence of reduced nitrogen fixation in the ice age Atlantic. Science, Volume 323, p. doi.org/10.1126/science.1165787.

Ren, H. et al., 2017. 21st-century rise in anthropogenic nitrogen deposition on a remote coral reef. Science, Volume 356.

Ren, H., Sigman, D., Thunell, R. & Prokopenko, M., 2012. Nitrogen isotopic composition of planktonic foraminifera from the modern ocean and recent sediments. Limnology and Oceanography, 57(4), p. doi.org/10.4319/lo.2012.57.4.1011.

Resplandy, L. et al., 2009. Seasonal and intraseasonal biogeochemical variability in the thermocline ridge of the southern tropical Indian Ocean. Journal of Geophysical Research, Volume 114, p. doi:10.1029/2008JC005246.

Richardson, P., 2007. Agulhas leakage into the Atlantic estimated with subsurface floats and surface drifters. Deep-Sea Research Part 1, Volume 54, p. doi.org/10.1016/j.dsr.2007.04.010.

Ridderinkhof, H. et al., 2010. Seasonal and interannual variability in the Mozambique Channel from moored current observations. Journal of Geophysical Research, 115(C06010), p. doi:10.1029/2009JC005619.

Ridderinkhof, H., Lutjeharms, J. & Ruijter, W. d., 2001. A research cruise to investigate the Mozambique Current. South African Journal of Science, Volume 97, pp. 461-464.

Ridgway, K. & Dunn, J., 2007. Observational evidence for a Southern Hemisphere oceanic supergyre. Geophysical Research Letter, 34(L13612), p. doi:10.1029/2007GL030392.

Rijkenberg, M. et al., 2014. The Distribution of Dissolved Iron in the West Atlantic Ocean. PLoS ONE, Volume 9, p. doi.org/10.1371/journal.pone.0101323.

Robinson, R., Brunelle, B. & Sigman, D., 2004. Revisiting nutrient utilization in the glacial Antarctic; evidence from a new diatom-bound N isotope method. Paleoceanography, Volume 19, p. doi.org/10.1029/2003PA000996.

Roden, J., 1986. Thermohaline fronts and baroclinic flow in the Argentine Basin during the austral spring of 1984. Journal of Geophysical Research, 91(C4), pp. 5075-5093.

Roemmich, D. & Gilson, J., 2009. The 2004-2008 mean and annual cycle of temperature, salinity, and steric height in the global ocean from the Argo Program. Progress in Oceanography, Volume 82, pp. 81-100.

Rohde, M., Granger, J., Sigman, D. & Lehmann, M., 2015. Coupled nitrate N and O stable isotope fractionation by a natural marine plankton consortium. Frontiers in Marine Science, p. doi.org/10.3389/fmars.2015.00028.

Roman, R. & Lutjeharms, J., 2007. Red Sea Intermediate Water at the Agulhas Current termination. Deep-Sea Research I, Volume 54, pp. 1329-1340.

Roman, R. & Lutjeharms, J., 2009. Red Sea Intermediate Water in the source regions of the Agulhas Current. Deep-Sea Research I, Volume 56, pp. 939-962.

Rowell, K., Dettman, D. & Dietz, R., 2010. Nitrogen isotopes in otoliths reconstruct ancient trophic position. Nature Environmental Biology of Fishes, Volume 89, pp. doi.org/10.1007/s10641-010-9687-9.

Russo, C. et al., 2019. Hydrography of a shelf ecosystem inshore of a major western boundary current. Estuarine, coastal and shelf science, Volume 228.

Sachs, J., Repeta, D. & Goericke, R., 1999. Nitrogen and carbon isotopic ratios of chlorophyll from marine phytoplankton. Geochimica et Cosmochimica Acta, Volume 63, pp. doi:10.1016/S0016-7037(99)00097-6.

Santoro, A., Buchwald, C., McIlvin, M. & Casciotti, K., 2011. Isotopic Signature of N2O Produced by Marine Ammonia-Oxidizing Archaea. Science, Volume 333, p. doi:10.1126/science.1208239.

Sañudo-Wilhelmy, S. et al., 2001. Phosphorus limitation of nitrogen fixation by Trichodesmium in the central Atlantic Ocean. Nature, Volume 411, pp. 66-69.

Sarmiento, J. & Toggweiler, J., 1984. A new model for the role of the oceans in determining atmospheric P CO2. Nature, Volume 308, p. doi.org/10.1038/308621a0.

Sarmiento, J., Gruber, N., Brzezinksi, M. & Dunne, J., 2004. High-latitude controls of thermocline nutrients and low latitude biological productivity. Nature, Volume 427, pp. 56-69.

Sarthou, G. et al., 2003. Atmospheric iron deposition and sea-surface dissolved iron concentrations in the eastern Atlantic Ocean. Deep-Sea Research Part I, Volume 50.

Sato, O. & Polito, P., 2014. Observation of South Atlantic subtropical mode waters with Argo profiling float data. Journal of Geophysical Research: Oceans.

Schaeffer, A., Roughan, M. & Morris, B., 2013. Cross-Shelf Dynamics in a Western Boundary Current Regime: Implications for Upwelling. Journal of Physical Oceanography, 43(5), pp. doi:10.1175/JPO-D-12-0177.1.

Schiebel, R. et al., 2018. Advances in planktonic foraminifer research: New perspectives for paleoceanography. Revue de Micropaléontologie, 61(3-4), pp. 113-138.

Schlosser, C. et al., 2014. Seasonal ITCZ migration dynamically controls the locations of the (sub)tropical Atlantic biogeochemical divide. PNAS, 11(4), pp. 1438-1442.

Schmidt, G., Bigg, G. & Rohling, E., 1999. Global Seawater Oxygen-18 Database - v1.22. p. https://data.giss.nasa.gov/o18data/.

Schmidt, H. & Medina, R., 1991. Possibilities and scope of the double isotope effect method in the elucidation of mechanisms of enzyme catalyzed-reactions. Isotopenpraxis, Volume 27, pp. 1-4.

Scholz, F. et al., 2014. The impact of ocean deoxygenation on iron release from continental margin sediments. Nature Geoscience Letters, p. DOI: 10.1038/NGEO2162.

Schott, F. & Fieux, M., 1985. The Somali Current in autumn 1984, before the onset of the north-east monsoon. Nature, Volume 315, pp. 50-52.

Schubert, R. et al., 2019a. The Submesoscale Kinetic Energy Cascade: Mesoscale Absorption of Submesoscale Mixed Layer Eddies and Frontal Downscale Fluxes. Journal of Physical Oceanography, Volume 50, pp. DOI: 10.1175/JPO-D-19-0311.1.

Sharp, Z., 2017. Principles of Stable Isotope Geochemistry. Second ed. s.l.:doi.org/10.25844/h9q1-0p82.

Shcherbina, A., Gregg, M., Alford, M. & Harcourt, R., 2009. Characterizing Thermohaline Intrusions in the North Pacific Subtropical Frontal Zone. Journal of Physical Oceanography, Volume 39, p. doi:10.1175/2009JPO4190.1.

Shiozaki, T. et al., 2014. Heterotrophic bacteria as major nitrogen fixers in the euphotic zone of the Indian Ocean. Global Biogeochemical Cycles, Volume 28, p. DOI:10.1002/2014GB004886.

Shiozaki, T. et al., 2015. Trichodesmium and nitrogen fixation in the Kuroshio. Biogeosciences, Volume 12, pp. doi:10.5194/bgd-12-11061-2015.

Shiozaki, T. et al., 2017. Basin scale variability of active diazotrophs and nitrogen fixation in the North Pacific, from the tropics to the subarctic Bering Sea. Global Biogeochemical Cycles, Volume 31, p. doi.org/10.1002/2017GB005681.

Shulenberger, E. & Reid, J., 1981. The Pacific shallow oxygen maximum, deep chlorophyll maximum, and primary productivity, reconsidered. Deep Sea Research A Oceanographic Papers, 28(9), pp. doi.org/10.1016/0198-0149(81)90009-1.

Siefert, R., Johansen, A. & Hoffmann, M., 1999. Chemical characterization of ambient aerosol collected during the southwest monsoon and intermonsoon seasons over the Arabian Sea: Labile-Fe(II) and other trace metals. Journal of Geophysical Research, Volume 104, p. doi.org/10.1029/1998JD100067.

Siegenthaler, U. & Wenk, T., 1984. Rapid atmospheric CO2 variations and ocean circulation. Nature, Volume 308, p. doi.org/10.1038/308624a0.

Sigman, D. & Fripiat, F., 2019. Ocean Process Tracers: Nitrogen Isotopes in the Ocean. In: J. Steele, ed. Encyclopaedia of Ocean Sciences . New York: Academic Press, pp. 263-278.

Sigman, D. & Hain, M., 2012. The Biological Productivity of the Ocean. Nature Education, 3(10).

Sigman, D. et al., 1999a. The isotopic composition of diatom-bound nitrogen in Southern Ocean Sediments. Paleoceanography and Paleoclimatology, Volume 14, p. doi.org/10.1029/1998PA900018.

Sigman, D. et al., 1999b. The d15N of nitrate in the Southern Ocean: Consumption of nitrate in surface waters. Global Biogeochemical Cycles, 13(4), pp. 1149-1166.

Sigman, D. et al., 2000. The δ15N of nitrate in the Southern Ocean: Nitrogen cycling and circulation in the ocean interior. Journal of Geophysical Research, 105(C8), pp. 19599-19614.

Sigman, D. et al., 2001. A bacterial method for the nitrogen isotopic analysis of nitrate in seawater and freshwater. Analytical Chemistry, 73(17), pp. 4145-4153.

Sigman, D. et al., 2005. Coupled nitrogen and oxygen isotope measurements of nitrate along the eastern North Pacific margin. Global Biogeochemical Cycles, Volume 19, p. DOI: 10.1029/2005GB002458.

Sigman, D. et al., 2009. The dual isotopes of deep nitrate as a constraint on the cycle and budget of oceanic fixed nitrogen. Deep-Sea Research I, Volume 56, pp. 1419-1439.

Sigman, D. et al., 2009a. Sinking organic matter spreads the nitrogen isotope signal of pelagic denitrification in the North Pacific.. Geophysical Research Letters, 36(L08605).

Sigman, D., Hain, M. & Haug, G., 2010. The polar ocean and glacial cycles in atmospheric CO(2) concentration. Nature Review, Volume 1, p. doi:10.1038/nature09149.

Sigman, D., Karsh, K. & Casciotti, K., 2009c. Ocean process tracers: nitrogen isotopes in the ocean. In: Elsevier, p. 4138-4152

Singh, A. et al., 2017. Niche construction by non-diazotrophs for N2 fixers in the eastern tropical North Atlantic Ocean. Geophysical Research Letters, Volume 44, p. doi:10.1002/2017GL074218.

Sloyan, B. & Rintoul, S., 2001. Circulation, Renewal, and Modification of Antarctic Mode and Intermediate Water. Journal of Physical Oceanography, 31(4).

Smart, S. et al., 2015. Isotopic evidence for nitrification in the Antarctic winter mixed layer. Global Biogeochemical Cycles, Volume 29, p. DIO:10.1002/2014GB005013.

Smart, S. et al., 2018. Ground-truthing the planktic foraminifer-bound nitrogen isotope paleo-proxy in the Sargasso Sea. Geochemica et Cosmochimica Acta, Volume 235, p. doi.org/10.1016/j.gca.2018.05.023.

Smart, S. M. et al., 2020. The Nitrogen Isotopic Composition of Tissue and Shell-Bound Organic Matter of Planktic Foraminifera in Southern Ocean Surface Waters. Geochemistry, Geophysics; Geosystems, Volume 21, p. doi.org/ 10.1029/2019GC008440.

Smith, J., Chavez, F. & Francis, C., 2014. Ammonium Uptake by Phytoplankton Regulates Nitrification in the Sunlit Ocean. PLoS ONE, 9(9), p. doi.org/10.1371/journal.pone.0108173.

Smith, R., Huyer, A., Godfrey, J. & Church, J., 1991. The Leeuwin Current off western Australia. Journal of Physical Oceanography, Volume 21, pp. 322-345.

Smith, S., 1984. Phosphorus versus nitrogen limitation in the marine environment. Limnology and Oceanography, 29(1149-1160).

Snow, J. et al., 2015. Environmental controls on the biogeography of diazotrophy and Trichodesmium in the Atlantic Ocean. Global Biogeochemical Cycles, Volume 29, p. doi:10.1002/ 2015GB005090.

Sohm, J. & Capone, D., 2006. Phosphorus dynamics of the tropical and subtropical north Atlantic: Trichodesmium spp. versus bulk plankton. Marine Ecological Progress Series, Volume 317, p. doi:10.3354/meps317021.

Sohm, J. et al., 2011. Nitrogen fixation in the South Atlantic Gyre and the Benguela Upwelling System. Geophysical Research Letters, 38(L16608), p. doi:10.1029/2011GL048315.

Sohm, J., Webb, E. & Capone, D., 2011a. Emerging patterns of marine nitrogen fixation. Nature Reviews Microbiology, Volume 9, p. doi:10.1038/nrmicro2594.

Somes, C. & Oschlies, A., 2015. On the influence of “non-Redfield” dissolved organic nutrient dynamics on the spatial distribution of N2 fixation and the size of the marine fixed nitrogen inventory. Global Biogeochemical Cycles, Volume 29, p. doi:10.1002/2014GB005050.

Somes, C. et al., 2010. Simulating the global distribution of nitrogen isotopes in the ocean. Global Biogeochemical Cycles, Volume 24, p. doi:10.1029/2009GB003767.

Somes, C., Landolfi, A., Koeve, W. & Oschlies, A., 2016. Limited impact of atmospheric nitrogen deposition on marine productivity due to biogeochemical feedbacks in a global ocean model. Geophysical Research Letters, Volume 43, p. doi:10.1002/2016GL068335.

Souza, J., Montégut, C. d. M., Cabanes, C. & Klein, P., 2011. Estimation of the Agulhas ring impacts on meridional heat fluxes and transport using ARGO floats and satellite data. Geophysical Research Letters, Volume 38, p. doi:10.1029/2011GL049359.

Speich, S., Blanke, B. & Cai, W., 2007. Atlantic meridional overturning circulation and the Southern Hemisphere supergyre. Geophysical Research Letters, Volume 34, p. doi.org/10.1029/2007GL031583.

Srokosz, M. et al., 2015. Could the Madagascar bloom be fertilized by Madagascan iron?. Journal of Geophysical Research: Oceans, Volume 120, pp. 5790-5803.

Staal, M., Meysman, F. & Stal, L., 2003. Temperature excludes N2-fixing heterocystous cyanobacteria in the tropical oceans. Nature, Volume 425, pp. 504-507.

Stanley, R., Jenkins, W., Doney, S. & III, E. L., 2015. The 3He flux gauge in the Sargasso Sea: A determination of physical nutrient fluxes to the euphotic zone at the Bermuda Atlantic Time-series Site. Biogeosciences, Volume 12, pp. doi:10.5194/bg-12-5199-2015.

Stramma, L. & England, M., 1999. On the water masses and mean circulation of the South Atlantic Ocean. Journal of Geophysical Research, 104(C9), pp. 20863-20883.

Stramma, L. & Lutjeharms, J., 1997. The flow field of the subtropical gyre of the South Indian Ocean. Journal of Geophysical Research, 102(C3), pp. 5513-5530.

Stramma, L. & Schott, F., 1999. The mean flow field of the tropical Atlantic Ocean. Deep-Sea Research II, Volume 46, pp. 279-303.

Stramma, L., Johnson, G., Sprintall, J. & Mohrholz, V., 2008. Expanding Oxygen-Minimum Zones in the Tropical Oceans. Science, Volume 320.

Stramska, M. & Cieszyńska, A., 2015. Ocean colour estimates of particulate organic carbon reservoirs in the global ocean – revisited. International Journal of Remote Sensing, Volume 34, p. DOI:10.1080/01431161.2015.1049380.

Straub, M. et al., 2013. Changes in North Atlantic nitrogen fixation controlled by ocean circulation. Nature, Volume 501, p. doi.org/10.1038/nature12397.

Strickland, J. & Parsons, T., 1972. A practical handbook of seawater analysis. second ed. Ottawa: Fisheries Research Board of Canada.

Studer, A. et al., 2013. Size-specific opal-bound nitrogen isotope measurements in North Pacific sediments. Geochimica et Cosmochimica Acta, Volume 120, p. doi.org/10.1016/j.gca.2013.06.041.

Subramaniam, A., Mahaffey, C., Johns, W. & Mahowald, N., 2013. Equatorial upwelling enhances nitrogen fixation in the Atlantic Ocean. Geophysical Research Letters, Volume 40, pp. 1766-1771; doi:10.1002/grl.50250.

Swart, N., Lutjeharms, J., Ridderinkhof, H. & de Ruijter, W., 2010. Observed characteristics of Mozambique Channel eddies. Journal of Geophysical Research, 115(C09006), p. doi:10.1029/2009JC005875.

Tagliabue, A. et al., 2010. Hydrothermal contribution to the oceanic dissolved iron inventory. Nature Geoscience, Volume 3, p. doi.org/10.1038/ngeo818.

Tagliabue, A. et al., 2016. How well do global ocean biogeochemistry models simulate dissolved iron distributions?. Global Biogeochemical Cycles, Volume 30, p. doi:10.1002/2015GB005289.

Tagliabue, A. et al., 2019. The interplay between regeneration and scavenging fluxes drives ocean iron cycling. Nature Communications, Volume 10, pp. doi.org/10.1038/s41467-019-12775-5.

Takahashi, T. et al., 2009. Climatological mean and decadal changes in surface ocean pCO2, and net sea-air CO2 flux over the global oceans. Deep-Sea Research II, Volume 56, p. doi.org/10.1016/j.dsr2.2008.12.009.

Talley, L., 2013. Closure of the global overturning circulation through the Indian, Pacific, and Southern Oceans: Schematics and transports. Oceanography, 26(1), p. doi.org/10.5670/oceanog.2013.07.

Talley, L., Pickard, G., Emery, W. & Swift, J., 2011. Descriptive Physical Oceanography. 6th edition ed. s.l.: Elsevier Ltd.

Tang, W. et al., 2019. Revisiting the distribution of oceanic N2 fixation and estimating diazotrophic contribution to marine production. Nature Communication, Volume 10, pp. doi-org.ezproxy.uct.ac.za/10.1038/s41467-019-08640-0.

Tedesco, P. et al., 2019. Generation of Submesoscale Frontal Eddies in the Agulhas Current. Journal of Geophysical Research: Oceans, Volume 124, p. doi.org/10.1029/2019JC015229.

Tew-Kai, E. & Marsac, F., 2009. Patterns of variability of sea surface chlorophyll in the Mozambique Channel: a quantitative approach. Journal of Marine Systems, Volume 77, p. doi:10.1016/j.jmarsys.2008.11.007.

Thomas, L., Taylor, J., Ferrari, R. & Joyce, T., 2013. Symmetric instability in the Gulf Stream. Deep-Sea Research II, Volume 91, p. doi.org/10.1016/j.dsr2.2013.02.025.

Toole, J. & Warren, B., 1993. A hydrographic section across the subtropical South Indian Ocean. Deep-Sea Research Part I, Volume 40, pp. 1973-2019.

Tsuchiya, M., Talley, L. & McCartney, M., 1994. Water-mass distributions in the western South Atlantic: A section from South Georgia Island (54S) northward across the equator. Journal of Marine Research, Volume 52, pp. 55-81.

Tuerena, R. et al., 2015. Nutrient cycling in the Atlantic basin: The evolution of nitrate isotope signatures in water masses. Global Biogeochemical Cycles, volume 29, doi:10.1002/2015GB005164.

Uz, B., 2007. What causes the sporadic phytoplankton bloom southeast of Madagascar?. Journal of Geophysical Research, 112(C09010), p. doi:10.1029/2006JC003685.

Vieira, L. et al., 2020. Unprecedented Fe delivery from the Congo River margin to the South Atlantic Gyre. Nature Communications, 11(556).

Volk, T. & Hoffert, M., 1985. Ocean carbon pumps: analysis of relative strengths and efficiencies in ocean-driven atmospheric CO2 changes. AGU Washington, The carbon cycle and atmospheric CO2: natural variations Archean to Present.

Voss, M. et al., 2013. The marine nitrogen cycle: recent discoveries, uncertainties and the potential relevance of climate change. Philosophical Transactions of the Royal Society; Biological Sciences, Volume 368, p. doi:10.1098/rstb.2013.0121.

Wada, E. & Hattori, A., 1976. Natural abundance of 15N in particulate organic matter in the north Pacific Ocean. Geochimica et Cosmochimica Acta, 40(2), pp. 249-251.

Wada, E. & Hattori, A., 1978. Nitrogen isotope effects in the assimilation of inorganic nitrogenous compounds. Geomicrobiology, Volume 1, p. doi.org/10.1080/01490457809377725.

Walker, N., 1986. Satellite observations of the Agulhas Current and episodic upwelling south of Africa. Deep-Sea Research, Volume 33A, pp. doi:10.1016/0198-0149(86)90032-4.

Wallschuss, S. et al., 2022. The influence of Agulhas leakage on primary production and nitrogen cycling in the southeastern Atlantic Ocean. Journal of Geophysical Research: Oceans, p. doi.org/10.1029/2022JC018971.

Wang, W., Moore, K., Martiny, A. & Primeau, F., 2019. Convergent estimates of marine nitrogen fixation. Nature Article, Volume 566, pp. 205-211.

Wang, X. T. et al., 2015. Isotopic composition of skeleton-bound organic nitrogen in reef-building symbiotic corals: A new method and proxy evaluation at Bermuda. Geochimica et Cosmochimica, Issue 143, p. doi.org/10.1016/j.gca.2014.09.017.

Wang, X. T., Cohen, A., Luu, V. & Sigman, D., 2018. Natural forcing of the North Atlantic nitrogen cycle in the Anthropocene. Proceedings of the National Academy of Sciences, Volume 115, p. doi.org/10.1073/pnas.1801049115.

Wankel, S. et al., 2007. Nitrification in the euphotic zone as evidenced by nitrate dual isotopic composition: Observations from Monterey Bay, California. Global Biogeochemical Cycles, Volume 21, p. doi:10.1029/2006GB002723.

Ward, B., 1985. Light and substrate concentration relationships with marine ammonium assimilation and oxidation rates. Marine Chemistry, 16(4), pp. doi.org/10.1016/0304-4203(85)90052-0.

Waser, N. A. D., Harrison, P. J., B. Nielsen, S. E. C. & Turpin, D. H., 1998. Nitrogen isotope fractionation during the uptake and assimilation of nitrate, nitrite, ammonium, and urea by a marine diatom. Limnology & Oceanography, Volume 43, p. doi.org/10.4319/lo.1998.43.2.0215.

Waser, N. et al., 1998. Nitrogen isotope fractionation during nitrate, ammonium and urea uptake by marine diatoms and coccolithophores under various conditions of N availability. Marine Ecology Progress Series, Volume 169, pp. 29-41.

Wasmund, N. et al., 2015. Missing nitrogen fixation in the Benguela region. Deep-Sea Research I, Volume 106, p. doi.org/10.1016/j.dsr.2015.10.007.

Watson, A. J. et al., 2020. Revised estimates of ocean-atmosphere CO2 flux are consistent with ocean carbon inventory. Nature Communications, Volume 11, pp. doi.org/10.1038/s41467-020-18203-3.

Weber, T. & Deutsch, C., 2010. Ocean nutrient ratios governed by plankton biogeography. Nature, Volume 467, pp. 550-554.

Weber, T. & Deutsch, C., 2012. Oceanic nitrogen reservoir regulated by plankton diversity and ocean circulation. Nature Letters, Volume 489, p. doi:10.1038/nature11357.

Weber, T. & Deutsch, C., 2014. Local versus basin-scale limitation of marine nitrogen fixation. PNAS, 111(24), pp. 8741-8746.

Weigand, A. et al., 2016. Updates to instrumentation and protocols for isotopic analysis of nitrate by the denitrifier method. Rapid Communication in Mass Spectrometry: Protocol, Volume 30, p. doi.10.1002/rcm.7570.

Wen, Z. et al., 2022. Nutrient regulation of biological nitrogen fixation across the tropical western North Pacific. Science Advances, Volume 8, p. doi:10.1126/sciadv.abl7564.

White, A. et al., 2013. Nitrogen fixation in the Gulf of California and the Eastern Tropical North Pacific. Progress in Oceanography, Volume 109, p. doi.org/10.1016/j.pocean.2012.09.002.

White, A. et al., 2020. A critical review of the 15N2 tracer method to measure diazotrophic production in pelagic ecosystems. Limnology and Oceanography: Methods, Volume 18, p. doi:10.1002/lom3.10353.

White, A., Spitz, Y., Karl, D. & Letelier, R., 2006. Flexible elemental stoichiometry in Trichodesmium spp. and its ecological implications. Limnology and Oceanography, 51(4), pp. 1777-1790.

White, A., Watkins-Brandt, K. & Church, M., 2018. Temporal Variability of Trichodesmium spp. and Diatom-Diazotroph Assemblages in the North Pacific Subtropical Gyre. Frontiers in Marine Science, Volume 5, p. doi.org/10.3389/fmars.2018.00027.

Williams, R. & Follows, M., 1998. The Ekman transfer of nutrients and maintenance of new production over the North Atlantic. Deep-Sea Research I, Volume 45, pp. doi:10.1016/S0967-0637(97)00094-0.

Williams, R. & Follows, M., 2003. Chapter 2: Physical Transport of Nutrients and the Maintenance of Biological Production. In: M. Fasham, ed. Ocean Biogeochemistry. s.l.: Springer, pp. 19-51.

Williams, R., Roussenov, V. & Follows, M., 2006. Nutrient streams and their induction into the mixed layer. Global Biogeochemical Cycles, 20(1), p. doi:10.1029/2005gb002586.

Wong, A., 2005. Subantarctic Mode Water and Antarctic Intermediate Water in the South Indian Ocean based on profiling float data 2000–2004. Journal of Marine Research, Volume 63, p. DOI:10.1357/0022240054663196.

Wrightson, L. & Tagliabue, A., 2020. Quantifying the Impact of Climate Change on Marine Diazotrophy: Insights From Earth System Models. Frontiers in Marine Science, Volume 7, p. doi.org/10.3389/fmars.2020.00635.

Wu, C. et al., 2018. Nitrogen Fixation by Trichodesmium and unicellular diazotrophs in the northern South China Sea and the Kuroshio in summer. Nature Scientific Reports, Volume 8, pp. doi:10.1038/s41598-018-20743-0.

Wyrtki, K., 1971. Oceanographic Atlas of the International Indian Ocean Expedition, Washington D.C.: National Science Foundation.

Yamamoto, A. et al., 2018. Roles of the Ocean Mesoscale in the Horizontal Supply of Mass, Heat, Carbon, and Nutrients to the Northern Hemisphere Subtropical Gyres. Journal of Geophysical Research: Oceans, Volume 123, p. https://doi.org/10.1029/2018JC013969.

Yang, S. & Gruber, N., 2016. The anthropogenic perturbation of the marine nitrogen cycle by atmospheric deposition: Nitrogen cycle feedbacks and the 15N Haber-Bosch effect. Global Biogeochemical Cycles, Volume 30, p. doi:10.1002/2016GB005421.

Yool, A., Martin, A., Fernández, C. & Clark, D., 2007. The significance of nitrification for oceanic new production. Nature Letters, Volume 447, p. doi:10.1038/nature05885.

Yu, L. & Weller, R., 2007. Objectively Analyzed Air-Sea Heat Fluxes for the Global Ice-Free Oceans (1981-2005). American Meteorological Society, 88(4), pp. DOI:0.1175/BAMS-88-4-527.

Zehr, J. & Capone, D., 2021. Marine Nitrogen Fixation. doi.org/10.1007/978-3-030-67746-6 ed. s.l.:Springer.

Zhang, R. et al., 2020. Dissolved Organic Nitrogen Cycling in the South China Sea From an Isotopic Perspective. Global Biogeochemical Cycles, Volume 34, p. doi.org/10.1029/2020GB006551.

Zhang, Y., Xu, H., Qiao, F. & Dong, C., 2018. Seasonal variation of the global mixed layer depth: comparison between Argo data and FIO-ESM. Frontiers in Earth Science, Volume 12, pp. doi.org/10.1007/s11707-017-0631-6.